4. Site 1173[1]

Shipboard Scientific Party[2]

SITE SUMMARY

We drilled Site 1173 in the trench outer margin in order to provide a reference for the predeformation status of geological and geochemical characteristics of the incoming sedimentary section. We recognized five lithostratigraphic units: Unit I (0 to 102 meters below seafloor [mbsf]) is Quaternary in age and composed of sandy to muddy turbidites and hemipelagic mud of the outer Nankai trench–wedge facies. Unit II (102 to 344 mbsf) is Quaternary to Pliocene in age and made up of hemipelagic mud with abundant interbeds of volcanic ash that were probably derived from the Kyushu and/or Honshu volcanic arcs (upper Shikoku Basin facies). Unit III (344 to 688 mbsf) consists of Pliocene to middle Miocene bioturbated silty claystone (lower Shikoku Basin facies). The boundary between Units II and III is controlled, in part, by diagenesis. Unequivocal ash beds are abruptly lost and are replaced downsection by siliceous claystones. Unit IV (688 to 725 mbsf) is probably of middle Miocene age and is composed of variegated siliceous claystone and silty claystone (volcaniclastic facies). Unit V (725 mbsf) is middle Miocene basalt.

Biostratigraphic ages provided by calcareous nannofossils indicate a total of 25 biostratigraphic events. The continuous sedimentary section spans the time interval from the Pleistocene (Subzone NN21b) through the middle Miocene (Zone NN5). Magnetostratigraphy clearly identified the Bruhnes/Matuyama boundary (0.78 Ma), Matuyama/Gauss boundary (2.581 Ma), the Gauss/Gilbert boundary (3.58 Ma), and the termination of the Gilbert Chron (5.894 Ma). Paleomagnetic and biostratigraphic ages indicate high sedimentation rates (450–650 m/m.y.) for the turbidite deposits, decreasing rates for the upper Shikoku Basin section (72–77 m/m.y.), and lowest rates for the lower Shikoku Basin section (27–37 m/m.y.).

Deformation structures at Site 1173 are sparse, as expected from a reference site oceanward of the prism. The section above 375 mbsf is characterized by horizontal bedding with occasional steeper dips and microfaults between 250 and 275 mbsf. Bedding dips exceeding 30°, perhaps due to lateral extension associated with normal faulting, occur abruptly at 375 mbsf and continue down to 550 mbsf and sporadically to the bottom of the hole. A 30-cm zone of foliated breccia indicates somewhat greater deformation at ~440 mbsf. Deeper cores contain rare mineralized veins; a few possible dewatering structures such as thin, sediment-filled veins reflect early compaction processes.

Variations in physical properties correlate well with the lithostratigraphic units. High variability characterizes the turbidites of the outer Nankai Trench wedge, and porosities decrease with depth. Porosity increases at the boundary between the outer Nankai Trench wedge and the upper Shikoku Basin facies and continues to increase slightly with depth. These elevated porosities deviate from a typical compaction profile. An increase in P-wave velocities within this interval of increasing porosity suggests that there may be slight cementation. At the boundary between the upper and lower Shikoku Basin facies (~340 mbsf), grain densities increase slightly and porosities decrease sharply. This porosity decrease is accompanied by increasing thermal conductivity, P-wave velocity, and resistivity. A gas-probe permeameter showed that ash bands in the upper Shikoku Basin sediments are several orders of magnitude more permeable than the hemipelagites, although the contrast disappears in the lower Shikoku Basin section.

Seven reliable determinations of downhole temperatures were made at depths of 35 to 284 mbsf in Hole 1173A, using the advanced hydraulic piston corer (APC) temperature tool, water-sampling temperature probe (WSTP), and Davis-Villinger temperature probe (DVTP). The measured temperatures closely define a linear gradient of 0.183°C/m in the upper 300 m, where the average measured thermal conductivity is ~1.0 W/(m·°C), yielding a conductive heat flow of ~180 mW/m² at Site 1173. Deeper than 300 m, thermal conductivities increase by 30%–50%, so the gradient should decrease proportionally. In situ temperatures of ~110°C are estimated for the bottom of the hole—similar to the basement temperature estimated for Site 808. The heat flow value is somewhat higher than prior determinations of high heat flow near the site and greater than the predicted heat transfer for the 15-m.y. crustal age.

A high-resolution pore fluid concentration-depth profile shows that the pore fluid chemistry has been extensively modified from seawater by both microbially mediated reactions and by abiological, inorganic fluid-rock reactions. The chemical modifications from the microbially mediated reactions provide crucial independent information on the depth range, intensity, and nature of microbial activity in the deep subsurface. Each inorganically controlled dissolved species analyzed (i.e., Cl, Ca, Mg, SiO_2, K, and Na) shows a distinct to sharp discontinuity at 340 mbsf, which corresponds to the lithologic boundary between Units II and III. Furthermore, minima in Cl and Na concentrations and significant inflections in the Mg and Ca profiles occur at ~380–390 mbsf. These features suggest that this horizon may be hydrologically active. A broad ~350-m-thick low-Cl zone within Unit III, with ~9% dilution relative to seawater, requires a source of low-Cl fluid. The geometric similarities between this low-Cl zone and that at Ocean Drilling Program (ODP) Site 808 are striking, except that at Site 808 the dilution relative to seawater is more than twice that observed at this site.

Total organic carbon (TOC) values are low (average = 0.35 wt%) and decrease with depth (0.85 to 0.20 wt%). The C/N ratios indicate the presence of marine organic matter throughout the hole and show a slight increase in the lower ~200 m. The low sulfate and high methane concentrations in the upper section below the sulfate reduction zone are consistent with a bacterial origin. The increase in sulfate concentrations from ~400 to 700 mbsf coupled with the low concentrations of methane may indicate that sulfate is inhibiting production of hydrocarbons that were more abundant at Site 808. The presence of low concentrations of light hydrocarbons (ethane and propane) below 300 mbsf to total depth may be due to some in situ thermal maturation of kerogen in the sediments. The low concentrations of methane at depth and the lack of evidence for any migration of hydrocarbons from above the facies transition (347.3 mbsf) support these conclusions. The microbes observed (~480 mbsf) at temperatures above 90°C in the presence of elevated sulfate concentrations suggest that methanogenesis due to microbial activity is not completely inhibited, although at these temperatures, thermogenic hydrocarbons are likely being produced.

Samples taken for bacterial enumeration show that bacteria are present in all samples to 500 mbsf and thereafter are absent (the detection limit is 4.75×10^5). The population profile generally follows the average line obtained from other ODP sites for the upper 250 m of the hole with a rapid decrease in population size in the upper few meters as the sulfate was depleted. Between 43 and 80 mbsf, there is a significant (sevenfold) increase in bacterial numbers coincident with elevated methane concentrations. At 250 mbsf, there is both a temperature boundary for bacteria (45°–50°C; the change from mesophilic to thermophilic populations) and significant differences in interstitial water (IW) chemistry, which complicates interpretation. Further changes occur in IW chemistry at a lithologic boundary at 343 mbsf. Between 250 and 460 mbsf, bacterial numbers are lower than average. Another microbiological temperature boundary (thermophilic to hyperthermophilic populations) occurs at 460 mbsf as temperatures exceed 80°C. One positive enumeration was made in this zone at 500 mbsf and ~85°C, where populations increase by a factor of 13. At this depth there were relatively high concentrations of organic carbon plus increasing concentrations of sulfate, methane, and hydrogen that could support a deep hyperthermophilic population of sulfate-reducing bacteria.

Tracer tests were successfully carried out on two APC cores and two extended core barrel (XCB) cores with both perfluorocarbon tracer (PFT) and fluorescent microspheres. PFT was detected in the center and midway between the center and the outside in some APC core sections; however, PFT was absent from the center of the XCB core sections. In contrast, microspheres were generally absent in samples taken midway between the center and the outside of the core in both APC cores and one of the XCB cores and were only present in the centers of some of the XCB core sections. These results suggest that intrusion of microspheres into the center of the cores was a result of postrecovery handling and not diffusion of drilling fluid during coring. This is the first time fluorescent microsphere tracers have been used during the collection of cores with the XCB.

Hole 1173A was logged with both the triple combination logging string (spectral gamma ray, dual-induction resistivity, lithodensity, and neutron porosity tools) and the Formation MicroScanner (FMS) and dipole sonic imager (DSI) tools. The interval from 65 to 373 mbsf was logged in two passes, and high-quality compressional and shear travel

time data and FMS images were acquired. During the second pass, a new low-frequency (<1 kHz) dipole source was used on the DSI and produced excellent shear waveforms despite the very low formation velocity. Logging results are generally consistent with the homogeneous hemipelagic core lithology, with few identifiable lithologic boundaries in the logged interval. Density is low from 97 to 336 mbsf, with a slight gradual decrease with depth and then a sharp increase in the 358- to 440-mbsf interval. Compressional and shear wave velocities are nearly constant with depth to 225 mbsf and then increase with depth. Velocities decrease sharply in the short logged interval below 348 mbsf, corresponding to the Unit II/III boundary. Numerous ash layers and other sedimentologic and diagenetic features observed in the cores were well imaged by both FMS passes, which should permit high-resolution core-log integration.

OPERATIONS

Transit from Guam
to Proposed Site ENT-01A (Site 1173)

The 1210-kt transit from Guam to proposed Site ENT-01A (Site 1173) was accomplished at an average speed of 11.8 kt in 4.25 days. During the transit, the drilling and coring equipment were prepared. A variety of repairs to the accommodations were made during the transit, including replacement of some of the ceiling tiles in the hotel hallways, replacement of sinks and toilets, painting, and so forth. The clocks were turned back 1 hr at midnight on the night of 27 May so the ship would be on Japan local time.

When approaching the site, the ship slowed from transit speed to ~5 kt to conduct a seismic reflection survey that covered 48 nmi and lasted 9.8 hr (Figs. F1, F2). Once the survey passed over proposed Site ENT-01A (Site 1173), the seismic gear was retrieved and the vessel moved to the Global Positioning System (GPS) coordinates of the site. Once over the GPS coordinates, a seafloor positioning beacon was dropped at 1202 hr on 28 May, establishing Site 1173.

Site 1173

After the hydrophones and thrusters were lowered and the vessel settled on location, the precision depth recorder indicated a water depth of 4794.4 meters below rig floor (mbrf). An eight-collar APC/XCB bottom-hole assembly (BHA) was made up with a 9.875-in polycrystalline diamond compact bit, lockable float valve (LFV), seal bore drill collar, landing saver sub, top sub, head sub, nonmagnetic drill collar, five 8.25-in drill collars, one tapered drill collar, six joints of 5.5-in drill pipe, and a crossover sub to 5-in drill pipe. Once the BHA was made up it was run down to the seafloor. Running the drill string to the seafloor took longer than usual because of the measuring and internal clearance inspection (strapping and rabbiting) that is routinely performed during the first deployment of the drill string during a leg. The pipe trip down to the seafloor was also interrupted for an hour while the active heave compensator (AHC) hydraulic umbilical sheath was repaired.

Once the bit was near the seafloor at 4780 mbrf and before we circulated any seawater through the drill string, the WSTP was deployed to

F1. Location of the *JOIDES Resolution* seismic profile, p. 38.
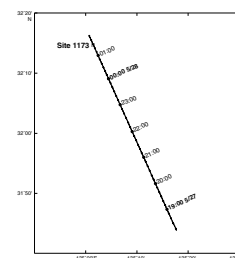
F2. Single-channel seismic profile, p. 39.

obtain a water sample near the seafloor. Because the WSTP could not be pumped to bottom, ~3 hr was required to obtain the water sample.

Hole 1173A

After successfully obtaining a seafloor water sample, seawater was circulated through the drill string and a "pig" pumped through it to clean the interior of the drill pipe. The bit was placed at 4778.8 meters below sea level (mbsl) (4790 mbrf) and an APC was shot but did not recover any sediment. The bit was lowered to 4788.34 mbsl (4799.54 mbrf), the APC was shot again, and Hole 1173A was spudded at 1125 hr on 29 May. Core 1H recovered 7.14 m of core, indicating that the seafloor depth as determined by drill-pipe measurement was 4790.7 mbsl (4801.9 mbrf) (Tables T1, T2). APC coring continued to 225.6 mbsf (5027.5 mbrf), recovering 222.35 m of core (99%). Once the APC pull-out force reached 60,000 lbs, we switched to coring with the XCB.

We cored with the XCB from 225.6 to 734.3 mbsf (5027.5 to 5536.2 mbrf). A total of 53 XCB cores were taken over the 508.7-m interval, recovering 436.01 m of core for an overall XCB recovery of 86%. Although the XCB recovery was very good, the last four XCB cores recovered only 1.79 m (5% recovery). In addition, while we cored the last 7 m of the hole, the rate of penetration dropped to <5 m/hr and high erratic torque was experienced. When we lifted the bit off bottom, there was virtually no torque and the XCB cutting shoe was recovered in good condition; therefore, we presumed that the bit might have failed. At this point, we decided to stop coring and to log the hole. Subsequently, we found small pieces of basalt in the bottom of the last core, so we infer that the high and erratic torque may have been caused by rotating the bit on basaltic basement.

We circulated a 50-bbl pill of sepiolite mud to clean the hole of any cuttings and then filled it with sepiolite mud. The bit was raised to 95.12 mbsf (4897.0 mbrf), and the logging tools were rigged up. The triple combination tool (triple combo) was lowered in the hole but could not pass a bridge at 344.1 mbsf (5146 mbrf); therefore, we logged up from that point to the bit.

The logging tools were laid out, the drill string was lowered to 444.7 mbsf (5246.4 mbrf), and the drill string did not encounter any resistance when passing through the bridge. The bit was raised to 364.8 mbsf (5166.8 mbrf), and the logging tools were rigged up again. The triple combo was lowered down the drill string, and after having some trouble getting through the bit, it was able to reach 438.1 mbsf (5240.0 mbrf), where yet another bridge prevented the tool from passing any farther. Once again, the hole was logged from that point up to the bit. The logging tool had to be worked through the bit into the drill string. Once back inside the drill string, the logging tools were recovered and laid out.

The drill string was then lowered in an effort to clean out the hole. When the drill string was picked up off the slips, 70,000 lb of overpull was required to free the bit, which had become stuck in the hole. The drill string had to be worked with as much as 20,000 lb of overpull and set down weight to get to 637.1 mbsf (5439 mbrf), where the hole starting packing off. The drill string was then pulled to 628.1 mbsf (5430 mbrf), where 226 bbl of 10.5 ppg weighted mud was pumped to displace the hole. The drill string was then raised to 95 mbsf (4879 mbrf), and the logging tools were rigged up once more.

T1. Coring summary, p. 93.

T2. Coring summary by section, p. 95.

This final logging run included the sonic and FMS tools. This time the tools encountered a bridge at 378 mbsf (5180 mbrf), and we logged up from there. After the logging tools were recovered and laid out, we tripped the drill string back to the ship. Hole 1173A officially ended at 0445 hr on June 7 when the bit reached the rig floor.

LITHOSTRATIGRAPHY

We recognized five lithostratigraphic units at Site 1173 (Fig. F3) and correlated them with the lower five of six units at Site 808 (ODP Leg 131), located 13.5 km to the northwest (Table T3).

Unit I (Trench-Wedge Facies)

Unit I is Quaternary in age and extends from the seafloor to Section 190-1173A-12H-1, 0 cm, at a sub-bottom depth of 102.14 mbsf (Fig. F3). We recognized two subunits within this part of the stratigraphic succession. Subunit IA (outer trench–wedge facies) consists of 83.37 m of silty clay interbedded with silt, sandy silt, silty sand, and rare beds of volcanic ash (Fig. F4). The dominant lithology is greenish gray silty clay to clayey silt. This muddy sediment is typically homogeneous but may be faintly laminated or mottled as a result of bioturbation. The mud includes abundant clay minerals, quartz, and feldspar, with lesser amounts of volcanic glass, lithic fragments, and a variety of diatoms, sponge spicules, and radiolarians (see **"Site 1173 Smear Slides,"** p. 78). Layers of silty sand and silt range from medium bedded (10–30 cm) to very thin bedded (1–3 cm) or laminated (<1 cm); thick beds (>30 cm) are unusual. Lower contacts are sharp, plane parallel, scoured, or loaded. Grain size typically fines upward from medium sand to silt, and plane-parallel laminae are common in the upper parts of beds. Tops are gradational into overlying silty clay. The sand and silt deposits contain subrounded to subangular grains of quartz, feldspar, and lithic fragments together with lesser amounts of ferromagnesium minerals, volcanic glass, microfossils, and mica (see **"Site 1173 Smear Slides,"** p. 78). Fine-grained sulfide and framboidal pyrite are present throughout Subunit IA as a black mottling. Laminae to thin beds of volcanic ash are rare; one notable example of crystal-rich ash (at 36 mbsf) is a 31-cm-thick bed with normal grading.

Hemipelagic settling and fine-grained (muddy) turbidity currents probably deposited the silty clay to clayey silt of Subunit IA. Calcareous nannofossils are common in the muddy turbidites because of their rapid deposition and burial near the calcite compensation depth; hemipelagic mud, in contrast, contains few preserved nannofossils. We also interpret the silt and sand beds as thin tubidites. The overall character of Subunit IA is consistent with its depositional position on the outer trench floor, marginal to the trench axis. The unit is equivalent to Subunits IIB and IIC documented at Site 808 (Shipboard Scientific Party, 1991).

The base of Subunit IB (trench to basin transition facies) is defined by the deepest occurrence of medium-bedded silty sand (Section 190-1173A-12H-1, 0 cm). The top of the subunit is defined by the uppermost interval containing multiple ash layers (Section 190-1173A-10H-1, 23 cm). Subunit IB is 18.77 m thick and contains silty clay with scattered interbeds of silt- to clay-sized volcanic ash and rare volcanic lapilli (Fig. F3). The greenish gray silty clay to clayey silt is typically structure-

F3. Stratigraphic column, p. 40.
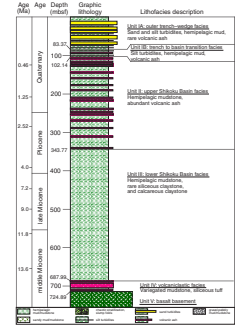
T3. Site 1173 stratigraphic units compared with correlative units at Site 808, p. 106.

F4. Distribution and thickness of volcanic ash layers, p. 41.
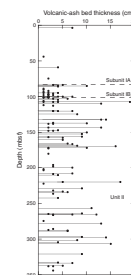
less with faint laminae of darker green color and rare, normally graded laminae. Ash layers range from laminae to very thin beds, with the latter typically showing normal grading (Figs. F4, F5). Contacts with overlying clayey silt are gradational.

Subunit IB is stratigraphically transitional between the upper Shikoku Basin facies and the outer trench–wedge facies. Deposition occurred predominantly by hemipelagic settling interrupted by sporadic influx of pyroclastic particles and siliciclastic turbidites. Subunit IB is equivalent to Unit III at Site 808 (Shipboard Scientific Party, 1991).

Unit II (Upper Shikoku Basin Facies)

Unit II is Pliocene to Quaternary in age and 343.77 m thick (Fig. F3). The most common lithology ranges in texture from silty clay to clayey silt and changes with increasing compaction to silty claystone and clayey siltstone. Interbeds of volcanic ash and tuff are common (Fig. F4). The deepest unequivocal ash bed (Section 190-1173A-37X-3, 3 cm) defines the base of Unit II (343.77 mbsf). Silty claystone to clayey siltstone in Unit II is typically massive or faintly laminated. Mottling caused by bioturbation is present throughout; *Zoophycos* trace fossils are common, and *Chondrites* trace fossils are rare. There are also scattered green laminae, pyrite nodules, clasts of pumice and scoria, and bundles of sponge spicules. The silty claystone of Unit II appears to be finer in grain size than equivalent lithologies of Unit I, and it contains fewer siliceous microfossils.

Volcanic ash and tuff layers are typically very thin bedded (1–2 cm) but are present in beds up to 25 cm thick with many beds 5 to 15 cm thick (Fig. F4). The ash layers have sharp, plane-parallel to irregular lower contacts and gradational upper contacts. Color varies considerably among and within volcanic ashes, ranging from pink, gray, and brown to green (Figs. F6, F7). Particle size varies from silt to coarse sand and gravel-sized lapilli. Many of the ash beds are normally graded although some coarsen upward and then fine upward (Fig. F6). Diffuse plane-parallel laminae are present in some ash layers. The volcanic debris is composed predominantly of clear, unaltered glass shards together with variable amounts of quartz, plagioclase, amphibole, opaque minerals, and pumice fragments (see "Site 1173 Smear Slides," p. 78).

Unit II represents the upper part of the Shikoku Basin succession. Deposition probably occurred by hemipelagic settling interrupted by pyroclastic particle settling from air falls. The most likely sources of ash are the volcanic centers of Kyushu and/or Honshu. This unit is equivalent to Subunit IVA at Site 808 (Shipboard Scientific Party, 1991).

Unit III (Lower Shikoku Basin Facies)

Unit III is Pliocene to middle Miocene in age and consists of 344.22 m of bioturbated silty claystone and minor calcareous and siliceous claystone (Fig. F3). The top of the unit is located immediately beneath the deepest unequivocal ash bed that contains fresh glass shards (343.77 mbsf). As at Site 808 (Shipboard Scientific Party, 1991), the upper tens of meters of the lower Shikoku Basin facies displays a gradational change from ash to siliceous claystone. Thus, the facies boundary is partially controlled by diagenesis.

The dominant lithology of silty claystone in Unit III is gray to greenish gray with local faint laminae. A characteristic mottled appearance was imparted by bioturbation. There are common *Zoophycos* and rare

F5. Sandy turbidite of Subunit IA interbedded with silty clay, p. 42.
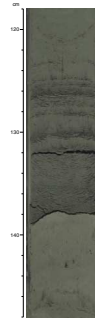
F6. Gray and green and pink and brown volcanic ash beds from Unit II interbedded with silty clays, p. 43.
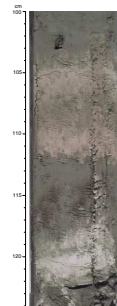
F7. Volcanic ash bed from Unit II interbedded with silty clays, p. 44.
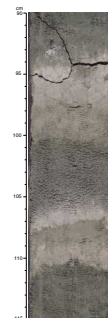
Chondrites trace fossils. Silty claystone of Unit III is devoid of siliceous microfossils, but calcareous nannofossils are locally abundant. Laminae to thin beds of siliceous claystone vary in color from pale gray to green and dark gray, and beds have sharp to diffuse or irregular contacts (Fig. F8). The siliceous claystone contains variable amounts of opaque grains, amphiboles, and zeolites in a groundmass of cryptocrystalline silica (see "Site 1173 Smear Slides," p. 78). In samples from the upper few tens of meters of Unit III, smear-slide observations show that some fragments of cryptocrystalline silica retain relict shapes indicative of altered volcanic glass shards. Also scattered throughout the middle and lower part of Unit III are pale brown carbonate-cemented intervals up to a few centimeters thick, as well as smaller nodules of calcite, dolomite, and siderite. We classified the layered intervals as carbonate-cemented claystone where they are continuous across the core width. The carbonate-rich beds have diffuse to sharp margins.

We regard the silty claystone of Unit III as a typical hemipelagic deposit that accumulated in the lower part of the Shikoku Basin. Two origins are likely for the carbonate-rich claystones: (1) diagenetic precipitation of carbonate cement to form nodules and (2) partial recrystallization of primary beds of nannofossil-rich pelagic ooze. Such primary beds of nannofossil chalk and calcareous claystone are relatively common in more distal portions of the Shikoku Basin (Shipboard Scientific Party, 1980), as well as on the nearby Kyushu-Palau Ridge to the west (Shipboard Scientific Party, 1975). The siliceous claystone also could have formed in more than one way. One possibility is diagenetic alteration of volcanic ash. We favor this interpretation where such components as opaque grains are common. Some of the more heavily altered examples, however, could be recrystallized beds of biogenic silica, as exemplified by coeval deposits in the Sea of Japan (Tamaki et al., 1990) and the Japan Trench (Shipboard Scientific Party, 1986b).

Unit IV (Volcaniclastic Facies)

Unit IV begins at a depth of 687.99 mbsf (Section 190-1173A-73X-2, 15 cm) and consists of 36.90 m of variegated siliceous claystone and silty claystone (Fig. F3). The probable age is middle Miocene, but recovery from this interval was very poor and heavily disrupted by drilling disturbance. Greenish gray to mottled green, maroon, and red silty claystone is interlayered with slurried intervals of siliceous claystone that range from very thin to medium bedded, green to pale gray, and clay sized to medium sand sized. The silty claystone contains calcareous nannofossils, clay minerals, and cryptocrystalline silica. In contrast, siliceous intervals contain more cryptocrystalline silica and opaque minerals. Thin bands of claystone at the base of Unit IV (interval 190-1173A-77X-CC, 20–25 cm) are variably and irregularly colored from pale gray to yellow to reddish brown (Fig. F9), partly a result of the formation of iron oxide cements.

Silty claystone of Unit IV is probably a hemipelagic deposit, whereas the light gray siliceous intervals appear to be altered volcaniclastic deposits. This interpretation is consistent with the recovery of 47 m of thick-bedded silicic volcaniclastic deposits at Site 808. This volcanism was linked to a middle Miocene episode of anomalous near-trench magmatism, as currently exposed in the Outer Zone of southwest Japan (Shipboard Scientific Party, 1991).

F8. Bioturbated silty claystone and interbedded siliceous claystone from Unit III, p. 45.

F9. Basalt (Unit V) and silty claystone (Unit IV), p. 46.

Unit V

The core catcher of Core 190-1173A-77X (724.89 mbsf) contains a 2-cm fragment of basalt (Fig. F9). By analogy with basalt from Site 808 (Shipboard Scientific Party, 1991), the probable age is middle Miocene (13–15 Ma). It is unclear whether or not this fragment was part of a basaltic breccia or lava flow. The basalt is porphyritic with euhedral plagioclase crystals up to 3 mm long in a partially altered glassy groundmass with abundant fine-grained radiating plagioclase crystals and clusters of oxides. Silty claystone of Unit IV, where adjacent to the basalt clast, displays a considerable amount of alteration, similar to sediment-basalt contacts documented in ridge-flank environments elsewhere (e.g., Davis et al., 1997).

X-Ray Diffraction Mineralogy

The results of X-ray diffraction (XRD) analyses of randomly oriented bulk-sediment powders are shown in Figure F10 (and listed in Tables T4 and T5). The mean values of relative mineral abundance in Unit I are quartz = 35%, plagioclase = 17%, calcite = 2%, and total clay minerals = 46%. Quartz content decreases slightly within Unit II (mean = 33%), whereas calcite content increases (mean = 9%). A gradual increase in quartz content begins near the boundary between Units II and III; this compositional gradient is followed by a reduction in quartz below 515 mbsf. Total clay-mineral content increases abruptly below the Unit II/Unit III boundary (mean = 54%). Calcite content is erratic in Unit III because of scattered nannofossil-rich beds and nodules of carbonate.

The peak-area ratio of (101) cristobalite to (100) quartz also changes with stratigraphic position (Fig. F10). The cristobalite to quartz ratio increases at ~200–220 mbsf. This depth coincides with a temperature of ~40°C, and the change in mineralogy is probably due to the transition from opal-A (amorphous silica) to opal-CT (cristobalite). The cristobalite to quartz ratio decreases at ~320–340 mbsf near the boundary between Units II and III. The depth of this shift occurs at a temperature of ~60°C.

XRD analysis of representative volcanic ash beds shows a clear transformation downsection from glass-rich deposits with crystals of plagioclase and quartz to smectite-rich claystone (Table T6). Other common minerals include cristobalite, calcite (from nannofossils), pyroxene, halite (from pore water), and pyrite.

STRUCTURAL GEOLOGY

Deformation structures at Site 1173 are sparse as expected for a site designed to be a reference site oceanward of the prism. Most of them were observed in Unit III, the lower Shikoku Basin sequence. Bedding dips <5° characterize the upper part of the hole; dips up to 25° were observed between ~375 and 550 mbsf and sporadically below this interval (Table T7; Fig. F11). It was often difficult, however, to detect actual bedding surfaces in the highly bioturbated hemipelagic sediments in the deeper units. The lack of systematic trends in bedding dips from core to core suggests that these dips are not due to hole deviation from vertical. Using paleomagnetic declination data (see "Paleomagnetism," p. 14), we were able to correct 42 bedding measurements to true geographic

F10. Abundances of clay minerals, quartz, plagioclase, and calcite, p. 47.
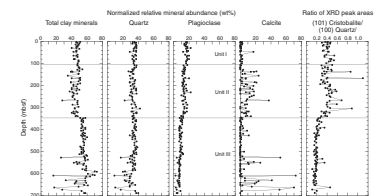
T4. Peak intensity and peak area XRD analyses, p. 107.

T5. Mineral abundances and peak-area ratios from XRD analyses, p. 111.

T6. X-ray diffraction analysis, Hole 1173A, p. 114.

T7. Structural data, p. 115.

F11. Bedding dips relative to the core liner plotted against depth, p. 48.
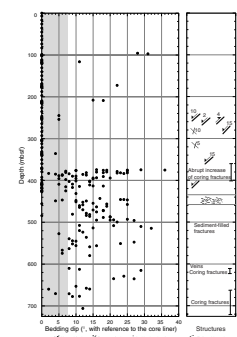
coordinates. The resulting distribution of poles to bedding shows scatter about vertical, but with a general north-south strike (Fig. F12).

Drilling disturbances, particularly biscuiting, fracturing, and brecciation, occurred throughout the cores, complicating identification of primary deformation structures. Moreover, many of these apparently artificial fractures are slickensided and lineated. However, several zones of breccia and planar, high-angle microfaults were observed entirely within coherent drill biscuits and hence were taken to be natural. The microfaults are concentrated between 250 and 275 mbsf (Fig. F11). Where displacement could be determined, the microfaults typically show a normal sense of movement on the order of 2–10 mm. At 270 mbsf, a healed fault showing apparent normal displacement is underlain by a zone of antithetic faults and chaotic breccia (e.g., interval 190-1173A-33X-4, 111–122 cm; Fig. F13). At ~440 mbsf, a 30-cm zone of foliated breccia, intensely broken in places and characterized by low-angle planar contacts between variably colored, elongate fragments of silty claystone, suggests a narrow interval of greater deformation extending from 190-1173A-47X-2, 140 cm, to 47X-3, 0–24 cm (Fig. F14). High-angle fractures are also present, one of which contains a white mineral, probably microcrystalline silica.

A few thin veins were observed below 500 mbsf. Sediment-filled veins, in one case associated with a possible fluid-escape structure (interval 190-1173A-53X-5, 90–97 cm; Fig. F15), crosscut and distort stratigraphic and diagenetic boundaries. A set of subvertical, white, mineralized extensional veins are present in a rare carbonate horizon at 615 mbsf (interval 190-1173A-65X-CC, 30–36 cm; Fig. F16). The white veins, possibly composed of calcite, extend across the carbonate layer and die out in the overlying silty claystone within a zone of fine mineralized pores. The veins crosscut a darker set of en echelon veinlike features (not visible in Fig. F16, being apparent only on the working half) with an apparent orientation perpendicular to the 41° dipping bedding plane.

In general, the deformation structures observed at Site 1173 are consistent with lateral extension and with vertical compaction of the sediments during burial. Deviations of bedding from horizontal may be associated with the bending of the Philippine Sea plate at the outer trench high of the Nankai Trough or related to the normal faults apparent on the seismic sections oceanward of the site. The core-scale faults and sediment-filled veins are likely to have formed in relatively soft sediments during burial and compaction. The greater abundance of deformation features within the lower Shikoku Basin sequence relative to the trench-wedge deposits also implies an early deformation history. The microfaults and extensional veins are reminiscent of similar features observed at Deep Sea Drilling Project (DSDP) Site 582, the reference site along the western Nankai transect (Shipboard Scientific Party, 1986a).

Documentation of the structures at Site 1173 provides a further important structural datum against which the more highly deformed sites within the prism can be compared and helps us to recognize structures at other sites that are a result of deformation within the prism.

Uncalibrated Gas-Permeameter Measurements

Reconnaissance uncalibrated gas-permeability data were collected using the gas-probe permeameter (see **"Strucutral Geology,"** p. 6, in the "Explanatory Notes" chapter) and, encouragingly, showed good correla-

tion with the kinds of values expected from the lithologic variations (Fig. F17). Measurements on cores from above 100 mbsf are unreliable because of the softness of the sediments and because the measurements were made while we refined the technique. In lithostratigraphic Unit II, the hemipelagites consistently showed poor uncalibrated permeabilities, whereas ash bands showed markedly higher values, possibly by at least four orders of magnitude. Figure F18 shows detailed variations within two of the ash bands and illustrates well the high resolution allowed by the probe permeameter. Measurements in Unit III are at the lower limit of the instrument's capabilities but appear to be uniformly low. Although thin ash bands are present in this unit, in contrast with Unit II, they are no more permeable than the hemipelagites, perhaps because of their greater degree of alteration.
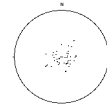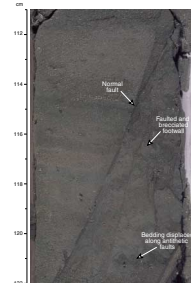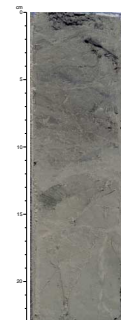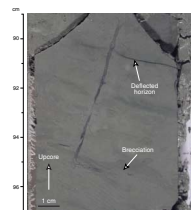
BIOSTRATIGRAPHY

Introduction

Sediments recovered from Hole 1173A provide a continuous sedimentary record from the Pleistocene through the middle Miocene. Calcareous nannofossils were used for developing the biostratigraphic framework using the biostratigraphy of Gartner (1977) and Martini (1971) with zonal modifications proposed by Young (1998) (Table T8). Abundance and preservation of calcareous nannofossils vary throughout the sequence. The interval (core and section) and depth (mbsf) constraints of calcareous nannofossil events recognized at Site 1173 throughout the succession are reported in Table T9. The epoch boundaries have been placed as in Table T10. For nannofossil ranges see Tables T11, T12, and T13.

Calcareous Nannofossils

Hole 1173A recovered core to 724.90 mbsf. In addition to the corecatcher samples, samples from core sections have been examined for calcareous nannofossils. The sediments recovered from Hole 1173A range in age from Subzone NN21b of the Pleistocene to Zone NN5 of the middle Miocene. The nannofossil assemblages decrease in abundance with greater depth. The nannofossils recovered from the sediments display a wide range of preservation states from good to poor. Some intervals are even barren of nannofossils. Cores 190-1173A-2H to 25X (7.14 to 235.33 mbsf) bear mostly moderately to well-preserved nannofossil assemblages. This interval is followed by an interval from Cores 190-1173A-26X to 39X (235.24 to 369.38 mbsf) that is affected by dissolution and is therefore characterized by poor preservation except for Core 32X (292.65 to 302.24 mbsf) and Cores 37X through 39X (340.74 to 369.83 mbsf), which have moderately to well-preserved specimens. From Core 190-1173A-40X to the bottom of the hole (369.64 to 724 mbsf), strong overgrowth and etching affected the nannofossil assemblages severely, with some intervals (Cores 190-1173A-40X, 41X, 53X, 54X, 60X, 61X, and 68X to 71X) barren of nannofossils. Thus, zonal assignments were very difficult, leading to displaced first and last appearance datums. Additional shore-based work may resolve these problems.

F16. Mineralized veins transecting a carbonate horizon, p. 54.
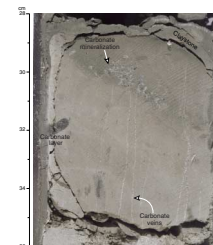
F17. Variation of uncalibrated gas permeability with depth, p. 55.
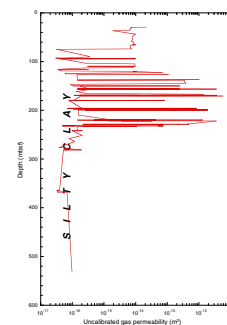
F18. Uncalibrated gas-permeability variations, p. 56.
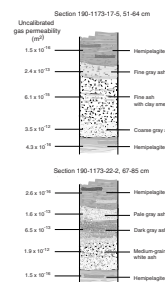
T8. Recognized nannofossil events, p. 120.

T9. Interval and depth constraints of calcareous nannofossil events, p. 121.

T10. Epoch boundaries, p. 122.

T11. Calcareous nannofossil range chart (Zones NN21–NN19), p. 123.

Pleistocene

Moderately to well-preserved Pleistocene nannofossils were recovered from Sample 190-1173A-2H-CC (17.14 mbsf) to 25X-CC (235.33 mbsf). The Pleistocene interval is characterized by the dominance of placoliths (i.e., *Emiliania huxleyi* and *Gephyrocapsa* spp.). Reworked Neogene taxa such as discoasterids, *Reticulofenestra pseudoumbilicus,* and *Sphenolithus* spp., were found in low numbers throughout the Pleistocene samples.

The relative abundance of *E. huxleyi* out of 300 specimens per sample was counted in selected samples to determine the onset of the *E. huxleyi* acme (0.085 Ma), which defines the base of Subzone NN21b. This event is placed between Samples 190-1173A-6H-1, 75–76 cm, and 7H-CC. The first occurrence of *E. huxleyi* (0.26 Ma) was observed between Samples 190-1173A-13H-4, 75–76 cm, and 13H-6, 75–76 cm. The last occurrence of *Pseudoemiliania lacunosa* (0.46 Ma) was recorded between Samples 190-1173A-14H-4, 75–76 cm, and 14H-CC. The last occurrence of *Reticulofenestra asanoi* (0.8 Ma) (between Samples 190-1173A-19H-3, 75–76 cm, and 19H-CC), its first occurrence (1.06 Ma) (between Samples 190-1173A-21-CC to 22H-3, 75–76 cm) and the last occurrence of *Helicosphaera sellii* (1.46 Ma) (between Samples 190-1173A-22H-CC and 23H-4, 70–71 cm) provide further datum levels to subdivide Zone NN19. The first occurrence of *Gephyrocapsa oceanica* (1.77 Ma), which approximates the Pleistocene/Pliocene boundary, was observed between Samples 190-1173A-25X-CC and 26X-4, 96–97 cm.

Pliocene

The Pliocene sediments retrieved from Hole 1173A contain mostly poorly preserved nannofossils (Samples 190-1173A-26X-4, 96–97 cm, [240.7 mbsf] and 43X-4, 66–67 cm [403.68 mbsf]). The abundance of nannofossils is generally lower than in the Pleistocene assemblages. The Pliocene nannofossil assemblages are dominated by different morphotypes of reticulofenestrids and discoasterids; associated are mainly *Coccolithus* spp., *Calcidiscus* spp., and sphenoliths. Reworked specimens were encountered sporadically.

The last occurrence of *Discoaster brouweri* (1.95 Ma) was used to determine the top of Zone NN18 between Samples 190-1173A-28X-4, 71–72 cm, and 28X-CC. The top of Zone NN17 as marked by the last occurrence of *Discoaster pentaradiatus* was recorded between Samples 190-1173A-31X-2, 75–76 cm, and 31X-4, 75–76 cm. Because the interval above (Samples 190-1173A-29X-CC and 30X-CC) contains only few poorly preserved specimens or is depleted of nannofossils, the top of Zone NN16 cannot be precisely identified. The last occurrence of *Discoaster surculus* (2.55 Ma), which defines the top of Zone NN16, was observed between Samples 190-1173A-31X-4, 75–76 cm, and 31X-6, 75–76 cm. The last occurrence of *R. pseudoumbilicus* (>7 µm) defines the top of Zone NN15 (3.75 Ma) between Samples 190-1173A-41X-4, 39–40 cm, to 41X-4, 82–83 cm. In the same interval, the last occurrence of *Sphenolithus abies,* an additional event indicating the top of Zone NN15, was recorded. The last appearance of *Amaurolithus* spp. (4.0 Ma) was used to determine the top of Zone NN14 between Samples 190-1173A-42X-2, 75–76 cm, and 42X-4, 75–76 cm. Because of the low abundance and poor preservation of nannofossils in the interval above from Samples 190-1173A-41X-6, 30 cm, to 41X-CC, the actual last occurrence of *Amaurolithus* spp. might occur higher in the sequence. Neither the last

common occurrence of *Discoaster asymmetricus* at the top of Zone NN13 (4.13 Ma) nor the last occurrence of *Ceratolithus cristatus,* which defines the top of Zone NN12 (5.05 Ma), were assessed because of poor preservation and thus impoverished nannofossil assemblages. The last occurrence of *Discoaster quinqueramus* (5.54 Ma) at the top of Subzone NN11b, which approximates the Pliocene/Miocene boundary (5.32 Ma), was observed between Samples 190-1173A-43X-5, 75–76 cm, and 43X-CC.

Miocene

Miocene sediments (403.68–724.90 mbsf) recovered from Hole 1173A yield poorly preserved nannofossils diminishing in abundance toward the base of the sequence. The Miocene assemblage is characterized by diverse discoasterids, sphenoliths, and placoliths, mainly *Calcidiscus* spp. and *Coccolithus* spp.

The top of the Subzone NN11a, marked by the first occurrence of *Amaurolithus primus* (7.2 Ma), was assessed between Samples 190-1173A-47X-CC and 48X-2, 73–74 cm. The first occurrence of *Discoaster quinqueramus* was used to define the boundary between Zones NN10 and NN11 (8.6 Ma) between Samples 190-1173A-50X-CC to 53X-4, 70–71 cm. The absence of nannofossils or zonal marker species precludes a precise zonal assignment for the interval between Samples 190-1173-51X-4, 33 cm, to 55X-2, 115 cm, except from rare and scattered specimens of *R. pseudoumbilicus* (>7 μm) and strongly altered discoasterids. The last occurrence of *R. pseudoumbilicus* (>7 μm), marking the top of Subzone NN10a, was observed between Samples 190-1173A-50X-CC and 51X-6, 21–22 cm. Bounding the barren interval, the last occurrence of *Discoaster hamatus* (9.63 Ma), a species characteristic of Zone NN9, was recorded between Samples 190-1173A-54X-4, 94–95 cm, and 55X-CC. Its first occurrence (10.7 Ma) was observed between Samples 190-1173A-57X-4, 75–76 cm, and 57X-CC. The basis of Zone NN8 is marked by the first occurrence of *Catinaster coalitus* (10.83 Ma) between Samples 190-1173A-58X-4, 77–78 cm, and 58X-CC. This event approximates the late/middle Miocene boundary (11.2 Ma) as placed at 549.34 mbsf. *Discoaster kugleri,* marking the boundary between Zones NN7 and NN6 (11.8 Ma), could not be determined precisely. Its first occurrence was recorded between the Samples 190-1173A-59X-CC and 64X-CC. The last occurrence of *Orthorhabdus serratus* (12.3 Ma) between Samples 190-1173A-66X-CC and 67X-CC and the first occurrence of large (>7 μm) *R. pseudoumbilicus* (13.4 Ma) between Samples 190-1173A-67X-CC and 68X-CC were used as further events to subdivide Zone NN6. The last occurrence of *Spenolithus heteromorphus* (13.6 Ma), strongly altered by overgrowth, was recorded as the lowermost biostratigraphic zonal event in the sequence defining the top of Zone NN5 between Samples 190-1173A-67X-CC and 69X-CC. Additional datums were provided by the presence of two species confined to an interval (14.0 to 15.3 Ma) within Zone NN5: the last occurrences of *Helicosphaera waltrans* and *Discoaster musicus,* recorded between Samples 190-1173A-75X-CC and 76X-CC. *Helicosphaera ampliaperta,* the last occurrence of which marks the top of Zone NN4 (15.6 Ma), was absent in the lowermost Sample (190-1173A-77X-CC). Therefore, the basal part of the cored sequence is assigned to Zone NN5 of the middle Miocene.

PALEOMAGNETISM

Introduction

After measuring the natural remanent magnetization (NRM), all sections of the archive half of the core were partially demagnetized using alternating-field (AF) magnetization up to 20 mT in increments of 5 mT at 5-cm intervals. Additionally, the maximum demagnetization level was changed to 30 mT at 101.69 mbsf (Section 190-1173A-11H-7, 5 cm) to remove magnetic overprints.

Two oriented discrete samples were routinely collected from each section of the working half of the core primarily for shore-based analysis of the anisotropy of magnetic susceptibility. Additional measurements of polarity and basic magnetic character of selected discrete samples were used to aid in the interpretation of the archive long-core magnetization record. Most of the discrete samples were demagnetized up to 50 mT in 5-mT increments to permit principal component analysis.

Paleomagnetic Results

The majority of NRM inclinations are strongly biased toward steep inclinations of ~60°–80° (Fig. F19A). These steep inclinations do not correspond to the direction expected (52°) for a geomagnetic axial dipole field at the current latitude (32°14.6634′N) of Site 1173. The steep inclinations are interpreted as magnetic overprints acquired during drilling, a problem identified on many previous DSDP and ODP legs. These overprints were successfully removed by AF demagnetization at 20 and 30 mT (Fig. F19B). This drilling-induced magnetic remanence (steeply positive with a low coercivity) is thought to be an isothermal remanent magnetization (Musgrave et al., 1993). After AF demagnetization, stable magnetic remanence inclinations were measured. These inclinations provide information about middle Miocene to Holocene magnetic polarity changes and were used in conjuction with the standard geomagnetic polarity time scale (GPTS) of Cande and Kent (1995) to date the sediments.

Declinations from APC cores (0 to ~160 mbsf) show stable directions after correction by the Tensor tool. Declinations of all XCB cores below 160 mbsf show rapid changes in direction within each section (Fig. F20). These anomalous declinations are interpreted to have been caused by rotation of individual core pieces in each section during XCB coring. However, the measurements taken from the rotated pieces of archive halves were used to correct the core orientation for structural analysis.

Discrete samples were AF demagnetized at fields up to 80 mT to isolate the characteristic stable magnetic component. Typical examples of demagnetization plots for discrete samples and archive-half sections are presented in Figure F21. Stable magnetization components were obtained for most sediments after removal of the steep drilling-induced overprint. After removal of this overprint, the directions of discrete samples and archive-half sections of corresponding horizons agreed very well.

The value of magnetic intensity is strongly associated with the magnetic mineralogy of the sediments. From 0 to ~160 mbsf, markedly high magnetic intensity is observed (Fig. F22). This is especially prominent in the lower part of lithostratigraphic Subunit IA from 60 to 80 mbsf (see "Lithostratigraphy," p. 6) and is marked with a very high inten-

F19. Paleomagnetic inclination, p. 57.
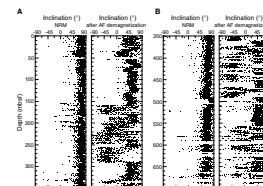
F20. Paleomagnetic declination, p. 58.
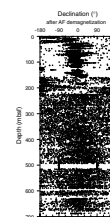
F21. Vector end-point diagrams for discrete samples and archive-half sections, p. 59.
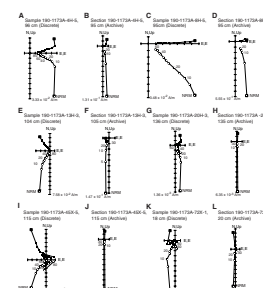
F22. Comparison of magnetic intensity and MST magnetic susceptibility, p. 60.
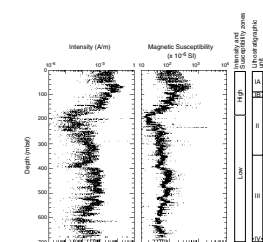
sity peak. These high-intensity values gradually decrease downhole toward 160 mbsf. In contrast to the high-intensity peak, an anomalous low-intensity zone appears in Unit II (upper Shikoku Basin) at ~160 to 350 mbsf. These contrasting variations of intensities correspond to the changing character of the magnetic susceptibility (Fig. **F22**) measured with the multisensor track (MST) (see **"Physical Properties,"** p. 24). These corresponding magnetic susceptibility and intensity values suggest a change in lithology and/or magnetic minerals in the sediments at this depth. A few high peaks in the low-intensity zone also correspond to peaks in the susceptibility values.

The boundary between high- and low-intensity values at the depth of 160 mbsf does not correspond to a lithostratigraphic boundary (Fig. **F23**). A previous rock magnetic study from Site 808 (Lu et al., 1993) also shows high- and low-intensity zones that do not correspond to lithostratigraphic boundaries.

Magnetostratigraphy

Magnetic polarity was determined by measuring the magnetic inclination of archive-half samples after AF demagnetization at 20 and 30 mT. This was supported by AF demagnetization of discrete samples. As a result, many middle Miocene to Pleistocene magnetic polarity records were successfully identified using biostratigraphic datums (calcareous nannofossils) (see **"Biostratigraphy,"** p. 11) and correlated with the GPTS of Cande and Kent (1995) (Fig. **F24**). The identified chrons and subchrons are given in Table **T14.**

A change from normal to reversed polarity at 159.69 mbsf (Section 190-1173A-18H-1, 55 cm) is interpreted as the Bruhnes/Matuyama Chron boundary dated at 0.78 Ma (Cande and Kent, 1995). The Matuyama Chron (0.780–2.581 Ma), observed at 159.69–291.69 mbsf (Section 190-1173A-31X-6, 95 cm), is characterized by a predominantly reversed polarity. The Gauss Chron (2.581–3.58 Ma), interpreted to extend from 291.69 to 374.39 mbsf (Section 190-1173A-40X-4, 25 cm), is characterized by a change to a predominantly normal polarity. The magnetic polarity change at 374.39–423.84 mbsf (Section 190-1173A-45X-5, 20 cm) is interpreted as the Gilbert Chron. Subchrons C3An (5.894–6.567 Ma), C4r (8.257–8.699 Ma), and C4An (8.699–9.025 Ma) are observed at 423.84–439.44 mbsf (Section 190-1173A-47X-3, 0 cm), 478.94–491.49 mbsf (interval 190-1173A-51X-4, 10 cm, through 52X-5, 145 cm), and 491.49–500.34 mbsf (Section 190-1173A-53X-5, 60 cm), respectively. The boundary between normal and reversed polarities at 557.79 mbsf (Section 190-1173A-59X-5, 45 cm) is identified as the termination of Subchron C5n (10.949 Ma). The two characteristic normal polarities below Chron C5 (9.740–11.935 Ma) are clearly observed at 578.49–589.9 mbsf (interval 190-1173A-61X-6, 25 cm, to 62X-CC, 0 cm). However, it is difficult to identify magnetic events near the lower part of the hole because of poor core recovery. Based on biostratigraphic results, the two normal polarities at 635.89 and 662.69 mbsf (Sections 190-1173A-67X-5, 145 cm, and 70X-4, 75 cm) are estimated to be Subchrons C5ACn (13.703–14.076 Ma) and C5ADn (14.178–14.612 Ma), respectively.

Sedimentation Rates

Comparison of the magnetic stratigraphy and biostratigraphy (see **"Biostratigraphy,"** p. 11) shows a strong correlation in the interpreted

F23. Magnetic intensity correlation between Holes 1173A and 808C, p. 61.
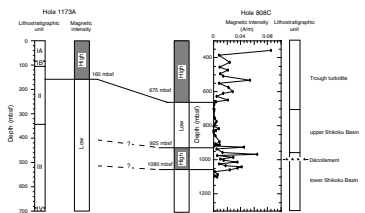
F24. Magnetostratigraphy, p. 62.
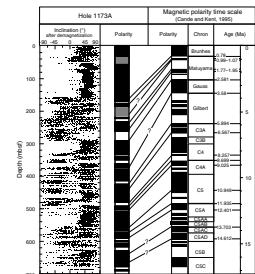
T14. Depths and ages of magnetic chrons and subchrons, p. 130.

age of the sediments. The marked change in sedimentation rate was estimated at the lithologic boundary between the upper and lower parts of Shikoku Basin at an age of ~3 Ma. The sedimentation rate for lithostratigraphic Unit II (upper Shikoku Basin) has been calculated at ~7.78 cm/k.y. This rate is in sharp contrast to lithostratigraphic Unit III (lower Shikoku Basin), which has a sedimentation rate of ~2.74 cm/k.y. (Fig. F25).

INORGANIC GEOCHEMISTRY

Introduction

Eighty-five interstitial water samples were squeezed from selected 10- to 50-cm-long whole-round samples for chemical and isotopic analyses at Site 1173. Sample depths ranged from 1.4 to 687.5 mbsf. In Cores 190-1173A-1H and 2H, samples were collected from every section; in Core 3H, samples were collected from three sections; in Cores 4H and 5H, two samples were collected per core; and from Cores 6H to 73X, one sample was collected per core (except for Cores 62X and 69X, which were not sampled). Elemental concentrations are reported in Table T15 and plotted as a function of depth in Figure F26. Bottom water was sampled with the WSTP. All samples were analyzed for concentrations of 10 major and minor dissolved anions and cations that sensitively reflect microbially mediated or inorganic water-rock (sediment and oceanic basement) reactions. The former include alkalinity, sulfate, ammonium, and phosphate, and the latter are Cl, Ca, Mg, Na, K, and Si. Salinity and pH were also measured. The microbially mediated reactions are most intense in the top 150 m of the sediment section, where organic carbon is most abundant (0.85–0.27 wt%) (see "Organic Geochemistry," p. 19) and porosities are highest (60%–70%) (see "Physical Properties," p. 24). Each of the dissolved species controlled by inorganic water-rock reactions shows the most dramatic changes in concentration values between ~345 mbsf, which corresponds to the boundary between lithostratigraphic Unit II (upper Shikoku Basin facies) and Unit III (lower Shikoku Basin facies), and ~390 mbsf, which corresponds to the décollement-equivalent horizon (~390–420 mbsf), based on preliminary interpretations. A distinct minimum in alkalinity is also observed at the latter depth.

Geochemistry Controlled by Inorganic Reactions

Chloride

Cl concentrations were all determined in duplicate, resulting in a relative analytical uncertainty of 0.1%. Concentrations increase from near bottom-water concentrations of 555 to 572 mM (a 3.1% increase) at a depth of 80 mbsf. This trend is consistent with the diffusion of lower chlorinity interglacial water into the sediments. Cl concentrations then smoothly decrease to 563 mM at a depth of 337 mbsf, where the gradient changes sharply. Between 337 and 620 mbsf, concentrations drop to 496 mM, corresponding to ~9% dilution relative to seawater Cl. The gradient between these depths is not smooth. There are significant minima centered at ~377 and 499 mbsf. Below 620 mbsf, concentrations monotonically increase to 518 mM. The source of the impressive broad (~350 m) low-Cl zone in lithostratigraphic Unit III cannot be resolved
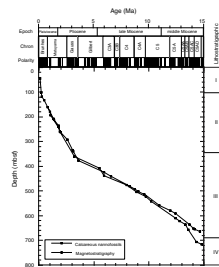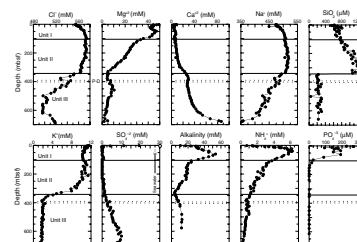
aboard ship. Distinguishing between an in situ source from hydrous mineral dehydration reactions or fluid transported from a deeper-seated source situated arcward will be possible with shore-based mineralogical, chemical, and isotopic analyses of the sediments and interstitial waters. It is interesting to note that the low-Cl zone is found in the same litho-stratigraphic unit as at ODP Site 808 (Leg 131), but the dilution at Site 808 is larger, ~20%.

Sodium

Na concentrations increase from a near-seawater value to a broad maximum, an 8% increase, between ~100 and 300 mbsf. This increase is due to a combination of processes: diffusion of low salinity interglacial water, ion exchange driven by ammonium production, and ash alteration. Below the Unit II/III boundary, concentrations generally decrease toward basement with a concentration of 355 mM at 680 mbsf. The decrease in Na in Unit III is charge balanced by an increase in Ca. This Ca for Na exchange is consistent with albitization of the basement. It is also interesting to note that similar to Cl, there is a local minimum just above the approximate stratigraphic level of the décollement, but that the molar decrease in Cl is approximately twice that of Na, indicating that the decrease is not simply due to dilution but also is the result of fluid/rock reaction.

Potassium

K concentrations are ~10% higher than bottom-water concentrations from the sediment-water interface to 300 mbsf. The difference is caused by K expulsion from clay mineral ion exchange sites, partial dissolution of volcanic ash, and slightly elevated concentrations during the glacial ocean. Similar to Si (see "Silica," p. 17), K concentrations decrease sharply between 300 and 360 mbsf, across the Unit II/III boundary, and increase slightly near the approximate stratigraphic level of the décollement zone. Below this, concentrations remain constant to basement at ~2 mM, indicating that >80% of the original K in the interstitial waters was incorporated into solid phases between 60° and 110°C. The relative invariance of both Si and K concentrations below 360 mbsf suggests that they are involved in the same diagenetic reaction of authigenic silicate formation. The most likely candidates are K zeolites. The sharp boundary between the two K concentration depth intervals suggests high rates of reaction above and below this sharp boundary. At temperatures below ~150°C, K is depleted from the aqueous phase, as seen here, whereas, at elevated temperatures, as at hydrothermal vents, K is released into the aqueous phase.

Silica

Dissolved Si concentrations increase from ~600 to 1250 μM at 304 mbsf. There is a small decrease to 1065 mM at 336.9 mbsf and then a sharp decrease within the distance of one core to 230 mM at 346.5 m. There is no concentration trend from this depth to the bottom of the hole. The sharp discontinuity in silica concentrations at this depth range, which corresponds to the lithostratigraphic boundary between Units II and III, indicates that (1) distinct water-sediment reactions control the silica concentrations above and below this depth interval and (2) that both reaction rates are greater than the diffusive transport rate.

Biogenic silica, mostly diatom and sponge spicule dissolution, controls the high dissolved silica values above the boundary, as indicated by the diatom and sponge spicule abundances in lithostratigraphic Units I and II and absence in Unit III (see **"Biostratigraphy,"** p. 11). An as-yet-unidentified authigenic silicate reaction(s), possibly zeolite formation, controls Si concentrations below the boundary.

Magnesium and Calcium

Mg concentrations generally decrease with depth, whereas Ca concentrations generally increase. There are, however, significant changes in their concentration gradients that indicate the occurrence of a variety of distinct reactions. Mg and Ca concentrations decrease from near seawater values to a local minimum of ~46 mM for Mg and 4 mM for Ca at 23 mbsf. This decrease may be due to the formation of dolomite. Dolomite formation and other carbonate reactions are driven by high alkalinity. Both then increase, Mg to 54 mM at 48 mbsf and Ca to 7.6 mM at 70 mbsf. The Mg increase is due to ion exchange driven by increasing ammonium concentrations, whereas Ca is involved in carbonate reactions. Mg then smoothly decreases to a second local minimum just below the Unit II/III lithostratigraphic boundary, consistent with the uptake of Mg into a silicate phase (see **"Silica,"** p. 17). There is a small increase in Mg with a maximum of 10.5 mM at 459 mbsf and then a smooth decrease toward basement reaching a concentration of 1.7 mM at 678 mbsf, consistent with a low-Mg basement fluid.

Ca concentrations increase smoothly from the Unit I/II boundary to a small local maximum at ~400 mbsf (coincident with a local Cl minimum). Concentrations then smoothly increase with depth reaching a concentration of 87 mM at 678 mbsf, indicating a significant source of Ca from the basement.

Geochemistry Controlled by Microbially Mediated Reactions

Sulfate

Microbially mediated reactions and diffusion control sulfate concentrations in interstitial waters. Sulfate concentrations decrease nearly linearly with depth in Core 190-1173A-1H. By a depth of 5.9 mbsf, sulfate is undetectable. This is consistent with shallow sulfate reduction being dominated by reduction by methane produced at greater depth. Sulfate concentrations remain below detection until a depth of 238 mbsf. Between this depth and 634 mbsf, there is a smooth increase to 10 mM. In the last three cores, concentrations appear to decrease, with the deepest sample having a concentration of ~8 mM. Unlike Si and Cl, there is no discontinuity in the sulfate concentration gradient at 340 mbsf. The reappearance of dissolved sulfate below 200 mbsf is most likely a relic, a result of the rapid burial of the sulfate-containing Shikoku Basin sediments by the overlying turbidites. The sulfate profile below ~600 mbsf, where temperatures are ~90°C, is controlled by slow microbial activity (see **"Microbiology,"** p. 22). Below this, inorganic reactions in the sediment and oceanic basement (i.e., anhydrite precipitation) occur as evidenced by the reversal in the sulfate gradient at the base of the section.

Ammonium and Phosphate

Ammonium concentrations monotonically increase from 0.7 mM at 1.4 mbsf to a maximum of 6.2 mM between 24 and 40 mbsf. Ammonium production is microbially mediated by organic matter fermentation, as is phosphate production. An active ion exchanger, ammonium at high concentration expels other ions (particularly Mg and K) from clay mineral ion exchange sites, as indicated, for example, by the increase in Mg concentrations in the same depth interval. Ammonium concentrations then decrease to 0.2 mM at 678 mbsf with a decreasing gradient with depth. The change in gradient suggests that more than one sink for ammonium exists. We propose that an as-yet-unidentified microbially mediated reaction influences the concentration-depth profile below ~100 mbsf, and at greater depths, where temperatures are too high for microbial activity, it diffuses into oceanic basement. As with sulfate, there is no gradient discontinuity at 340 mbsf. Phosphate concentrations peak at a shallower depth than alkalinity or ammonium. The very low concentration of phosphate below 100 mbsf is controlled by the solubility of apatite, the major sink for phosphate.

Alkalinity

Similar to ammonium, alkalinity has a concentration maximum in the upper part of the hole that is driven by the microbial fermentation of organic matter and sulfate reduction. However, the maximum is found at greater depth. At 10 mbsf, the alkalinity concentration is 10 mM, rising to a maximum of 54 mM at 60.5 mbsf.

ORGANIC GEOCHEMISTRY

The objectives (other than hydrocarbon monitoring for safety reasons) of the shipboard organic geochemistry studies included assessments of the amount, type, and maturity of the organic matter preserved in cores recovered from the Nankai Trough. Another point of interest was to determine the genetic characterization of light hydrocarbons that can be generated by biogenic or thermogenic (thermal cracking) maturation of organic matter and the relationship of gas production to accretionary processes. The strong correlation of temperature to the formation and production of light hydrocarbons represents a sensitive indicator of the thermal history of the accretionary wedge. In addition, several samples were collected in an attempt to measure bulk hydrogen, a first for an ODP drilling project. This work involved developing a sample collection and handling protocol that would minimize contamination and ensure reproducibility of the measurements (see "Inorganic Geochemistry," p. 11, in the "Explanatory Notes" chapter).

At Hole 1173A, 74 sediment samples were collected at ~10-m intervals from 4.5 to 724 mbsf. All sediments were analyzed for methane concentration and light hydrocarbon composition during headspace analyses (Fig. F27; Table T16). In addition, nine gas samples were collected with gas-tight syringes (vacutainer) from gas pockets trapped in the core liner and were analyzed for molecular composition. TOC, inorganic carbon (carbonate), nitrogen, and carbon/nitrogen (C/N) ratios were determined on all sediments collected for headspace analyses (Fig. F28; Table T17).

F27. Molecular compositions and concentrations of headspace gases, p. 65.
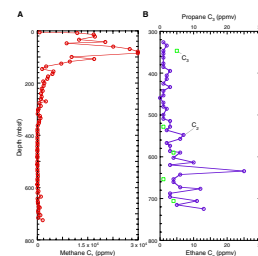
T16. Headspace and vacutainer gas analyses, Hole 1173A, p. 133.

T17. Carbon, nitrogen, sulfur, and hydrogen analyses, p. 135.

F28. TOC and nitrogen contents in sediments, p. 66.
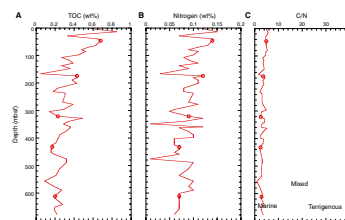
TOC contents in the analyzed sediment samples are low, ranging from 0.14 to 0.85 wt% and averaging 0.3 wt% (Fig. F28). A decrease in the amount of organic matter with increasing depth is reflected in the low concentrations (average = 0.2 wt%) in the deepest 220 m of the hole. Variations in the TOC content can also be correlated with changes in the lithostratigraphy. For example, a sharp decrease in the amount of TOC was observed in the transition from upper Shikoku Basin (hemipelagic mudstone with abundant volcanic ash layers) to lower Shikoku Basin facies (hemipelagic mudstone with rare siliceous and calcareous mudstones). The decrease continues to the bottom of the hole with TOC values as low as 0.14 wt%. Inorganic carbon (carbonate) concentrations are also low (average = ~5 wt%), except from 100 to 300 mbsf, where values increase slightly up to ~10–15 wt%, and in some thin sediment layers below 500 mbsf, where values increase sharply up to 70 wt% (Fig. F29). High concentrations of carbonate nodules were seen in these sediments, which explains these high carbonate values (Fig. F29).

Nitrogen contents of the sediments are also low (0.06–0.15 wt%) and decrease with increasing depth, similar to organic matter. The C/N ratios are consistent with a marine origin; however, as was previously noted at Site 808 (Leg 131), the upper Shikoku Basin sediments may also contain a significant terrigenous component from the flux of terrestrial organic matter to these sediments. Postcruise measurements of the carbon isotopic compositions of kerogens and dissolved organic matter extracted from pore-water fluids in whole rounds will allow for a more careful assessment of the contributions of various sources (marine vs. terrestrial) to these sediments. At lower depths, the C/N ratios remain constant with a slight increase in the lower 150 mbsf, possibly reflecting thermogenic or catagenic hydrocarbon generation that has been observed in previous legs (see the Leg 131 *Initial Reports* volume). Unlike at Site 808, however, the generation of light hydrocarbons is extremely low (1–3 ppm) and is attributed to the higher temperature gradient in Hole 1173A. For example, temperatures at depths below 300 mbsf are already >50°C (see **"In Situ Temperature and Pressure Measurements,"** p. 34), which is in the range of thermogenic hydrocarbon generation (Tissot and Welte, 1984). Below 400 mbsf, temperatures are in excess of 80°C and are approaching levels at which catagenic stages of hydrocarbon production occur. However, the very low TOC content, coupled with low methane and light hydrocarbon concentrations, is consistent with the low hydrocarbon production and/or preservation of organic-rich material in these sediments.

Hydrocarbon Gases

Headspace gas concentrations are moderately low (~700 ppm) in the first core (5.85 mbsf) within the sulfate reduction zone (see **"Inorganic Geochemistry,"** p. 16). A significant increase in methane concentrations is observed just below this zone (up to 16,914 ppm) through the first 100 mbsf. Methane then decreases to lower concentrations (~1000–9000 ppm) down to 300 mbsf. As has been observed in past legs, an increase in methane in sediments below the sulfate reduction zone is indicative of bacterial origin (Claypool and Kvenvolden, 1983). The presence of small concentrations of methane in the sulfate reduction zone, however, may be due to migration from below, with methane partly consumed by sulfate reducing bacteria. Shore-based measurements of the stable carbon isotopes of methane and kerogens will allow for a more complete assessment of the origin of hydrocarbons from

F29. Percentage of inorganic carbon (carbonate) in sediments, p. 67.
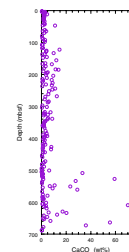
these zones. Just below 300 mbsf, small concentrations of ethane and propane (1–3 ppm) first appeared and show an increase below 500 mbsf (up to 25 ppm) to the bottom of the hole. At depths >350 mbsf, methane is very low (10–73 ppm), increasing slightly to 1632 ppm below 600 mbsf. The low concentrations of methane between 350 and 550 mbsf may suggest that the production of light hydrocarbons is due to thermogenic processes. There is no evidence of migration of hydrocarbons below the facies boundary at ~343 mbsf nor does there appear to be migration of hydrocarbons from the deeper section (>550 mbsf). This is in contrast to observations at Site 808 that indicated an enrichment of lighter hydrocarbons, methane, ethane, and propane in sediment that was attributed to their higher mobility.

An increase in the sulfate concentration from ~400 mbsf to total depth (TD) may have inhibited the production of biogenic methane in these sediments; however, in the deeper part of the section (550 mbsf to TD), a slight increase in both methane and light hydrocarbons is observed, consistent with the production of hydrocarbons from either thermogenic or catagenic processes. The increase in both carbon and nitrogen concentration at ~480 mbsf is coincident with an increase in the number of microbes detected (see "Microbiology," p. 22). Shore-based measurements will further address the sources and production mechanisms for hydrocarbons.

Hydrogen

For the first time, bulk hydrogen was measured in sediments collected at an ODP coring site. In this study, we measured hydrogen concentrations in sediments at in situ temperatures over time (days) in cores from Hole 1173A. Sediment samples were taken throughout the core to establish an appropriate sampling protocol.

Preliminary results suggest that hydrogen is detectable and correlates with other biogeochemical data. Although the observation of some correlations with hydrogen concentrations and other geochemical measurements is encouraging, these results are preliminary and thus should be considered as a first attempt at understanding the role hydrogen plays in the various geochemical environments encountered in Hole 1173A.

Conclusions

Organic geochemical analysis at Site 1173 leads to the following conclusions:

1. In Hole 1173A the organic matter content decreases with depth as indicated by the TOC values (0.85–0.20 wt%; average = ~0.35) throughout the core.
2. The C/N ratios indicate that marine organic matter dominates throughout the core and show a slight increase in the lower ~200 mbsf.
3. The low sulfate and high methane concentrations in the upper section below the sulfate reduction zone are consistent with a bacterial origin. The increase in sulfate concentrations from ~400 to 700 mbsf, coupled with the low concentrations of methane in the same section, may indicate that sulfate is inhibiting the production of hydrocarbons.

4. The presence of low concentrations of light hydrocarbons (ethane and propane) below 300 mbsf to TD may be due to some in situ thermal maturation of kerogen in the sediments. The low concentrations of methane at depth and the lack of evidence for any migration of hydrocarbons from above the facies transition support these conclusions.

5. The detection of microbes at ~480 mbsf at temperatures above 80°C along with elevated sulfate concentrations may suggest that methanogenesis as a result of microbial activity is not completely inhibited, although at these temperatures some thermogenic hydrocarbons are likely being produced.

6. Bulk hydrogen was measured in sediment samples throughout Hole 1173A.

MICROBIOLOGY

Samples for microbiological analysis were obtained from Hole 1173A. Twenty-six samples were obtained for direct microscopic examination on board ship. Eight whole-round samples were taken for shore-based microbiological analysis to measure potential bacterial activities, culture microorganisms, extract DNA, and investigate fatty acid biomarkers.

Total Bacterial Enumeration

Bacteria were present in 21 samples (Table **T18;** Fig. **F30**) to 500 mbsf. The near-surface sample (Sample 190-1173A-1H-1, 139–140 cm) contained 7.23×10^7 cells/cm^3. A population of this size at Site 1173 follows a trend observed at other ODP sites where near-surface bacterial populations decrease as overlying water depth increases (Table **T19**).

The deepest sample containing bacteria was at 499.19 mbsf, with a local maximum of 1.82×10^6 cells/cm^3, some 2.5% of the near-surface population. Below this, the five further samples to 672.84 mbsf contained no detectable bacterial cells (detection limit = 4.75×10^5 cells/cm^3).

The depth distribution of total bacterial numbers in sediments from Site 1173 conforms to the general model for bacterial populations in deep-sea sediments (Parkes et al., 1994) only in the upper section of Hole 1173A from the surface to ~250 mbsf (Fig. **F30**). The bacterial profile departs significantly from the average line in samples at 43, 60.5, and 79.5 mbsf. Below 250 mbsf, rising temperatures affect interpretation of this data. The temperature at 250 mbsf was ~45°–50°C (see **"In Situ Temperature Measurements,"** p. 34), which is the boundary between mesophilic (medium temperature) and thermophilic (high temperature) bacteria. From this depth downward, bacterial population sizes decrease overall by a factor of 7. At ~460 mbsf, the temperature is estimated to be 80°C, which represents another microbiological boundary where the hyperthermophilic (very high temperature) bacteria are found. In the single datum in the hyperthermophilic zone with bacteria present (500 mbsf), population size surprisingly increased by a factor of 13. Procedural contamination was investigated and eliminated, and bacteria in a sample of drill fluid (surface seawater) were enumerated and also eliminated as a cause of contamination, with only 1.4×10^5 cells/cm^3. Thus, the high bacterial population at 499.19 mbsf appears to be real.

T18. Total bacterial populations in sediments, p. 138.

F30. Depth and temperature distribution of total bacterial populations in sediment samples, p. 68.
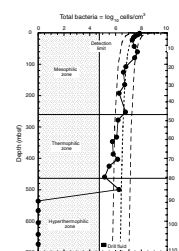
T19. Comparison of near-surface sediment bacterial populations, p. 139.

Interpretation of the microbiological data is complicated by the sediment geochemistry (see "Organic Geochemistry," p. 19, and "Inorganic Geochemistry," p. 16) and a lithofacies change at 343 mbsf (see "Lithostratigraphy," p. 6). Sulfate is rapidly removed in the upper few meters and is completely depleted at 6.8 mbsf, remaining at, or near, zero until 240 mbsf (Fig. F31). Thereafter, it steadily increases to a maximum of 10 mM at 634 mbsf. This reappearance of sulfate begins at the same depth as the mesophile/thermophile transition. Between 6.8 and 240 mbsf, significant quantities of methane are present with a maximum of ~30,000 ppmv between 79 and 85 mbsf, with a broad band generally exceeding 12,000 ppmv between 8 and 108 mbsf. This coincides with the observed increase in bacterial numbers in the upper sediment layers. Evidence of bacterial activity and organic carbon degradation within this zone is provided by significant increases in both alkalinity and ammonium over the same depth range. This activity is fueled by TOC, which has a maximum concentration of 0.85 wt% at 14.53 mbsf and averages 0.54 wt% between the surface and 107 mbsf. Below 107 mbsf, TOC decreases to an average of 0.31 wt% to 343 mbsf and thereafter to an average of 0.23 wt% to the base of the hole.

The lithofacies change at 343 mbsf represents a transition to a sediment with a different geochemistry consisting of low TOC, low but increasing sulfate, negligible methane, low alkalinity and ammonium (indicative of low bacterial activity), and reduced chloride. Here, unsurprisingly, bacterial numbers are lower than average (Fig. F30) except for the population at 500 mbsf. This depth coincides with the highest TOC concentration below 343 mbsf (0.32 wt% at 489 mbsf). It is likely that the significant increase in bacterial numbers at this depth is related to the locally high TOC, rising sulfate concentrations (<5 mM), rising (possibly thermogenic) methane concentrations, and increasing hydrogen concentrations. It is also possible that acetate released by the heating of sediments (Wellsbury et al., 1997, 2000) may be fueling these bacteria. This may represent an isolated hyperthermophilic sulfate-reducing bacterial population. Bacterial sulfate reduction and methanogenesis, plus determination of interstitial water acetate concentrations, form part of the shore-based work that will test this hypothesis.

Apart from the upper 7 m, the microbiology of Hole 1173A appears to be dominated by methane. A correlation (from below the sulfate-reduction zone; 0–7 mbsf) between total bacterial numbers and methane concentration was extremely significant (r = 0.887; N = 19; P = <0.001) (Fig. F32). It is interesting to note that the small but persistent increase in methane from 10 to 180 ppmv between 460 and 557 mbsf occurs below the last record of bacterial presence, providing circumstantial evidence for a thermogenic source.

Contamination Tests

Tracer tests were conducted while coring with APC (Cores 190-1173A-4H and 5H) and XCB (Cores 190-1173A-28X and 29X) at this site. In order to estimate the amount of drilling fluid intrusion into the recovered cores, chemical and particulate tracers were deployed as previously described (Smith et al., 2000a).

Chemical Tracer

Perfluoro(methylcyclohexane) was used as the PFT. Calibration of the gas chromatograph (HP 5890) with standard solutions yielded a slope of

F31. TOC, ammonium, alkalinity, methane, and sulfate profiles vs. depth, p. 69.
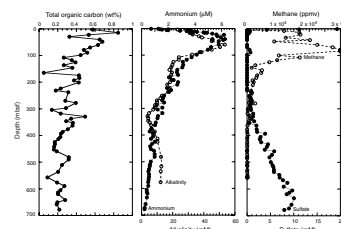
F32. Relationship between total bacterial populations and in situ methane concentrations, p. 70.
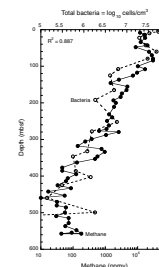
9.2×10^{11} area units/gram of PFT. The detection limit for these samples was equivalent to 0.01 µL of drilling fluid. The tracer was detected on the outer edge of each core, indicating successful delivery (Table T20). The PFT was found in the centers of nine of twelve sections of the APC cores examined (Fig. F33). Estimates of drilling fluid intrusion in these samples ranges from below detection to 0.86 µL/g. Eight of the twelve samples taken midway between the center and the core liner tested positive for the presence of PFT and yielded estimates from below detection limit to 1.51 µL/g. These values are very similar to previous estimates of APC-cored sediments (Smith et al., 2000b). Drilling fluid intrusion into the center of XCB cores were all below the detection limit (Fig. F34). The tracer was detected in three of ten samples collected midway from the center to the core liner. The intrusion of drilling fluid in the three positive samples ranged from 0.03 to 0.14 µL/g. This is the first time PFTs have been used while collecting cores with the XCB.

Particulate Tracer

Fluorescent microspheres were detected on the outside of all cores, indicating successful delivery (Table T21). Twelve sections of APC-cored sediment were examined for the presence of the fluorescent microspheres. They were observed in one sample collected from the center of a core (Section 190-1173A-4H-3) and in two samples collected midway between the center and the core liner (Sections 190-1173A-4H-3 and 5H-2). Microspheres were shown not to penetrate into APC-cored material in previous experiments (Smith et al., 2000b). Ten sections of XCB-cored sediment were examined for the presence of microspheres. The center samples from six of ten sections examined from both the centers of the cores and the midway samples contained microspheres. This is the first time fluorescent microsphere tracers have been used during the collection of cores with the XCB.

The results from the two tracers in the XCB cores are inconsistent. Whereas the PFT was not detected in the centers of the cores, microspheres were present. Because the microspheres are relatively large compared to the chemical tracer, they should not penetrate into the interior of the core as readily as the chemical tracer. Because both tracers were analyzed on the exact same samples, this discrepancy can not be explained by differences in sample handling. Examination of XCB cores at future sites will determine whether this discrepancy persists.

PHYSICAL PROPERTIES

Introduction

At Site 1173, laboratory measurements were made to provide a downhole profile of physical properties at a reference site seaward of the accretionary complex. Data from tectonically undeformed sediments at the reference site allow comparison of physical properties with those from Site 808 (Leg 131) and from other sites drilled during Leg 190.

With the exception of extremely short (<50 cm) sections, all cores were initially passed through the MST before being split. Gamma-ray attentuation (GRA) and magnetic susceptibility measurements were taken at 4-cm intervals with 2-s acquisition times for all cores. *P*-wave velocity logger (PWL) measurements were taken at 4-cm intervals with 2-s ac-

T20. Drilling fluid intrusion estimates based on PFT tracer experiments, p. 140.

F33. Drilling fluid intrusion into APC cores, p. 71.
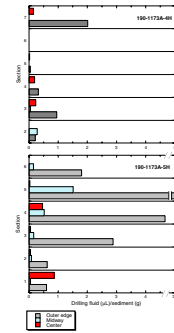
F34. Drilling fluid intrusion into XCB cores, p. 72.
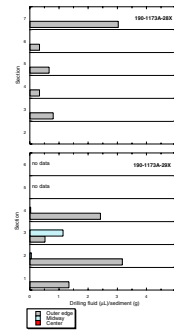
T21. Drilling fluid intrusion estimated based on fluorescent microsphere tracer experiments, p. 141.

quisition times for APC cores. The PWL device yielded extremely scattered values on the APC cores and was turned off for XCB cores. These data are not discussed further. Natural gamma ray (NGR) was counted every 20 cm for 20-s intervals. Because abnormally slow data acquisition on the NGR caused delays, the interval was increased to 40 cm between 493.74 and 570.74 mbsf. Voids and cracking caused by gas expansion were noted in cores between 7 and 83 mbsf and degraded the MST measurements. Biscuiting in XCB cores also degraded measurements.

Moisture and density samples were selected from undisturbed core at regularly spaced intervals of two per section (75-cm resolution) between the mudline and 168.64 mbsf. Below this depth, time constraints and equipment capacity limited the sample frequency to one sample per section. Measurements of dry volume and wet and dry mass were uploaded to the ODP (Janus) database and were used to calculate water content, bulk density, grain density, porosity, void ratio, and dry bulk density. *P*-wave velocities were measured at a frequency of two to three per core. Measurements were taken in three directions when core conditions permitted.

Shear strength measurements were made near the *P*-wave core measurement locations from the mudline to 234 mbsf, at which point XCB coring began and the cores became too stiff for insertion of the vane shear device. Resistivity measurements were taken at least once per core, with additional measurements made if time permitted. Raw and calculated physical properties data are available from the Janus database for all MST, moisture and density, velocity, thermal conductivity, and shear strength measurements (see the "Related Leg Data" contents list). Because electrical conductivity and formation factor data are not currently available from the database, they are included in Tables **T22** and **T23,** respectively.

Density and Porosity

Sediment bulk density was determined by both the gamma-ray attenuation (GRA) method on unsplit cores and the mass/volume ("index properties") method on discrete samples (see "Physical Properties," p. 19, in the "Explanatory Notes" chapter). The GRA density data and the bulk densities determined by the mass/volume method are in good agreement for APC cores (Fig. **F35A, F35B**). On average, the GRA bulk densities are 0.1 g/cm³ lower than those determined from discrete samples because of the smaller diameter and biscuited nature of XCB cores from below 250 mbsf. Both moisture and density measured on discrete samples and GRA density measurements show similar downhole trends.

Grain densities determined from dry mass and volume measurements exhibit a shift at 340 mbsf from an average value of 2.70 g/cm³ above 340 mbsf to 2.77 g/cm³ below (Fig. **F35C**). The calculated porosity profile (which accounts for grain density) is shown in Figure **F35D.** Changes in porosity or the porosity-depth gradient generally correlate with the major lithostratigraphic boundaries identified at Site 1173 (see "Lithostratigraphy," p. 6).

Porosities within lithostratigraphic Unit I (outer trench–wedge facies) are characterized by a general decrease with depth, from 72% to 79% at the seafloor to 56%–66% by 100 mbsf. Porosity values within lithostratigraphic Unit I show considerable scatter, which reflects lithologic variability within the turbidite-rich trench wedge. Typically, the lower porosity values (<55%) represent sands and silty sands, whereas the

T22. Formation factor obtained by the needle-probe method, p. 142.

T23. Electrical conductivity and formation factor obtained on sample cubes, p. 144.

F35. Bulk density, grain density, and porosity, p. 73.
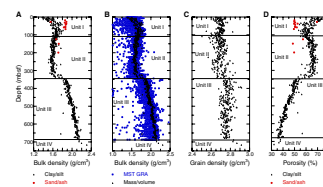
silty clays maintain consistently higher porosities at shallow depths (Fig. F35D). Additional scatter within the silty sand samples may reflect subtle differences in grain size and composition that were not distinguishable in hand specimens.

Although there is some scatter, porosity increases slightly within lithostratigraphic Unit II (upper Shikoku Basin facies; 102.14–343.77 mbsf), from 57% to 65% at ~102 mbsf to 62% to 69% at ~340 mbsf. This is a significant deviation from both normal compaction trends for silty clays (e.g., Hamilton, 1976; Athy, 1930) and the porosity trend within Units I and III above and below.

At 340 mbsf, porosity drops sharply to ~50%. This depth coincides with the boundary between lithostratigraphic Units II and III (upper and lower Shikoku Basin facies). The correlation between the sharp porosity decrease at ~340 mbsf and the boundary between lithostratigraphic Units II and III suggests that this porosity shift is controlled by lithology. Within the lower Shikoku Basin facies, porosities generally follow compaction trends for fine-grained marine sediments (e.g., Hamilton, 1976), decreasing to below 41% at 680 mbsf (Fig. F35A, F35D). A decrease in porosity is observed below 680 mbsf within lithostratigraphic Unit IV (volcaniclastic facies). However, core recovery was insufficient to determine if these values are representative.

Shear Strength

Undrained shear strength measurements were made using a miniature automated vane shear (AVS) and were conducted exclusively in fine-grained silty clays. Shear strength was measured on samples above 234 mbsf (Core 190-1173A-25X). Below this depth, samples were sufficiently indurated that insertion of the AVS caused fracturing of the sediments. Shear strength increases systematically downhole from near zero at the seafloor to >100 kPa at 200 mbsf (Fig. F36). Scatter in the data increases below ~120 mbsf as a result of fracturing of sediment and opening of fractures at the tips of the AVS vanes during some measurements. For this reason, actual sediment strength is probably best reflected by the highest measured values.

Thermal Conductivity and Projected Temperatures

Thermal conductivity was measured using one of two methods depending on core condition. For shallow, nonindurated samples, a needle probe was inserted into the unsplit core for a full-space conductivity measurement. For samples from below 285 mbsf, insertion of the needle caused fracturing, so a half-space method was used on split cores. Thermal conductivities range from 0.85 to 1.71 W/(m·°C) and generally increase with depth (Fig. F37A). Between the mudline and ~320 to 340 mbsf, thermal conductivities range from 0.85 to 1.2 W/(m·°C) with no distinct trend. Conductivities increase sharply below 340 mbsf and range from 1.32 to 1.71 W/(m·°C) to the base of the borehole. The sharp change in thermal conductivity at ~340 mbsf correlates with the abrupt drop in porosity at ~340 mbsf (Fig. F35D). This relationship is expected because the thermal conductivity of sediment grains is higher than that of pore fluid.

Assuming one-dimensional vertical conductive heat flow, shipboard thermal conductivities and downhole temperature measurements to 284 mbsf (see "In Situ Temperature and Pressure Measurements," p. 34) define a heat flow of 180 mW/m². Using this estimated heat flow

F36. Undrained peak shear strength, p. 74.
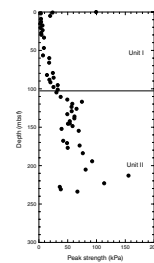
F37. Thermal conductivity and temperature trends, p. 75.
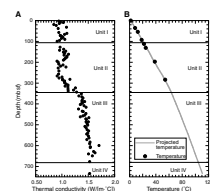
and measured thermal conductivities, projected downhole temperatures reach ~110°C at 734 mbsf (Fig. **F37B**).

Acoustic Velocity

In APC cores, *P*-wave velocities were measured using the *P*-wave sensors 1 and 2 (PWS1 and PWS2) insertion probe system along the core axis (z-axis) and across the core axis (y-axis), respectively. The PWS3 contact probe system was used to measure *P*-wave velocities across the core liner (x-axis) (Fig. **F38A**). Measurements in more than one direction could rarely be obtained in the same interval because of unfavorable core conditions. Gas expansion within the sediment from the upper 83 m produced cracks in the cores, which increased attenuation and probably resulted in the very low and dispersed velocity values between 25 and 83 mbsf. In XCB cores, sample cubes were cut, and measurements in all three directions were performed using the PWS3 contact probe system.

Between 83 and 230 mbsf, velocities are ~1600 m/s and show no significant trend. Velocity progressively increases between 230 and 390 mbsf, whereas porosity does not decrease below ~102 mbsf until it drops sharply at 340 mbsf. The velocity profile does not exhibit the sharp changes seen in porosity and resistivity data at ~340 mbsf. At ~390 mbsf, there is a small (50 m/s) but sharp decrease in velocity that does not correlate with a porosity change or a lithostratigraphic boundary. However, this transition coincides with the décollement-equivalent horizon (see **"Development of the Decollement Zone, Muroto Transect,"** p. 28, in the "Leg Summary" chapter).

In Figure **F38B,** data acquired from Hole 1173A are compared to a velocity-porosity relationship based on a weighted average approach with parameters appropriate for clayey silt (Lee et al., 1996). As expected for data acquired without confining pressure, velocities from Units I and III generally plot near or below this reference curve. However, the anomalous behavior of the lower part of Unit II is apparent on this velocity-porosity crossplot, where velocity is slightly higher than expected for the measured porosity. *P*-wave anisotropy appears significant only in lithostratigraphic Unit III (Fig. **F38C**). Between 340 and 460 mbsf, anisotropy in the vertical plane is constant at ~2% and then increases to 4%–6% at the bottom of the hole. Over this interval, porosity decreases from 45%–55% to 35%–40%.

Electrical Conductivity

Measurements were made on APC cores with a four-needle, 10-kHz electrode array. On XCB cores, conductivity was measured on the same sample cubes used for *P*-wave measurements with a two-electrode, 30-kHz system. Different frequencies were used in an attempt to minimize out-of-phase potentials that result from electrode polarization and dielectric effects. These effects were small in both cases, and tests performed during the cruise showed that measured conductivity was independent of frequency at least over the 5- to 50-kHz range.

Electrical conductivity and formation factor (see **"Physical Properties,"** p. 19, in the "Explanatory Notes" chapter) measured on the sample cubes are given in Table **T22.** For the needle-probe measurements, only the apparent formation factor is given. Needle-probe measurements in the first 260 m of the hole yield formation factors mostly between 3 and 5, with some values up to 7 (Fig. **F39A**). Coarser litholo-

F38. *P*-wave velocity and velocity anisotropy, p. 76.
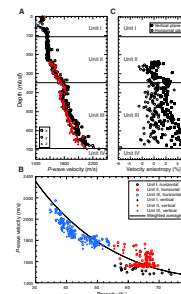
F39. Formation factor and anisotropy of electrical conductivity, p. 77.
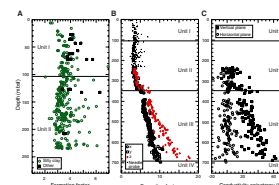
gies, which include silt, sand, and ash layers, appear more resistive. Between 50 and 250 mbsf, formation factor decreases slightly with depth. This is probably caused by the anomalously high porosity in the upper Shikoku Basin facies. Formation factor increases between lithostatigraphic Units II and III, following a porosity decrease (Fig. F39B). Formation factor increases steadily with depth below 450 mbsf.

Because measurements were performed along all three axes, conductivity anisotropy could be assessed. The most striking feature is the high conductivity anisotropy in lithostratigraphic Unit III, in which the sediment is generally more conductive across than along the core (Fig. F39C). Anisotropy is small (~5%) in Unit II and increases sharply to ~20% across the transition to lithostratigraphic Unit III between 320 and 360 mbsf. Anisotropy increases progressively downward to reach ~60% in the lower part of the section. The electrical conductivity anisotropy thus follows the same trend as P-wave anisotropy but is approximately 10 times larger. The conductivity anisotropy of the 8-cm^3 cubes is much larger than the dispersion of the conductivity measurements on individual samples. This suggests that sample-scale anisotropy may cause formation-scale anisotropy in Unit III.

Anisotropy increases as porosity decreases (r = –0.853 on all data), suggesting that anisotropy may be related to clay compaction fabric. Tortuosity anisotropy that is caused by preferential orientation of clay particles has been proposed to explain the permeability anisotropy in clays (Arch and Maltman, 1990). The same mechanism could be applied to resistivity anisotropy. Note, however, that this explanation only takes into account the geometry of the porous network, and that surface conductivity of clays may also contribute significantly to the anisotropy of clayey sediments.

Magnetic Susceptibility

Volumetric magnetic susceptibilities were measured in all recovered cores from Site 1173 (Fig. F40). Uncorrected values of magnetic susceptibility from the Janus database were used. Large magnetic susceptibility values and large scatter between 0 and 100 mbsf are correlated with the occurrence of sand-rich turbidites. Less scatter occurs below 100 mbsf, and a minimum occurs at ~200 mbsf. Below 200 mbsf, magnetic susceptibility increases continuously to 400 mbsf. The hemipelagic mudstones between 400 and 540 mbsf are characterized by three cycles of increasing magnetic susceptibility up to 150×10^{-5} SI. Magnetic susceptibility data show a slight decrease from 540 to 734 mbsf.

Natural Gamma Ray

NGR results are presented in counts per second (cps) (Fig. F41). The background scatter, produced by Compton scattering, photoelectric absorption, and pair production, was measured at the beginning (6.39 cps) and subtracted from the measured gamma-ray values. In general, NGR counts are low and are consequently likely to be affected by the short counting interval and by porosity variations. Between 0 and 70 mbsf, NGR shows an increase from ~7 to 17 cps. There is considerable scatter between 70 and 100 mbsf. It is not clear what causes the downhole increase of radioactivity in these turbidites containing clays and fine to medium sands. Between ~100 and 340 mbsf, NGR is characterized by a continuous decrease from 10 to 3 cps and considerably less scatter. NGR exhibits an abrupt increase at 340 mbsf to ~10 cps, fol-

F40. Magnetic susceptibility, p. 78.
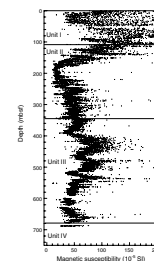
F41. Natural gamma ray, p. 79.
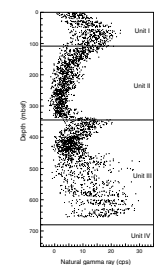
lowed by a decrease to ~6 cps down to ~405 mbsf. From 405 to 734 mbsf, NGR shows an increase to 15 cps, with increasing scatter downhole. This variation does not correspond to any observed variations in porosity or density. Because these silty claystones show only slight changes in composition, the high scatter in count rates may be produced by an insufficient counting rate or changes in clay mineralogy.

Comparison with Downhole Measurements

Bulk-density, porosity, gamma-ray, and velocity values derived from core measurements can be compared with wireline logging measurements obtained with the triple-combo tool (see "Downhole Measurements," p. 30).

Bulk-density data measured on cores and logging data show a reasonably good agreement (Fig. F42A). In the upper section (100–340 mbsf), bulk-density values from logging data show slightly higher values (~0.05 g/cm^3) than those derived from core measurements. The sharp increase of bulk densities at 340 mbsf is observed in both the core and logging measurements. The logging data from 360 to 435 mbsf are characterized by a higher scatter, possibly as a result of downhole conditions (see "Downhole Measurements," p. 30). At this depth, the bulk densities measured on cores are ~0.1 g/cm^3 higher than the logging data.

The velocity data measured on cores (z-axis) and those logged by the DSI show a similar trend (Fig. F42B), although the logging data are characterized by higher values (~100 m/s) than the core data. Higher downhole velocities are not surprising because of the greater confining stress within the borehole. A comparison of the MST NGR data with downhole logging gamma-ray measurements shows that there is almost no agreement (Fig. F42C). These differences may be caused by problems with the counting rate on the MST.

Summary and Discussion

Variations in physical properties correlate well with lithostratigraphic units. The turbidites of the outer trench wedge are characterized by highly variable porosity, which generally decreases with depth. Porosity increases at the boundary between the outer trench–wedge and the upper Shikoku Basin facies and continues to increase slightly with depth. These elevated porosities deviate from a typical compaction profile for silty clays. At the boundary between the upper and lower Shikoku Basin facies (~340 mbsf), grain densities increase slightly and porosities decrease sharply. This porosity decrease is accompanied by increasing thermal conductivity, electrical resistivity, and P-wave velocity.

The anomalously high porosities within the upper Shikoku Basin facies may be caused by slight cementation, which could support the overburden and thus maintain high porosities. This explanation is supported by the observed increase in P-wave velocity with depth below ~220 mbsf, which is not accompanied by any porosity decrease. Alternatively, the apparent high porosity may be an artifact of shipboard measurements caused by a significant component of water-bearing minerals, such as smectite (e.g., Brown and Ransom, 1996). The increase in grain density at ~340 mbsf may indicate a primary lithologic difference or a diagenetic boundary (e.g., Nobes et al., 1992) across the upper to lower Shikoku Basin facies boundary.

F42. Bulk density, P-wave velocity, and gamma-ray data, p. 80.
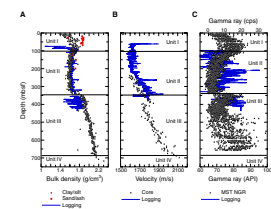
Shipboard measurements indicate a sharp increase in thermal conductivity at 340 mbsf that corresponds to the sharp porosity decrease observed at this depth. Using the shipboard thermal conductivity measurements and shallow (<284 mbsf) temperature measurements that indicate a basal heat flow of 180 mW/m², temperatures are projected to the base of the borehole at 734 mbsf. This extrapolation assumes only vertical conductive heat flow and predicts a bottom-hole temperature of ~110°C.

The physical properties of sediments drilled at Site 1173 are consistent with the results of previous DSDP and ODP sites in the region (Sites 582 and 808). Site 582, in the Nankai Trough southwest of Site 1173, penetrated the outer trench–wedge and the upper Shikoku Basin facies. Data from Site 582 show the same pattern of decreasing porosity with depth in the outer trench wedge and a gradual increase of 4%–8% in porosity into the upper Shikoku Basin facies as seen at Site 1173 (Kagami, Karig, Coulbourn, et al., 1986). Site 808, located ~13 km landward of Site 1173 and ~3 km landward of the deformation front, penetrated the outer trench–wedge and the upper and lower Shikoku Basin facies. As at Site 1173, a decrease in porosity was observed at the top of the lower Shikoku Basin facies (Taira, Hill, Firth, et al., 1991). At Site 808, however, porosities decrease with depth within the upper Shikoku Basin facies, indicating an increase in consolidation with depth that is not observed at Site 1173. This may be attributable to tectonic loading and deformation at Site 808 and could also reflect deformation and collapse of weakly cemented sediments.

At Site 808, the décollement zone occurs within the lower Shikoku Basin facies. Based on physical properties data, it is difficult to distinguish a potential protodécollement horizon. Most of Unit III shows continuously decreasing porosities and increasing velocities. At ~390 mbsf (the décollement-equivalent horizon), *P*-wave velocities decrease.

DOWNHOLE MEASUREMENTS

Introduction

The only downhole measurement program planned for Leg 190 was at Site 1173 because a full suite of logging while drilling (LWD) is planned for key Leg 190 sites during Leg 196 in 2001. However, there is at present no LWD capability for sonic velocity measurement in slow, poorly consolidated formations, nor for FMS imaging. Velocity in particular is a key desirable parameter because it is required to convert three-dimensional (3-D) seismic data to accurate depths, as well as to interpret porosity and other physical properties from seismic data. Additionally, the capability to record shear wave traveltimes with new logging instruments permits calculation of V_P/V_S and Poisson's ratio, which are useful for interpreting petrophysical properties from the logs. Consequently, velocity and FMS imaging were the highest priority objectives for logging at Site 1173. As expected, logging Site 1173 was technically challenging; several logging passes were completed from 0 to 440 mbsf with difficulty, but no deeper logs were obtained.

Downhole Measurement Operations

Downhole measurement operations in Hole 1173A consisted of runs with both the triple-combo (spectral gamma ray, dual-induction resis-

tivity, lithodensity, and neutron porosity tools) and FMS-sonic (FMS and dipole shear sonic imager) tool strings (see Fig. F13, p. 45, in the "Explanatory Notes" chapter). Downhole conditions prevented the entire 734-m-long drilled interval from being logged. The triple-combo and temperature/acceleration/pressure tool were run in two stages because of hole bridging; logs were collected from 97 to 338 and then from 358 to 440 mbsf after the pipe was lowered to span the bridge (Table T24). Log data quality is generally good from 97 to 338 mbsf, but poor in the deeper interval as a result of large and highly variable hole diameter. A wiper trip was then made to try to open the hole to the bottom before we attempted to collect the FMS-sonic velocity logs, and the hole was filled with heavy barite mud because of deteriorating conditions and ODP hole abandonment requirements. The FMS-sonic logging string was run in to the hole but could not be lowered beyond a bridge at 380 mbsf. The interval from 65 to 373 mbsf was then successfully logged twice. High-quality FMS images and compressional and shear-wave velocity data were acquired. During the second pass, a new low-frequency (<1 kHz) dipole sonic energy source was used for the first time in an ODP hole, producing excellent shear and compressional waveforms despite very low formation velocity.

Gamma Ray, Resistivity, Density, and Porosity

A summary of the logging results is presented in Figure F43, and the complete logging data are available (see the "Related Leg Data" contents list). The caliper log shows that the hole was in generally fair to good condition down to 332 mbsf, although it is consistently 14–18 in wide from 100 to 220 mbsf. The hole was drilled with a 9.875-in bit. Logs from this interval are of good quality. Below 350 mbsf, the hole is wide and highly rugose, considerably degrading the log data. Spectral gamma-ray data (Fig. F44) are consistent with the homogeneous silty clay lithology in the logged interval, staying in a narrow range of ~50–80 API units throughout. No strong lithologic variations are detected. Hostile environment standard gamma ray (HSGR) is the borehole-compensated log generated on the triple-combo string, and it can be considered a more accurate measurement of true formation natural gamma-ray values than the standard gamma-ray (SGR) tool on the FMS-sonic string, which is not corrected for borehole diameter effects. The SGR is primarily used for depth registration of the logging runs.

Resistivity is low overall, ranging only between ~0.4 and 0.7 Ωm (Fig. F43). The interval from 70 to 336 mbsf has an overall trend of decreasing resistivity, which is an unusual pattern. We attribute this reversed trend to the strong downhole increase in porosity over the same interval because resistivity is primarily sensitive to the saline pore fluids. In the deeper logged interval, resistivity is higher, again consistent with the lower core porosity. Numerous narrow high-resistivity spikes, especially well exhibited by the high-resolution spherically-focused induction log, appear to correlate well with ash layers identified in the cores and in the FMS microresistivity log.

Density data indicate an unusually low density zone from 93 to 336 mbsf, with a trend of slightly decreasing density with depth from 93 to ~130 mbsf, then nearly constant density of ~1.63–1.66 g/cm³ to 320 mbsf. Several higher density intervals at 172, 265, and 325 mbsf do not clearly correlate with specific features in the cores. Log densities are significantly higher in the 358- to 440-mbsf interval than above, although the scatter is much higher because of poor hole conditions. Trends in
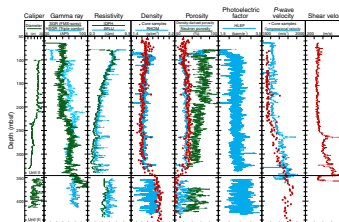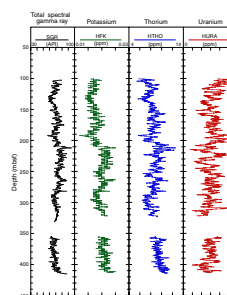
these data are well matched by core density measurements, although the latter are systematically lower above 336 mbsf, probably as a result of elastic rebound effects in the cores. Because they are in situ measurements, the log values are more likely to be close to the true formation density. Below 358 mbsf, core-based density measurements are higher than log values, reversing the difference observed in the shallower interval. The quality of the density measured by the high-temperature lithodensity sonde tool is sensitive to borehole diameter and smoothness; therefore, the noisy caliper log in this interval suggests the log data are suspect. However, the upper bound of the log values ought to be representative of the formation density; the small discrepancy between this upper bound and the core-based data remains unexplained.

Neutron porosity logging resulted in very high values of 70% to 90% porosity throughout most of the logged interval. This log is uncorrected for the effect of the clay mineral hydrogen content, which has a significant effect on neutron absorption (Schlumberger Corp., 1989). The highly clay-rich lithologies at Site 1173 suggest that this log should be considered unreliable without correction. The highly scattered neutron log exhibits a weak compaction trend with depth, with a sharp break to lower porosity at ~193 mbsf. Although there is a local washout at this depth, the reason for the downhole shift in the neutron log is not clear. The core- and density log–derived porosity (essentially the same data set as presented in the density log column) are shown for comparison (Fig. **F43**). We are not confident that even the general trends in the neutron log can be attributed to real porosity variations without correction for quantitative clay content, and we consider the porosity calculated from the density log to be more reliable.

Sonic Velocity

Both compressional and shear-wave slowness (inverse of velocity) were measured with the new low-frequency, high-power dipole source transducer in the DSI. Traveltimes were picked through automated semblance coherence analysis of the arrivals at 16 receivers and converted to *P*- and *S*-wave velocity. Both logs appear to be of good quality over the logged interval (90–360 mbsf), which is especially remarkable given the very low shear-wave velocities of 300–600 m/s. *P*-wave velocities range from 1575 to 1675 m/s and show no trend down to 220–230 mbsf, where there is a well-defined change to an increasing trend with depth (Fig. **F45**). *P*-wave velocity reaches values of ~1850 m/s at ~345 mbsf. Velocities appear to decrease back to values of ~1700 m/s in the short logged interval below 345 mbsf but return to ~1800 m/s at the very bottom of the log. The overall trend is closely followed by the core-based measurements of *P*-wave velocity (except for the sharp decrease below 340 mbsf), although core values are 50 to 100 m/s lower, again attributed to the removal of in situ stress from the cores. A crossplot of velocity and density-derived porosity (Fig. **F46**) illustrates the decoupling between velocity and porosity. Taking the break in slope of the velocity-depth curve at ~230 mbsf as a dividing point, the zones above and below this depth plot in different fields, with little overlap. Porosity remains in the same range across this boundary, but velocity changes markedly.

In Figure **F45,** *P*-wave velocities are compared to the two-ship, split-spread, seismic experiment interval velocity values determined by Stoffa et al. (1992) near this site. They reported a velocity of 1965 m/s between 133 and 388 mbsf. There is an unexplained discrepancy of 100
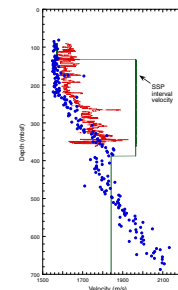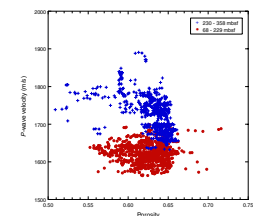
to >300 m/s between this value and the log data throughout this interval.

Shear-wave velocity follows a similar trend to that of the *P*-wave velocity log, varying from just over 300 to >650 m/s. There is a change in slope of the shear-wave velocity curve at the same ~220- to 230-mbsf depth as that exhibited by the *P*-wave velocity. The shear-wave velocity has near-constant values of ~320 m/s above 220 mbsf, then an increasing trend with depth to a peak value of ~650 m/s at 345 mbsf, the depth of the Unit II/III boundary. Shear-wave velocity declines sharply to 330 m/s below this level to the bottom of the logged interval. Both *P*- and *S*-wave velocities exhibit a sharp local peak value at ~265 mbsf that coincides with resistivity and density peaks. This zone corresponds to an interval with a high concentration of ash layers in the cores and FMS logs.

Formation MicroScanner Imaging

The volcanic ash beds and other features observed in the cores were well imaged by both FMS passes. The two passes followed essentially the same azimuthal track over the entire logged interval, so no increase in borehole wall coverage was obtained. The second pass did confirm that even subtle variations in microresistivity were reproducible and hence image real features of the borehole wall. Both passes of the FMS data are presented in their entirety on the accompanying Log and Core Data CD.

Much of the logged interval exhibits horizontal or near-horizontal bands of high resistivity, which we interpret as individual ash layers identified in the cores (Fig. F47). These bands typically have sharp bases above conductive intervals then grade upward back to background resisitivity values. In the intervening hemipelagic silty clay between the ash bands, subtle features are imaged in the FMS microresistivity log, including narrow bands interpreted as *Zoophycos* trace fossils and mottled intervals interpreted as bioturbation and diagenetic sulfide mineralization, again based on correlation with core observations (Fig. F48). The Unit II/III boundary at ~343 mbsf was logged with FMS, and a change in resistivity character can be seen across this interval (Fig. F49). Above the boundary, bedding and ash layers are more apparent, whereas below it, the sediment has a more uniformly bioturbated appearance.

Summary

Overall, the logging data expand upon core-based observations and provide in situ data at Site 1173. The resistivity and density profiles document the anomalous maintenance of high porosity in lithostratigraphic Unit II as well as the abrupt shift to lower porosity below the Unit II/III boundary. In the upper part of this interval, above 225 mbsf, the sonic velocities remain low, suggesting possible compaction disequilibrium but a normal (still compaction dominated) relationship between velocity and porosity. The deviation of the two velocity-log trends from the density-log trend between 225 and 345 mbsf (Fig. F46) is more unusual. The increased formation velocity over this interval coupled with the near-constant density (or porosity) may be an indicator of cementation increasing the rigidity (bulk and/or shear modulus) of sediments in this interval, even though porosity is unchanged. The sharp increase in density seen in the core physical properties data and the abrupt decrease in *P*- and *S*-wave velocity at 345 mbsf would then

F47. FMS image of ash layers, p. 85.
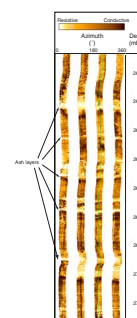
F48. FMS image of bioturbated interval with ash layer, p. 86.
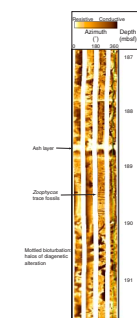
F49. FMS image of the Unit II/III boundary, p. 87.
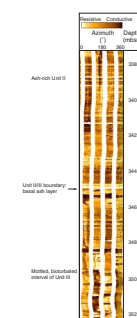
mark a front below which this cementation is absent. Reasons for both the abrupt onset of this pattern at ~225 mbsf and its abrupt end at 345 mbsf remain unclear, although core-based evidence suggests the latter represents a diagenetic front (see "Lithostratigraphy," p. 6).

IN SITU TEMPERATURE AND PRESSURE MEASUREMENTS

Seven reliable determinations of downhole temperatures were made at depths between 35 and 284 mbsf in Hole 1173A using the Adara APC temperature tool, the WSTP, and the DVTP. Table T25 summarizes the deployments, and the station data are shown in Figures F50 and F51. Measurements were not attempted deeper in the hole because the formation became sufficiently stiff that it probably would have been cracked by even the streamlined probe tip of the DVTP.

As described in "In Situ Temperature and Pressure Measurements," p. 26, in the "Explanatory Notes" chapter, in situ temperatures were estimated by extrapolation of the station data to correct for the frictional heating on penetration, using an average thermal conductivity of 1.0 W/(m·°C) (see "Physical Properties," p. 24). The estimated in situ temperatures from all three tools define a linear gradient of 0.183°C/m in the upper 300 m (Fig. F52), yielding a conductive heat flow of ~180 mW/m² at Site 1173. This value is generally consistent with, but slightly higher than, prior determinations of high heat flow near the toe of the Nankai accretionary prism in the vicinity of the Leg 190 transect (e.g., Kinoshita and Yamano, 1986; Yamano et al., 1992). Deeper than 300 m, thermal conductivities increase by 30%–50%, so the gradient should decrease proportionally, and in situ temperatures of ~110°C are estimated for the bottom of the hole (Fig. F52).

Pressures were also recorded during the two DVTP-P deployments at 198 and 284 msbf (Fig. F53). As noted in "In Situ Temperature and Pressure Measurements," p. 26, in the "Explanatory Notes" chapter, postcruise modeling and processing is required to estimate in situ pressures, but preliminary examination of the raw data seems only to indicate a hydrostatic pressure differential between the two stations—not unexpected at these relatively shallow depths at the reference site, outboard of the active tectonic domain in the accretionary prism.

SEISMIC STRATIGRAPHY

Comparison of 3-D seismic line 215 with Site 1173 physical properties and lithology data suggests a direct correlation between seismic stratigraphy and lithostratigraphy (Fig. F54). Unit I (trench-wedge facies) extends from the seafloor to the strong reflection at 4860 m (core depth of 102.14 mbsf) and is characterized by high-amplitude, laterally continuous reflections. The trench wedge thickens landward and onlaps the seaward flank of the trench. Unit II (upper Shikoku Basin facies) consists of wavy stratifications that are laterally continuous from the base of Unit I to 5108 m (343.77 mbsf core depth). Reflection amplitudes diminish in the lower third of the unit. The base of Unit II is sharp, dips toward the trench, and is angularly unconformable with the underlying unit. Unit III (lower Shikoku Basin facies) has mounded, laterally continuous, moderate-amplitude reflections in the upper part, is reflection free in the middle, and has laterally continuous, low-ampli-

tude reflections at its base. Its thickness varies along strike. Unit IV (volcaniclastic facies) is a very thin, distinct reflection that drapes the basement reflection and varies in thickness laterally.
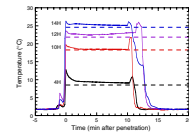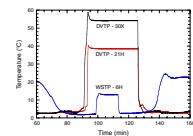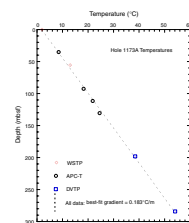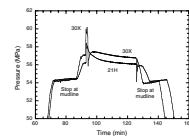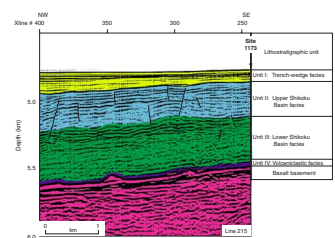
The Shikoku Basin facies (Units II and III) are deformed by numerous subtle faults (Fig. F54). Individual reflections are offset less than one seismic wavelength (<30–40 m). Faults extend neither to basement nor above the top of the Unit I/II boundary. Fault offsets are predominantly normal, although reverse faults are also present. The faults are traceable laterally up to 700 m in the 3-D seismic data set.

REFERENCES

Arch, J., and Maltman, A., 1990. Anisotropic permeability and tortuosity in deformed wet sediments. *J. Geophys. Res.,* 95:9035–9046.

Athy, L.F., 1930. Density, porosity, and compaction of sedimentary rocks. *AAPG Bull.,* 14:1–24.

Brown, K.M., and Ransom, B., 1996. Porosity corrections for smectite-rich sediments: impact on studies of compaction, fluid generation, and tectonic history. *Geology,* 24:43–84.

Cande, S.C., and Kent, D.V., 1995. Revised calibration of the geomagnetic polarity timescale for the Late Cretaceous and Cenozoic. *J. Geophys. Res.,* 100:6093–6095.

Claypool, G.E., and Kvenvolden, K.A., 1983. Methane and other hydrocarbon gases in marine sediment. *Annu. Rev. Earth Planet. Sci.,* 11:299–327.

Davis, E.E., Fisher, A.T., Firth, J.V., et al., 1997. *Proc. ODP, Init. Repts.,* 168: College Station, TX (Ocean Drilling Program).

Gartner, S., 1977. Calcareous nannofossil biostratigraphy and revised zonation of the Pleistocene. *Mar. Micropaleontol.,* 2:1–25.

Hamilton, E.L., 1976. Variations of density and porosity with depth in deep-sea sediments. *J. Sediment. Petrol.,* 46:280–300.

Kagami, H., Karig, D.E., Coulbourn, W.T., et al., 1986. *Init. Repts. DSDP,* 87: Washington (U.S. Govt. Printing Office).

Kinoshita, H., and Yamano, M., 1986. The heat flow anomaly in the Nankai Trough area. *In* Kagami, H., Karig, D.E., Coulbourn, W.T., et al., *Init. Repts DSDP,* 87: Washington (U.S. Govt. Printing Office), 737–743.

Lee, M.W., Hutchinson, D.R., Collett, T.S., and Dillon, W.P., 1996. Seismic velocities for hydrate-bearing sediments using weighted equation. *J. Geophys. Res.,* 101:20347–20358.

Lu, R., Banerjee, S.K., Jackson, M., and Marvin, J., 1993. Rock magnetic study of sediments from Site 808, Leg 131. *In* Hill, I.A., Taira, A., Firth, J.V., et al., *Proc. ODP, Sci. Results,* 131: College Station, TX (Ocean Drilling Program), 293–300.

Martini, E., 1971. Standard Tertiary and Quaternary calcareous nannoplankton zonation. *In* Farinacci, A. (Ed.), *Proc. 2nd Int. Conf. Planktonic Microfossils Roma:* Rome (Ed. Tecnosci.), 2:739–785.

Musgrave, R.J., Delaney, M.L., Stax, R., and Tarduno, J.A., 1993. Magnetic diagenesis, organic input, interstitial water chemistry, and paleomagnetic record of the carbonate sequence on the Ontong Java Plateau. *In* Berger, W.H., Kroenke, L.W., Mayer, L.A., et al., *Proc. ODP, Sci. Results,* 130: College Station, TX (Ocean Drilling Program), 527–546.

Nobes, D.C., Langseth, M.G., Kuramoto, S., Holler, P., and Hirata, N., 1992. Comparison and correlation of physical-property results from Japan Sea Basin and Rise sites, Legs 127 and 128. *In* Tamaki, K., Suyehiro, K., Allan, J., McWilliams, M., et al., *Proc. ODP, Sci. Results,* 127/128 (Pt. 2): College Station, TX (Ocean Drilling Program), 1275–1296.

Parkes, R.J., Cragg, B.A., Bale, S.J., Getliff, J.M., Goodman, K., Rochelle, P.A., Fry, J.C., Weightman, A.J., and Harvey, S.M., 1994. A deep bacterial biosphere in Pacific Ocean sediments. *Nature,* 371:410–413.

Schlumberger, 1989. *Log Interpretation Principles/Applications:* Houston (Schlumberger Educ. Services), SMP–7017.

Shipboard Scientific Party, 1975. Site 296. *In* Karig, D.E., Ingle, J.C., Jr., et al., *Init. Repts. DSDP,* 31: Washington, DC (U.S. Govt. Printing Office), 191–206.

————, 1980. Site 443, Shikoku Basin, Deep Sea Drilling Project Leg 58. *In* Klein, G. deV., Kobayashi, K., et al., *Init. Repts. DSDP,* 58: Washington (U.S. Govt. Printing Office), 109–218.

————, 1986a. Site 582. *In* Kagami, H., Karig, D.E., Coulbourn, W.T., et al., *Init. Repts. DSDP,* 87: Washington (U.S. Govt. Printing Office), 35–122.

————, 1986b. Site 584. *In* Kagami, H., Karig, D.E., Coulbourn, W.T., et al., *Init. Repts. DSDP,* 87: Washington (U.S. Govt. Printing Office), 257–305.

————, 1991. Site 808. *In* Taira, A., Hill, I., Firth, J.V., et al., *Proc. ODP, Init. Repts.,* 131: College Station, TX (Ocean Drilling Program), 71–269.

Smith, D.C., Spivack, A.J., Fisk, M.R., Haveman, S.A., Staudigel, H., and ODP Leg 185 Scientific Party, 2000a. Methods for quantifying potential microbial contamination during deep ocean coring. *ODP Tech. Note,* 28 [Online]. Available from World Wide Web: <http://www-odp.tamu.edu/publications/tnotes/tn28/INDEX.HTM>.

————, 2000b. Tracer-based estimates of drilling-induced microbial contamination of deep sea crust. *Geomicrobiol. J.,* 17:207–219.

Stoffa, P.L., Wood, W.T., Shipley, T.H., Moore, G.F., Nishiyama, E., Bothelo, M.A.B., Taira, A., Tokuyama, H., and Suyehiro, K., 1992. Deepwater high-resolution expanding spread and split spread marine seismic profiles in the Nankai Trough. *J. Geophys. Res.,* 97:1687–1713.

Taira, A., Hill, I., Firth, J.V., et al., 1991. *Proc. ODP, Init. Repts.,* 131: College Station, TX (Ocean Drilling Program).

Tamaki, K., Pisciotto, K., Allan, J., et al., 1990. *Proc. ODP, Init. Repts.,* 127: College Station, TX (Ocean Drilling Program).

Tissot, B.P., and Welte, D.H., 1984. *Petroleum Formation and Occurrence* (2nd ed.): Heidelberg (Springer-Verlag).

Wellsbury, P., Goodman, K., Barth, T., Cragg, B.A., Barnes, S.P., and Parkes, R.J., 1997. Deep marine biosphere fueled by increasing organic matter availability during burial and heating. *Nature,* 388:573–576.

Wellsbury, P., Goodman, K., Cragg, B.A., and Parkes, R.J., 2000. The geomicrobiology of deep marine sediments from Blake Ridge containing methane hydrate (Sites 994, 995, and 997). *In* Paull, C.K., Matsumoto, R., Wallace, P.J., and Dillon, W.P. (Eds.), *Proc. ODP, Sci. Results,* 164: College Station, TX (Ocean Drilling Program), 379–391.

Yamano, M., Foucher, J.-P., Kinoshita, M., Fisher, A., Hyndman, R.D., and ODP Leg 131 Shipboard Scientific Party, 1992. Heat flow and fluid flow regime in the western Nankai accretionary prism. *Earth Planet. Sci. Lett.,* 109:451–462.

Young, J.R., 1998. Neogene. *In* Bown, P.R. (Ed.), *Calcareous Nannofossil Biostratigraphy* (Vol. 8): Dordrecht (Kluwer Academic), 225–265.

Figure F1. Location of the *JOIDES Resolution* seismic profile collected on the transit to Site 1173. The seismic profile is shown in Figure F2, p. 39.
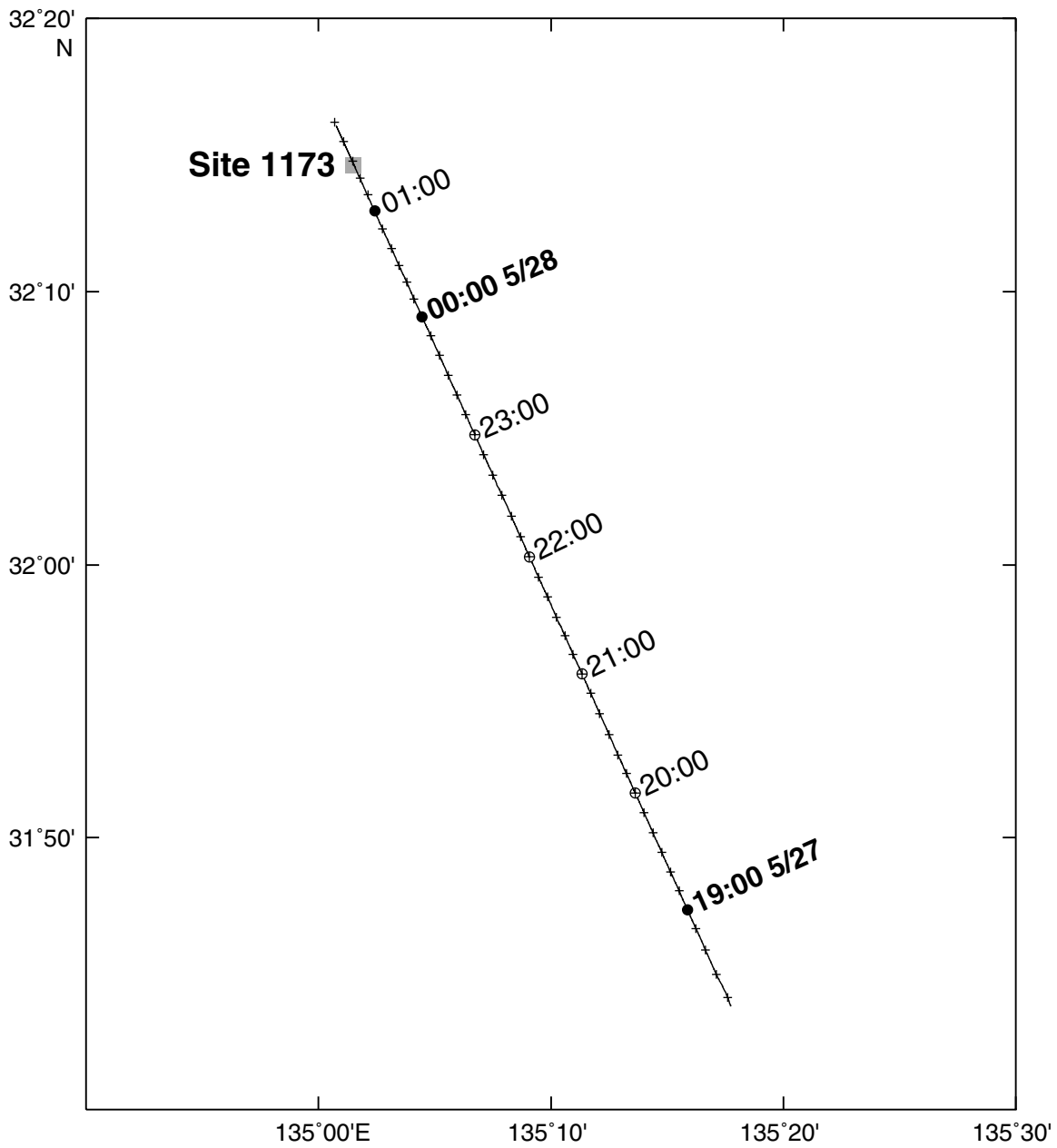
Figure F2. Single-channel seismic profile collected on the transit to Site 1173. Location of seismic profile is shown in Figure F1, p. 38. A single 80-in³ water gun was used. Processing includes despiking, notch filtering (60 Hz), bandpass filtering (10–80 Hz), three-trace mix, F-K migration (constant velocity at 1550 m/s), bandpass filtering (10–80 Hz) three-trace mix, automatic gain control (500 ms), and mute to water bottom. (This figure is also available in an **oversized format** along with Fig. F1 for reference.)
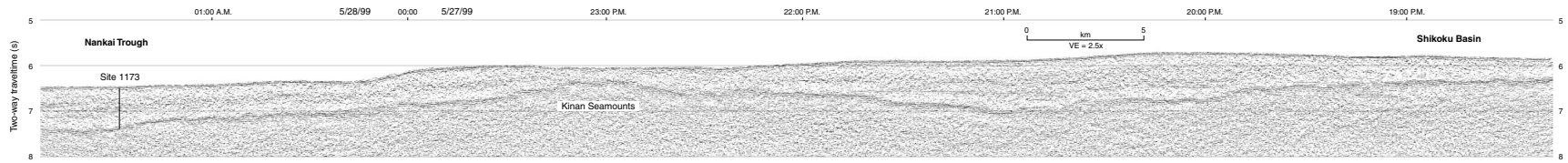
Figure F3. Stratigraphic column for Site 1173, showing stratigraphic units and their characteristic lithologies.

Unit IA: outer trench–wedge facies
Sand and silt turbidites, hemipelagic mud, rare volcanic ash

Unit IB: trench to basin transition facies
Silt turbidites, hemipelagic mud, volcanic ash

Unit II: upper Shikoku Basin facies
Hemipelagic mudstone, abundant volcanic ash

Unit III: lower Shikoku Basin facies
Hemipelagic mudstone, rare siliceous claystone, and calcareous claystone

Unit IV: volcaniclastic facies
Variegated mudstone, siliceous tuff

Unit V: basalt basement

Figure F4. Distribution and thickness of volcanic ash layers in Hole 1173A. Beds greater than or equal to 4 cm in thickness are highlighted with horizontal lines.
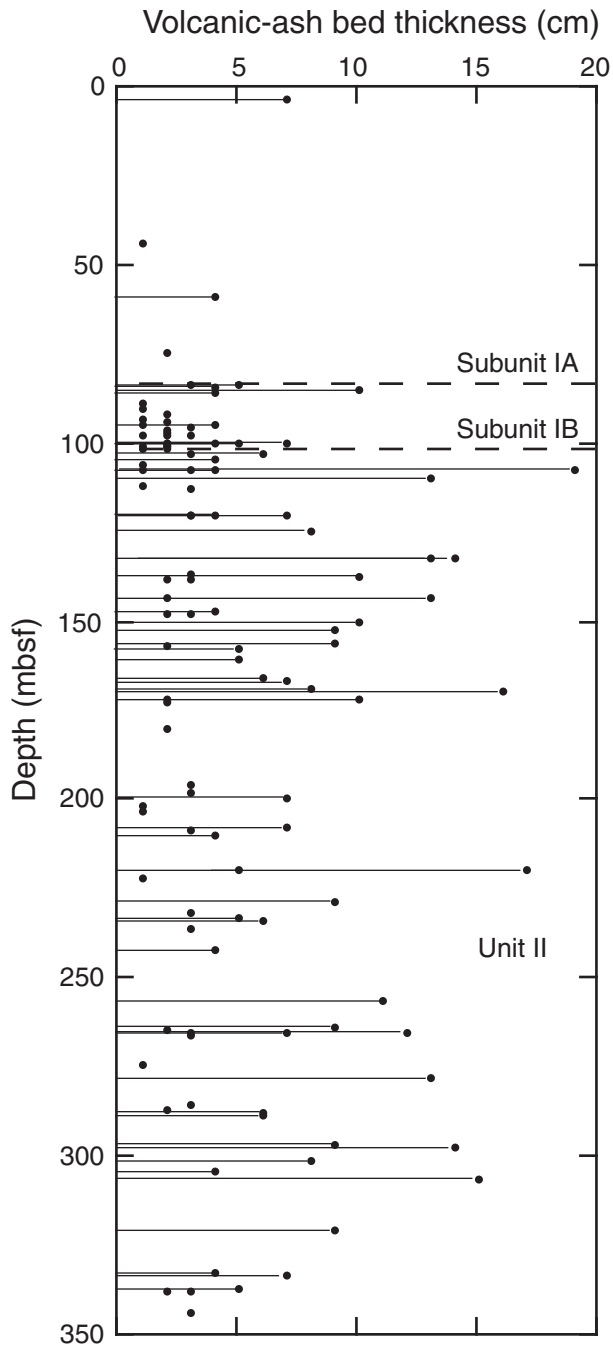
Figure F5. Sandy turbidite interbedded with silty clay from Subunit Unit IA (outer trench–wedge facies; interval 190-1173A-9H-1, 118–148 cm). The sandy turbidite has a sharp irregular base, fines upward, and has plane-parallel laminae in the upper part.
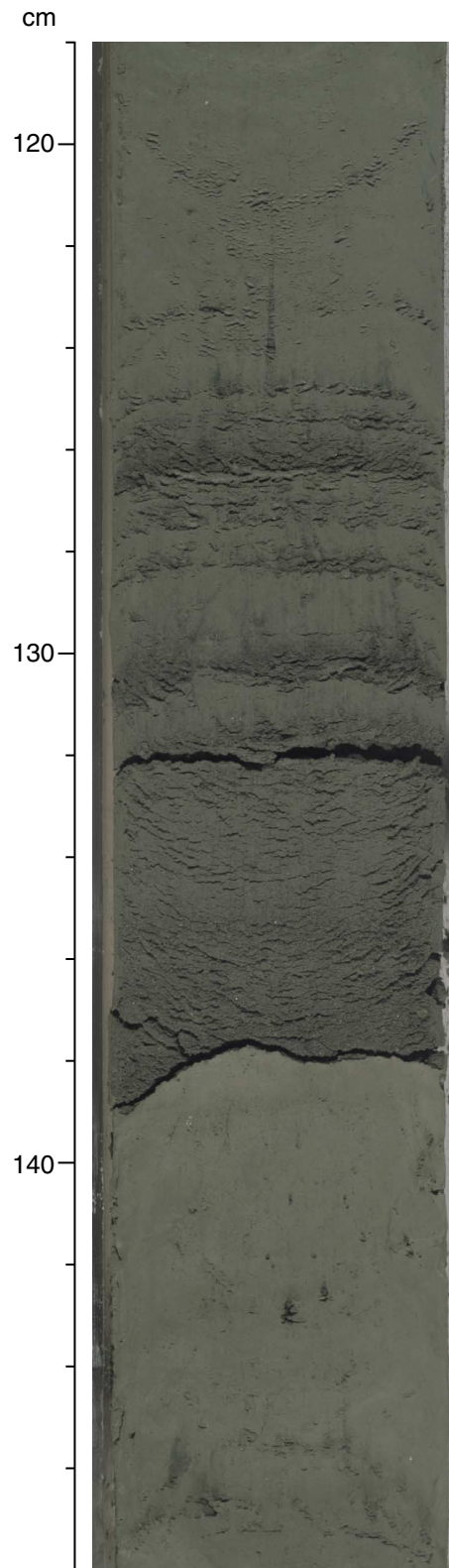
Figure F6. Volcanic ash beds interbedded with silty clays from Unit II (upper Shikoku Basin facies; interval 190-1173A-13H-6, 100–124 cm). The lower ash bed has a sharp plane-parallel base, a gradational upper contact, and pale gray and green diffuse layers. The upper volcanic ash has a sharp, irregular bioturbated base, a gradational upper contact, and diffuse pale pink and brown layers.
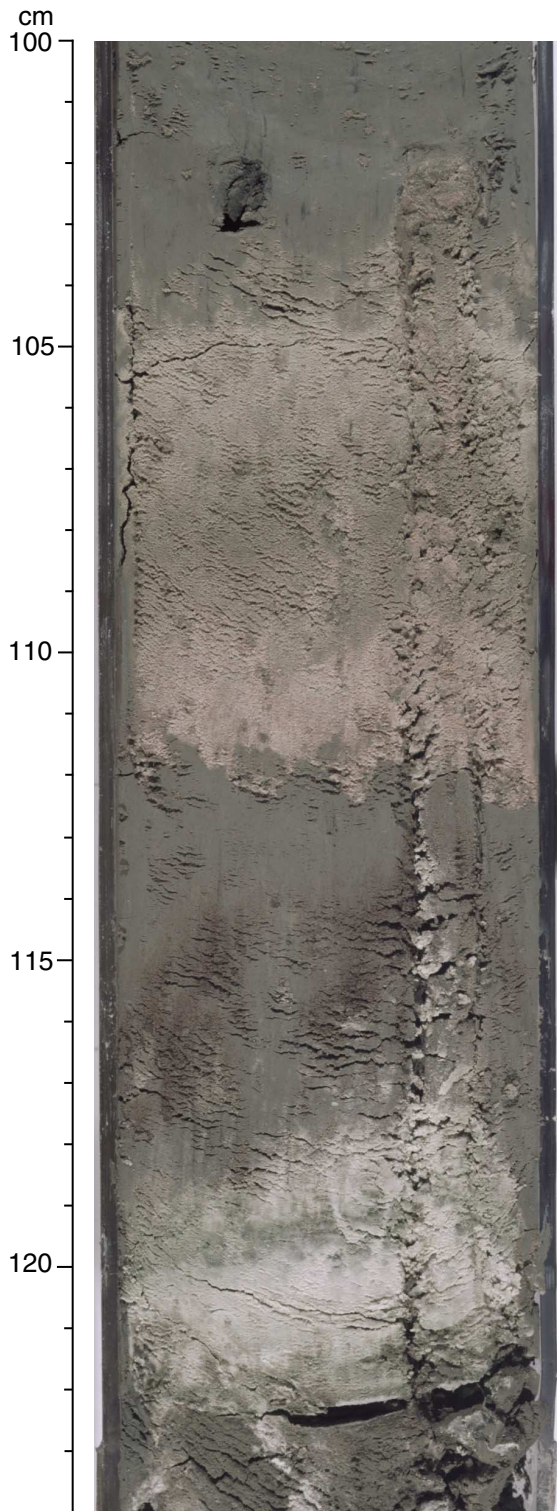
Figure F7. Volcanic ash bed interbedded with silty clay from Unit II (upper Shikoku Basin facies; interval 190-1173A-24H-3, 90–115 cm). The lower contact of the volcanic ash is sharp and irregular, and the upper contact is diffuse and irregular. The volcanic ash layer coarsens upward from silt to medium sand grade and then fines upward to silt.
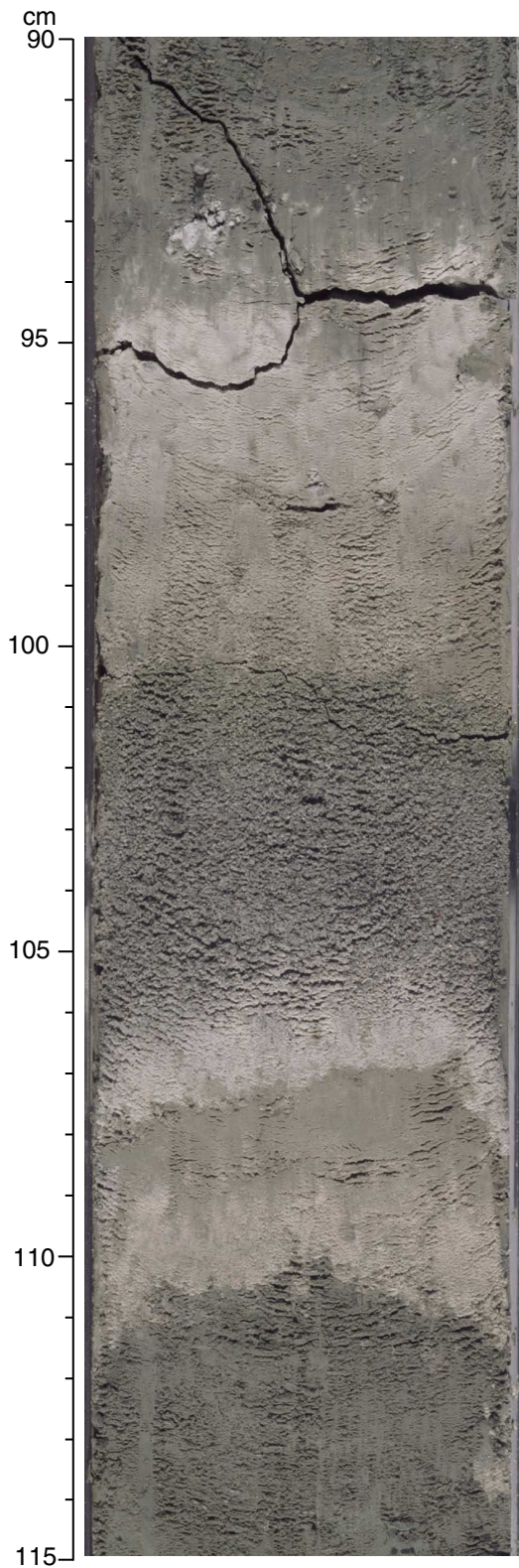
Figure F8. Bioturbated silty claystone and interbedded siliceous claystone from Unit III (lower Shikoku Basin facies; interval 190-1173A-57X-4, 66–71 cm). The dark gray thin bed (68–69 cm) is a siliceous claystone with a sharp, irregular base and diffuse, irregular, heavily bioturbated upper surface. A *Zoophycos* burrow is infilled with gray silty clay.
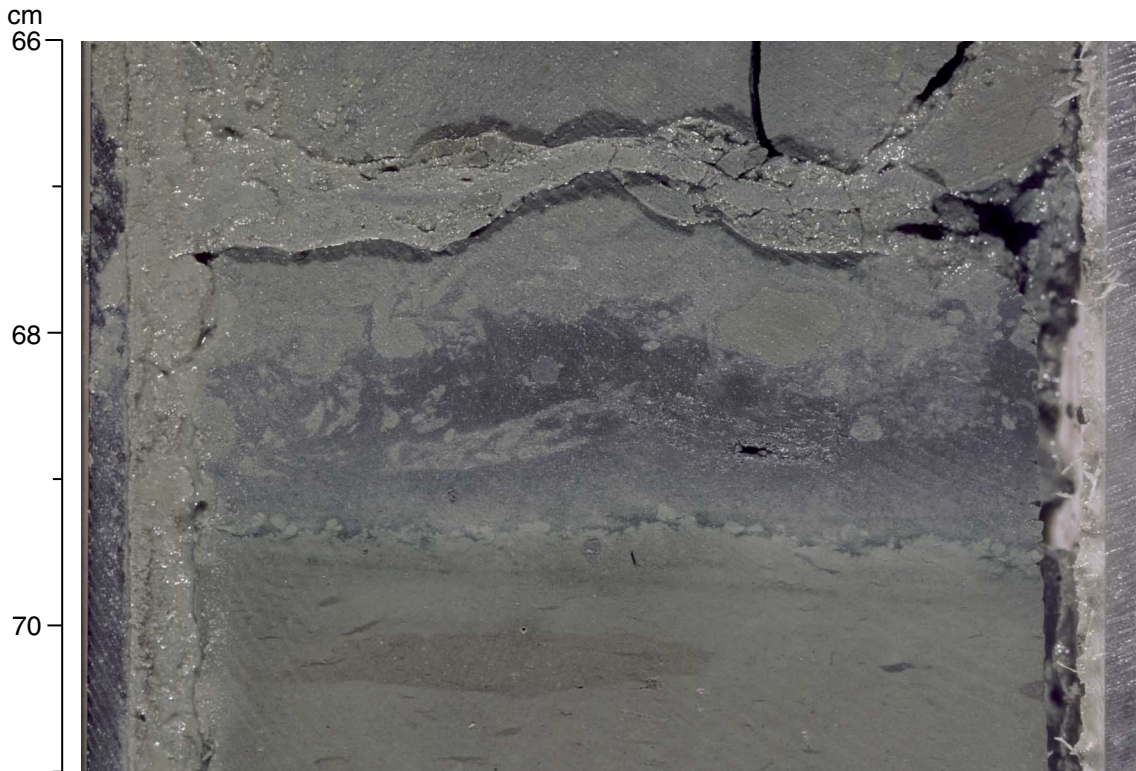
Figure F9. Dark gray to black basalt (Unit V) and variably colored silty claystone from Unit IV (volcaniclastic facies; interval 190-1173A-77X-CC, 20–26 cm). Note the alteration of silty claystone at the sediment/basalt contact.
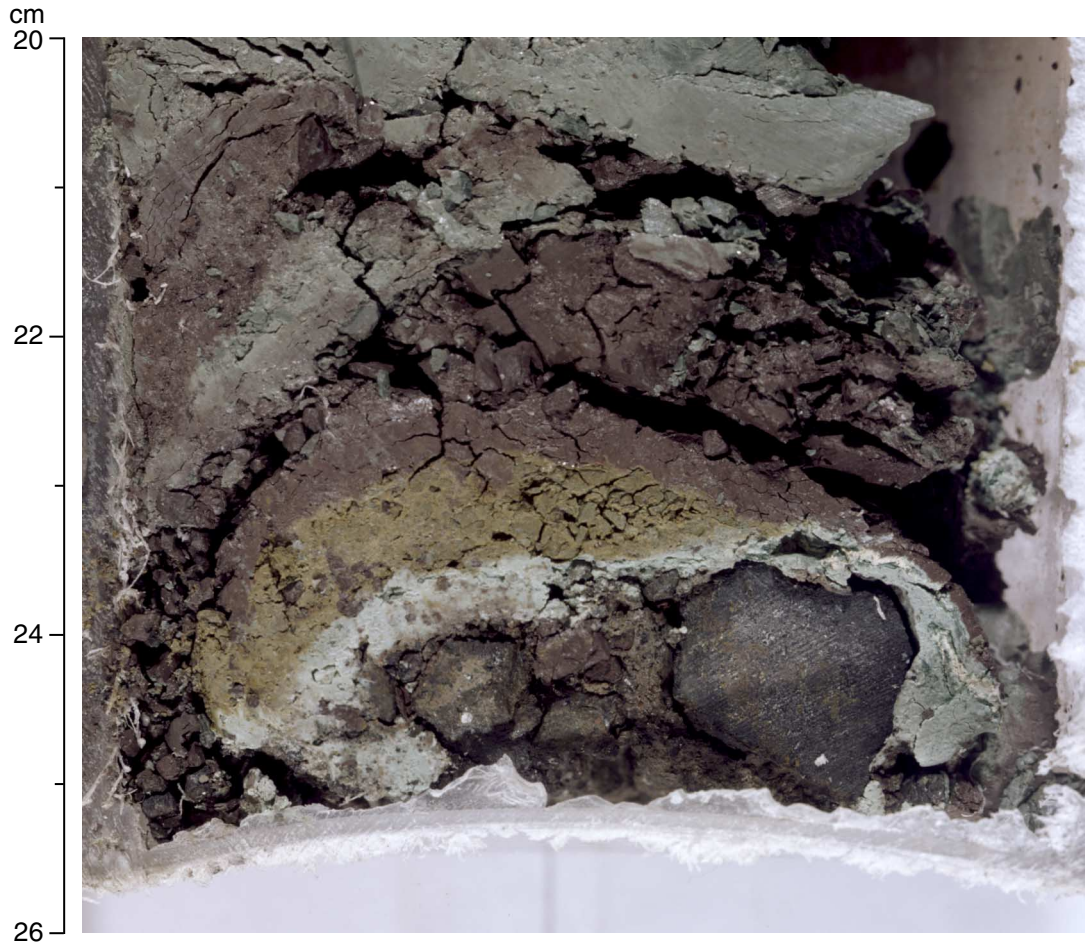
Figure F10. Normalized relative abundances of total clay minerals, quartz, plagioclase, and calcite at Site 1173 based on X-ray diffraction analyses of randomly oriented bulk sediment powders. Also shown are ratios of X-ray diffraction peak areas of (101) cristobalite to (100) quartz.
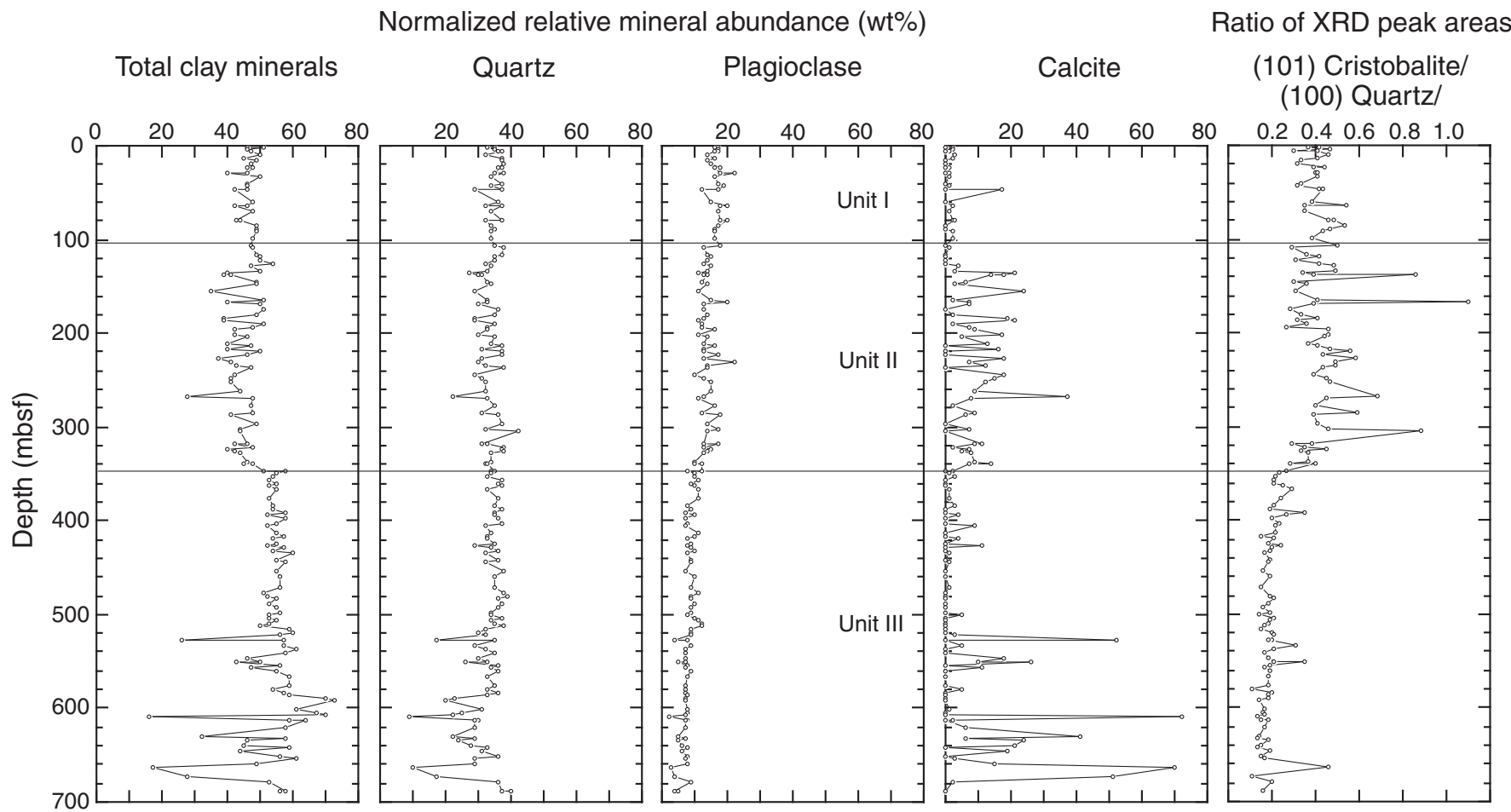
Figure F11. Bedding dips relative to the core liner plotted against depth; dips <7.5° (shaded zone) are not thought to be significantly different from 0°. Bedding dips increase abruptly at ~375 mbsf, and moderate dips occur sporadically to the base of the hole. Note that bioturbation features suggest that approximately horizontal orientations are also present in the lowest few hundred meters of the hole, but indistinct bedding precluded measurement. Generalized distribution of structural features is shown to the right, along with observed displacements in millimeters (symbols are defined in **"Structural Geology,"** p. 6, in the "Explanatory Notes" chapter) (**Figure shown on next page**).

Figure F11 (continued). (Caption shown on previous page.)

Bedding dip (°, with reference to the core liner)

Structures

Normal fault   Reverse fault   Antithetic microfractures   Foliated breccia
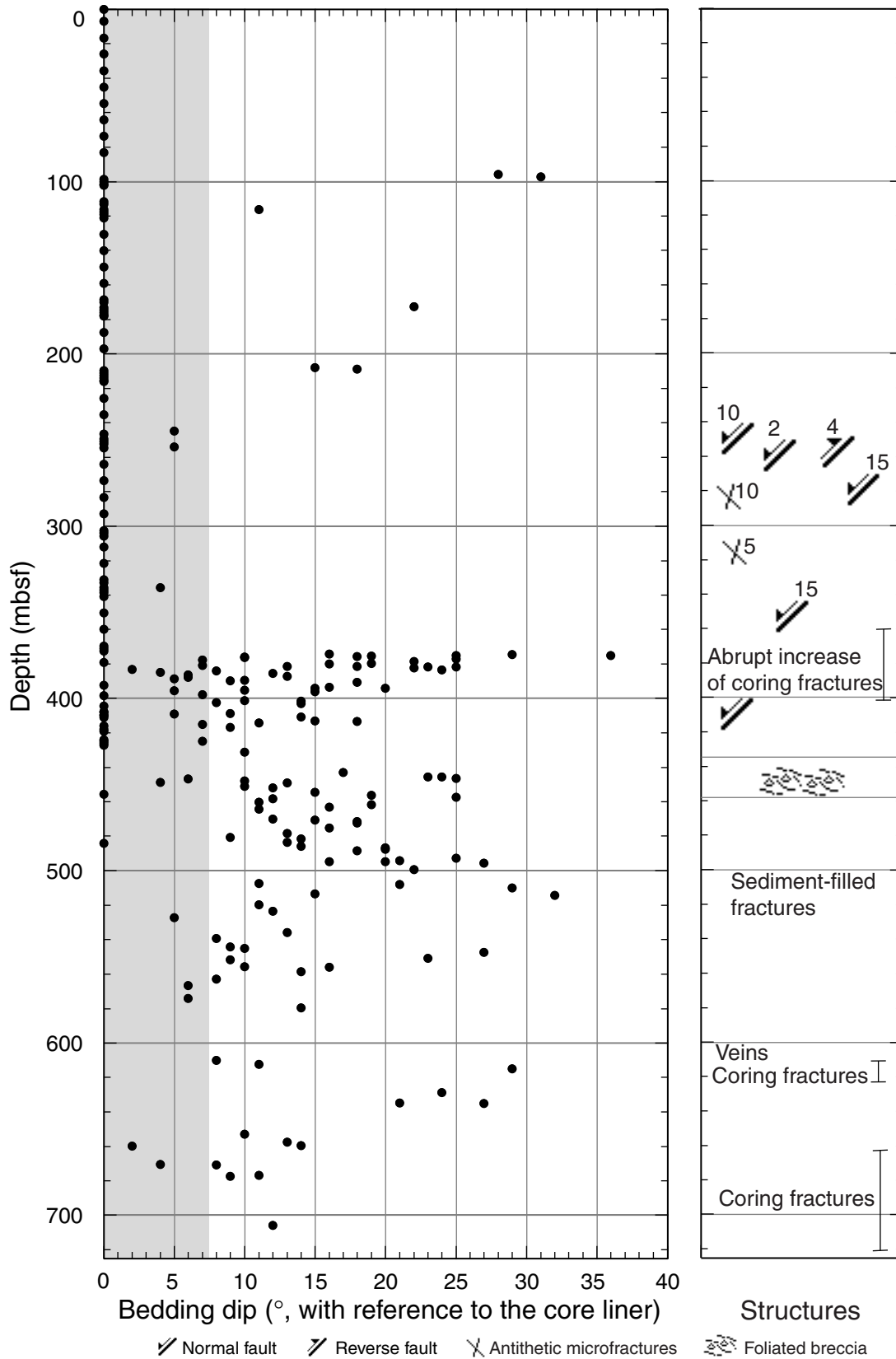
Figure F12. Equal-area lower-hemisphere stereographic plot of poles to bedding after paleomagnetic reorientation to true geographic coordinates.
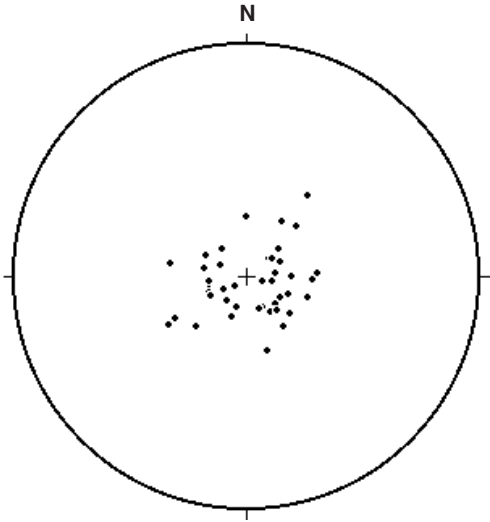
Figure F13. Healed high-angle normal fault showing antithetic faults and brecciation in the footwall (interval 190-1173A-33X-4, 111–122 cm).
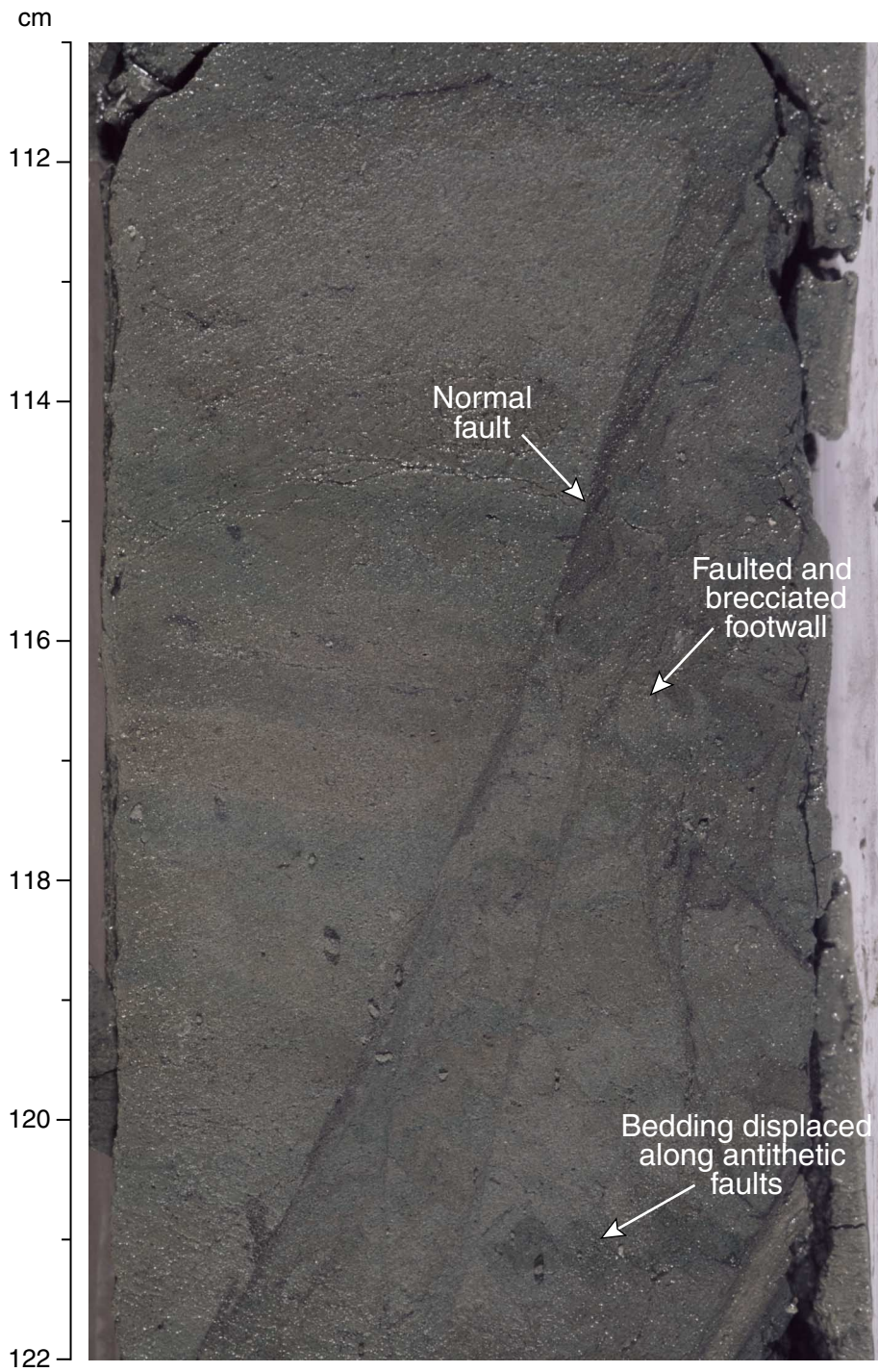
Figure F14. Zone of foliated breccia (interval 190-1173A-47X-3, 0–23 cm). Note the foliated character and low-angle planar contacts between clasts. A mineralized vein lies along a high-angle fracture over interval 190-1173A-47X-3, 20–25 cm, confirming the natural origin of the breccia.
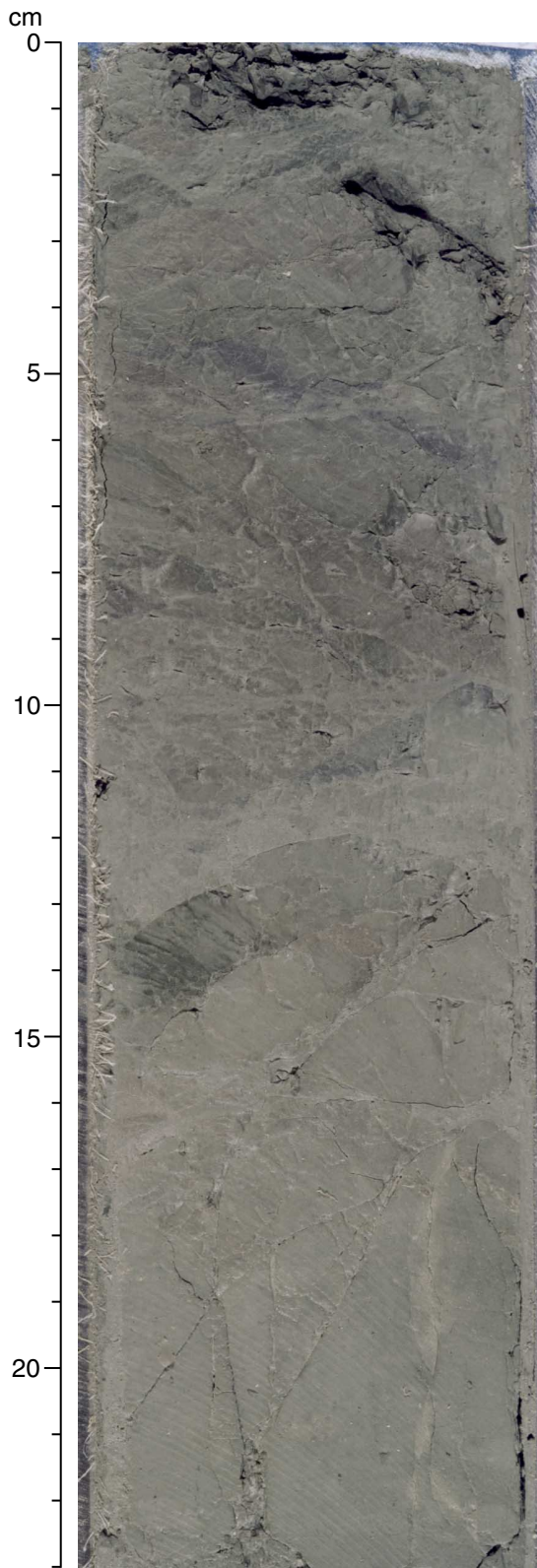
Figure F15. Sediment-filled structure, probably caused by fluid escape (interval 190-1173A-53X-5, 89–97 cm). Note the zone of sediment brecciation near base of the feature and the funnel-shaped top. A sediment horizon has been deflected adjacent to the structure.
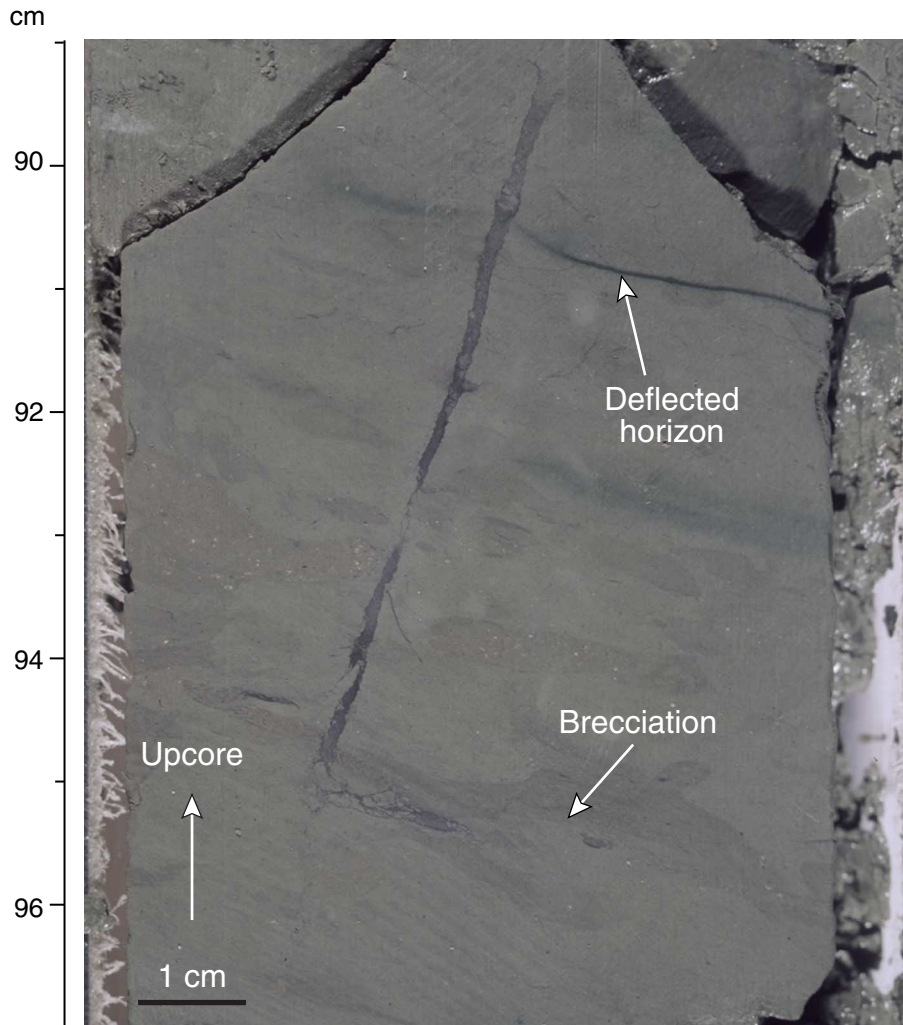
Figure F16. Subvertical, white, mineralized veins transecting a carbonate horizon (interval 190-1173A-65X-CC, 28–36 cm). Several veins die out near the base of the overlying silty claystone in a zone of carbonate mineralization.
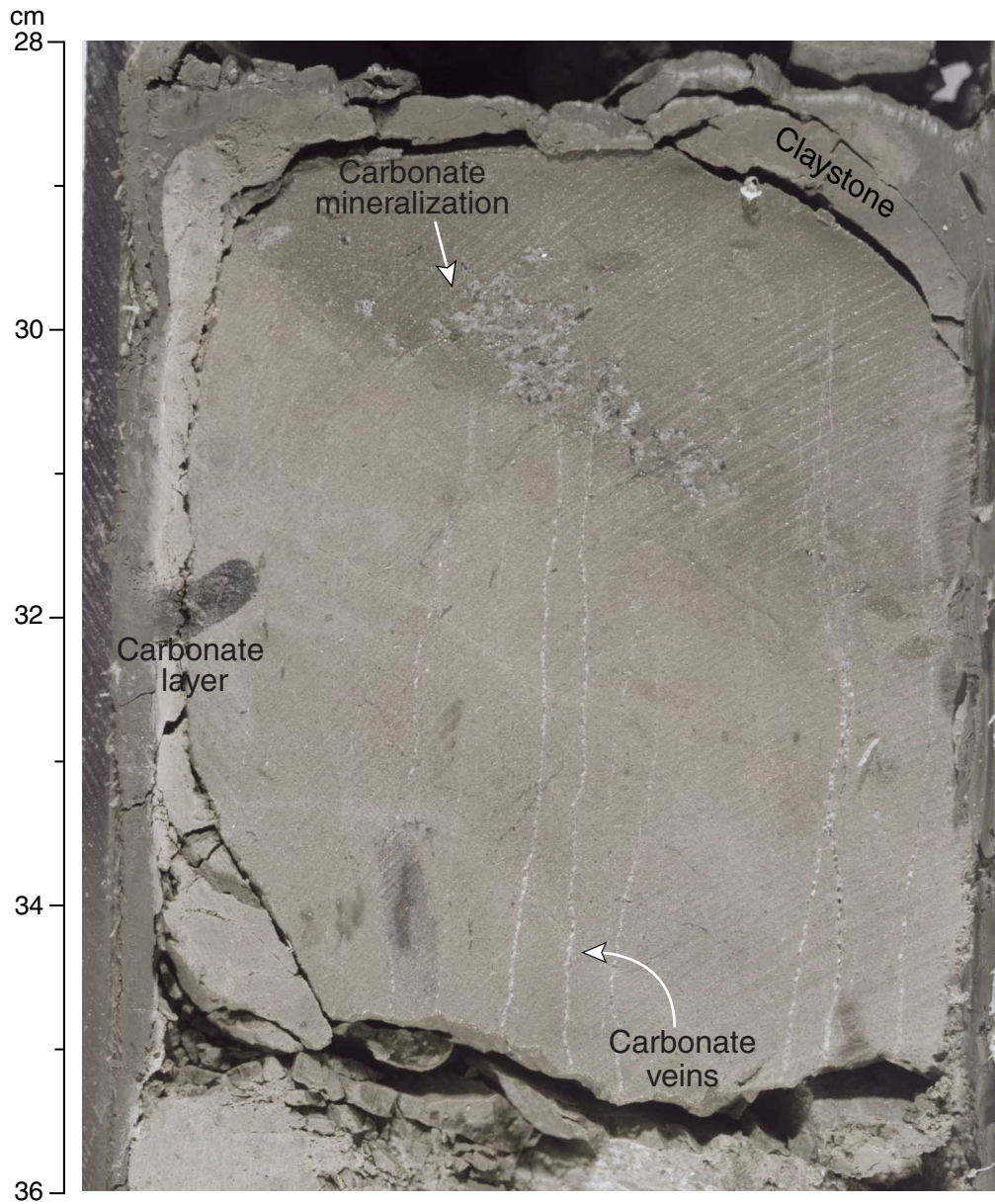
Figure F17. Variation of uncalibrated gas permeability with depth. The peaks derive from the high values in the ash bands.
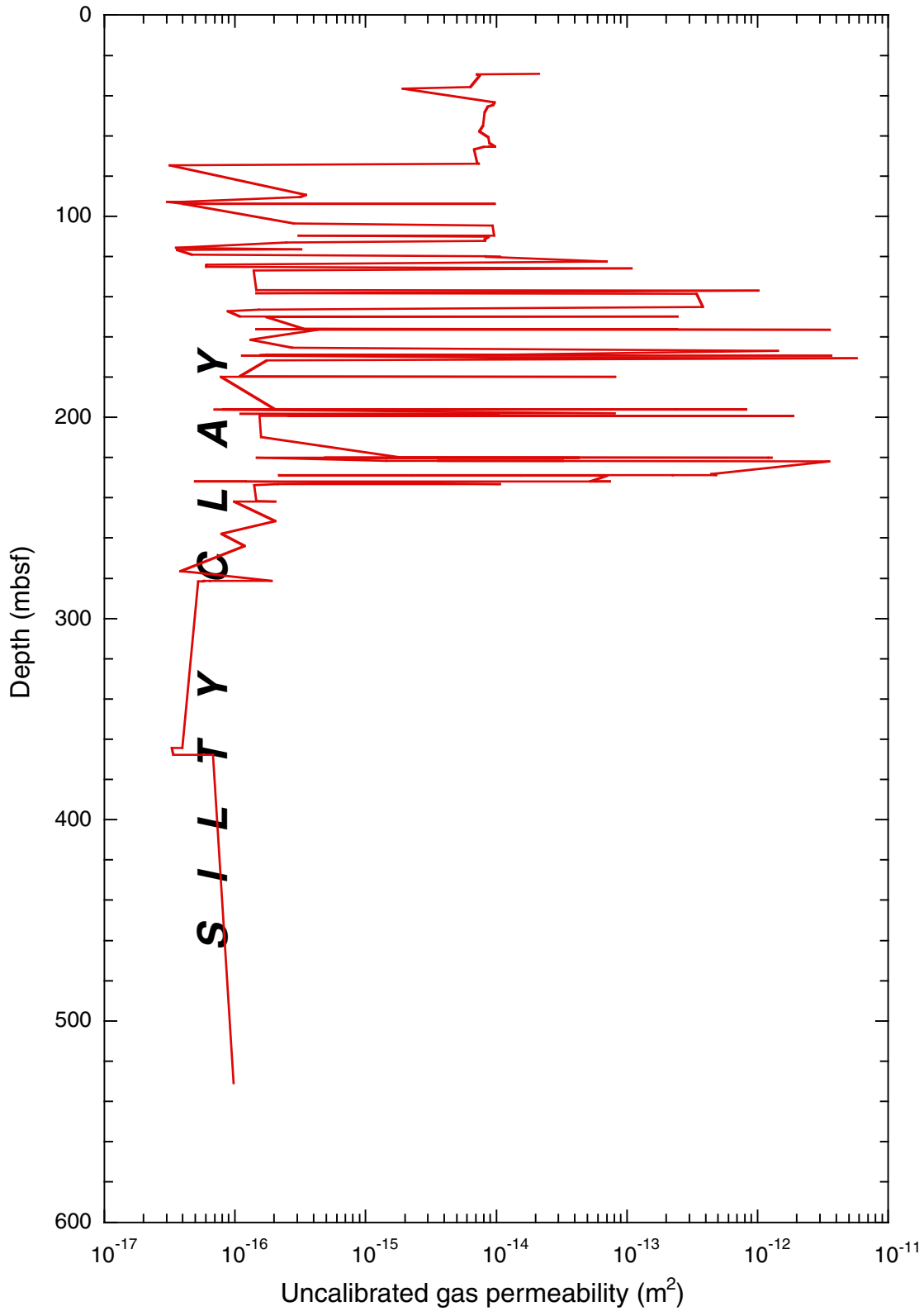
Figure F18. Details of uncalibrated gas-permeability variations within and adjacent to two representative ash layers in lithostratigraphic Unit II.

Section 190-1173-17-5, 51-64 cm

Uncalibrated
gas permeability
(m^2)

1.5×10^{-16} ——— Hemipelagite

2.4×10^{-13} ——— Fine gray ash

6.1×10^{-15} ——— Fine ash
with clay smears

3.5×10^{-12} ——— Coarse gray ash

4.3×10^{-16} ——— Hemipelagite

Section 190-1173-22-2, 67-85 cm

2.6×10^{-16} ——— Hemipelagite

1.6×10^{-13} ——— Pale gray ash

6.5×10^{-13} ——— Dark gray ash

1.9×10^{-12} ——— Medium-grained
white ash

1.5×10^{-16} ——— Hemipelagite
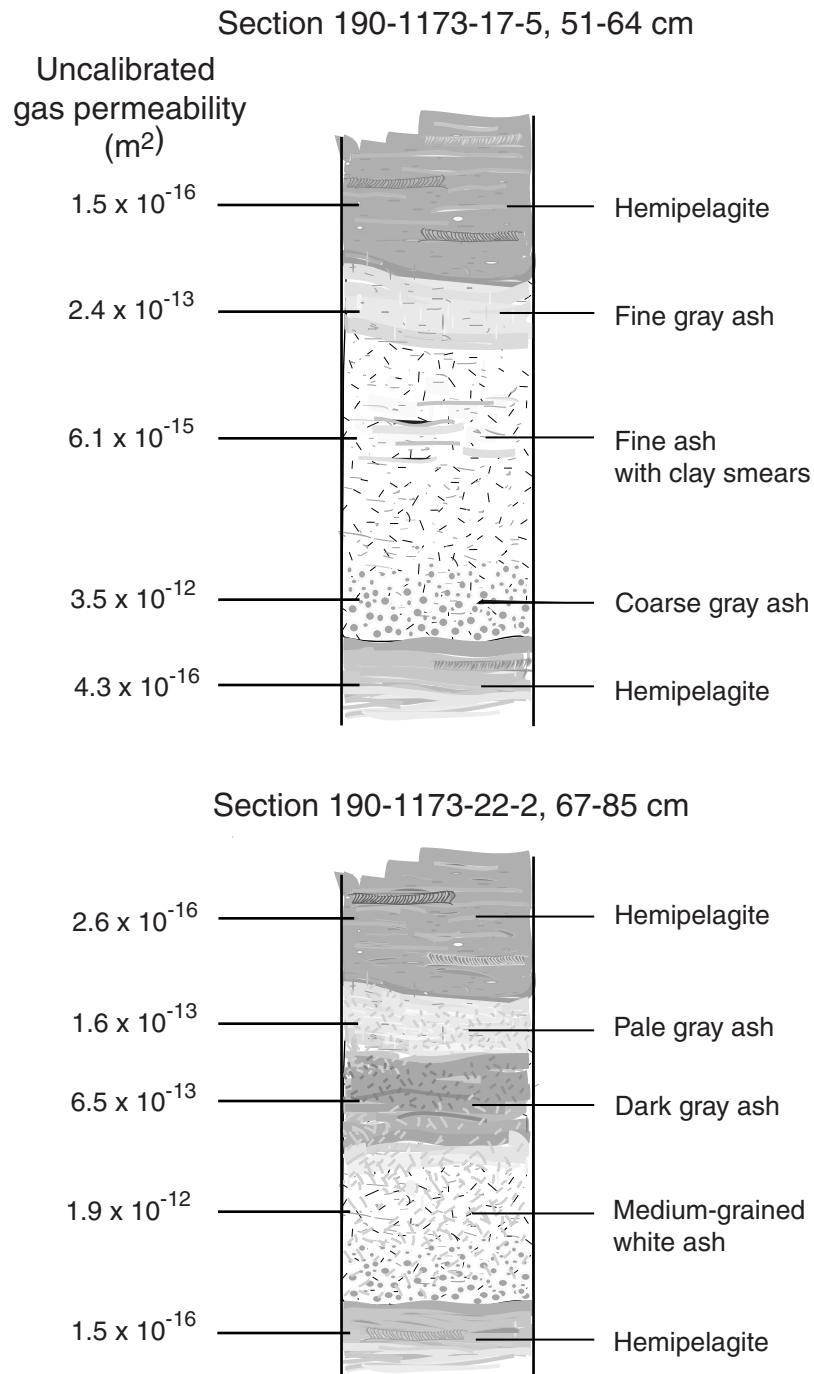
Figure F19. The inclination of the remanent magnetization before (NRM) and after alternating-field (AF) demagnetization at Hole 1173A. **A.** 0–350 mbsf. **B.** 350–700 mbsf.
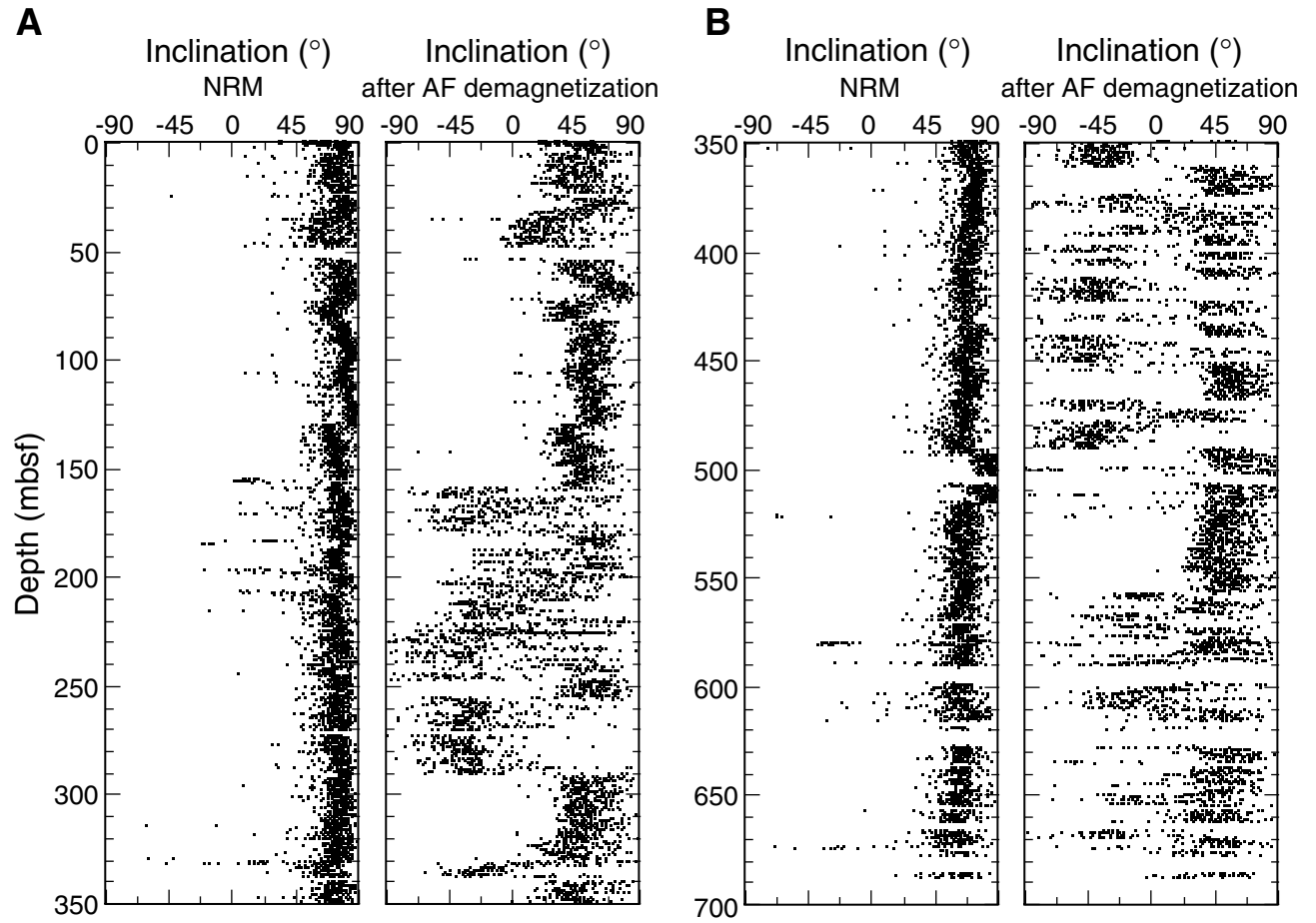
Figure F20. Declination after alternating-field (AF) demagnetization at Hole 1173A. Clear paleomagnetic declination records are observed after Tensor tool correction of the APC cores. Noisy declinations below ~160 mbsf reflect individual core piece rotation during XCB coring.
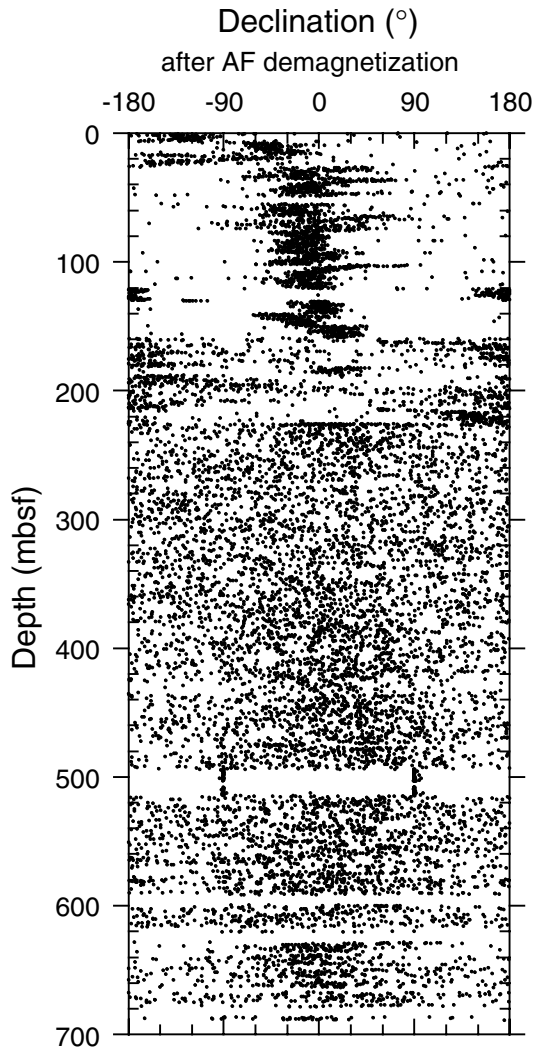
Figure F21. Examples of vector end-point diagrams for (**A, C, E, G, I,** and **K**) discrete samples and (**B, D, F, H, J,** and **L**) archive-half sections at Hole 1173A. Solid circles = horizontal plane, open circles = vertical plane, NRM = natural remanent magnetization. Demagnetization levels are given in milliteslas.
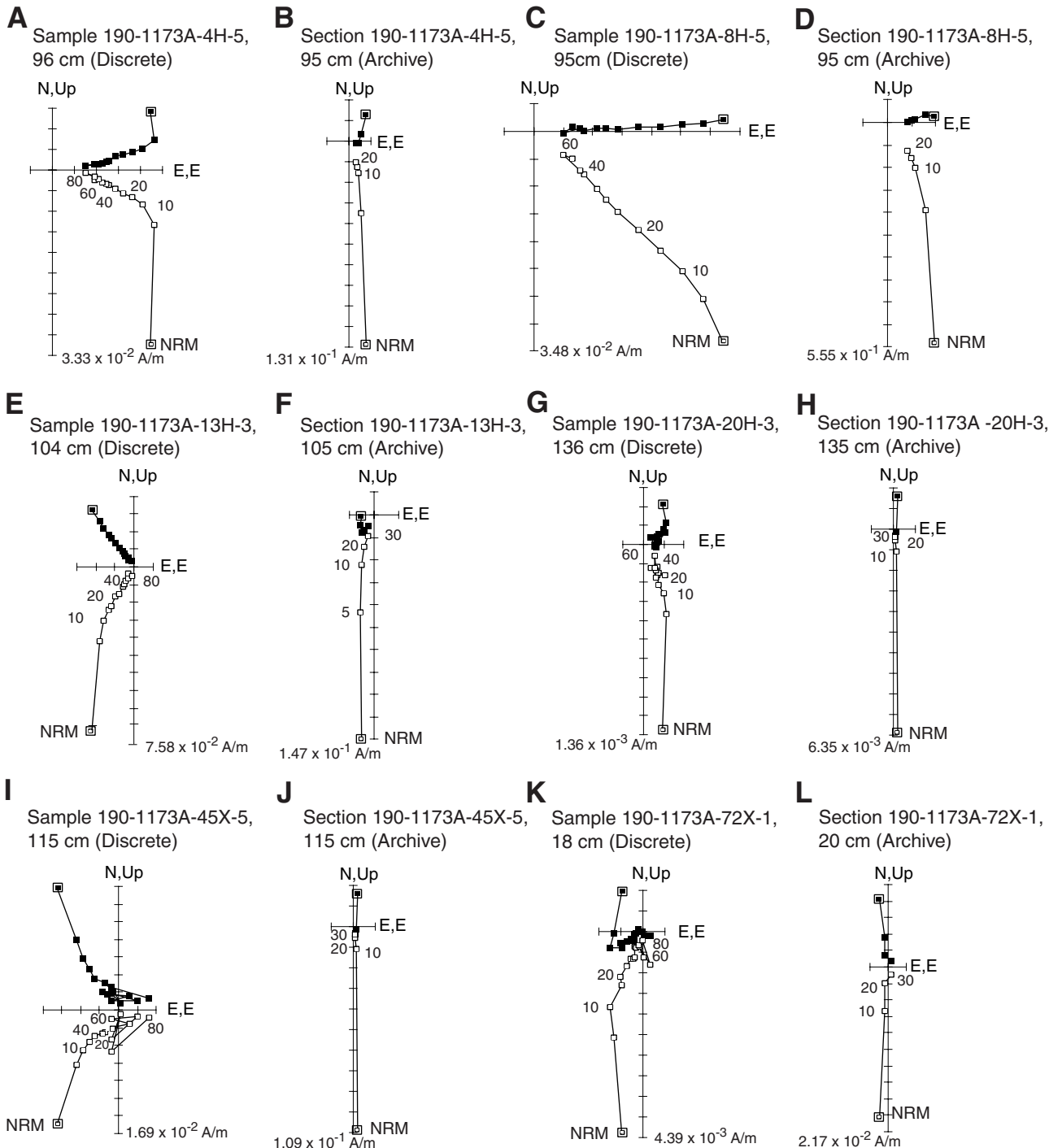
Figure F22. Comparison of magnetic intensity (after AF demagnetization) and MST magnetic susceptibility. The marked high-intensity and high-susceptibility zones at the upper part of Hole 1173A occur in Subunits IA (turbidite successions) and IB (sedimentary transition zone from turbidites to hemipelagite). In contrast, the sediments below 140 mbsf show low values of magnetic intensity and susceptibility.
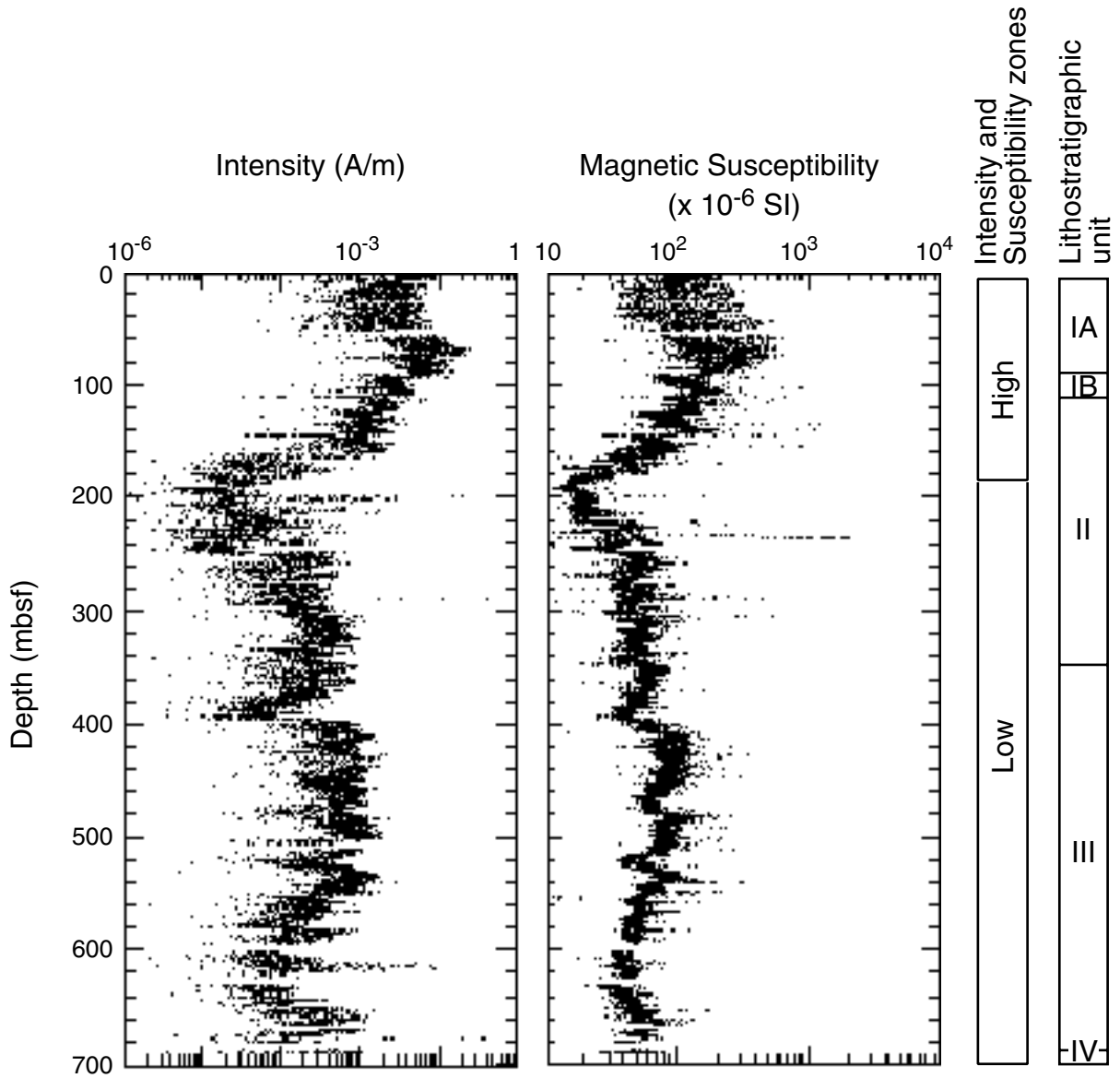
Figure F23. Magnetic intensity correlation between Holes 1173A and 808C. The magnetic intensity at Hole 808C was measured on discrete samples (Taira et al., 1991).
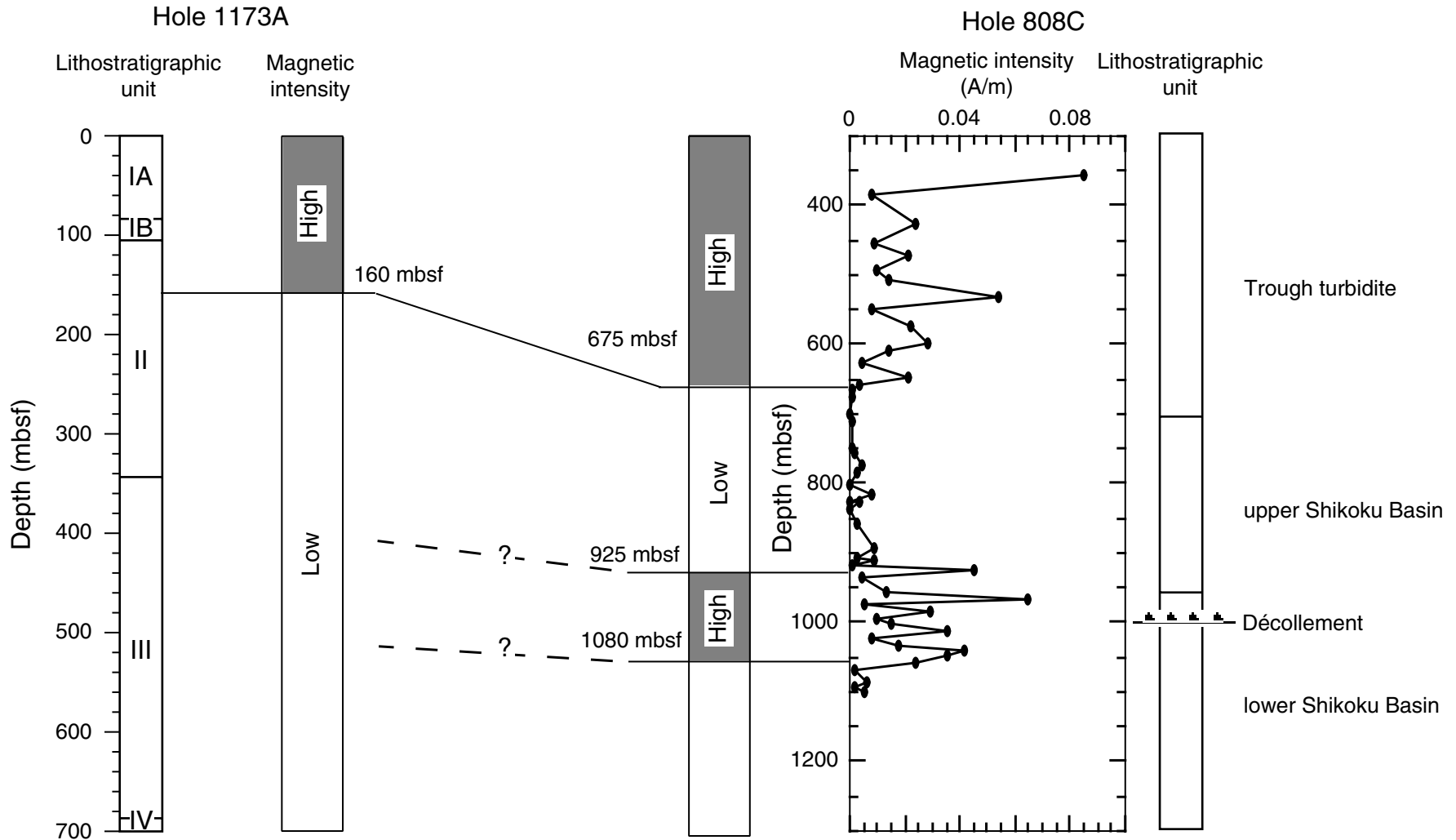
Figure F24. Site 1173 magnetostratigraphy. Middle Miocene to Pleistocene magnetic polarity intervals compared with the magnetic polarity time scale (Cande and Kent, 1995). Black = normal polarity, white = reversed polarity, gray = unknown polarity, ? = questionable correlation.
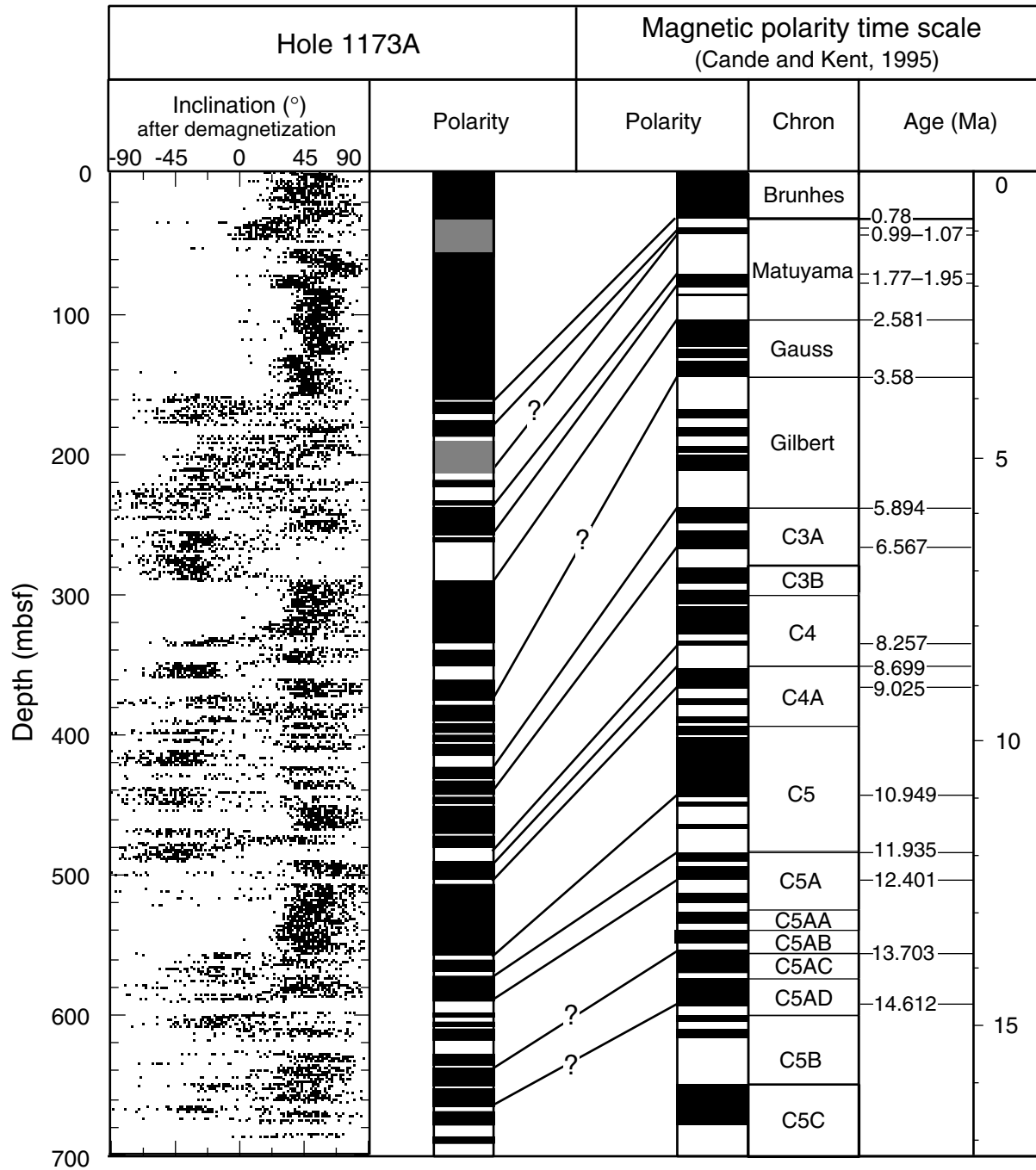
Figure F25. Site 1173 age-depth plot obtained by magnetostratigraphy and biostratigraphy. Note the change in the sedimentation rate at 350 mbsf. Black = normal polarity, white = reversed polarity.
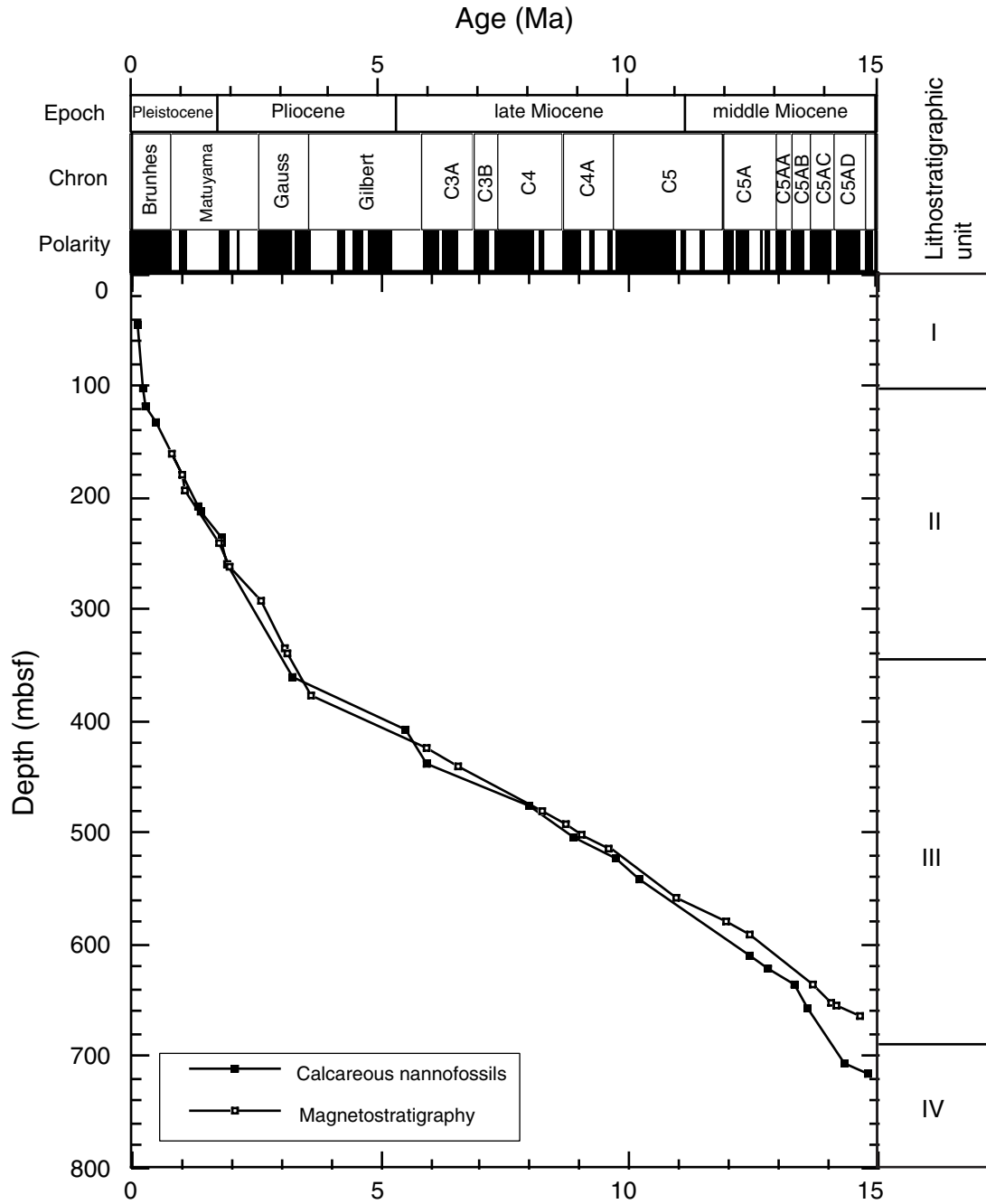
Figure F26. Pore fluid composition as a function of depth at Site 1173. Solid horizontal lines indicate lithostratigraphic boundaries. Dashed lines = the décollement-equivalent horizon.
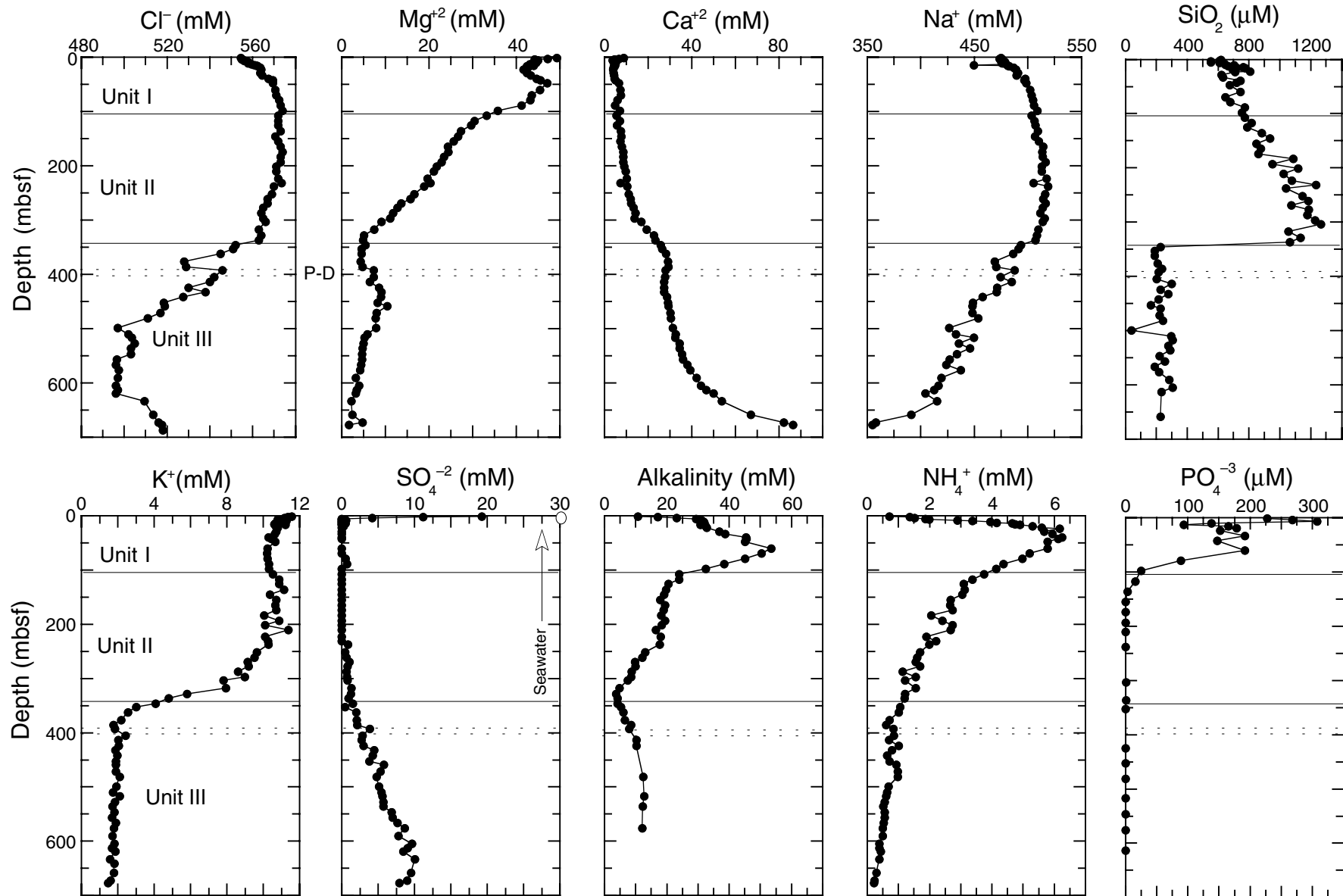
Figure F27. Molecular compositions and concentrations of headspace (**A**) methane and (**B**) ethane and propane from Hole 1173A. Gas concentrations are given in parts per million.
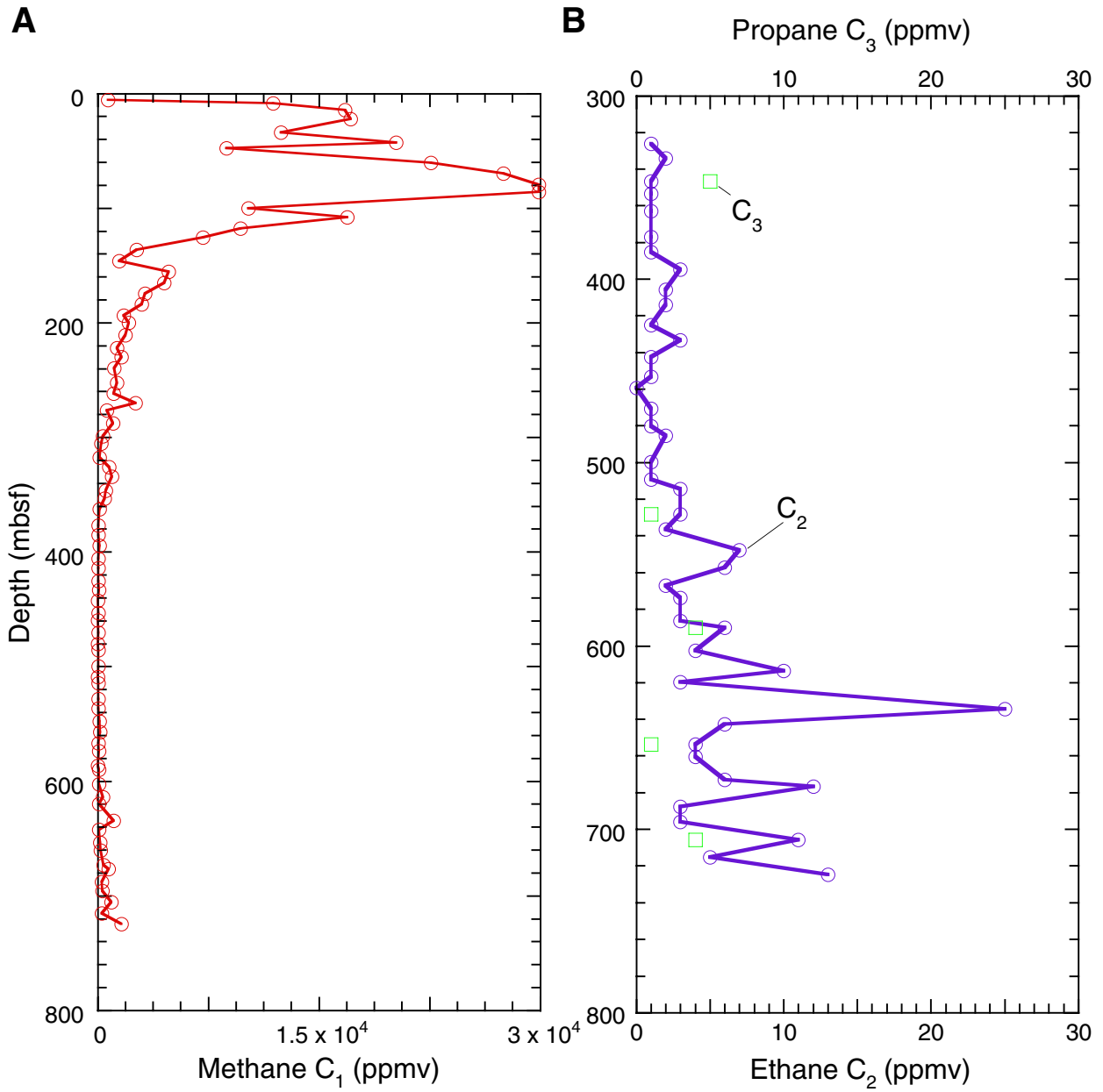
Figure F28. (**A**) Total organic carbon (TOC) and (**B**) nitrogen contents in sediments from Hole 1173A and (**C**) C/N ratio.
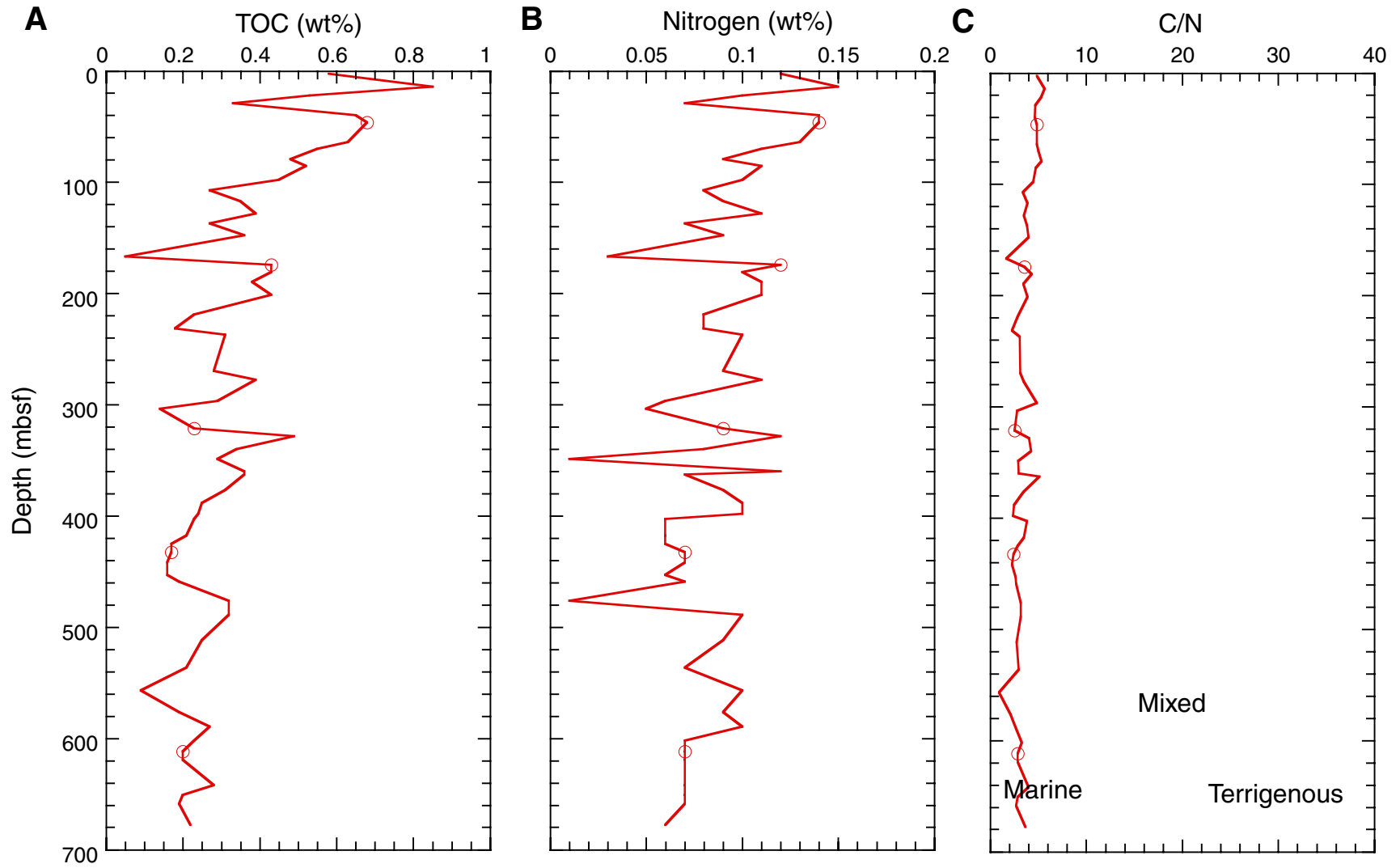
Figure F29. Percentage of inorganic carbon (carbonate) in sediments from Hole 1173A.
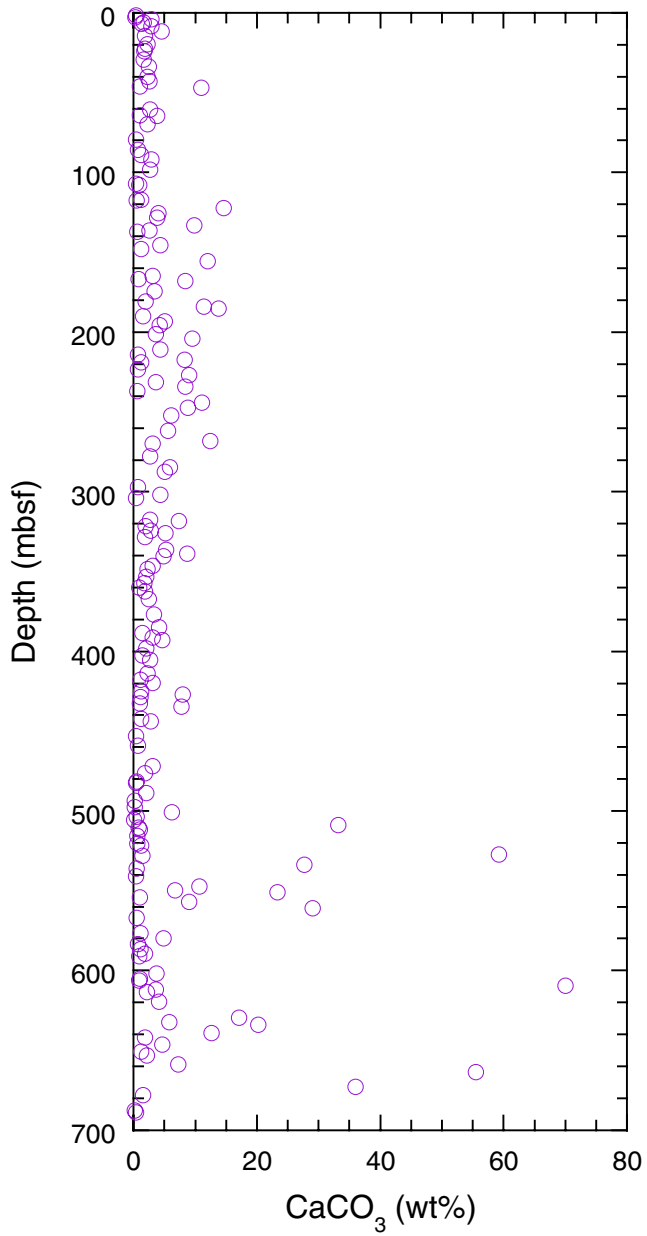
Figure F30. Depth and temperature distribution of total bacterial populations in sediment samples from Hole 1173A. The curved dashed line represents a general regression line of bacterial numbers vs. depth in deep-sea sediments (Parkes et al., 1994), with 95% upper and lower prediction limits shown by the curved lines of longer dashes. The shaded area to the left of the figure indicates levels where bacterial populations are too low to be detected with the acridine orange direct counts technique (detection limit is ~6 × 10^4 cells/cm^3). The two horizontal lines separate bacterial groups with different temperature ranges for growth. The solid square at the base of the graph is the bacterial numbers contained in the drill fluid (surface seawater); these were 1.4 × 10^5 cells/cm^3.
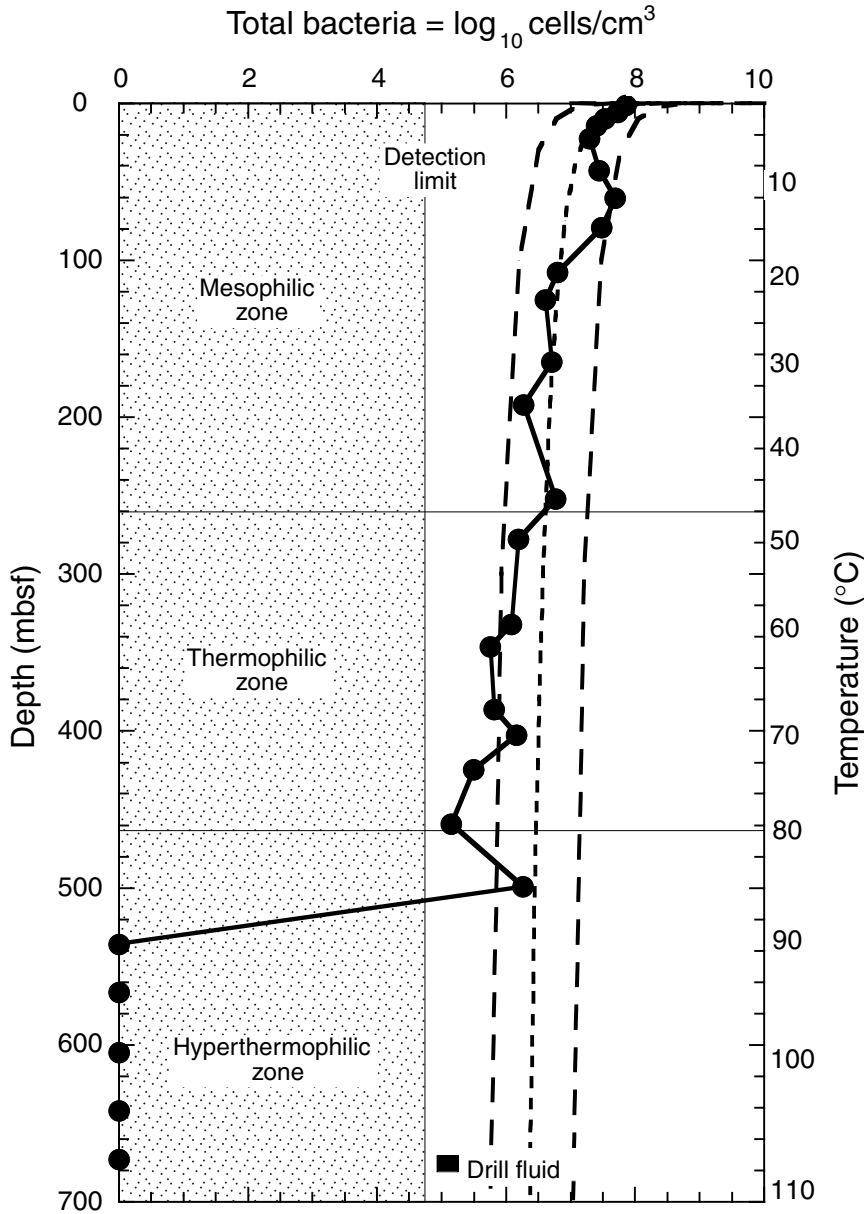
Figure F31. Selected geochemistry at Hole 1173A. Total organic carbon, ammonium, alkalinity, methane, and sulfate profiles vs. depth.
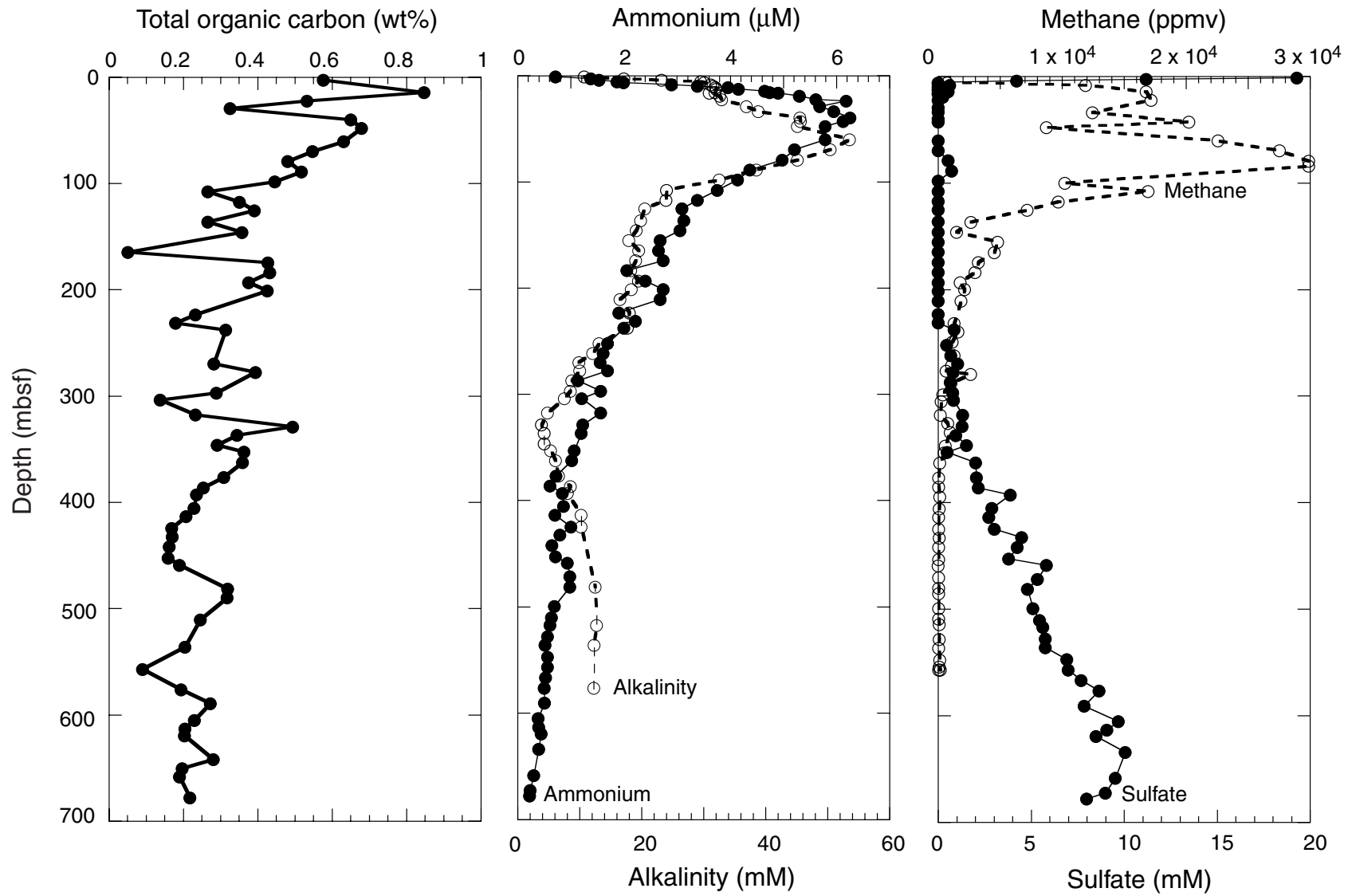
Figure F32. Relationship between total bacterial populations and in situ methane concentrations in sediments of Hole 1173A. Results of a Pearson's "R" correlation are given in the upper left corner of the figure.
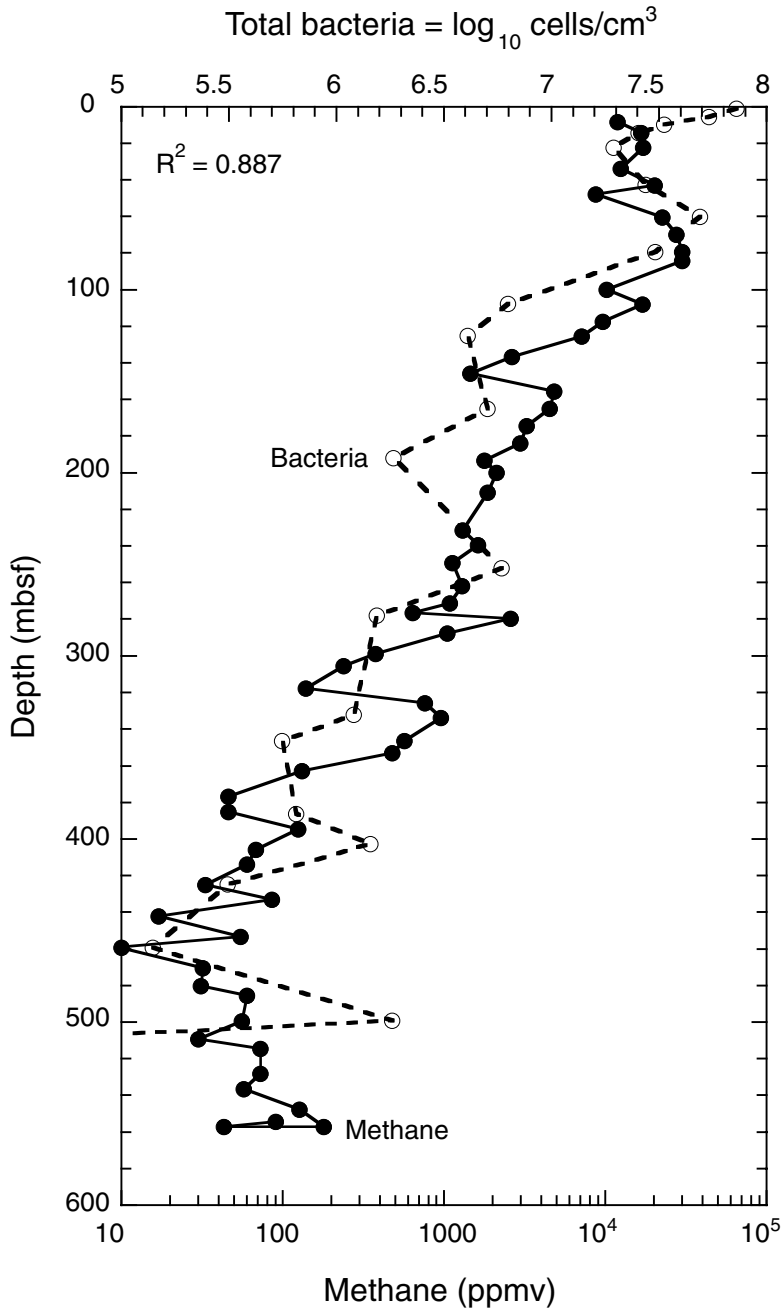
Figure F33. Drilling fluid intrusion into APC cores as determined by perfluoro(methylcyclohexane) penetration.
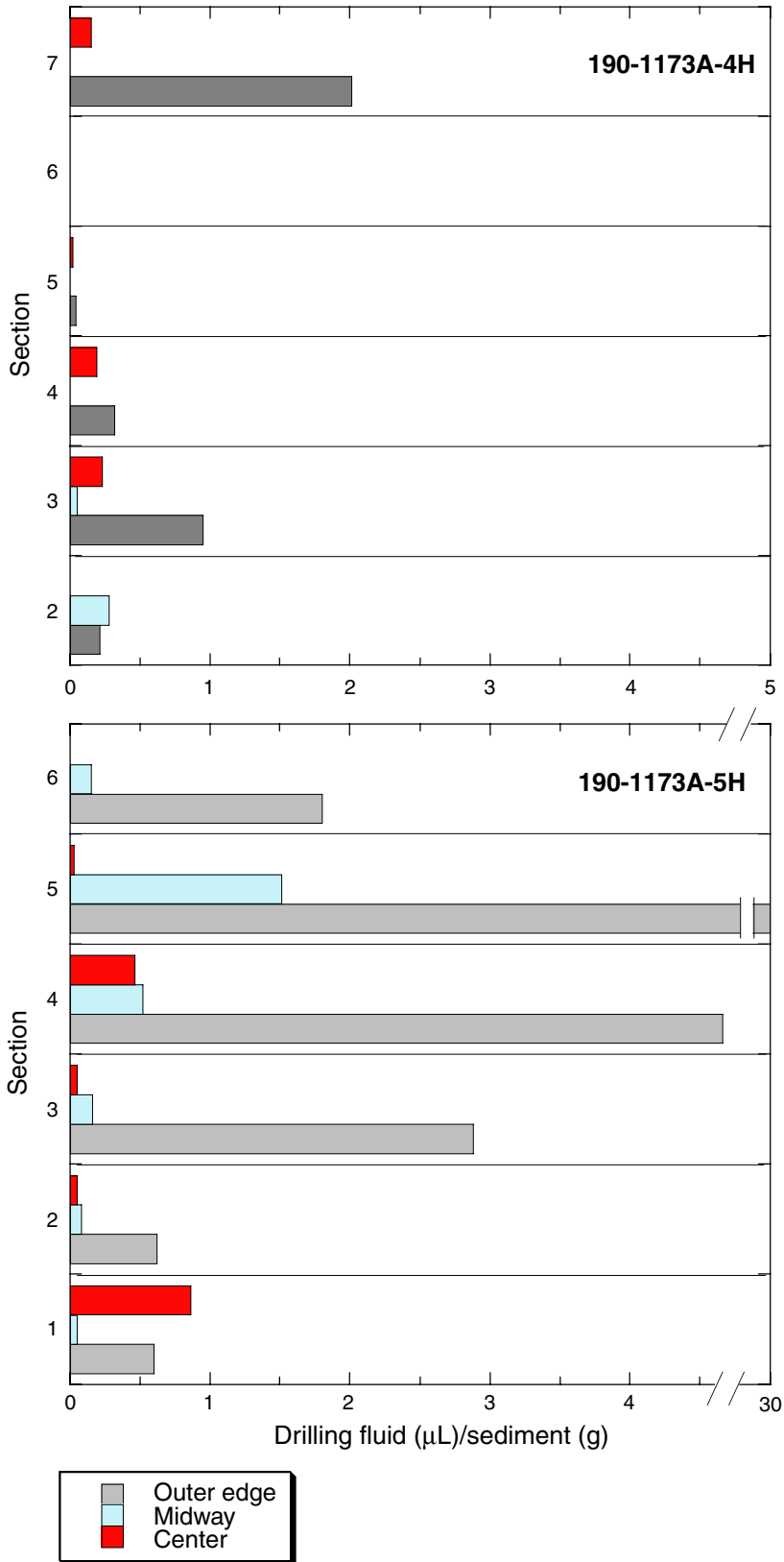
Figure F34. Drilling fluid intrusion into XCB cores as determined by perfluoro(methylcyclohexane) penetration.
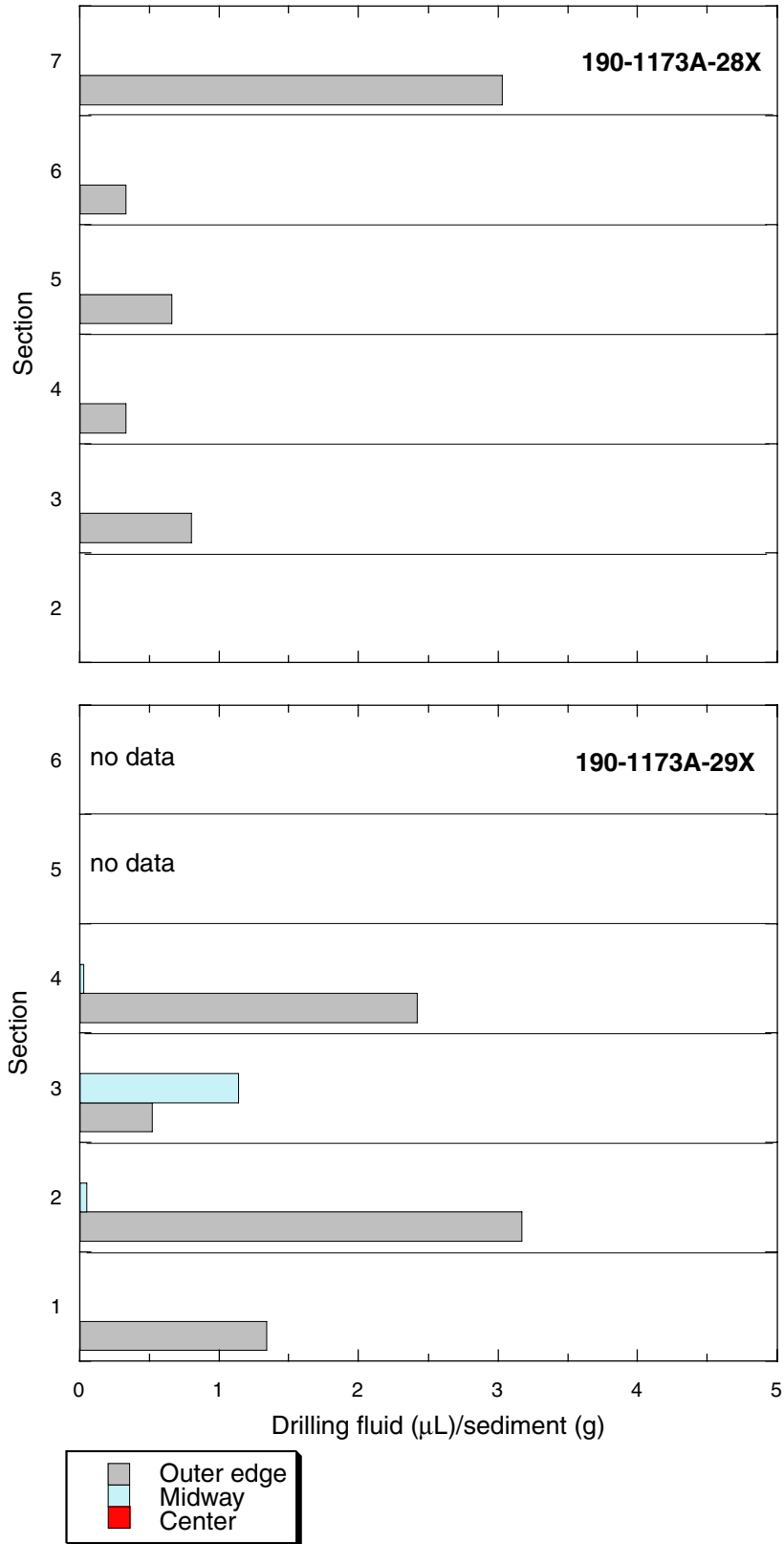
Figure F35. A. Site 1173 bulk density measurements. **B.** Multisensor track gamma-ray attenuation (MST GRA) and mass/volume bulk density. **C.** Grain density. **D.** Porosity.
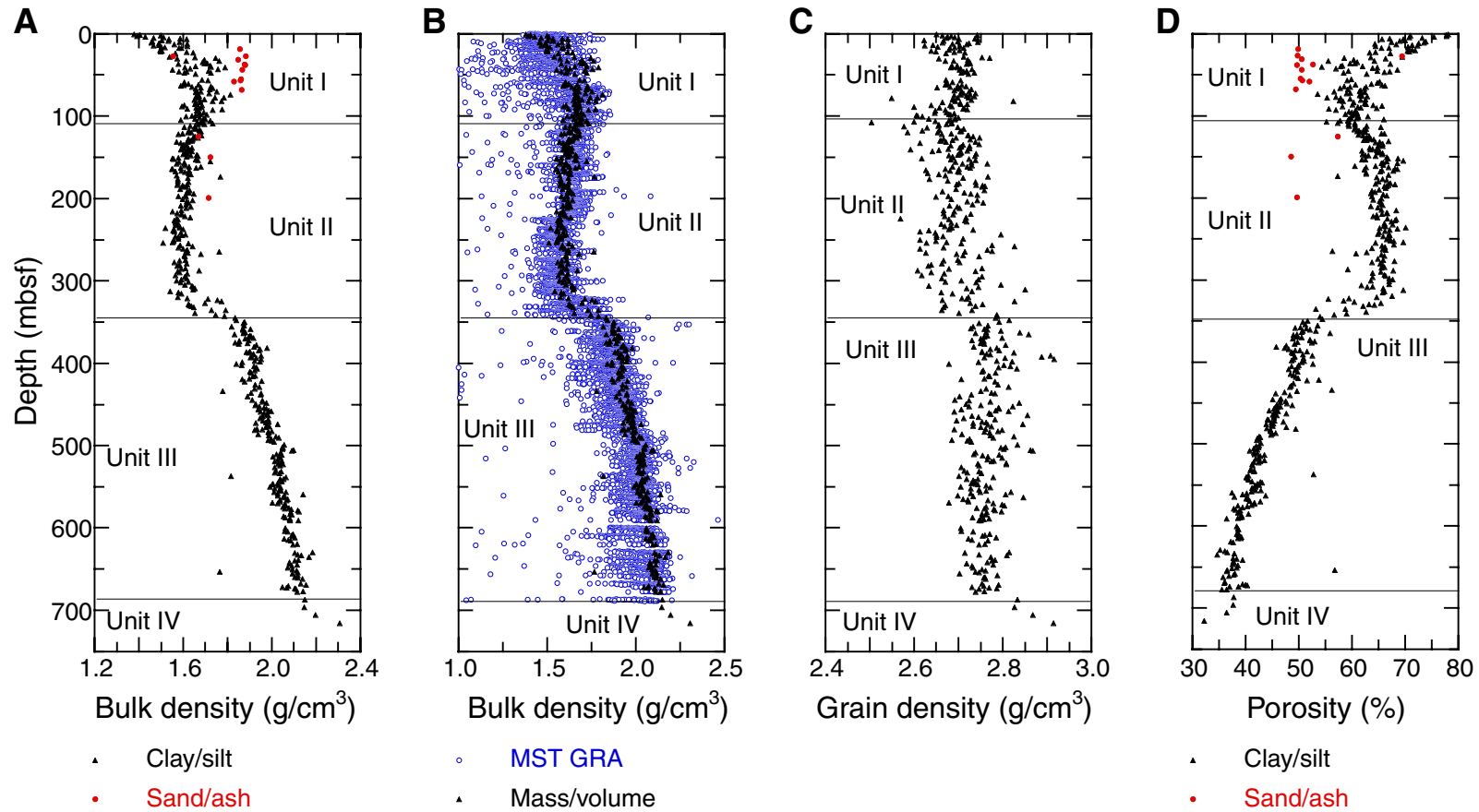
Figure F36. Site 1173 undrained peak shear strength.
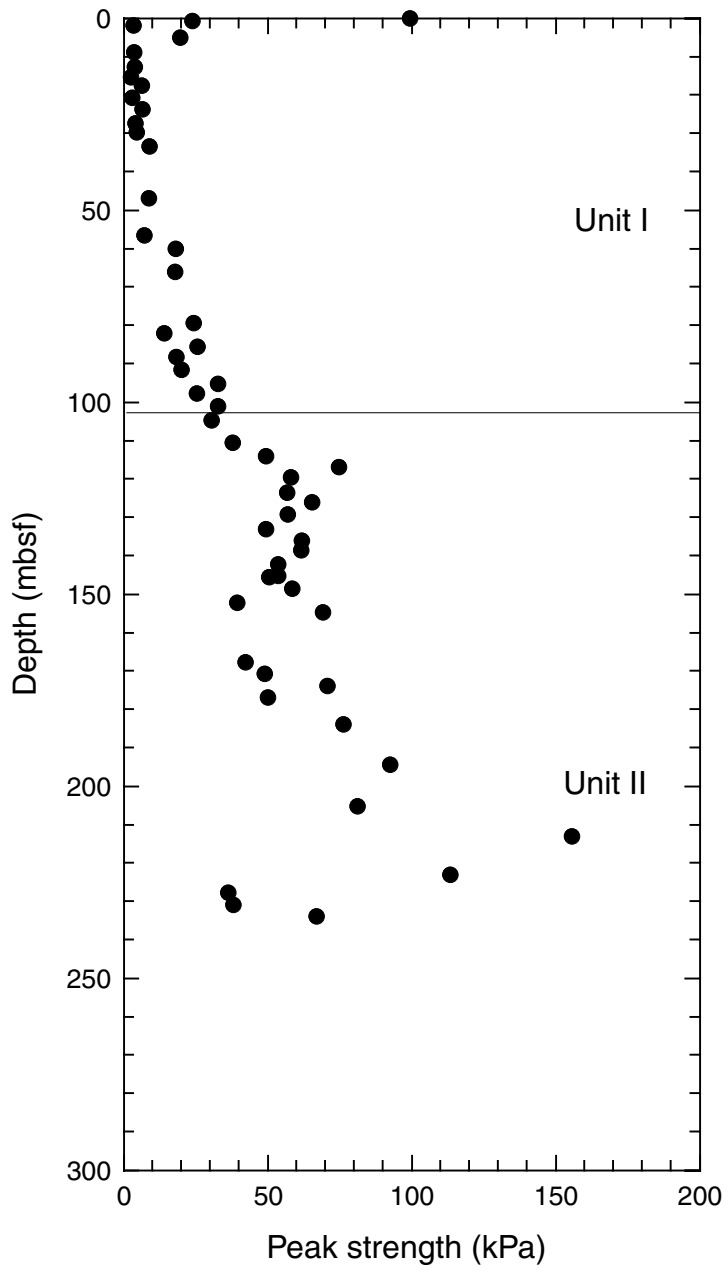
Figure F37. A. Site 1173 thermal conductivity. **B.** Observed and projected temperatures.
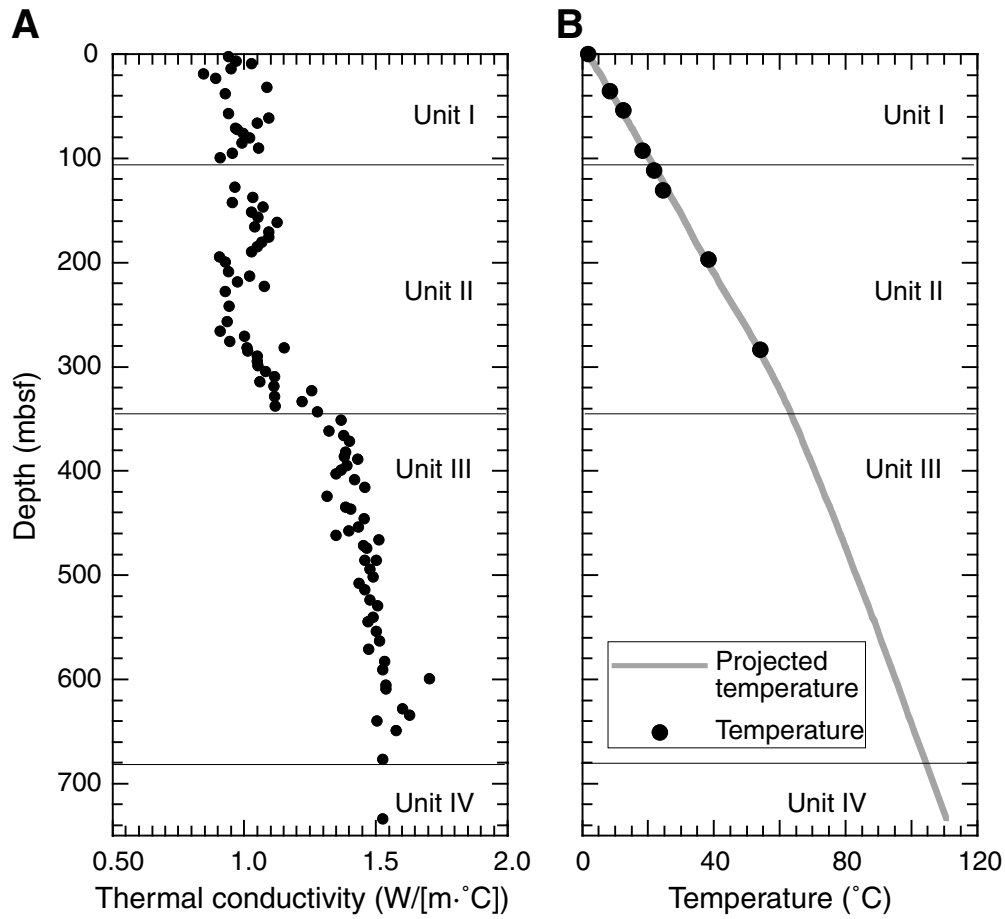
Figure F38. A. Hole 1173A PWS *P*-wave velocity. **B.** Horizontal and vertical *P*-wave velocity as a function of porosity. The line represents a typical relationship for clayey silt computed from a weighted average equation using a matrix velocity of 4500 m/s and a weighting parameter of 1.1 (Lee et al., 1996). **C.** *P*-wave velocity anisotropy. The vertical plane anisotropy compares velocity along the two transverse axes (x and y) to that parallel to the core (z), whereas the horizontal plane anisotropy compares velocity of the x- and y-axes. Because cores are randomly rotated, horizontal plane anisotropy should average zero.
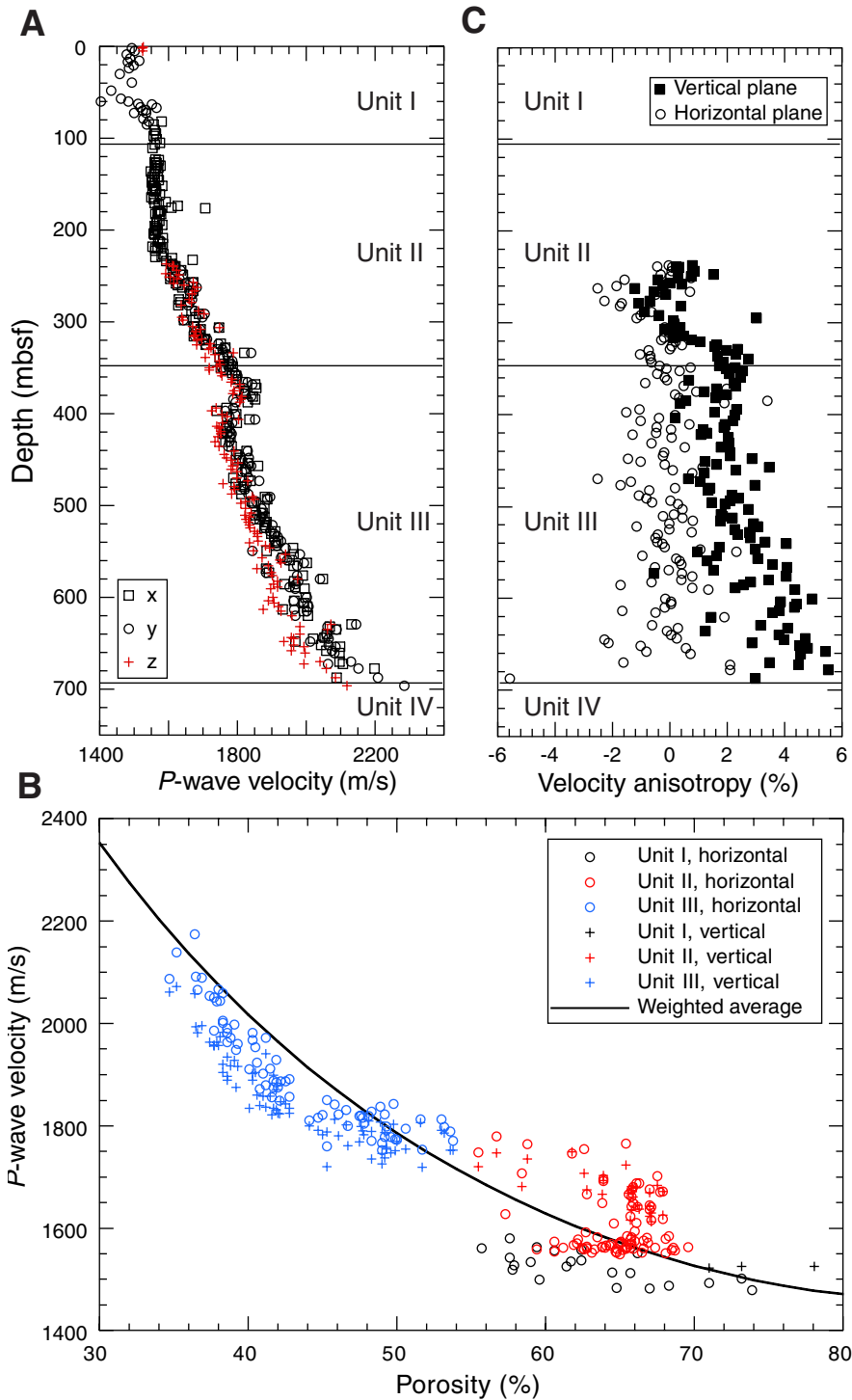
Figure F39. A. Formation factor measured with the needle probe method on APC cores at Hole 1173A. **B.** All measurements. Measurements on cut samples were performed in x- and y- (orthogonal to core) and z- (parallel to core) directions. **C.** Anisotropy of electrical conductivity in the horizontal (x- and y-axes) and vertical (z-axis) planes.
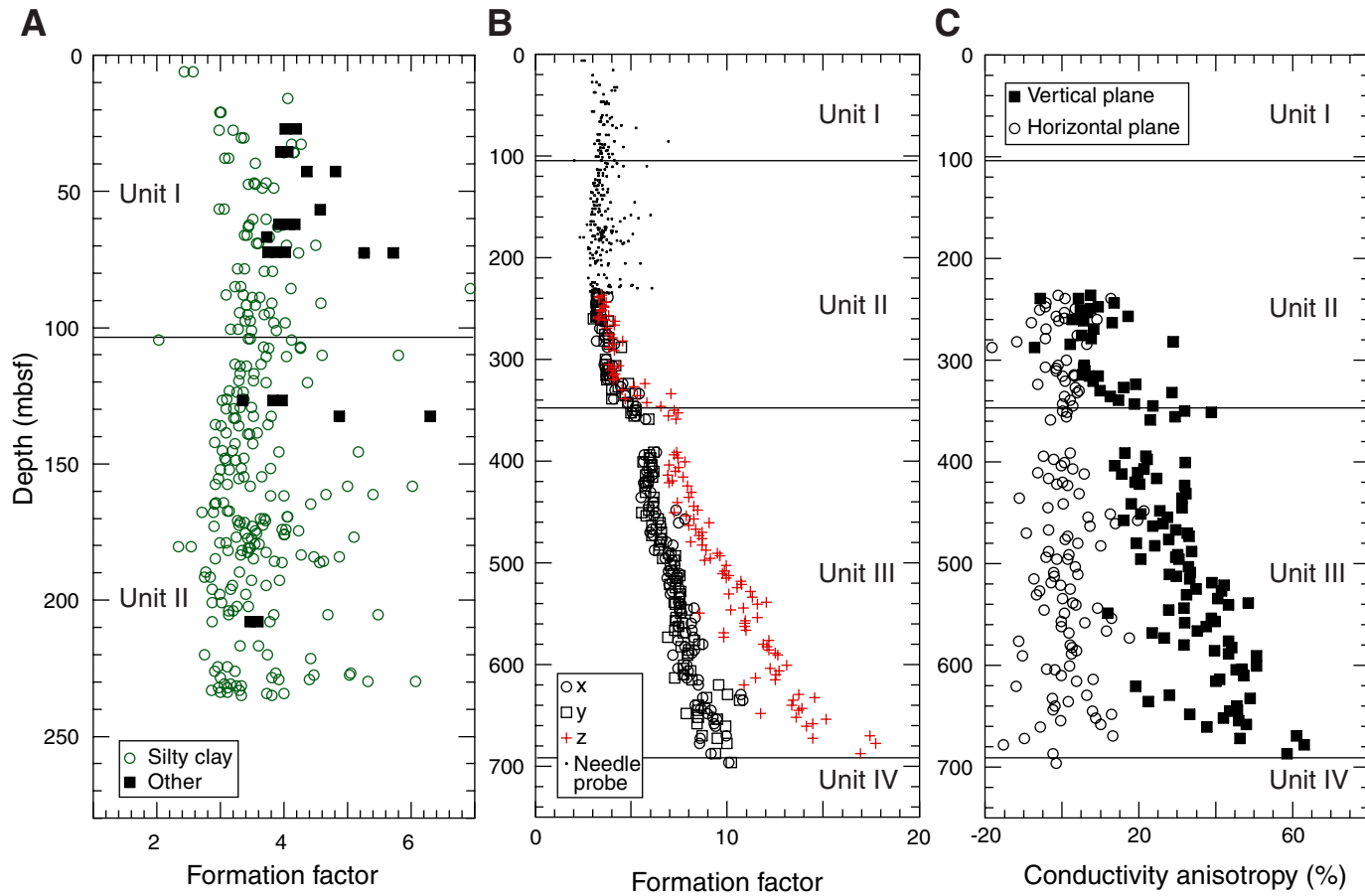
Figure F40. Site 1173 magnetic susceptibility.
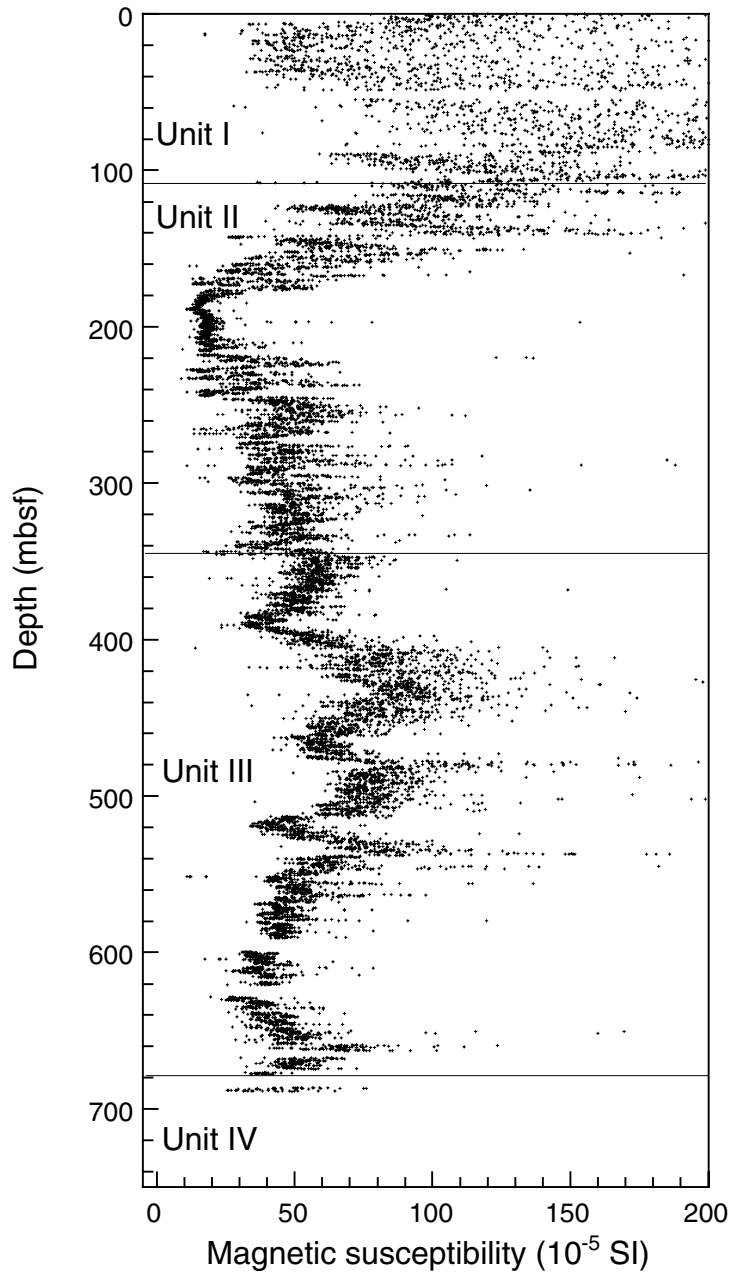
Figure F41. Site 1173 natural gamma ray.
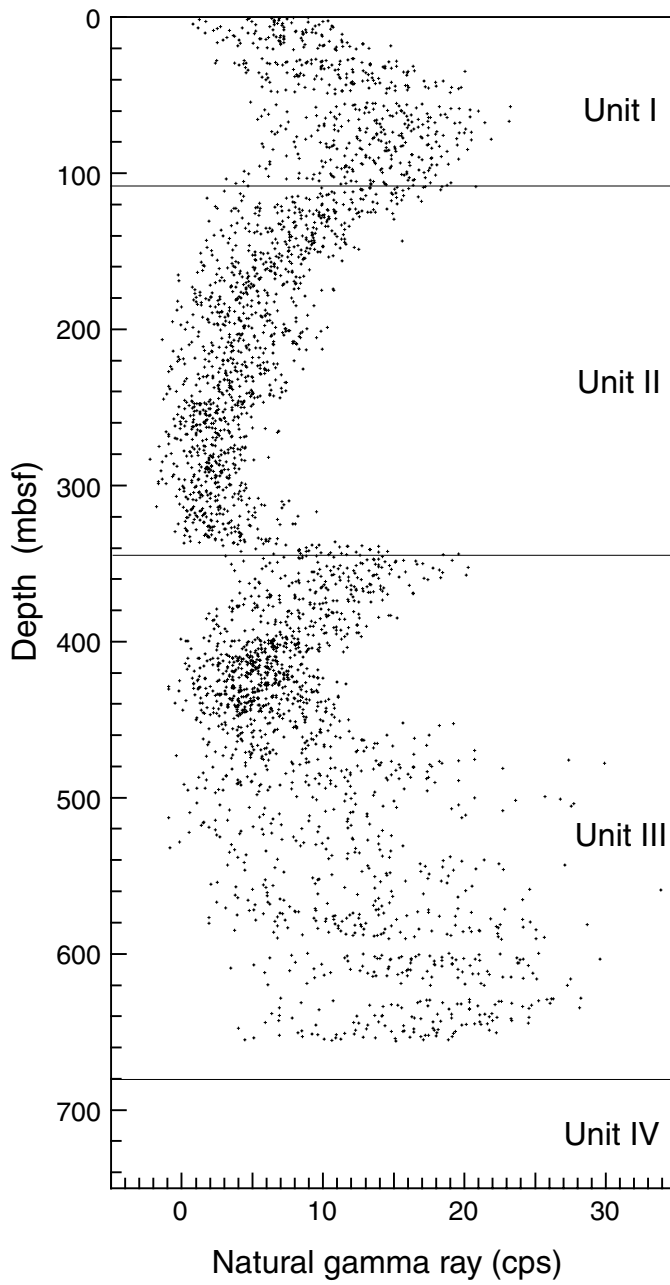
Figure F42. Comparison of core sample measurements and logging data from the triple-combination tool. **A.** Bulk density. **B.** *P*-wave velocity. **C.** Gamma ray. API = American Petroleum Institute units; cps = counts per second; MST = multisensor track; NGR = natural gamma ray.
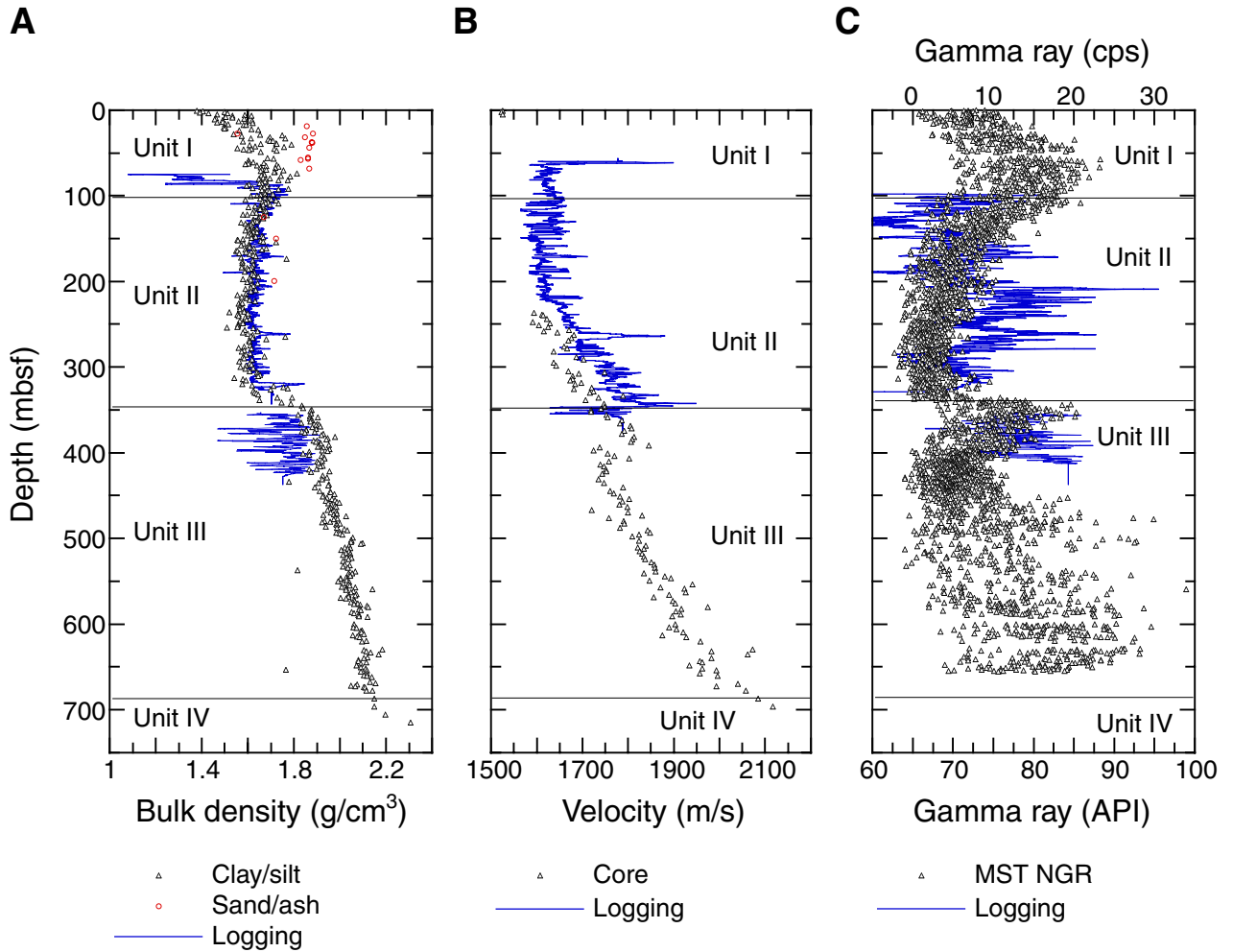
Figure F43. Hole 1173A summary plot of logs and selected core physical properties data for comparison. HSGR spectral gamma-ray data were collected with the triple-combo tool string, whereas SGR data were collected with the FMS-sonic tool string; both are included for comparison and depth ties. See Table T6, p. 51, in the "Explanatory Notes" chapter for definitions. Circles in porosity column represent porosity measured on discrete core samples.
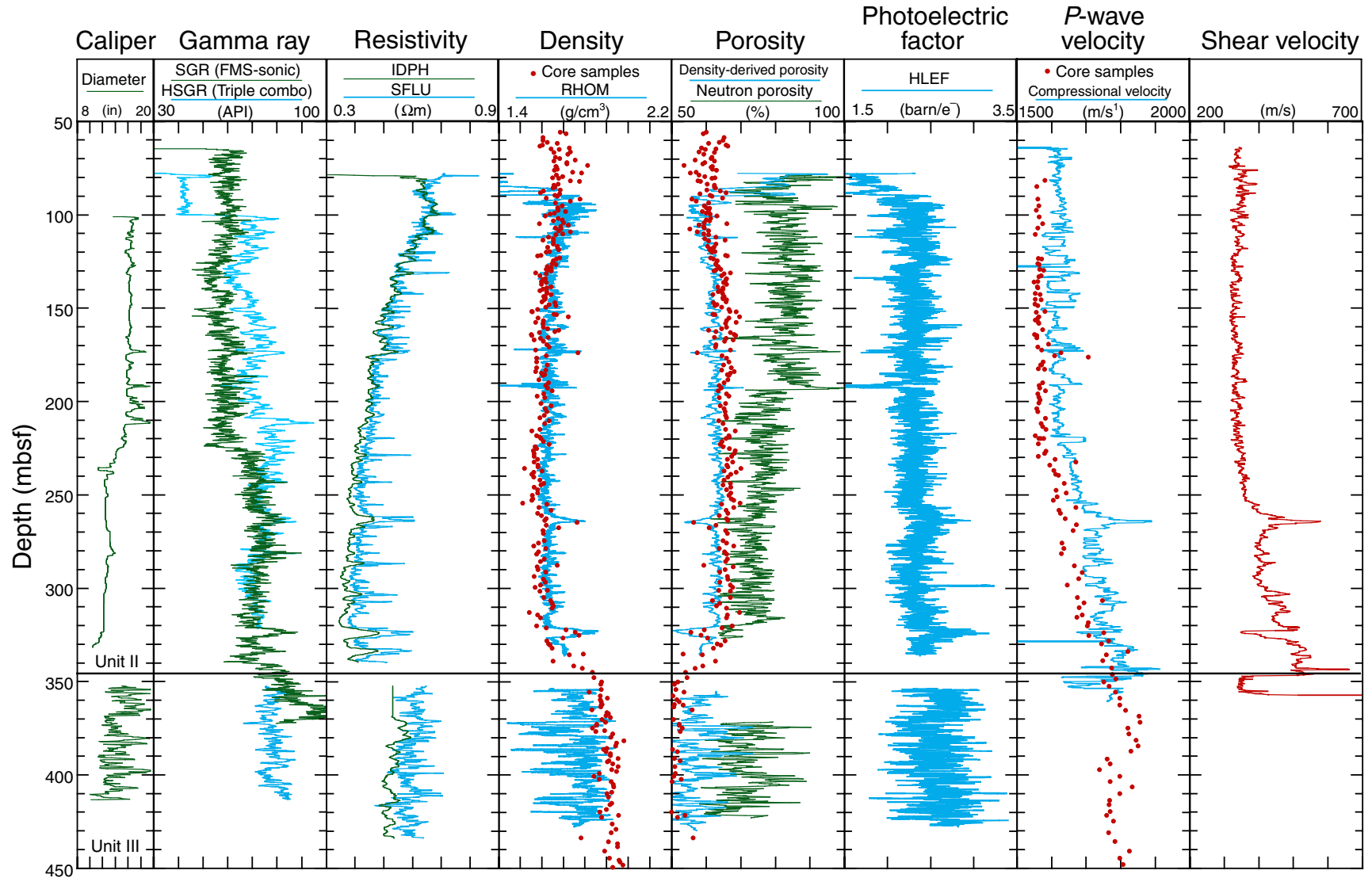
Figure F44. Spectral gamma-ray, potassium, thorium, and uranium data from Site 1173. See Table T6, p. 51, in the "Explanatory Notes" chapter for definitions.
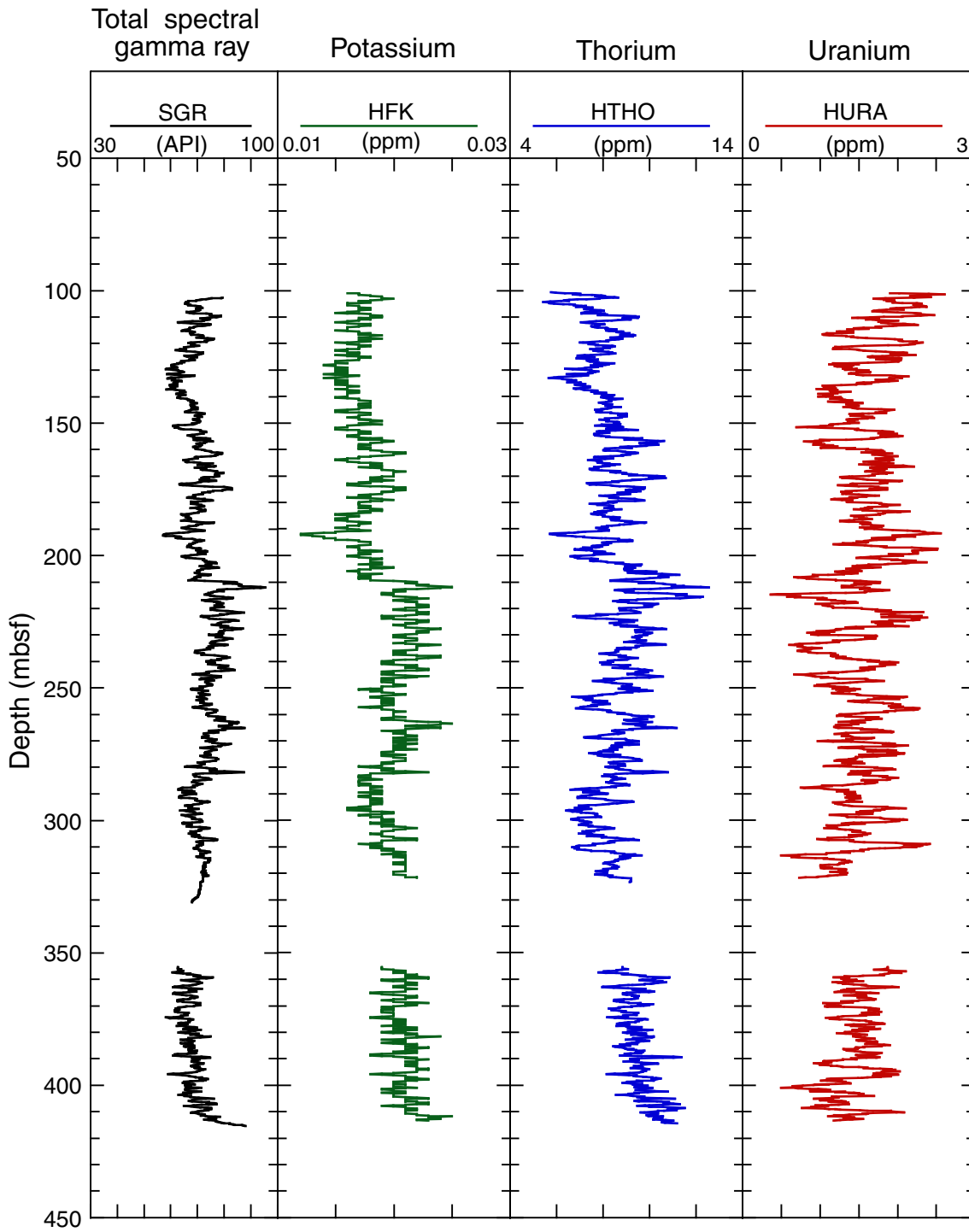
Figure F45. *P*-wave velocity (thin line) measured with the DSI tool, core-based ultrasonic velocity (solid circles), and split-spread profile (SSP) interval velocities obtained by Stoffa et al. (1992) (thick line).
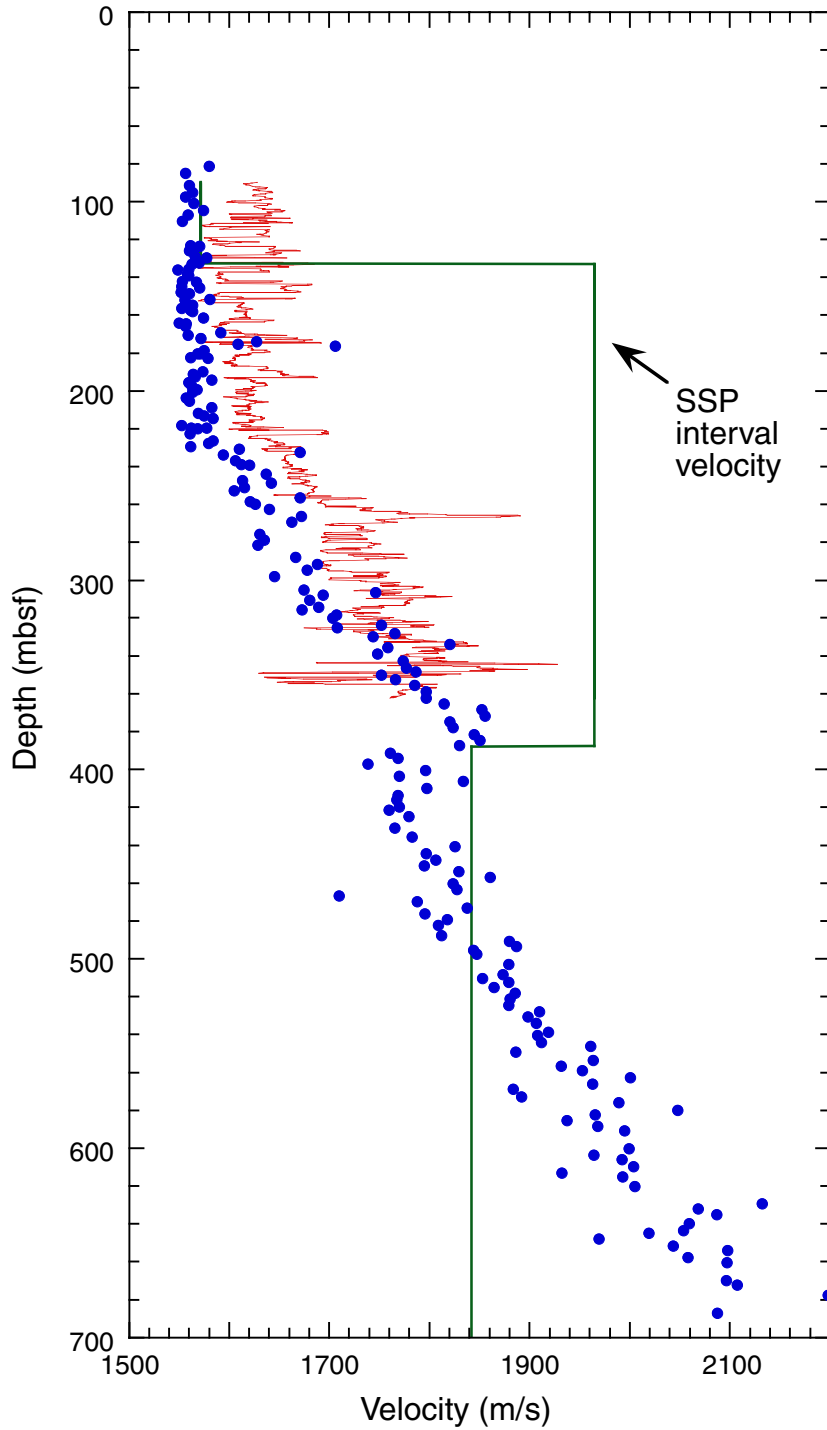
Figure F46. *P*-wave velocity vs. density-derived porosity calculated using grain density values measured on cores. Zones above and below 230 mbsf—the approximate depth where the velocity curve changes slope—generally fall into different velocity-porosity fields, suggesting that processes besides burial compaction exert an influence on velocity below 230 mbsf.
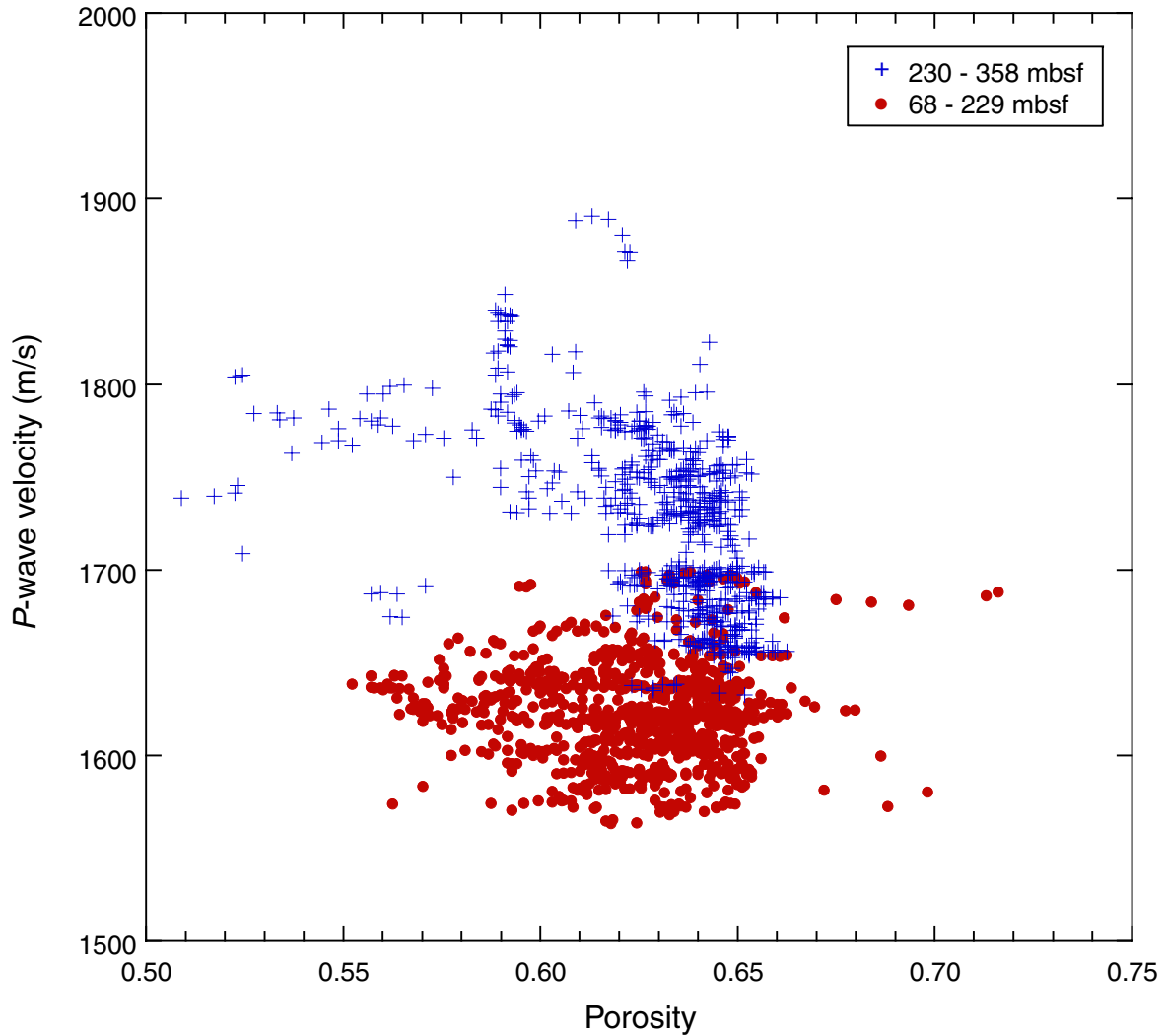
Figure F47. FMS image of ash layers commonly observed in the logged interval above 345 mbsf.
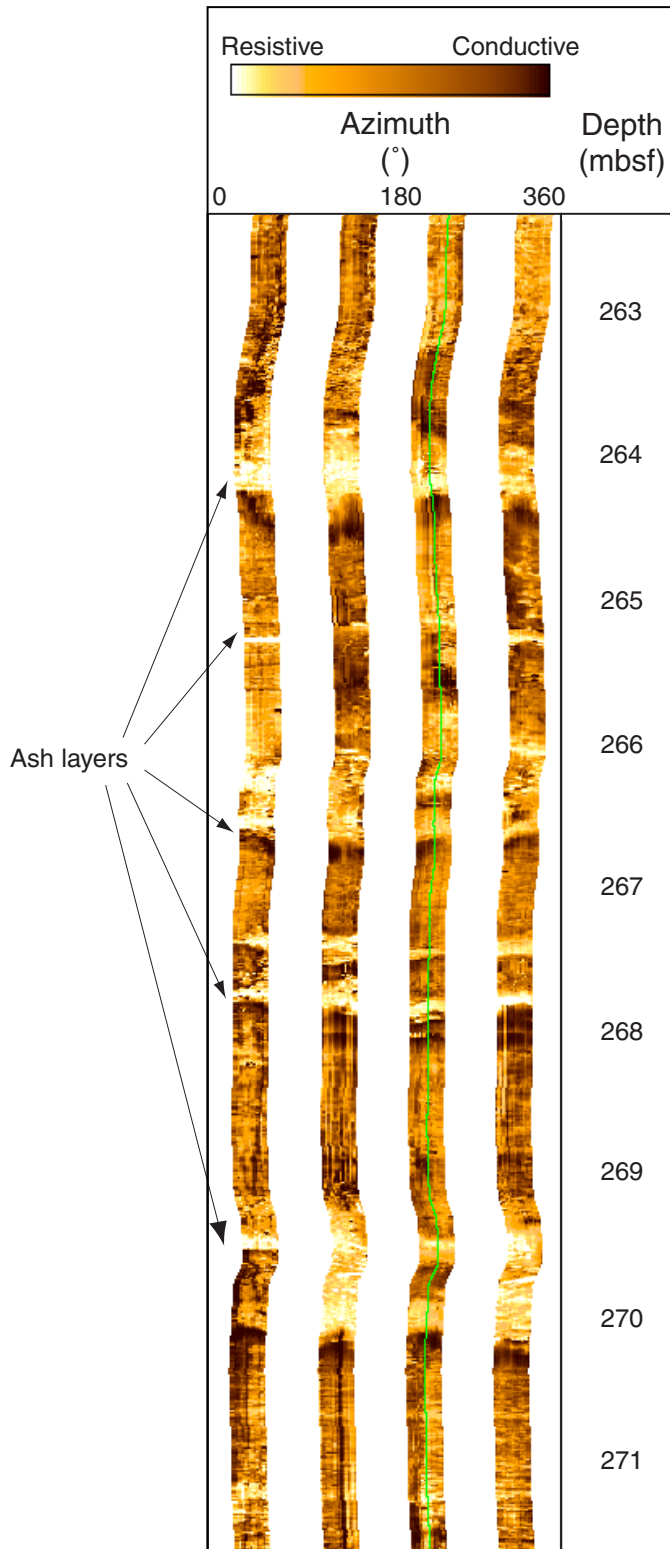
Figure F48. FMS image of bioturbated interval with an ash layer in Unit II. The "mottled" zone with concentric rings of variable resistivity is interpreted as an interval with authigenic alteration and sulfide mineralization.
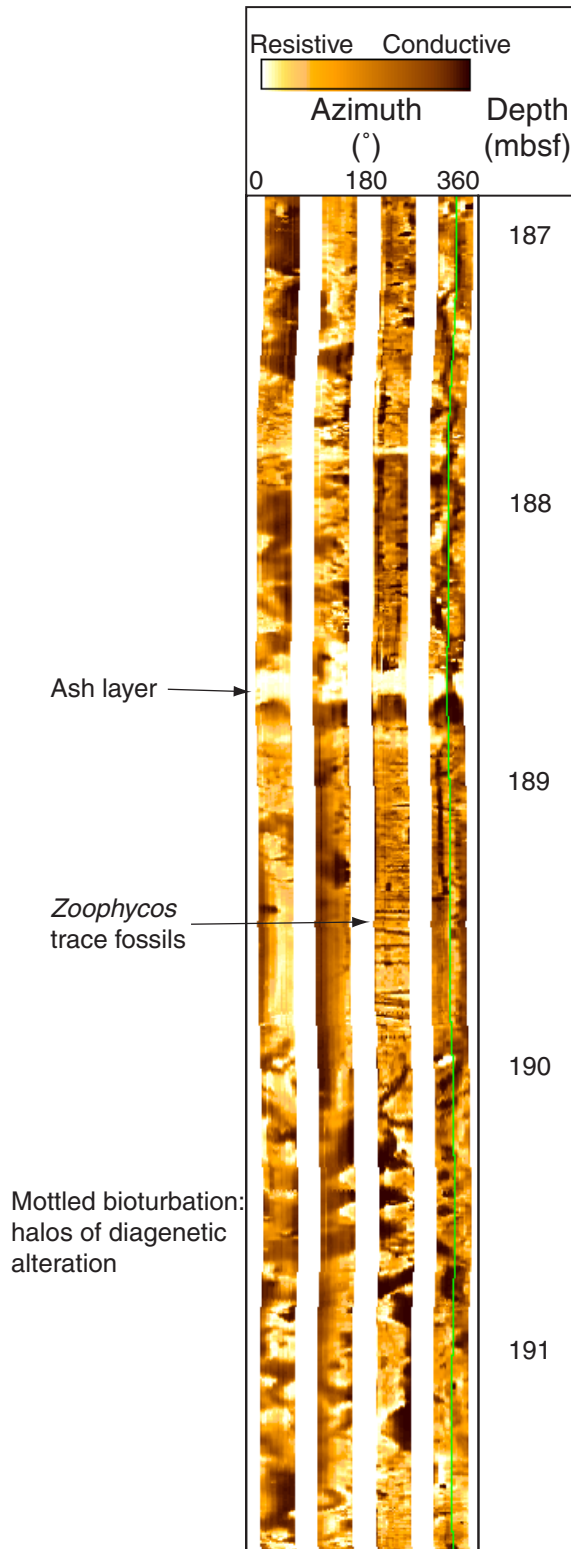
Figure F49. FMS image of the interval spanning the boundary between Units II and III. Although this boundary is somewhat gradational, it is placed at the occurrence of the deepest significant unaltered ash layer imaged here. The differing character of the intervals above and below this diagenetically controlled boundary is evident, with more prominent ash layers above and homogeneous bioturbated mudstone below. FMS data were processed with dynamic normalization.
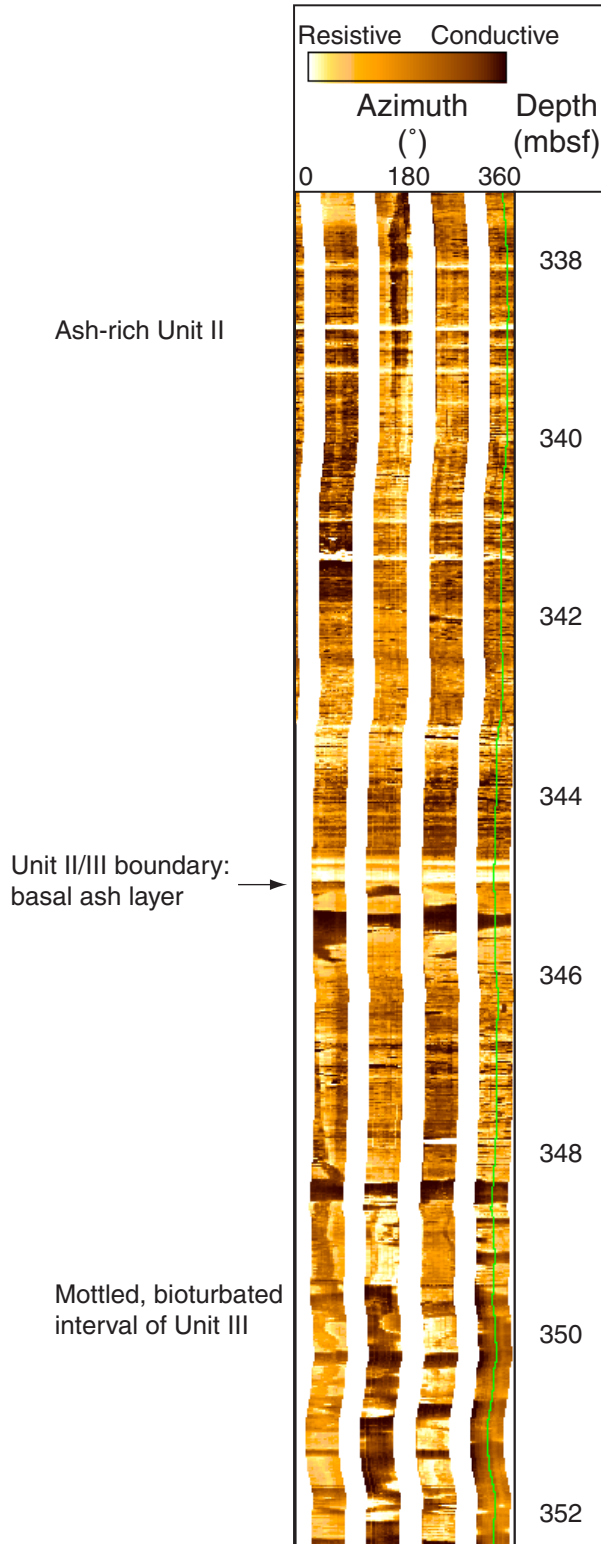
Figure F50. Temperatures measured during the four deployments of the APC temperature tool in Hole 1173A. Dashed lines = extrapolated in situ temperatures. (For Core 190-1173A-12H, data from only the first 4.5 min after penetration were used in the extrapolation.) Depths and temperature values are given in Table T25, p. 147.
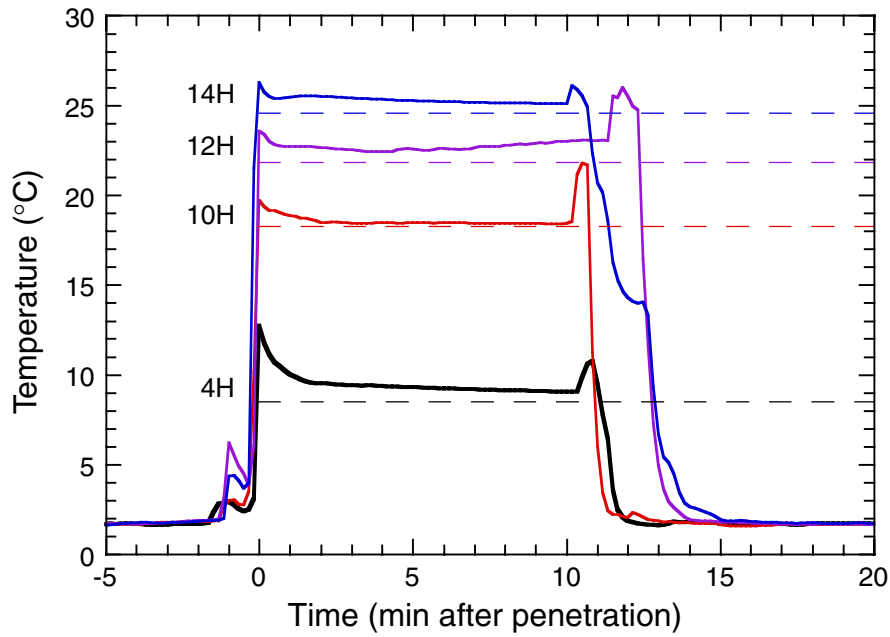
Figure F51. Temperatures measured in Hole 1173A during the WSTP station after Core 190-1173A-6H and DVTP stations after Cores 21H and 30X. (The time scale for the WSTP station is arbitrarily shifted so the data appear clearly on this plot.)
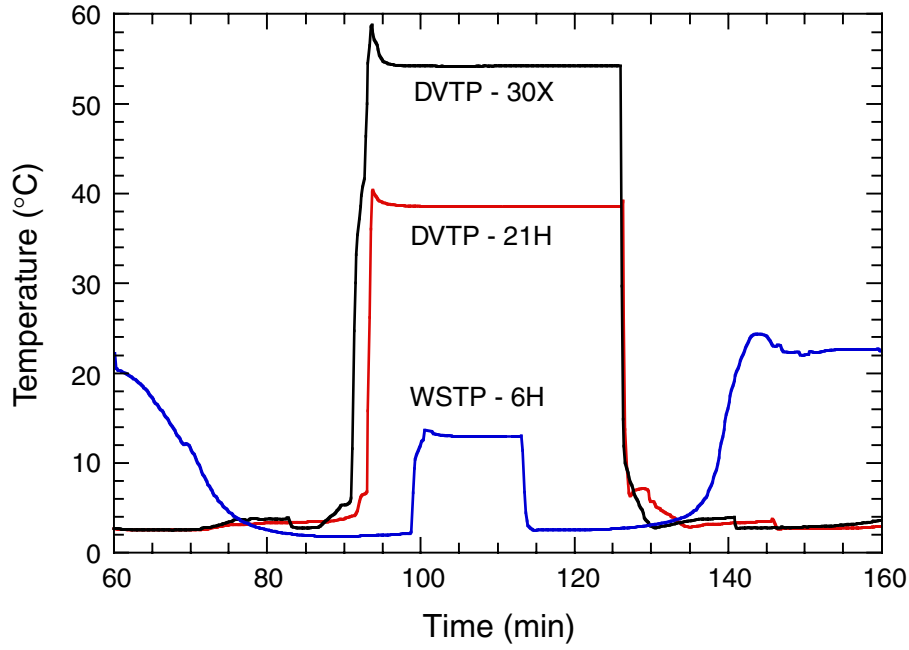
Figure F52. All temperatures measured in Hole 1173A plotted vs. depth.
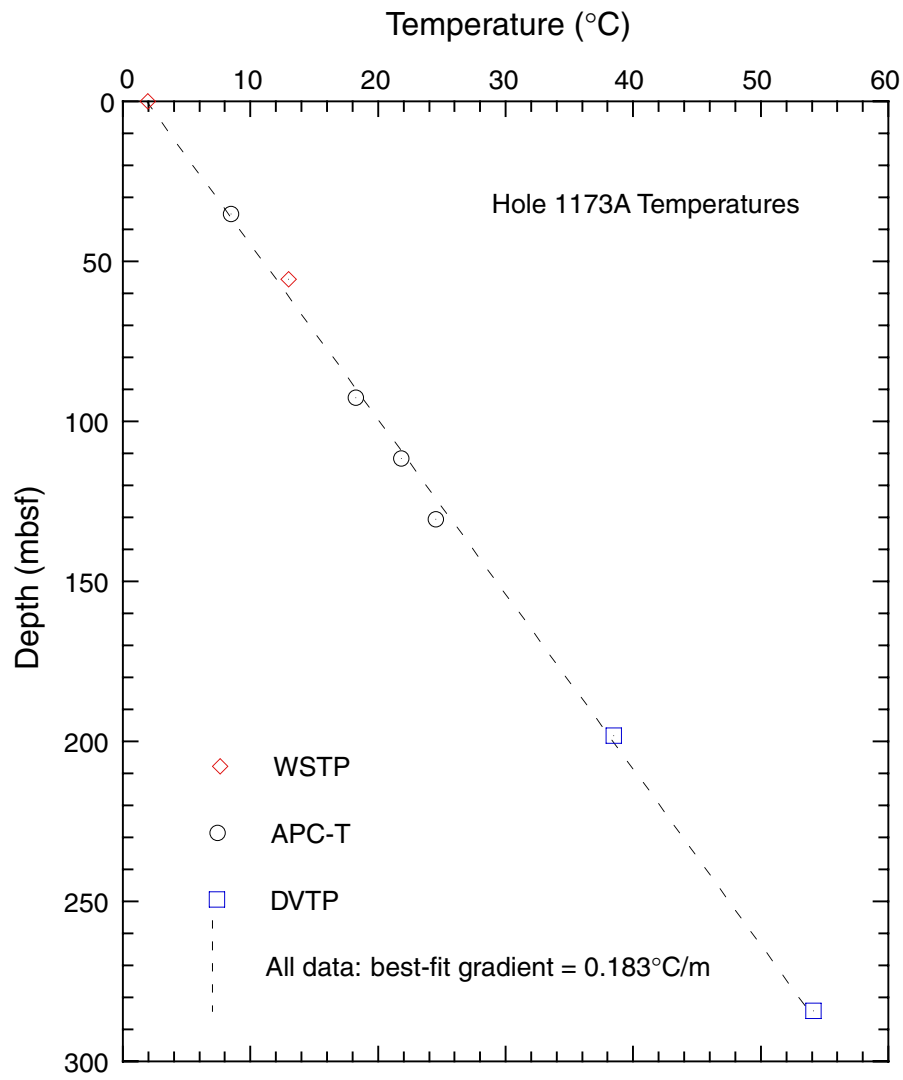
Figure F53. Pressures measured in Hole 1173A during the DVTP-P stations after Cores 190-1173A-21H and 30X.
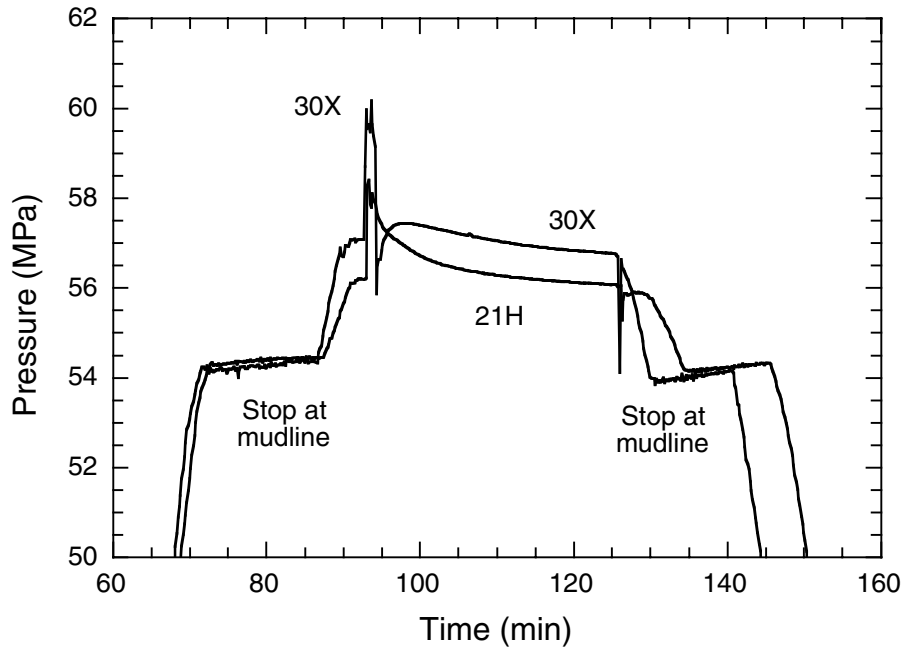
Figure F54. Three-dimensional seismic reflection line 215 from Site 1173 (left edge of section) to the seaward margin of the trench. This line has been 3-D stacked and migrated. Depth conversion used velocity data of Stoffa et al. (1992).
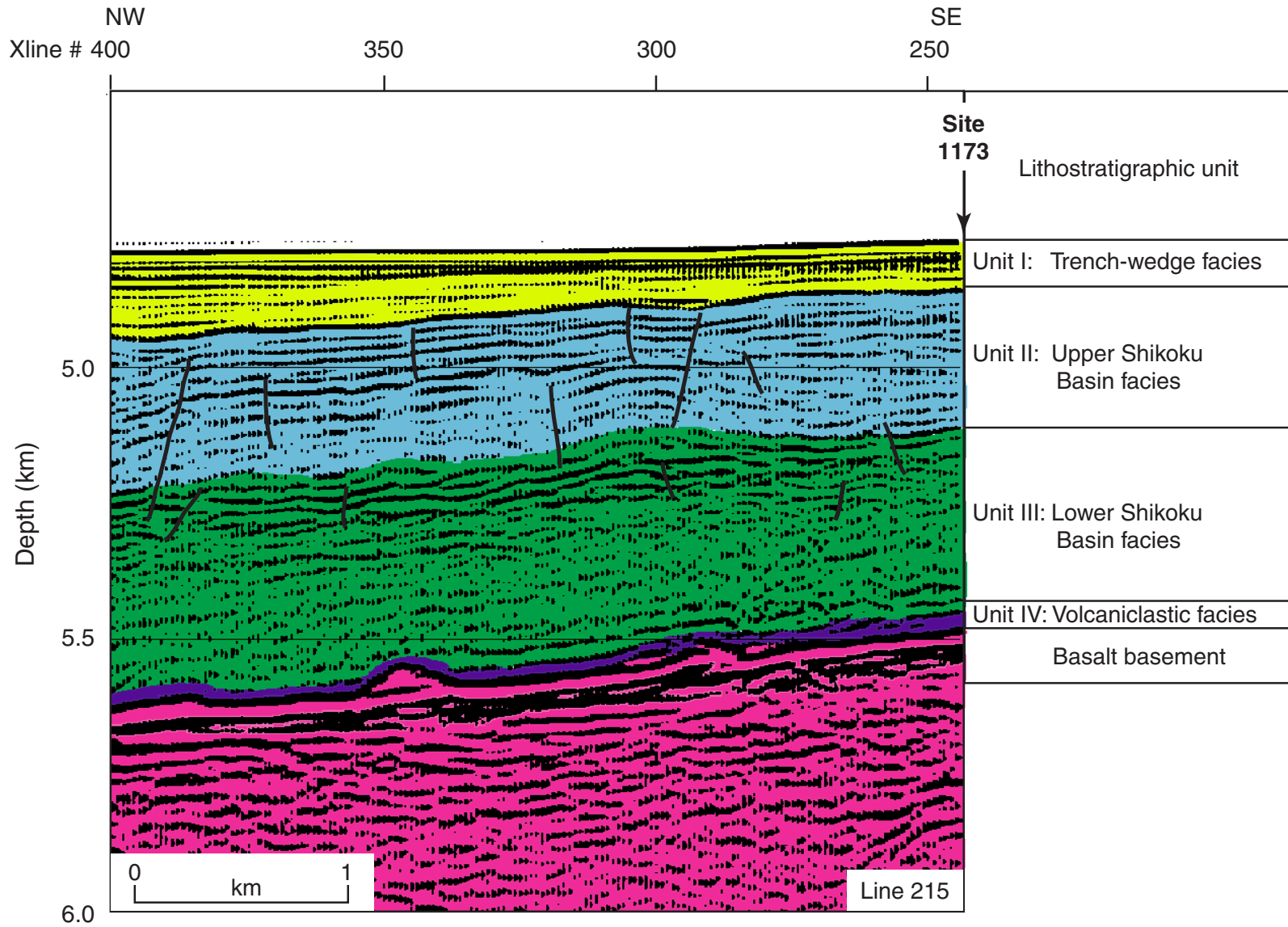
Table T1. Coring summary, Site 1173. (**See table note.** Continued on next page.)

Core	Date (2000)	Time (local)	Top	Bottom	Cored	Recovered	Recovery (%)	Comments
			Depth (mbsf)		**Length (m)**			
190-1173A-								
1H	29 May	1205	0.0	7.1	7.1	7.14	100.0	Ran WSTP at 4780 m
2H	29 May	1350	7.1	16.6	9.5	10.00	105.3	
3H	29 May	1535	16.6	26.1	9.5	9.53	100.3	Tensor started at 13:45
4H	29 May	1710	26.1	35.6	9.5	10.35	108.9	Whirl-Pak and inject tracer
5H	29 May	1845	35.6	45.1	9.5	10.09	106.2	Whirl-Pak and inject tracer
6H	29 May	2015	45.1	54.6	9.5	3.92	41.3	WSTP after 6H
7H	30 May	0005	54.6	64.1	9.5	10.00	105.3	Oriented tensor started at 22:15
8H	30 May	0150	64.1	73.6	9.5	10.10	106.3	
9H	30 May	0315	73.6	83.1	9.5	9.98	105.1	WSTP after 9H
10H	30 May	0730	83.1	92.6	9.5	10.25	107.9	Tensor at 06:00
11H	30 May	0900	92.6	102.1	9.5	9.64	101.5	
12H	30 May	1040	102.1	111.6	9.5	9.83	103.5	
13H	30 May	1210	111.6	121.1	9.5	9.31	98.0	
14H	30 May	1405	121.1	130.6	9.5	9.59	100.9	Changed outer seals
15H	30 May	1530	130.6	140.1	9.5	9.73	102.4	Started tensor at 13:55
16H	30 May	1650	140.1	149.6	9.5	9.46	99.6	
17H	30 May	1825	149.6	159.1	9.5	9.00	94.7	Broken liner at top, hole at bottom
18H	30 May	1955	159.1	168.6	9.5	9.44	99.4	Liner imploded at bottom, cracked at top
19H	30 May	2130	168.6	178.1	9.5	9.61	101.2	Liner imploded at bottom, tensor at 21:20
20H	30 May	2255	178.1	187.6	9.5	8.07	84.9	
21H	31 May	0015	187.6	197.1	9.5	9.69	102.0	Note: run DVTP after 21H
22H	31 May	0435	197.1	206.6	9.5	8.85	93.2	Tensor at 03:10, liner bottom imploded
23H	31 May	0605	206.6	216.1	9.5	9.43	99.3	Liner imploded on bottom
24H	31 May	0735	216.1	225.6	9.5	9.34	98.3	
25X	31 May	0925	225.6	235.2	9.6	9.69	100.9	
26X	31 May	1100	235.2	244.9	9.7	9.86	101.6	AHC on
27X	31 May	1245	244.9	254.5	9.6	9.79	102.0	AHC on
28X	31 May	1420	254.5	264.0	9.5	9.94	104.6	Whirl-Pak and inject tracer
29X	31 May	1600	264.0	273.6	9.6	7.67	79.9	Whirl-Pak and inject tracer
30X	31 May	1730	273.6	283.2	9.6	9.34	97.3	AHC, DVTP after 30X
31X	31 May	2145	283.2	292.9	9.7	9.81	101.1	AHC on
32X	31 May	2305	292.9	302.6	9.7	9.30	95.9	AHC on
33X	1 June	0025	302.6	311.9	9.3	8.49	91.3	AHC on
34X	1 June	0145	311.9	321.5	9.6	9.81	102.2	AHC on
35X	1 June	0305	321.5	331.1	9.6	9.83	102.4	AHC on
36X	1 June	0445	331.1	340.7	9.6	9.06	94.4	AHC on
37X	1 June	0620	340.7	350.3	9.6	9.79	102.0	AHC on
38X	1 June	0745	350.3	359.9	9.6	9.91	103.2	AHC on
39X	1 June	0910	359.9	369.6	9.7	9.89	102.0	AHC on
40X	1 June	1030	369.6	379.2	9.6	9.84	102.5	AHC on
41X	1 June	1200	379.2	388.8	9.6	9.92	103.3	AHC on
42X	1 June	1400	388.8	398.4	9.6	9.90	103.1	AHC on
43X	1 June	1515	398.4	408.0	9.6	9.23	96.1	AHC on
44X	1 June	1645	408.0	417.6	9.6	9.95	103.6	AHC on
45X	1 June	1805	417.6	427.2	9.6	9.87	102.8	AHC on
46X	1 June	1925	427.2	436.4	9.2	9.92	107.8	AHC on
47X	1 June	2045	436.4	445.8	9.4	9.91	105.4	AHC on
48X	1 June	2200	445.8	455.0	9.2	9.99	108.6	AHC on
49X	1 June	2325	455.0	464.6	9.6	9.87	102.8	
50X	2 June	0045	464.6	474.3	9.7	9.92	102.3	AHC on
51X	2 June	0220	474.3	484.0	9.7	9.91	102.2	AHC on
52X	2 June	0340	484.0	493.7	9.7	9.93	102.4	AHC on
53X	2 June	0525	493.7	503.3	9.6	9.95	103.6	AHC on
54X	2 June	0740	503.3	513.0	9.7	9.92	102.3	AHC on, sinker bars out
55X	2 June	0955	513.0	522.3	9.3	9.85	105.9	AHC on
56X	2 June	1300	522.3	532.0	9.7	9.89	102.0	AHC on, note firm at 5328.41 m (526.51 mbsf)
57X	2 June	1520	532.0	541.7	9.7	9.90	102.1	AHC on
58X	2 June	1745	541.7	551.3	9.6	9.93	103.4	AHC on
59X	2 June	2000	551.3	561.0	9.7	9.85	101.5	AHC on
60X	2 June	2230	561.0	570.7	9.7	9.83	101.3	AHC on
61X	3 June	0045	570.7	580.4	9.7	9.88	101.9	Drilled without AHC, Tru Vu crashed
62X	3 June	0320	580.4	589.9	9.5	9.86	103.8	AHC on
63X	3 June	0620	589.9	599.5	9.6	1.59	16.6	AHC on
64X	3 June	0930	599.5	609.2	9.7	9.45	97.4	AHC on
65X	3 June	1230	609.2	618.8	9.6	7.46	77.7	AHC on
66X	3 June	1445	618.8	628.4	9.6	1.99	20.7	AHC on
67X	3 June	1730	628.4	638.1	9.7	7.84	80.8	AHC on
68X	3 June	1945	638.1	647.7	9.6	8.67	90.3	AHC on

Table T1 (continued).

Core	Date (2000)	Time (local)	Depth (mbsf) Top	Bottom	Length (m) Cored	Recovered	Recovery (%)	Comments
69X	3 June	2215	647.7	657.4	9.7	8.68	89.5	AHC on
70X	4 June	0045	657.4	667.1	9.7	6.05	62.4	AHC on
71X	4 June	0330	667.1	676.7	9.6	8.00	83.3	AHC on
72X	4 June	0615	676.7	686.3	9.6	2.09	21.8	AHC on
73X	4 June	0940	686.3	695.9	9.6	2.94	30.6	AHC on, note firm at 5328.41 m (526.51 mbsf)
74X	4 June	1245	695.9	705.6	9.7	0.86	8.9	AHC on, 2 m fill at 5497.84 m
75X	4 June	1545	705.6	715.3	9.7	0.29	3.0	AHC on
76X	4 June	1925	715.3	724.6	9.3	0.38	4.1	AHC on
77X	4 June	2310	724.6	734.3	9.7	0.26	2.7	AHC off
				Totals:	734.3	658.10	89.6	

Note: WSTP = water-sampling temperature probe, DVTP = Davis-Villinger temperature probe, AHC = advanced hydraulic piston corer.

Table T2. Coring summary by section, Site 1173. (**See table notes.** Continued on next 10 pages.)

Core	Date (2000)	Time (local)	Core depth (mbsf) Top	Core depth (mbsf) Bottom	Length (m) Cored	Length (m) Recovered	Recovery (%)	Section	Length (m) Liner	Length (m) Curated	Section depth (mbsf) Top	Section depth (mbsf) Bottom	Catwalk samples
190-1173-													
1H	29 May	1205	0.00	7.10	7.14	7.14	100.0						
								1	1.5	1.5	0.0	1.5	IW, BACT
								2	1.5	1.5	1.5	3.0	IW
								3	1.5	1.5	3.0	4.5	IW, SPIVH, WRC
								4	1.5	1.5	4.5	6.0	HS, BGAS, IW, BACT
								5	0.9	0.9	6.0	6.9	IW
								CC(w/5)	0.24	0.24	6.9	7.14	PAL
								Totals:	7.14	7.14			
2H	29 May	1350	7.14	16.64	9.5	10.00	105.3						
								1	1.5	1.5	7.14	8.64	IW, BGAS
								2	1.5	1.5	8.64	10.14	IW, BACT
								3	1.5	1.5	10.14	11.64	IW, SPIVH
								4	1.5	1.5	11.64	13.14	IW
								5	1.5	1.5	13.14	14.64	HS, IW, HS, BGAS, B
								6	1.5	1.5	14.64	16.14	IW, VAC, BGAS, VAC
								7	0.71	0.71	16.14	16.85	VAC, IW, VAC
								CC(w/7)	0.29	0.29	16.85	17.14	PAL
								Totals:	10.00	10.00			
3H	29 May	1535	16.64	26.14	9.5	9.53	100.3						
								1	1.5	1.5	16.64	18.14	
								2	1.5	1.5	18.14	19.64	IW
								3	1.5	1.5	19.64	21.14	
								4	1.5	1.5	21.14	22.64	BACT, IW
								5	1.5	1.5	22.64	24.14	HS, IW, VAC
								6	1.0	1.0	24.14	25.14	SPIVH
								7	0.68	0.68	25.14	25.82	
								CC(w/7)	0.35	0.35	25.82	26.17	PAL, PAL
								Totals:	9.53	9.53			
4H	29 May	1710	26.14	35.64	9.5	10.35	108.9						
								1	0.24	0.24	26.14	26.38	
								2	1.5	1.5	26.38	27.88	SMTCR, VAC
								3	1.5	1.5	27.88	29.38	IW, SMTCR, BGAS, B
								4	1.5	1.5	29.38	30.88	SMTCR
								5	1.5	1.5	30.88	32.38	SMTCR
								6	1.5	1.5	32.38	33.88	IW, SPIVH, SMTCR,
								7	1.5	1.5	33.88	35.38	HS, HS, SMTCR
								8	0.74	0.74	35.38	36.12	VAC, VAC
								CC(w/8)	0.37	0.37	36.12	36.49	PAL
								Totals:	10.35	10.35			
5H	29 May	1845	35.64	45.14	9.5	10.09	106.2						
								1	1.5	1.5	35.64	37.14	SMTCR
								2	1.5	1.5	37.14	38.64	SMTCR
								3	1.5	1.5	38.64	40.14	SMTCR, IW, VAC
								4	1.5	1.5	40.14	41.64	SMTCR
								5	1.5	1.5	41.64	43.14	SMTCR, BACT, IW
								6	1.5	1.5	43.14	44.64	SMTCR, HS
								7	0.91	0.91	44.64	45.55	
								CC(w/7)	0.18	0.18	45.55	45.73	PAL
								Totals:	10.09	10.09			
6H	29 May	2015	45.14	54.64	9.5	3.92	41.3						
								1	1.5	1.5	45.14	46.64	PAL
								2	1.5	1.5	46.64	48.14	IW
								3	0.92	0.92	48.14	49.06	HS
								CC(NS)	0.0	0.0			
								Totals:	3.92	3.92			
7H	30 May	0005	54.64	64.14	9.5	10.00	105.3						
								1	1.5	1.5	54.64	56.14	
								2	1.5	1.5	56.14	57.64	
								3	1.5	1.5	57.64	59.14	BGAS
								4	1.5	1.5	59.14	60.64	BACT, IW, VAC
								5	1.5	1.5	60.64	62.14	HS, SPIVH
								6	1.5	1.5	62.14	63.64	
								7	0.78	0.78	63.64	64.42	
								CC(w/7)	0.22	0.22	64.42	64.64	PAL
								Totals:	10.0	10.0			
8H	30 May	1050	64.14	73.64	9.5	10.10	106.3						
								1	1.5	1.5	64.14	65.64	

Table T2 (continued).

Core	Date (2000)	Time (local)	Core depth (mbsf) Top	Core depth (mbsf) Bottom	Length (m) Cored	Length (m) Recovered	Recovery (%)	Section	Length (m) Liner	Length (m) Curated	Section depth (mbsf) Top	Section depth (mbsf) Bottom	Catwalk samples
								2	1.5	1.5	65.64	67.14	
								3	1.5	1.5	67.14	68.64	
								4	1.5	1.5	68.64	70.14	IW, VAC
								5	1.5	1.5	70.14	71.64	HS
								6	1.5	1.5	71.64	73.14	
								7	0.86	0.86	73.14	74.0	
								CC(w/7)	0.24	0.24	74.0	74.24	PAL
								Totals:	10.1	10.1			
9H	30 May	0315	73.64	83.14	9.5	9.98	105.1						
								1	1.5	1.5	73.64	75.14	
								2	1.5	1.5	75.14	76.64	
								3	1.5	1.5	76.64	78.14	VAC
								4	1.5	1.5	78.14	79.64	BACT, IW, BGAS
								5	1.5	1.5	79.64	81.14	HS
								6	1.5	1.5	81.14	82.64	
								7	0.83	0.83	82.64	83.47	
								CC(w/7)	0.15	0.15	83.47	83.62	PAL
								Totals:	9.98	9.98			
10H	30 May	0730	83.14	92.64	9.5	10.25	107.9						
								1	1.5	1.5	83.14	84.64	
								2	1.5	1.5	84.64	86.14	
								3	1.5	1.5	86.14	87.64	HS
								4	1.5	1.5	87.64	89.14	IW
								5	1.56	1.56	89.14	90.7	VAC
								6	1.5	1.5	90.7	92.2	
								7	0.88	0.88	92.2	93.08	
								CC(w/7)	0.31	0.31	93.08	93.39	PAL
								Totals:	10.25	10.25			
11H	30 May	0900	92.64	102.14	9.5	9.64	101.5						
								1	1.5	1.5	92.64	94.14	
								2	1.5	1.5	94.14	95.64	
								3	1.5	1.5	95.64	97.14	BGAS
								4	1.5	1.5	97.14	98.64	IW, WRC
								5	1.5	1.5	98.64	100.14	
								6	1.5	1.5	100.14	101.64	HS
								7	0.63	0.63	101.64	102.27	
								CC(NS)	0.01	0.01	102.27	102.28	PAL
								Totals:	9.64	9.64			
12H	30 May	1040	102.14	111.64	9.5	9.83	103.5						
								1	1.5	1.5	102.14	103.64	
								2	1.5	1.5	103.64	105.14	
								3	1.5	1.5	105.14	106.64	
								4	1.5	1.5	106.64	108.14	BACT, IW, WRSF, WR
								5	1.5	1.5	108.14	109.64	HS, HS, HS
								6	1.5	1.5	109.64	111.14	
								7	0.47	0.47	111.14	111.61	
								CC(w/7)	0.36	0.36	111.61	111.97	PAL
								Totals:	9.83	9.83			
13H	30 May	1210	111.64	121.14	9.5	9.31	98.0						
								1	1.5	1.5	111.64	113.14	
								2	1.5	1.5	113.14	114.64	
								3	1.5	1.5	114.64	116.14	
								4	1.5	1.5	116.14	117.64	IW, WRMT
								5	1.5	1.5	117.64	119.14	HS, BGAS
								6	1.24	1.24	119.14	120.38	
								7	0.46	0.46	120.38	120.84	
								CC(w/7)	0.11	0.11	120.84	120.95	PAL
								Totals:	9.31	9.31			
14H	30 May	1405	121.14	130.64	9.5	9.59	100.9						
								1	1.5	1.5	121.14	122.64	
								2	1.5	1.5	122.64	124.14	
								3	1.5	1.5	124.14	125.64	IW, BACT
								4	1.5	1.5	125.64	127.14	HS
								5	1.5	1.5	127.14	128.64	
								6	1.25	1.25	128.64	129.89	
								7	0.59	0.59	129.89	130.48	
								CC(w/7)	0.25	0.25	130.48	130.73	PAL
								Totals:	9.59	9.59			

Table T2 (continued).

Core	Date (2000)	Time (local)	Core depth (mbsf) Top	Core depth (mbsf) Bottom	Length (m) Cored	Length (m) Recovered	Recovery (%)	Section	Length (m) Liner	Length (m) Curated	Section depth (mbsf) Top	Section depth (mbsf) Bottom	Catwalk samples
15H	30 May	1530	130.64	140.14	9.5	9.73	102.4						
								1	1.5	1.5	130.64	132.14	
								2	1.5	1.5	132.14	133.64	
								3	1.5	1.5	133.64	135.14	
								4	1.5	1.5	135.14	136.64	IW, BGAS
								5	1.5	1.5	136.64	138.14	HS
								6	1.5	1.5	138.14	139.64	
								7	0.36	0.36	139.64	140.0	
								CC(w/7)	0.37	0.37	140.0	140.37	PAL
								Totals:	9.73	9.73			
16H	30 May	1650	140.14	149.64	9.5	9.46	99.6						
								1	1.5	1.5	140.14	141.64	
								2	1.5	1.5	141.64	143.14	
								3	1.5	1.5	143.14	144.64	
								4	1.5	1.5	144.64	146.14	SPIVH, IW
								5	1.5	1.5	146.14	147.64	HS
								6	1.5	1.5	147.64	149.14	
								7	0.46	0.46	149.14	149.6	PAL
								Totals:	9.46	9.46			
17H	30 May	1825	149.64	159.14	9.5	9.00	94.7						
								1	1.5	1.5	149.64	151.14	
								2	1.5	1.5	151.14	152.64	
								3	1.5	1.5	152.64	154.14	
								4	1.5	1.5	154.14	155.64	IW, BGAS
								5	1.5	1.5	155.64	157.14	HS
								6	1.5	1.5	157.14	158.64	PAL
								Totals:	9.0	9.0			
18H	30 May	1955	159.14	168.64	9.5	9.44	99.4						
								1	1.5	1.5	159.14	160.64	
								2	1.5	1.5	160.64	162.14	
								3	1.5	1.5	162.14	163.64	
								4	1.5	1.5	163.64	165.14	IW
								5	1.5	1.5	165.14	166.64	HS
								6	1.3	1.3	166.64	167.94	WRMT, WRMT
								7	0.64	0.64	167.94	168.58	PAL
								Totals:	9.44	9.44			
19H	30 May	2130	168.64	178.14	9.5	9.61	101.2						
								1	1.5	1.5	168.64	170.14	
								2	1.5	1.5	170.14	171.64	
								3	1.5	1.5	171.64	173.14	
								4	1.5	1.5	173.14	174.64	BACT, IW, BGAS
								5	1.5	1.5	174.64	176.14	HS
								6	1.5	1.5	176.14	177.64	
								7	0.38	0.38	177.64	178.02	
								CC(w/7)	0.23	0.23	178.02	178.25	PAL, SFRCC
								Totals:	9.61	9.61			
20H	30 May	2255	178.14	187.64	9.5	8.07	84.9						
								1	1.5	1.5	178.14	179.64	
								2	1.5	1.5	179.64	181.14	
								3	1.5	1.5	181.14	182.64	
								4	1.5	1.5	182.64	184.14	IW
								5	1.5	1.5	184.14	185.64	HS, WRSR
								6	0.56	0.56	185.64	186.2	
								CC(NS)	0.01	0.01	186.2	186.21	PAL
								Totals:	8.07	8.07			
21H	31 May	0015	187.64	197.14	9.5	9.69	102.0						
								1	1.5	1.5	187.64	189.14	
								2	1.5	1.5	189.14	190.64	
								3	1.5	1.5	190.64	192.14	BACT
								4	1.5	1.5	192.14	193.64	WRC, IW, CRG
								5	1.5	1.5	193.64	195.14	
								6	1.5	1.5	195.14	196.64	HS, BGAS
								7	0.55	0.55	196.64	197.19	
								CC(w/7)	0.14	0.14	197.19	197.33	PAL
								Totals:	9.69	9.69			
22H	31 May	0435	197.14	206.64	9.5	8.85	93.2						
								1	1.5	1.5	197.14	198.64	
								2	1.5	1.5	198.64	200.14	WRLZ

Table T2 (continued).

Core	Date (2000)	Time (local)	Core depth (mbsf) Top	Core depth (mbsf) Bottom	Length (m) Cored	Length (m) Recovered	Recovery (%)	Section	Length (m) Liner	Length (m) Curated	Section depth (mbsf) Top	Section depth (mbsf) Bottom	Catwalk samples
								3	1.5	1.5	200.14	201.64	IW, BGAS
								4	1.5	1.5	201.64	203.14	HS, SPIVH
								5	1.5	1.5	203.14	204.64	
								6	1.34	1.34	204.64	205.98	
								CC(w/CC)	0.01	0.01	205.98	205.99	PAL
								Totals:	8.85	8.85			
23H	31 May	0605	206.64	216.14	9.5	9.43	99.3						
								1	1.5	1.5	206.64	208.14	
								2	1.5	1.5	208.14	209.64	
								3	1.5	1.5	209.64	211.14	IW
								4	1.5	1.5	211.14	212.64	HS
								5	1.5	1.5	212.64	214.14	HYWR
								6	1.5	1.5	214.14	215.64	
								7	0.42	0.42	215.64	216.06	
								CC(w/7)	0.01	0.01	216.06	216.07	PAL
								Totals:	9.43	9.43			
24H	31 May	0735	216.14	225.64	9.5	9.34	98.3						
								1	1.5	1.5	216.14	217.64	WRSF
								2	1.5	1.5	217.64	219.14	WRTB
								3	1.5	1.5	219.14	220.64	
								4	1.5	1.5	220.64	222.14	
								5	1.5	1.5	222.14	223.64	HS, IW, BGAS
								6	1.5	1.5	223.64	225.14	
								7	0.29	0.29	225.14	225.43	
								CC(w/7)	0.05	0.05	225.43	225.48	PAL
								Totals:	9.34	9.34			
25X	31 May	0925	225.64	235.24	9.6	9.69	100.9						
								1	1.5	1.5	225.64	227.14	
								2	1.5	1.5	227.14	228.64	
								3	1.5	1.5	228.64	230.14	
								4	1.5	1.5	230.14	231.64	IW
								5	1.5	1.5	231.64	233.14	HS
								6	1.5	1.5	233.14	234.64	
								7	0.44	0.44	234.64	235.08	
								CC(w/7)	0.25	0.25	235.08	235.33	PAL
								Totals:	9.69	9.69			
26X	31 May	1100	235.24	244.94	9.7	9.86	101.6						
								1	1.5	1.5	235.24	236.74	
								2	1.5	1.5	236.74	238.24	IW
								3	1.5	1.5	238.24	239.74	
								4	1.5	1.5	239.74	241.24	HS, BGAS
								5	1.5	1.5	241.24	242.74	
								6	1.5	1.5	242.74	244.24	
								7	0.48	0.48	244.24	244.72	
								CC(w/7)	0.38	0.38	244.72	245.1	PAL
								Totals:	9.86	9.86			
27X	31 May	1245	244.94	254.54	9.6	9.79	102.0						
								1	1.5	1.5	244.94	246.44	
								2	1.5	1.5	246.44	247.94	
								3	1.5	1.5	247.94	249.44	
								4	1.5	1.5	249.44	250.94	
								5	1.5	1.5	250.94	252.44	BACT, IW
								6	1.5	1.5	252.44	253.94	HS
								7	0.41	0.41	253.94	254.35	
								CC(w/7)	0.38	0.38	254.35	254.73	PAL
								Totals:	9.79	9.79			
28X	31 May	1420	254.54	264.04	9.5	9.94	104.6						
								1	1.5	1.5	254.54	256.04	SMTCR
								2	1.5	1.5	256.04	257.54	SMTCR
								3	1.5	1.5	257.54	259.04	SMTCR
								4	1.5	1.5	259.04	260.54	SMTCR
								5	1.5	1.5	260.54	262.04	SMTCR, IW, BGAS
								6	1.5	1.5	262.04	263.54	SMTCR, HS
								7	0.51	0.51	263.54	264.05	SMTCR
								CC(w/7)	0.43	0.43	264.05	264.48	PAL
								Totals:	9.94	9.94			
29X	31 May	1600	264.04	273.64	9.6	7.67	79.9						
								1	1.5	1.5	264.04	265.54	SMTCR

Table T2 (continued).

Core	Date (2000)	Time (local)	Core depth (mbsf) Top	Core depth (mbsf) Bottom	Length (m) Cored	Length (m) Recovered	Recovery (%)	Section	Length (m) Liner	Length (m) Curated	Section depth (mbsf) Top	Section depth (mbsf) Bottom	Catwalk samples
								2	1.5	1.5	265.54	267.04	SMTCR
								3	1.5	1.5	267.04	268.54	SMTCR
								4	1.5	1.5	268.54	270.04	SMTCR, IW
								5	1.29	1.29	270.04	271.33	HS
								CC(w/CC)	0.38	0.38	271.33	271.71	
								Totals:	7.67	7.67			
30X	31 May	1730	273.64	283.24	9.6	9.34	97.3						
								1	1.5	1.5	273.64	275.14	
								2	1.5	1.5	275.14	276.64	
								3	1.5	1.5	276.64	278.14	IW
								4	1.5	1.5	278.14	279.64	HS, BGAS
								5	1.5	1.5	279.64	281.14	
								6	1.5	1.5	281.14	282.64	
								CC(w/CC)	0.34	0.34	282.64	282.98	PAL
								Totals:	9.34	9.34			
31X	31 May	2145	283.24	292.94	9.7	9.81	101.1						
								1	1.5	1.5	283.24	284.74	WRLZ
								2	1.5	1.5	284.74	286.24	
								3	1.5	1.5	286.24	287.74	IW
								4	1.5	1.5	287.74	289.24	HS
								5	1.5	1.5	289.24	290.74	SPIVH
								6	1.5	1.5	290.74	292.24	
								7	0.41	0.41	292.24	292.65	
								CC(w/7)	0.4	0.4	292.65	293.05	PAL
								Totals:	9.81	9.81			
32X	31 May	2305	292.94	302.64	9.7	9.30	95.9						
								1	1.5	1.5	292.94	294.44	
								2	1.5	1.5	294.44	295.94	
								3	1.5	1.5	295.94	297.44	WRC, PLUGS, IW, BA
								4	1.5	1.5	297.44	298.94	
								5	1.5	1.5	298.94	300.44	HS, BGAS
								6	1.5	1.5	300.44	301.94	WRSF
								CC(w/CC)	0.3	0.3	301.94	302.24	PAL
								Totals:	9.3	9.3			
33X	1 June	0025	302.64	311.94	9.3	8.49	91.3						
								1	1.5	1.5	302.64	304.14	IW
								2	1.5	1.5	304.14	305.64	
								3	1.5	1.5	305.64	307.14	HS
								4	1.5	1.5	307.14	308.64	
								5	1.5	1.5	308.64	310.14	
								6	0.56	0.56	310.14	310.7	
								CC(w/6)	0.43	0.43	310.7	311.13	PAL
								Totals:	8.49	8.49			
34X	1 June	0145	311.94	321.54	9.6	9.81	102.2						
								1	1.5	1.5	311.94	313.44	
								2	1.5	1.5	313.44	314.94	
								3	1.5	1.5	314.94	316.44	
								4	1.5	1.5	316.44	317.94	IW
								5	1.5	1.5	317.94	319.44	HS, WRTB
								6	1.5	1.5	319.44	320.94	BGAS
								7	0.44	0.44	320.94	321.38	
								CC(w/7)	0.37	0.37	321.38	321.75	PAL, SFRCC
								Totals:	9.81	9.81			
35X	1 June	0305	321.54	331.14	9.6	9.83	102.4						
								1	1.5	1.5	321.54	323.04	
								2	1.5	1.5	323.04	324.54	
								3	1.5	1.5	324.54	326.04	
								4	1.5	1.5	326.04	327.54	HS
								5	1.5	1.5	327.54	329.04	BACT, IW
								6	1.5	1.5	329.04	330.54	
								7	0.4	0.4	330.54	330.94	
								CC(w/7)	0.43	0.43	330.94	331.37	
								Totals:	9.83	9.83			
36X	1 June	0445	331.14	340.74	9.6	9.06	94.4						
								1	1.5	1.5	331.14	332.64	
								2	1.5	1.5	332.64	334.14	HYWR
								3	1.5	1.5	334.14	335.64	HS, BGAS
								4	1.5	1.5	335.64	337.14	IW, BACT, IW, WRSR

Table T2 (continued).

Core	Date (2000)	Time (local)	Core depth (mbsf) Top	Core depth (mbsf) Bottom	Length (m) Cored	Length (m) Recovered	Recovery (%)	Section	Length (m) Liner	Length (m) Curated	Section depth (mbsf) Top	Section depth (mbsf) Bottom	Catwalk samples
								5	1.5	1.5	337.14	338.64	HS
								6	1.31	1.31	338.64	339.95	WRTB
								CC(w/CC)	0.25	0.25	339.95	340.2	PAL, SFRCC
								Totals:	9.06	9.06			
37X	1 June	0620	340.74	350.34	9.6	9.79	102.0						
								1	1.5	1.5	340.74	342.24	
								2	1.5	1.5	342.24	343.74	
								3	1.5	1.5	343.74	345.24	
								4	1.5	1.5	345.24	346.74	PAL, IW, BACT
								5	1.5	1.5	346.74	348.24	HS
								6	1.5	1.5	348.24	349.74	WRHZ
								7	0.46	0.46	349.74	350.2	
								CC(w/7)	0.33	0.33	350.2	350.53	PAL
								Totals:	9.79	9.79			
38X	1 June	0745	350.34	359.94	9.6	9.91	103.2						
								1	1.5	1.5	350.34	351.84	
								2	1.5	1.5	351.84	353.34	IW
								3	1.5	1.5	353.34	354.84	HS, BGAS
								4	1.5	1.5	354.84	356.34	
								5	1.5	1.5	356.34	357.84	
								6	1.5	1.5	357.84	359.34	
								7	0.45	0.45	359.34	359.79	
								CC(w/7)	0.46	0.46	359.79	360.25	PAL, WRTB
								Totals:	9.91	9.91			
39X	1 June	0910	359.94	369.64	9.7	9.89	102.0						
								1	1.5	1.5	359.94	361.44	WRMG
								2	1.5	1.5	361.44	362.94	IW
								3	1.5	1.5	362.94	364.44	HS
								4	1.5	1.5	364.44	365.94	
								5	1.5	1.5	365.94	367.44	WRLZ
								6	1.5	1.5	367.44	368.94	
								7	0.44	0.44	368.94	369.38	
								CC(w/7)	0.45	0.45	369.38	369.83	
								Totals:	9.89	9.89			
40X	1 June	1030	369.64	379.24	9.6	9.84	102.5						
								1	1.5	1.5	369.64	371.14	
								2	1.5	1.5	371.14	372.64	
								3	1.5	1.5	372.64	374.14	WRSF
								4	1.5	1.5	374.14	375.64	
								5	1.5	1.5	375.64	377.14	IW, IW
								6	1.5	1.5	377.14	378.64	HS, BGAS, WRTB
								7	0.46	0.46	378.64	379.1	
								CC(w/7)	0.38	0.38	379.1	379.48	PAL
								Totals:	9.84	9.84			
41X	1 June	1200	379.24	388.84	9.6	9.92	103.3						
								1	1.5	1.5	379.24	380.74	
								2	1.5	1.5	380.74	382.24	
								3	1.5	1.5	382.24	383.74	
								4	1.5	1.5	383.74	385.24	
								5	1.5	1.5	385.24	386.74	BACT, IW, IW
								6	1.5	1.5	386.74	388.24	HS, HS
								7	0.34	0.34	388.24	388.58	
								CC(w/7)	0.58	0.58	388.58	389.16	PAL, SFRCC, WRLZ
								Totals:	9.92	9.92			
42X	1 June	1400	388.84	398.44	9.6	9.90	103.1						
								1	1.5	1.5	388.84	390.34	
								2	1.5	1.5	390.34	391.84	WRSR
								3	1.5	1.5	391.84	393.34	IW, SPIVH
								4	1.5	1.5	393.34	394.84	HS
								5	1.5	1.5	394.84	396.34	
								6	1.5	1.5	396.34	397.84	
								7	0.48	0.48	397.84	398.32	WRTB
								CC(w/7)	0.42	0.42	398.32	398.74	
								Totals:	9.9	9.9			
43X	1 June	1515	398.44	408.04	9.6	9.23	96.1						
								1	1.5	1.5	398.44	399.94	
								2	1.5	1.5	399.94	401.44	
								3	1.5	1.5	401.44	402.94	WRC, PLUGS, BACT

Table T2 (continued).

Core	Date (2000)	Time (local)	Core depth (mbsf) Top	Core depth (mbsf) Bottom	Length (m) Cored	Length (m) Recovered	Recovery (%)	Section	Length (m) Liner	Length (m) Curated	Section depth (mbsf) Top	Section depth (mbsf) Bottom	Catwalk samples
								4	1.5	1.5	402.94	404.44	
								5	1.5	1.5	404.44	405.94	IW, BGAS
								6	1.38	1.38	405.94	407.32	HS
								CC(w/CC)	0.35	0.35	407.32	407.67	PAL, SFRCC
								Totals:	9.23	9.23			
44X	1 June	1645	408.04	417.64	9.6	9.95	103.6						
								1	1.5	1.5	408.04	409.54	
								2	1.5	1.5	409.54	411.04	
								3	1.5	1.5	411.04	412.54	
								4	1.5	1.5	412.54	414.04	IW
								5	1.5	1.5	414.04	415.54	HS
								6	1.5	1.5	415.54	417.04	
								7	0.48	0.48	417.04	417.52	
								CC(w/7)	0.47	0.47	417.52	417.99	PAL, WRTB
								Totals:	9.95	9.95			
45X	1 June	1805	417.64	427.24	9.6	9.87	102.8						
								1	1.5	1.5	417.64	419.14	
								2	1.5	1.5	419.14	420.64	
								3	1.5	1.5	420.64	422.14	
								4	1.5	1.5	422.14	423.64	
								5	1.5	1.5	423.64	425.14	BACT, IW, SPIVH
								6	1.5	1.5	425.14	426.64	HS
								7	0.46	0.46	426.64	427.1	
								CC(w/7)	0.41	0.41	427.1	427.51	PAL, SFRCC
								Totals:	9.87	9.87			
46X	1 June	1925	427.24	436.44	9.2	9.92	107.8						
								1	1.5	1.5	427.24	428.74	WRLZ
								2	1.5	1.5	428.74	430.24	
								3	1.5	1.5	430.24	431.74	
								4	1.5	1.5	431.74	433.24	BGAS, IW, SPIVH
								5	1.5	1.5	433.24	434.74	HS, WRTB
								6	1.5	1.5	434.74	436.24	
								7	0.45	0.45	436.24	436.69	
								CC(w/7)	0.47	0.47	436.69	437.16	PAL
								Totals:	9.92	9.92			
47X	1 June	2045	436.44	445.84	9.4	9.91	105.4						
								1	1.5	1.5	436.44	437.94	
								2	1.5	1.5	437.94	439.44	
								3	1.5	1.5	439.44	440.94	
								4	1.5	1.5	440.94	442.44	IW
								5	1.5	1.5	442.44	443.94	HS, WRSR
								6	1.5	1.5	443.94	445.44	
								7	0.43	0.43	445.44	445.87	
								CC(w/7)	0.48	0.48	445.87	446.35	
								Totals:	9.91	9.91			
48X	1 June	2200	445.84	455.04	9.2	9.99	108.6						
								1	1.5	1.5	445.84	447.34	
								2	1.5	1.5	447.34	448.84	
								3	1.5	1.5	448.84	450.34	
								4	1.5	1.5	450.34	451.84	
								5	1.5	1.5	451.84	453.34	IW
								6	1.5	1.5	453.34	454.84	HS
								7	0.56	0.56	454.84	455.4	
								CC(w/7)	0.43	0.43	455.4	455.83	WRTB
								Totals:	9.99	9.99			
49X	1 June	2325	455.04	464.64	9.6	9.87	102.8						
								1	1.5	1.5	455.04	456.54	
								2	1.5	1.5	456.54	458.04	
								3	1.5	1.5	458.04	459.54	BACT, IW, BGAS
								4	1.5	1.5	459.54	461.04	HS
								5	1.5	1.5	461.04	462.54	
								6	1.5	1.5	462.54	464.04	
								7	0.46	0.46	464.04	464.5	
								CC(w/7)	0.41	0.41	464.5	464.91	PAL, SFRCC
								Totals:	9.87	9.87			
50X	2 June	0045	464.64	474.34	9.7	9.92	102.3						
								1	1.5	1.5	464.64	466.14	
								2	1.5	1.5	466.14	467.64	

Table T2 (continued).

Core	Date (2000)	Time (local)	Core depth (mbsf) Top	Core depth (mbsf) Bottom	Length (m) Cored	Length (m) Recovered	Recovery (%)	Section	Length (m) Liner	Length (m) Curated	Section depth (mbsf) Top	Section depth (mbsf) Bottom	Catwalk samples
								3	1.5	1.5	467.64	469.14	
								4	1.5	1.5	469.14	470.64	
								5	1.5	1.5	470.64	472.14	HS, IW
								6	1.5	1.5	472.14	473.64	
								7	0.44	0.44	473.64	474.08	
								CC(w/7)	0.48	0.48	474.08	474.56	PAL
								Totals:	9.92	9.92			
51X	2 June	0220	474.34	484.04	9.7	9.91	102.2						
								1	1.5	1.5	474.34	475.84	
								2	1.5	1.5	475.84	477.34	WRMG
								3	1.5	1.5	477.34	478.84	
								4	1.5	1.5	478.84	480.34	
								5	1.5	1.5	480.34	481.84	HS, IW
								6	1.5	1.5	481.84	483.34	WRHZ
								7	0.49	0.49	483.34	483.83	
								CC(w/7)	0.42	0.42	483.83	484.25	PAL
								Totals:	9.91	9.91			
52X	2 June	0340	484.04	493.74	9.7	9.93	102.4						
								1	1.5	1.5	484.04	485.54	
								2	1.5	1.5	485.54	487.04	HS, BGAS
								3	1.5	1.5	487.04	488.54	
								4	1.5	1.5	488.54	490.04	
								5	1.5	1.5	490.04	491.54	
								6	1.5	1.5	491.54	493.04	
								7	0.48	0.48	493.04	493.52	
								CC(w/7)	0.45	0.45	493.52	493.97	PAL
								Totals:	9.93	9.93			
53X	2 June	0525	493.74	503.34	9.6	9.95	103.6						
								1	1.5	1.5	493.74	495.24	
								2	1.5	1.5	495.24	496.74	
								3	1.5	1.5	496.74	498.24	WRC, BACT, IW, CRG
								4	1.5	1.5	498.24	499.74	
								5	1.5	1.5	499.74	501.24	HS, WRTB
								6	1.5	1.5	501.24	502.74	
								7	0.46	0.46	502.74	503.2	
								CC(w/7)	0.49	0.49	503.2	503.69	PAL, SFRCC
								Totals:	9.95	9.95			
54X	2 June	0740	503.34	513.04	9.7	9.92	102.3						
								1	1.5	1.5	503.34	504.84	
								2	1.5	1.5	504.84	506.34	
								3	1.5	1.5	506.34	507.84	
								4	1.5	1.5	507.84	509.34	
								5	1.5	1.5	509.34	510.84	HS, IW, BGAS
								6	1.5	1.5	510.84	512.34	
								7	0.48	0.48	512.34	512.82	
								CC(w/7)	0.44	0.44	512.82	513.26	PAL
								Totals:	9.92	9.92			
55X	2 June	0955	513.04	522.34	9.3	9.85	105.9						
								1	1.5	1.5	513.04	514.54	
								2	1.5	1.5	514.54	516.04	HS, IW
								3	1.5	1.5	516.04	517.54	IW
								4	1.5	1.5	517.54	519.04	
								5	1.5	1.5	519.04	520.54	HYWR
								6	1.5	1.5	520.54	522.04	
								7	0.4	0.4	522.04	522.44	
								CC(w/7)	0.45	0.45	522.44	522.89	PAL
								Totals:	9.85	9.85			
56X	2 June	1300	522.34	532.04	9.7	9.89	102.0						
								1	1.5	1.5	522.34	523.84	
								2	1.5	1.5	523.84	525.34	
								3	1.5	1.5	525.34	526.84	
								4	1.5	1.5	526.84	528.34	IW, BGAS, SPIVH
								5	1.5	1.5	528.34	529.84	HS, WRSR
								6	1.5	1.5	529.84	531.34	
								7	0.5	0.5	531.34	531.84	
								CC(w/7)	0.39	0.39	531.84	532.23	PAL
								Totals:	9.89	9.89			

Table T2 (continued).

Core	Date (2000)	Time (local)	Core depth (mbsf) Top	Core depth (mbsf) Bottom	Length (m) Cored	Length (m) Recovered	Recovery (%)	Section	Length (m) Liner	Length (m) Curated	Section depth (mbsf) Top	Section depth (mbsf) Bottom	Catwalk samples
57X	2 June	1520	532.04	541.74	9.7	9.90	102.1						
								1	1.5	1.5	532.04	533.54	
								2	1.5	1.5	533.54	535.04	
								3	1.5	1.5	535.04	536.54	BACT, IW
								4	1.5	1.5	536.54	538.04	HS
								5	1.5	1.5	538.04	539.54	
								6	1.5	1.5	539.54	541.04	
								7	0.41	0.41	541.04	541.45	
								CC(w/7)	0.49	0.49	541.45	541.94	PAL
								Totals:	9.9	9.9			
58X	2 June	1745	541.74	551.34	9.6	9.93	103.4						
								1	1.5	1.5	541.74	543.24	
								2	1.5	1.5	543.24	544.74	
								3	1.5	1.5	544.74	546.24	
								4	1.5	1.5	546.24	547.74	IW, BGAS
								5	1.5	1.5	547.74	549.24	HS
								6	1.5	1.5	549.24	550.74	
								7	0.47	0.47	550.74	551.21	
								CC(w/7)	0.46	0.46	551.21	551.67	PAL
								Totals:	9.93	9.93			
59X	2 June	2000	551.34	561.04	9.7	9.85	101.5						
								1	1.5	1.5	551.34	552.84	
								2	1.5	1.5	552.84	554.34	
								3	1.5	1.5	554.34	555.84	
								4	1.5	1.5	555.84	557.34	IW
								5	1.5	1.5	557.34	558.84	HS
								6	1.5	1.5	558.84	560.34	
								7	0.41	0.41	560.34	560.75	
								CC(w/7)	0.44	0.44	560.75	561.19	PAL
								Totals:	9.85	9.85			
60X	2 June	2230	561.04	570.74	9.7	9.83	101.3						
								1	1.5	1.5	561.04	562.54	
								2	1.5	1.5	562.54	564.04	
								3	1.5	1.5	564.04	565.54	
								4	1.5	1.5	565.54	567.04	BACT, IW, BGAS
								5	1.5	1.5	567.04	568.54	HS
								6	1.5	1.5	568.54	570.04	
								7	0.52	0.52	570.04	570.56	
								CC(w/7)	0.31	0.31	570.56	570.87	PAL
								Totals:	9.83	9.83			
61X	3 June	0045	570.74	580.44	9.7	9.88	101.9						
								1	1.5	1.5	570.74	572.24	
								2	1.5	1.5	572.24	573.74	
								3	1.5	1.5	573.74	575.24	HS
								4	1.5	1.5	575.24	576.74	IW
								5	1.5	1.5	576.74	578.24	
								6	1.5	1.5	578.24	579.74	
								7	0.48	0.48	579.74	580.22	
								CC(w/7)	0.4	0.4	580.22	580.62	PAL, SFRCC
								Totals:	9.88	9.88			
62X	3 June	0320	580.44	589.94	9.5	9.86	103.8						
								1	1.5	1.5	580.44	581.94	
								2	1.5	1.5	581.94	583.44	
								3	1.5	1.5	583.44	584.94	
								4	1.5	1.5	584.94	586.44	
								5	1.5	1.5	586.44	587.94	HS, BGAS
								6	1.5	1.5	587.94	589.44	
								7	0.46	0.46	589.44	589.9	
								CC(w/7)	0.4	0.4	589.9	590.3	PAL
								Totals:	9.86	9.86			
63X	3 June	0620	589.94	599.54	9.6	1.59	16.6						
								1	1.2	1.2	589.94	591.14	HS, IW
								CC(w/CC)	0.39	0.39	591.14	591.53	PAL
								Totals:	1.59	1.59			
64X	3 June	0930	599.54	609.24	9.7	9.45	97.4						
								1	1.5	1.5	599.54	601.04	
								2	1.5	1.5	601.04	602.54	WRMG
								3	1.5	1.5	602.54	604.04	HS, BGAS

Table T2 (continued).

Core	Date (2000)	Time (local)	Core depth (mbsf) Top	Core depth (mbsf) Bottom	Length (m) Cored	Length (m) Recovered	Recovery (%)	Section	Length (m) Liner	Length (m) Curated	Section depth (mbsf) Top	Section depth (mbsf) Bottom	Catwalk samples
								4	1.5	1.5	604.04	605.54	IW, CRG
								5	1.5	1.5	605.54	607.04	WRTB
								6	1.2	1.2	607.04	608.24	
								7	0.42	0.42	608.24	608.66	
								CC(w/7)	0.33	0.33	608.66	608.99	PAL
								Totals:	9.45	9.45			
65X	3 June	1230	609.24	618.84	9.6	7.46	77.7						
								1	1.5	1.5	609.24	610.74	
								2	1.5	1.5	610.74	612.24	WRSR
								3	1.5	1.5	612.24	613.74	IW
								4	1.5	1.5	613.74	615.24	HS
								5	1.06	1.06	615.24	616.3	
								CC(w/5)	0.4	0.4	616.3	616.7	PAL
								Totals:	7.46	7.46			
66X	3 June	1445	618.84	628.44	9.6	1.99	20.7						
								1	1	1	618.84	619.84	IW, BGAS
								2	0.64	0.64	619.84	620.48	HS
								CC(w/2)	0.35	0.35	620.48	620.83	PAL
								Totals:	1.99	1.99			
67X	3 June	1730	628.44	638.14	9.7	7.84	80.8						
								1	1.5	1.5	628.44	629.94	
								2	1.5	1.5	629.94	631.44	
								3	1.5	1.5	631.44	632.94	
								4	1.5	1.5	632.94	634.44	IW
								5	1.45	1.45	634.44	635.89	HS
								CC(w/CC)	0.39	0.39	635.89	636.28	PAL
								Totals:	7.84	7.84			
68X	3 June	1945	638.14	647.74	9.6	8.67	90.3						
								1	1.5	1.5	638.14	639.64	
								2	1.5	1.5	639.64	641.14	
								3	1.5	1.5	641.14	642.64	BACT, WRC, IW
								4	1.5	1.5	642.64	644.14	HS
								5	1.5	1.5	644.14	645.64	
								6	0.77	0.77	645.64	646.41	
								CC(w/6)	0.4	0.4	646.41	646.81	PAL
								Totals:	8.67	8.67			
69X	3 June	2215	647.74	657.44	9.7	8.68	89.5						
								1	1.5	1.5	647.74	649.24	
								2	1.5	1.5	649.24	650.74	
								3	1.5	1.5	650.74	652.24	
								4	1.5	1.5	652.24	653.74	
								5	1.5	1.5	653.74	655.24	HS
								6	0.79	0.79	655.24	656.03	
								CC(w/6)	0.39	0.39	656.03	656.42	PAL
								Totals:	8.68	8.68			
70X	4 June	0045	657.44	667.14	9.7	6.05	62.4						
								1	1.5	1.5	657.44	658.94	IW
								2	1.5	1.5	658.94	660.44	
								3	1.5	1.5	660.44	661.94	HS, BGAS
								4	1.2	1.2	661.94	663.14	
								CC(w/CC)	0.35	0.35	663.14	663.49	PAL
								Totals:	6.05	6.05			
71X	4 June	0330	667.14	676.74	9.6	8.00	83.3						
								1	1.5	1.5	667.14	668.64	
								2	1.5	1.5	668.64	670.14	
								3	1.5	1.5	670.14	671.64	
								4	1.5	1.5	671.64	673.14	BACT, IW
								5	1.5	1.5	673.14	674.64	HS, BGAS
								CC(w/CC)	0.5	0.5	674.64	675.14	PAL
								Totals:	8.0	8.0			
72X	4 June	0615	676.74	686.34	9.6	2.09	21.8						
								1	1.5	1.5	676.74	678.24	HS, IW
								2	0.21	0.21	678.24	678.45	
								CC(w/2)	0.38	0.38	678.45	678.83	PAL, SFRCC
								Totals:	2.09	2.09			
73X	4 June	0940	686.34	695.94	9.6	3.07	32.0						
								1	1.5	1.5	686.34	687.84	IW, BGAS
								2	1.2	1.2	687.84	689.04	HS

Table T2 (continued).

Core	Date (2000)	Time (local)	Core depth (mbsf) Top	Core depth (mbsf) Bottom	Length (m) Cored	Length (m) Recovered	Recovery (%)	Section	Length (m) Liner	Length (m) Curated	Section depth (mbsf) Top	Section depth (mbsf) Bottom	Catwalk samples
								CC(w/CC)	0.37	0.37	689.04	689.41	PAL
								Totals:	3.07	3.07			
74X	4 June	1245	695.94	705.64	9.7	0.86	8.9						
								1	0.53	0.53	695.94	696.47	HS
								CC(w/1)	0.33	0.33	696.47	696.8	
								Totals:	0.86	0.86			
75X	4 June	1545	705.64	715.34	9.7	0.29	3.0						
								CC(w/CC)	0.29	0.29	705.64	705.93	HS, PAL
								Totals:	0.29	0.29			
76X	4 June	1925	715.34	724.64	9.3	0.38	4.1						
								CC(w/CC)	0.38	0.38	715.34	715.72	PAL, HS
								Totals:	0.38	0.38			
77X	4 June	2310	724.64	734.34	9.7	0.26	2.7						
								CC(w/CC)	0.26	0.26	724.64	724.9	PAL, HS
								Totals:	0.26	0.26			
				Totals:	734.34	658.10	89.60						

Notes: Catwalk samples: IW = interstitial water, HS = headspace, PAL = paleontology, VAC = vacutainer. All other abbreviations are sample codes for postcruise research (see the **"Sample Codes"** database query). This table is also available in **ASCII** format

Table T3. Summary of stratigraphic units at Site 1173 and correlation with equivalent units at Site 808 (from Shipboard Scientific Party, 1991).

Unit	Sub-unit	Facies name	Interval (cm) Top	Interval (cm) Bottom	Depth (mbsf) Top	Depth (mbsf) Bottom	Thickness (m)	Stratigraphic age	Lithologic description	Processes of formation	Tectonic and physiographic setting	Stratigraphic correlation with Site 808
I	IA	Outer-trench wedge	190-1173A-1H-1, 0	190-1173A-10H-1, 23	0.00	83.37	83.37	Quaternary	Silty clay, sand, silt, and rare volcanic ash	Turbidity currents, hemipelagic settling, rare settling of ash	Outer-trench wedge	Units IIB, IIC
	IB	Trench to basin transition	10H-1, 23	12H-1, 0	83.37	102.14	18.77	Quaternary	Silty clay, abundant volcanic ash, rare thin silt	Hemipelagic settling, settling of ash, rare turbidity currents	Trench to basin transition	Unit III
II		Upper Shikoku Basin	12H-1, 0	37X-3, 3	102.14	343.77	241.63	Pliocene to Quaternary	Silty clay, abundant volcanic ash	Hemipelagic settling and frequent settling of volcanic ash	Shikoku Basin closer to trench; volcanism in Kyushu/Honshu	Unit IVA
III		Lower Shikoku Basin	37X-3, 3	73X-2, 15	343.77	687.99	344.22	middle Miocene to early Pliocene	Silty claystone, calcareous claystone, siliceous claystone	Hemipelagic settling, rare settling of ash, and diagenetic alteration	Shikoku Basin distal from trench	Unit IVB
IV		Volcaniclastic	73X-2, 15	77X-CC, 25	687.99	724.89	36.90	Probable middle Miocene	Siliceous claystone, silty claystone	Acidic volcanism, hemipelagic settling, and diagenetic alteration	Japan Outer Zone volcanism - triggered by ridge subduction	Unit V
V		Basalt basement	77X-CC, 25	77X-CC, 26	724.89	724.90	0.01	Probable middle Miocene	Basalt	Formation of igneous crust at spreading ridge	Oceanic basement of Shikoku Basin	Unit VI

Table T4. Peak intensities and peak areas from X-ray diffraction analysis of bulk-powder sediment samples, Hole 1173A. (**See table note.** Continued on next three pages.)

Core, section, interval (cm)	Depth (mbsf)	Smectite + chlorite	Illite	Chlorite + kaolinite	(101) Quartz	Plagioclase	Calcite	(100) Quartz	(101) Cristobalite	Smectite + chlorite	Illite	Chlorite + kaolinite	(101) Quartz	Plagioclase	Calcite	(100) Quartz	(101) Cristobalite
190-1173A-																	
1H-1, 134-135	1.35	62	126	155	2,019	404	146	338	129	2,506	2,459	2,970	26,871	11,753	2,045	4,306	1,805
1H-2, 133-134	2.84	60	134	137	1,903	434	0	386	116	2,628	2,831	2,512	24,822	11,019	0	4,663	1,707
1H-3, 110-111	4.11	65	110	139	2,016	471	150	359	146	2,760	2,384	2,428	26,287	12,269	2,104	4,514	2,121
1H-4, 135-136	5.86	61	117	166	2,077	464	89	377	102	2,500	2,585	2,873	27,499	11,863	1,515	4,733	1,408
1H-5, 77-78	6.78	47	98	124	1,904	389	51	327	122	2,448	2,131	2,749	24,494	9,856	943	4,052	1,678
2H-2, 139-140	10.04	74	132	172	1,823	392	171	326	170	2,748	2,887	2,943	24,946	10,266	2,610	4,331	2,008
2H-2, 139-140	10.04	59	90	135	2,078	430	145			2,524	2,453	2,460	26,634	10,997	2,071		
2H-4, 139-140	13.04	58	97	133	2,078	430	145	360	138	2,321	2,290	2,299	27,140	10,751	2,018	4,682	1,903
2H-6, 139-140	16.04	64	145	168	2,165	380	83	324	120	2,527	2,811	2,917	29,243	10,136	1,329	4,358	1,417
3H-2, 138-139	19.53	66	126	154	2,166	315	66	366	111	2,619	2,370	2,571	28,274	10,415	947	4,677	1,516
3H-2, 138-139	19.53	65	123	157	2,097	414	81			2,016	2,459	2,801	28,090	11,136	1,986		
3H-4, 134-135	22.49	65	125	167	2,174	505	97	371	150	2,650	2,516	2,934	28,085	12,742	1,606	4,555	1,994
3H-5, 138-139	24.03	67	124	157	2,098	415	82			2,642	2,559	2,753	27,768	11,183	1,319		
3H-5, 138-139	24.03	65	123	157	2,097	414	81	364	140	2,016	2,459	2,801	28,090	11,136	1,986	4,730	1,856
4H-3, 101-102	28.90	64	135	135	2,011	417	1,517	348	132	1,313	2,806	2,907	27,159	11,105	1,517	4,716	1,881
4H-3, 134-135	29.23	56	171	158	3,027	857	71	484	191	2,147	2,936	2,833	37,710	19,163	1,254	6,026	2,453
4H-6, 135-136	33.74	70	158	168	2,138	495	109	352	135	3,199	2,984	3,064	28,260	12,530	1,969	4,542	1,862
5H-3, 131-132	39.96	57	140	170	2,319	454	77	388	126	1,802	2,885	3,305	30,624	11,995	1,324	4,954	1,638
5H-5, 127-128	42.92	62	151	169	2,148	540	119	348	118	2,248	2,924	3,040	29,330	13,876	1,840	4,575	1,472
6H-1, 114-115	46.29	65	140	176	2,161	459	30	355	144	2,001	2,688	3,302	28,921	11,547	454	4,691	1,954
6H-2, 49-50	47.14	53	107	106	1,651	319	536	277	97	2,330	2,234	1,823	21,533	8,279	7,414	3,690	1,599
7H-4, 129-130	60.44	61	116	134	1,986	404	53	334	111	2,820	2,377	2,760	26,214	10,792	993	4,346	1,628
7H-7, 47-48	64.12	69	133	182	1,814	484	96	313	156	1,777	2,782	3,701	25,191	12,817	1,748	3,936	2,111
8H-1, 52-53	64.67	68	140	177	2,243	539	97	343	122	2,618	2,494	3,353	32,265	13,875	2,349	4,406	1,519
8H-4, 131-133	69.97	58	162	157	1,922	467	42	339	119	2,434	2,825	3,216	27,387	12,175	1,638	4,083	1,429
9H-4, 132-133	79.47	66	121	137	2,607	692	74	351	148	3,091	2,523	2,972	32,341	14,803	2,372	4,692	2,161
9H-5, 53-54	80.18	51	119	146	1,754	499	127	298	129	2,078	2,407	2,549	23,806	13,292	2,269	3,730	1,807
9H-5, 53-54	80.18	52	119	148	1,756	501	129			2,155	2,376	2,582	23,509	13,154	2,106		
10H-2, 105-106	85.70	66	127	140	1,893	436	0	289	147	2,528	2,600	2,442	25,110	11,705	0	3,844	2,026
10H-4, 123-124	88.88	62	106	142	1,910	426	0	337	142	3,000	2,530	2,650	25,360	11,610	0	4,445	2,086
10H-6, 105-106	91.76	62	132	139	1,919	370	106	315	128	1,706	2,907	2,774	26,001	10,123	1,854	4,199	1,795
11H-4, 111-112	98.26	62	132	147	2,070	416	59	341	123	2,433	2,858	2,643	27,207	11,228	2,170	4,516	1,716
12H-4, 46-47	107.11	47	91	102	1,446	419	0	270	130	1,889	1,921	1,960	20,042	9,404	0	3,829	1,904
12H-4, 134-135	107.99	64	114	115	2,081	394	53	498	126	2,623	2,447	2,274	27,643	9,021	1,694	5,728	1,652
13H-4, 82-83	116.97	74	131	157	2,259	376	72	356	129	2,677	2,726	2,883	29,482	10,172	1,447	4,588	1,669
13H-4, 131-132	117.46	60	121	138	2,145	451	0	335	142	3,001	2,916	2,684	28,776	11,365	0	4,597	1,943
14H-1, 103-104	122.18	64	152	141	2,095	419	98	388	107	2,685	2,986	2,704	28,588	10,856	1,544	5,192	1,611
14H-3, 131-132	125.46	69	131	148	1,918	372	0	320	127	3,043	3,376	3,044	26,469	10,431	0	4,480	1,872
14H-5, 102-103	128.17	49	104	104	1,837	361	178	329	141	2,506	2,311	2,162	24,049	10,251	2,649	4,527	2,169
15H-2, 94-95	133.09	74	128	141	1,889	408	196	333	168	3,033	2,748	2,836	25,826	10,788	2,521	4,763	2,355
15H-4, 132-133	136.47	64	95	96	1,723	343	767	261	88	2,915	2,322	2,250	22,571	9,455	10,785	3,886	1,327
15H-5, 58-59	137.23	52	74	84	1,443	327	401	266	99	2,227	1,657	1,895	19,888	8,306	7,241	3,684	1,441
15H-5, 103-104	137.68	33	41	48	647	150	217	140	87	1,764	671	1,074	9,011	5,045	3,055	2,091	1,805
16H-4, 92-94	145.58	65	118	112	1,763	304	263	310	96	2,703	2,659	2,103	24,105	8,753	3,648	4,284	1,289
16H-6, 48-50	148.14	72	124	135	1,962	420	162	332	120	2,702	2,721	2,561	26,542	10,148	2,407	4,574	1,650
17H-4, 132-133	155.47	53	81	97	1,614	283	647	274	74	2,288	1,595	1,831	21,209	7,976	10,248	3,658	1,136
17H-4, 132-133	155.47	53	81	97	1,614	283	647			2,141	1,595	1,831	21,209	7,976	10,368		

Table T4 (continued).

Core, section, interval (cm)	Depth (mbsf)	X-ray diffraction peak intensity (cps)								X-ray diffraction peak area (total counts)							
		Smectite + chlorite	Illite	Chlorite + kaolinite	(101) Quartz	Plagioclase	Calcite	(100) Quartz	(101) Cristobalite	Smectite + chlorite	Illite	Chlorite + kaolinite	(101) Quartz	Plagioclase	Calcite	(100) Quartz	(101) Cristobalite
18H-4, 132-133	164.97	61	98	107	1,652	294	121	276	111	2,700	2,490	2,143	22,199	9,803	1,876	4,209	1,720
18H-6, 15-16	166.80	24	17	26	369	144	66	77	58	1,675	192	437	5,757	5,161	1,425	1,144	1,263
18H-6, 129-130	167.94	56	69	80	1,086	258	213	197	78	2,719	1,762	1,580	15,269	7,481	3,088	2,855	1,112
19H-4, 132-133	174.47	60	147	140	2,160	346	75	364	100	2,866	2,821	2,713	28,157	9,475	1,496	4,788	1,333
20H-2, 134-135	180.99	63	127	138	1,979	350	119	329	109	3,046	2,627	2,647	26,937	10,587	2,211	4,779	1,594
20H-2, 134-135	180.99	63	127	138	1,979	350	119			2,916	2,657	2,547	26,922	10,173	1,666		
20H-4, 132-133	183.97	69	71	87	1,617	292	597	243	99	2,975	1,760	1,600	20,989	9,689	8,859	3,475	1,421
20H-4, 132-133	183.97	69	71	87	1,617	292	597			2,989	1,750	1,561	21,001	9,732	8,802		
20H-5, 130-131	185.45	60	96	90	1,660	313	674	271	93	2,722	2,000	1,853	22,198	8,446	9,722	3,692	1,187
20H-5, 130-131	185.45	60	96	90	1,660	674	313			2,393	1,996	1,999	22,257	9,722	7,519		
21H-2, 69-70	189.84	64	111	116	1,964	355	155	321	131	3,436	2,599	2,429	26,262	9,393	2,335	4,385	1,575
21H-2, 69-70	189.84	64	111	116	1,964	155	355			3,436	2,864	2,477	26,392	9,593	3,058		
21H-4, 108-109	193.23	58	103	101	1,658	300	272	311	93	2,923	2,287	1,772	22,518	8,820	3,947	4,340	1,178
21H-4, 108-109	193.23	58	103	101	1,658	300	272			2,567	2,450	1,791	22,551	9,167	4,513		
21H-6, 67-68	195.82	53	66	77	1,484	335	244	292	112	2,521	1,510	1,359	19,400	9,848	3,888	3,961	1,832
21H-6, 67-68	195.82	53	66	77	1,484	335	244			2,871	1,619	1,380	20,019	9,798	4,332		
22H-3, 131-132	201.46	52	79	83	1,452	268	516	259	111	2,972	1,837	1,693	19,731	8,303	7,524	3,850	1,787
22H-3, 131-132	201.46	52	79	83	1,452	268	516			2,684	2,144	2,086	23,853	9,878	3,019		
22H-5, 95-96	204.10	59	111	113	1,780	355	210	344	150	2,689	2,156	2,110	24,019	9,205	3,118	4,538	1,989
22H-5, 95-96	204.10	59	111	113	1,780	355	210			2,646	2,252	1,719	19,936	8,436	7,604		
23H-3, 134-135	210.99	64	67	74	1,765	334	429	299	110	2,969	1,653	1,599	23,365	9,220	6,193	4,237	1,555
23H-3, 134-135	210.99	64	67	74	1,765	334	429			3,091	1,901	1,617	23,769	9,393	7,149		
23H-3, 134-135	210.99	64	67	74	1,765	334	429			2,676	1,886	1,612	23,769	9,341	6,851		
23H-5, 136-137	214.01	68	83	111	1,800	358	0	314	118	2,998	1,913	2,197	24,072	10,600	0	4,506	1,831
23H-5, 136-137	214.01	68	83	111	1,800	358	0			3,143	2,258	2,201	24,281	10,370	0		
24H-1, 127-128	217.42	52	67	72	1,529	289	500	247	106	3,031	1,485	1,413	19,849	9,096	7,034	3,760	1,772
24H-1, 127-128	217.42	52	67	72	1,529	289	500			2,780	1,643	1,505	19,912	8,865	7,242		
24H-2, 132-133	218.97	58	70	71	1,366	290	0	205	105	3,018	1,592	1,315	18,590	8,001	0	3,056	1,700
24H-2, 132-133	218.97	58	70	71	1,366	290	0			2,926	1,524	1,401	18,681	8,546	0		
24H-5, 131-132	223.46	57	78	84	1,640	353	0	321	113	2,874	1,705	1,707	21,808	10,528	0	4,449	1,912
24H-5, 131-132	223.46	57	78	84	1,640	353	0			2,826	2,114	1,755	21,917	10,803	0		
25X-1, 123-124	226.88	56	74	82	1,459	366	510	221	107	2,782	1,375	1,523	19,764	9,240	7,798	3,210	1,845
25X-1, 123-124	226.88	56	74	82	1,459	366	510			2,783	1,368	1,522	19,761	9,240	7,775		
25X-1, 123-124	226.88	56	74	82	1,459	366	510			2,890	1,368	1,527	19,774	9,248	8,579		
25X-4, 128-129	231.43	61	85	85	1,536	1,157	289	243	114	3,319	1,766	1,617	20,470	16,632	4,158	3,562	1,761
25X-4, 128-129	231.43	62	85	85	1,536	1,157	289			3,315	1,834	1,620	20,325	16,909	4,715		
25X-6, 124-125	234.39	58	86	79	1,452	314	387	301	122	2,933	1,697	1,590	19,844	9,632	5,265	4,107	2,005
25X-6, 124-125	234.39	58	86	79	1,452	314	387			2,933	1,646	1,590	19,809	9,580	5,235		
25X-6, 124-125	234.39	59	71	79	1,453	316	388			3,464	1,799	1,719	19,539	9,811	5,185		
26X-2, 34-35	237.09	62	80	102	1,827	351	35	326	124	3,097	1,876	1,952	24,177	9,583	566	4,044	1,748
26X-2, 34-35	237.09	62	80	102	1,827	351	35			3,003	1,806	1,944	24,281	9,674	521		
26X-2, 34-35	237.09	62	80	102	1,827	351	76			2,886	2,029	2,010	24,305	9,590	1,732		
26X-6, 125-126	244.00	60	75	74	1,572	266	608	259	103	3,502	1,877	1,517	20,726	8,396	9,098	3,915	1,526
27X-2, 104-105	247.49	60	78	81	1,488	361	443	251	107	3,073	1,561	1,662	20,127	9,409	6,685	3,858	1,742
27X-5, 114-115	252.09	50	60	74	1,269	273	302	251	119	2,489	1,350	1,357	17,061	8,631	4,502	3,675	1,734
28X-5, 114-115	261.69	60	81	75	1,677	479	307			3,285	2,025	1,476	22,548	11,287	4,775		
29X-3, 141-142	268.46	24	45	45	752	166	555	135	75	871	895	928	10,312	5,544	9,129	1,956	1,327
29X-4, 117-118	269.72	54	87	84	1,447	277	255	261	107	3,056	1,958	1,666	19,616	7,723	3,833	3,800	1,712
30X-3, 119-120	277.84	59	99	107	1,748	423	140	312	114	3,093	2,033	2,016	23,415	10,955	1,949	4,258	1,690

Table T4 (continued).

Core, section, interval (cm)	Depth (mbsf)	X-ray diffraction peak intensity (cps)								X-ray diffraction peak area (total counts)							
		Smectite + chlorite	Illite	Chlorite + kaolinite	(101) Quartz	Plagioclase	Calcite	(100) Quartz	(101) Cristobalite	Smectite + chlorite	Illite	Chlorite + kaolinite	(101) Quartz	Plagioclase	Calcite	(100) Quartz	(101) Cristobalite
31X-1, 131-132	284.56	64	124	123	1,751	357	335	301	214	3,624	2,728	2,418	24,321	10,050	5,544	4,166	2,467
31X-3, 124-125	287.49	56	90	101	1,842	406	223	283	99	2,275	1,805	1,779	24,020	11,420	3,099	3,713	1,442
32X-3, 96-97	296.91	52	72	76	1,592	309	70	276	107	2,957	1,809	1,474	20,901	9,048	1,081	3,943	1,631
32X-6, 134-135	301.79	55	80	83	1,476	581	245	244	136	3,542	1,749	1,821	20,114	12,242	4,048	3,649	1,677
33X-1, 122-123	303.87	31	30	36	812	144	0	110	75	1,751	615	880	12,228	4,811	0	1,771	1,556
34X-4, 116-117	317.61	64	70	93	1,453	341	347	270	105	3,492	1,904	1,916	19,517	9,481	5,346	3,781	1,432
34X-5, 56-57	318.51	60	75	87	1,796	829	311	344	112	3,170	1,832	1,826	22,943	12,968	4,700	4,772	1,384
34X-CC, 18-19	321.57	54	85	86	1,864	324	144	322	105	3,227	1,907	1,621	23,745	8,895	1,943	4,222	1,475
35X-2, 141-142	324.46	68	89	96	2,309	467	293	325	168	2,512	2,005	1,727	28,436	11,321	4,115	4,589	2,064
35X-3, 149-150	326.04	50	83	90	1,516	507	241	281	92	3,877	1,770	1,770	29,227	12,109	3,717	3,887	1,268
35X-5, 106-107	328.61	61	82	92	1,740	357	241	268	96	3,546	1,789	1,848	22,720	9,980	4,521	4,038	1,502
36X-4, 91-92	336.56	65	66	71	1,759	322	306	292	109	4,663	1,612	1,545	21,918	8,808	5,323	4,315	1,600
36X-6, 35-36	339.00	66	67	73	1,470	268	362	276	82	4,468	1,549	1,351	19,439	8,408	7,064	3,774	1,071
36X-CC,19-20	340.15	62	67	81	1,498	288	219	269	117	3,952	1,639	1,565	19,130	8,460	3,795	3,743	1,513
37X-4, 124-125	346.49	63	76	77	1,628	329	164	272	85	5,462	1,609	1,715	21,219	10,169	2,437	3,899	1,043
37X-6, 40-41	348.65	64	90	89	1,810	308	118	375	95	5,081	2,457	1,610	23,126	9,109	1,927	4,954	1,151
38X-3, 4-5	353.39	61	97	91	1,804	311	180	320	81	4,700	2,557	1,979	23,244	8,776	2,932	4,507	987
38X-5, 116-117	357.51	71	88	107	2,017	331	87	339	81	5,284	2,292	2,235	26,197	9,945	1,327	4,918	1,036
38X-CC, 23-24	360.03	66	102	95	2,074	314	30	346	90	5,322	2,711	1,847	26,926	9,311	383	4,767	1,014
39X-2, 114-115	362.59	80	76	88	1,934	319	113	363	103	6,837	1,894	1,691	25,702	10,608	1,727	5,288	1,294
39X-5, 137-138	367.32	77	112	112	1,995	356	163	359	116	5,090	3,053	2,215	25,721	10,833	2,325	5,044	1,440
40X-5, 115-116	376.80	66	82	92	1,840	301	121	350	91	5,699	1,937	1,796	23,432	9,918	1,950	4,776	1,149
41X-4, 109-110	384.84	70	76	88	1,793	297	225	370	87	6,827	2,038	1,821	23,814	8,697	3,333	4,982	1,040
41X-7, 32-33	388.57	68	98	103	1,824	291	71	346	73	5,672	1,888	1,895	23,399	8,621	1,219	4,781	885
42X-2, 118-119	391.53	81	124	114	1,910	297	133	339	142	6,848	2,811	2,310	25,632	8,058	2,045	4,955	1,710
42X-3, 118-119	393.03	63	85	87	1,827	333	192	312	82	4,597	2,334	1,892	24,322	8,948	3,045	4,175	1,126
42X-7, 27-28	398.12	72	99	93	1,853	260	111	347	71	6,304	2,399	2,093	23,788	7,221	1,712	4,759	946
43X-3, 118-119	402.63	75	91	98	1,713	298	47	315	90	6,413	1,783	2,066	22,053	8,125	848	4,697	1,098
43X-5, 87-88	405.32	62	98	96	1,738	255	384	305	80	5,280	2,357	1,863	22,319	7,072	5,761	4,372	963
44X-4, 115-116	413.70	49	107	113	2,035	294	54	376	80	2,754	3,286	2,339	26,651	8,315	874	5,064	1,092
44X-CC, 29-30	417.82	52	117	112	1,953	289	26	342	67	3,101	3,333	2,096	25,213	8,183	457	4,738	717
45X-2, 59-60	419.74	65	83	81	1,540	225	212	277	71	4,920	2,215	1,741	20,643	7,010	3,233	4,269	883
45X-5, 125-126	424.90	60	107	104	1,761	249	112	295	66	3,956	2,466	2,294	22,953	7,227	1,558	4,360	784
45X-7, 39-40	427.04	49	97	95	1,765	239	417	281	87	3,170	3,137	2,089	22,914	6,614	5,935	4,336	1,029
46X-1, 125-126	428.50	57	106	107	1,906	290	32	351	78	4,374	3,015	2,480	24,749	7,888	454	4,859	974
46X-4, 101-102	432.76	54	101	105	1,926	273	36	329	78	3,705	2,730	2,326	26,306	8,084	774	4,718	879
46X-5, 121-122	434.46	61	106	106	1,761	264	130	337	65	5,106	3,269	2,546	23,049	7,293	1,992	4,574	783
47X-4, 115-116	442.10	56	100	113	1,993	285	45	342	77	3,890	2,676	2,364	25,362	7,612	765	4,675	890
47X-5, 128-129	443.73	56	87	103	1,797	271	111	325	72	3,902	3,139	2,294	23,368	7,370	1,917	4,776	881
48X-5, 119-120	453.04	58	80	91	1,873	285	0	346	72	6,431	1,981	1,913	24,631	7,641	0	5,055	815
49X-3, 116-119	459.23	54	100	94	2,135	345	98	380	83	3,885	3,206	2,024	27,292	8,583	1,395	5,273	983
50X-5, 118-119	471.83	68	96	117	2,271	359	150	397	73	5,602	3,097	2,748	29,203	9,003	2,138	5,518	817
51X-2, 41-42	476.26	44	87	88	2,253	323	53			3,108	2,695	2,239	28,906	8,294	773		
51X-5, 117-118	481.52	53	61	83	1,828	235	0	319	72	4,208	1,827	1,804	23,392	6,910	0	4,770	904
51X-6, 65-66	482.50	58	80	96	1,970	275	0	347	87	4,773	2,696	2,433	26,017	8,295	0	5,117	1,084
52X-4, 43-44	488.98	51	83	106	2,107	311	114	356	78	3,595	2,744	2,418	27,692	8,484	1,566	5,051	883
52X-7, 40-41	493.45	48	89	95	1,946	270	0	376	73	3,898	2,725	2,370	25,717	7,529	0	5,357	844
53X-3, 92-93	497.67	56	97	104	2,033	384	0	349	74	5,119	2,996	2,348	26,390	8,836	0	4,916	923
53X-5, 121-122	500.96	54	68	88	1,765	245	189	306	58	3,905	2,409	1,939	23,163	6,712	3,324	4,356	602

Table T4 (continued).

Core, section, interval (cm)	Depth (mbsf)	X-ray diffraction peak intensity (cps)								X-ray diffraction peak area (total counts)							
		Smectite + chlorite	Illite	Chlorite + kaolinite	(101) Quartz	Plagioclase	Calcite	(100) Quartz	(101) Cristobalite	Smectite + chlorite	Illite	Chlorite + kaolinite	(101) Quartz	Plagioclase	Calcite	(100) Quartz	(101) Cristobalite
53X-CC, 31-32	503.52	47	90	101	2,152	291	0	366	84	3,237	2,689	2,395	27,311	7,613	0	5,209	1,093
54X-2, 88-89	505.73	52	88	116	2,155	343	0	385	88	3,287	3,346	2,671	28,124	8,740	0	5,262	1,010
54X-5, 116-117	510.51	48	85	117	2,110	313	0	377	95	3,208	2,976	2,627	27,513	9,098	0	5,295	966
54X-6, 76-77	511.61	44	85	101	2,073	291	0	372	75	2,313	2,583	2,221	27,167	7,764	0	5,117	848
55X-2, 92-93	515.47	59	83	89	2,112	254	0	354	67	3,352	3,827	2,116	26,857	7,465	0	5,013	742
55X-5, 131-132	520.36	48	96	93	1,959	301	28	350	84	3,037	4,204	2,022	26,625	7,982	391	4,857	982
55X-6, 92-93	521.47	51	83	88	2,025	267	131	338	82	3,304	3,396	1,982	25,555	7,103	2,617	4,805	1,014
56X-4, 45-46	527.30	22	24	40	601	84	850	98	28	1,731	626	733	7,303	2,028	16,613	1,440	294
56X-4, 117-118	528.02	58	86	92	2,118	287	64	395	81	4,708	3,169	2,077	27,888	7,874	929	5,454	989
57X-2, 20-21	533.75	27	32	29	497	85	77	94	33	1,369	922	692	6,373	2,355	1,164	1,250	391
57X-3, 115-116	536.20	64	76	89	1,673	277	0	310	73	5,658	3,041	2,260	22,091	7,418	0	4,559	936
57X-7, 3-4	541.08	51	98	115	2,069	288	0	357	74	5,467	3,106	2,524	26,541	7,712	0	5,022	870
58X-4, 117-118	547.42	61	65	92	1,623	242	582	278	65	5,003	1,963	1,830	21,044	6,520	10,293	3,925	697
58X-6, 71-72	549.96	61	80	94	1,859	298	418	331	66	5,283	2,321	1,875	24,266	6,987	6,644	4,688	991
58X-7, 19-20	550.94	33	33	37	668	107	282	129	40	2,114	928	774	8,465	2,521	6,710	1,712	599
59X-2, 147-149	554.33	57	72	81	1,936	263	118	346	78	5,531	2,426	2,070	24,777	7,616	1,766	4,885	940
59X-4, 117-118	557.02	56	62	76	1,753	235	349	304	66	4,894	1,796	1,480	22,774	6,750	6,532	4,217	733
59X-7, 39-40	560.74	52	66	67	1,402	198	20	249	63	2,975	1,902	1,573	17,770	5,338	332	3,371	633
60X-4, 119-121	566.75	50	95	100	1,917	263	0	322	75	4,268	3,285	2,498	24,992	7,278	0	4,731	837
61X-4, 116-117	576.41	54	83	86	1,825	231	0	351	63	5,256	2,863	2,048	24,139	6,768	0	4,627	826
61X-7, 5-6	579.80	20	39	54	657	88	84	117	19	1,397	948	1,277	8,425	2,145	1,226	1,610	177
62X-2, 147-148	583.42	54	77	96	2,077	239	0	366	68	4,603	2,989	2,149	26,585	7,066	0	5,228	1,065
62X-4, 147-148	586.42	37	81	99	2,091	251	28	338	67	4,034	3,681	2,299	26,609	7,248	329	4,754	850
62X-6, 147-148	589.42	60	117	115	1,921	243	115	285	52	4,387	6,441	2,558	25,526	7,878	2,286	4,733	862
63X-1, 83-84	590.78	62	84	100	1,971	259	96	373	67	3,351	7,599	2,339	26,264	7,634	1,796	4,848	689
64X-2, 101-102	602.06	56	86	97	2,075	257	135	375	74	3,944	4,301	2,346	27,501	7,691	2,024	5,184	871
64X-4, 86-87	604.91	53	83	84	2,083	248	56	361	66	3,067	5,981	1,867	27,347	7,544	1,654	4,982	816
64X-5, 58-59	606.13	53	86	93	1,988	253	0	332	65	4,149	7,054	2,215	26,861	8,597	0	4,542	760
65X-1, 4-5	609.29	28	24	26	379	42	1,592	76	10	1,786	417	860	4,799	970	39,143	1,007	130
65X-2, 104-105	611.79	60	99	102	2,029	269	141	360	63	3,170	4,145	2,342	27,060	7,334	2,651	5,005	757
65X-3, 108-109	613.33	57	105	109	1,977	307	65	353	68	5,574	4,890	2,497	26,387	8,216	1,367	4,815	866
66X-1, 68-69	619.53	46	80	82	1,878	245	145	350	58	4,574	3,888	1,916	24,724	7,585	4,696	4,757	824
67X-1, 91-92	629.36	40	46	63	1,197	149	858	208	39	2,901	1,364	1,496	15,651	4,094	19,842	3,162	443
67X-3, 88-89	632.33	41	66	75	1,790	219	203	317	49	3,791	3,839	1,813	23,756	6,810	4,421	4,558	598
67X-4, 114-115	634.09	63	69	85	1,517	188	775	278	53	5,040	2,702	2,199	19,471	5,905	14,525	3,819	694
68X-1, 90.5-91.5	639.06	59	56	66	1,582	188	712	290	50	4,966	2,156	1,664	20,510	5,920	12,319	4,123	607
68X-3, 71-72	641.86	64	100	98	1,916	310	0	335	55	4,622	3,274	2,257	25,198	7,567	0	4,775	615
68X-6, 73-74	646.38	47	59	71	1,627	213	589	310	70	4,703	1,640	1,622	20,563	5,742	10,173	4,436	823
69X-2, 148-149	650.73	48	64	86	1,886	224	84	385	65	4,574	2,524	2,254	23,827	6,733	1,620	5,014	770
69X-4, 92-93	653.17	58	88	91	1,886	227	168	346	61	3,820	4,212	2,167	24,494	6,723	3,091	4,665	805
70X-1, 118-119	658.63	48	55	82	1,636	172	354			3,142	2,615	1,916	21,318	6,000	7,190		
70X-CC, 32-33	663.47	26	20	22	323	44	857	62	22	970	418	639	3,835	1,011	23,252	727	332
71X-4, 118.5-119.5	672.84	34	40	45	774	96	1,034	148	24	1,939	1,124	985	9,886	2,626	21,096	1,959	216
72X-1, 124-126	678.00	47	69	76	1,774	213	85	311	79	3,343	2,347	1,803	23,045	6,420	2,011	4,443	879
73X-1, 117-119	687.53	93	58	61	1,685	197	0	301	55	8,243	1,856	1,456	22,865	6,195	0	4,581	715
73X-2, 86-88	688.72	83	49	53	1,858	214	0	315	63	8,142	1,775	1,322	27,215	6,490	0	5,676	902

Note: This table is also available in ASCII format.

Table T5. Normalized relative mineral abundances based on X-ray diffraction analysis of random bulk-sediment powders, Site 1173. (See table note. Continued on next two pages.)

Unit	Core, section, interval (cm)	Depth (mbsf)	Total clay minerals	Quartz	Plagioclase	Calcite	Peak area ratio: (101) Cristobalite/ (100) Quartz
	190-1173A-						
	1H-1, 134-135	1.35	46	35	17	2	0.42
	1H-2, 133-134	2.84	51	33	16	0	0.37
	1H-3, 110-111	4.11	46	35	17	2	0.47
	1H-4, 135-136	5.86	47	36	17	1	0.30
	1H-5, 77-78	6.78	47	37	16	0	0.41
	2H-2, 139-140	10.04	50	32	14	3	0.46
	2H-2, 139-140	10.04	47	36	16	2	
	2H-4, 139-140	13.04	45	37	16	2	0.41
	2H-6, 139-140	16.04	49	37	14	0	0.33
	3H-2, 138-139	19.53	47	38	15	0	0.32
	3H-2, 138-139	19.53	44	37	17	2	
	3H-4, 134-135	22.49	46	36	18	1	0.44
	3H-5, 138-139	24.03	48	37	16	0	0.39
	3H-5, 138-139	24.03	44	37	17	2	
	4H-3, 101-102	28.90	46	35	18	1	0.40
	4H-3, 134-135	29.23	40	38	22	0	0.41
I	4H-6, 135-136	33.74	50	34	16	1	0.41
	5H-3, 131-132	39.96	46	37	17	0	0.33
	5H-5, 127-128	42.92	46	34	19	1	0.32
	6H-1, 114-115	46.29	46	37	17	0	0.42
	6H-2, 49-50	47.14	42	29	12	17	0.43
	7H-4, 129-130	60.44	48	36	15	0	0.38
	7H-7, 47-48	64.12	46	32	20	2	0.54
	8H-1, 52-53	64.67	42	37	18	2	0.35
	8H-4, 131-133	69.97	48	34	17	1	0.35
	9H-4, 132-133	79.47	43	37	18	2	0.46
	9H-5, 53-54	80.18	44	32	20	3	0.48
	9H-5, 53-54	80.18	45	32	20	3	
	10H-2, 105-106	85.70	49	34	17	0	0.53
	10H-4, 123-124	88.88	49	35	16	0	0.47
	10H-6, 105-106	91.76	49	34	16	2	0.43
	11H-4, 111-112	98.26	48	34	16	2	0.38
	Mean Unit I:		46	35	17	2	0.41
	12H-4, 46-47	107.11	47	35	18	0	0.50
	12H-4, 134-135	107.99	48	38	13	1	0.29
	13H-4, 82-83	116.97	49	37	14	0	0.36
	13H-4, 131-132	117.46	50	35	15	0	0.42
	14H-1, 103-104	122.18	50	35	14	0	0.31
	14H-3, 131-132	125.46	54	32	13	0	0.42
	14H-5, 102-103	128.17	47	34	15	4	0.48
	15H-2, 94-95	133.09	50	33	14	3	0.49
	15H-4, 132-133	136.47	40	27	11	21	0.34
	15H-5, 58-59	137.23	39	30	13	18	0.39
	15H-5, 103-104	137.68	41	31	14	14	0.86
	16H-4, 92-94	145.58	49	33	12	6	0.30
	16H-6, 48-50	148.14	49	34	14	3	0.36
	17H-4, 132-133	155.47	35	29	11	24	0.31
II	17H-4, 132-133	155.47	35	29	12	25	
	18H-4, 132-133	164.97	51	33	15	2	0.41
	18H-6, 15-16	166.80	40	33	20	7	1.10
	18H-6, 129-130	167.94	50	30	13	7	0.39
	19H-4, 132-133	174.47	51	36	13	0	0.28
	20H-2, 134-135	180.99	49	35	14	2	0.33
	20H-2, 134-135	180.99	50	36	14	1	
	20H-4, 132-133	183.97	39	29	13	19	0.41
	20H-4, 132-133	183.97	39	30	13	19	
	20H-5, 130-131	185.45	39	29	11	21	0.32
	20H-5, 130-131	185.45	40	30	14	17	
	21H-2, 69-70	189.84	51	35	12	2	0.36
	21H-2, 69-70	189.84	51	33	12	4	
	21H-4, 108-109	193.23	48	33	12	7	0.27
	21H-4, 108-109	193.23	47	31	13	9	
	21H-6, 67-68	195.82	42	33	16	9	0.46

Table T5 (continued).

Unit	Core, section, interval (cm)	Depth (mbsf)	Normalized relative mineral abundance (wt%)				Peak area ratio: (101) Cristobalite/ (100) Quartz
			Total clay minerals	Quartz	Plagioclase	Calcite	
	21H-6, 67-68	195.82	43	33	15	9	
	22H-3, 131-132	201.46	42	30	11	17	0.46
	22H-3, 131-132	201.46	44	28	12	17	
	22H-5, 95-96	204.10	46	35	14	5	0.44
	22H-5, 95-96	204.10	46	35	13	5	
	23H-3, 134-135	210.99	40	34	13	13	0.37
	23H-3, 134-135	210.99	41	32	12	14	
	23H-3, 134-135	210.99	40	33	13	15	
	23H-5, 136-137	214.01	47	37	16	0	0.41
	23H-5, 136-137	214.01	49	36	15	0	
	24H-1, 127-128	217.42	40	31	13	16	0.47
	24H-1, 127-128	217.42	40	31	13	17	
	24H-2, 132-133	218.97	50	37	13	0	0.56
	24H-2, 132-133	218.97	49	37	15	0	
	24H-5, 131-132	223.46	46	37	17	0	0.43
	24H-5, 131-132	223.46	49	35	17	0	
	25X-1, 123-124	226.88	37	31	13	18	0.58
	25X-1, 123-124	226.88	37	31	13	18	
	25X-1, 123-124	226.88	37	30	13	20	
	25X-4, 128-129	231.43	41	30	22	7	0.49
	25X-4, 128-129	231.43	41	29	22	8	
	25X-6, 124-125	234.39	43	32	14	12	0.49
	25X-6, 124-125	234.39	42	32	14	12	
	25X-6, 124-125	234.39	45	31	13	11	
II	26X-2, 34-35	237.09	47	38	14	0	0.43
	26X-2, 34-35	237.09	47	39	15	0	
	26X-2, 34-35	237.09	47	37	14	1	
	26X-6, 125-126	244.00	42	29	10	18	0.39
	27X-2, 104-105	247.49	41	31	13	15	0.45
	27X-5, 114-115	252.09	41	32	15	12	0.47
	28X-5, 114-115	261.69	44	32	15	9	
	29X-3, 141-142	268.46	28	22	13	37	0.68
	29X-4, 117-118	269.72	48	33	11	8	0.45
	30X-3, 119-120	277.84	47	35	16	2	0.40
	31X-1, 131-132	284.56	48	31	12	9	0.59
	31X-3, 124-125	287.49	41	36	18	6	0.39
	32X-3, 96-97	296.91	49	37	14	0	0.41
	32X-6, 134-135	301.79	44	32	17	7	0.46
	33X-1, 122-123	303.87	44	42	14	0	0.88
	34X-4, 116-117	317.61	46	31	13	11	0.38
	34X-5, 56-57	318.51	42	33	17	9	0.29
	34X-CC, 18-19	321.57	48	38	13	2	0.35
	35X-2, 141-142	324.46	40	37	15	7	0.45
	35X-3, 149-150	326.04	42	38	14	5	0.33
	35X-5, 106-107	328.61	44	34	13	8	0.37
	36X-4, 91-92	336.56	46	34	10	9	0.37
	36X-6, 35-36	339.00	45	32	10	14	0.28
	36X-CC, 19-20	340.15	48	33	12	7	0.40
	Mean Unit II:		44	33	14	9	0.44
	37X-4, 124-125	346.49	51	35	12	2	0.27
	37X-5, 128-129	348.03	58	34	8	0	
	37X-6, 40-41	348.65	55	34	10	1	0.23
	38X-3, 4-5	353.39	54	33	10	3	0.22
	38X-5, 116-117	357.51	53	37	11	0	0.21
	38X-CC, 23-24	360.03	55	36	9	0	0.21
	39X-2, 114-115	362.59	53	37	10	0	0.25
	39X-5, 137-138	367.32	55	33	11	1	0.29
III	40X-5, 115-116	376.80	53	36	11	1	0.24
	41X-4, 109-110	384.84	54	35	8	3	0.21
	41X-7, 32-33	388.57	54	37	9	0	0.19
	42X-2, 118-119	391.53	58	35	7	0	0.35
	42X-3, 118-119	393.03	52	35	10	4	0.27
	42X-7, 27-28	398.12	58	36	7	0	0.20
	43X-3, 118-119	402.63	55	37	8	0	0.23
	43X-5, 87-88	405.32	52	32	7	9	0.22
	44X-4, 115-116	413.70	55	34	11	0	0.22
	44X-CC, 29-30	417.82	57	33	10	0	0.15

Table T5 (continued).

Unit	Core, section, interval (cm)	Depth (mbsf)	Normalized relative mineral abundance (wt%)				Peak area ratio: (101) Cristobalite/ (100) Quartz
			Total clay minerals	Quartz	Plagioclase	Calcite	
	45X-2, 59-60	419.74	54	33	8	4	0.21
	45X-5, 125-126	424.90	55	35	9	0	0.18
	45X-7, 39-40	427.04	52	29	8	11	0.24
	46X-1, 125-126	428.50	57	34	9	0	0.20
	46X-4, 101-102	432.76	54	36	10	0	0.19
	46X-5, 121-122	434.46	60	32	8	1	0.17
	47X-4, 115-116	442.10	55	36	9	0	0.19
	47X-5, 128-129	443.73	58	32	9	1	0.18
	48X-5, 119-120	453.04	55	38	7	0	0.16
	49X-3, 116-119	459.23	56	35	10	0	0.19
	50X-5, 118-119	471.83	56	35	9	1	0.15
	51X-2, 41-42	476.26	51	38	11	0	
	51X-5, 117-118	481.52	52	39	9	0	0.19
	51X-6, 65-66	482.50	55	36	9	0	0.21
	52X-4, 43-44	488.98	53	37	10	0	0.18
	52X-7, 40-41	493.45	55	36	9	0	0.16
	53X-3, 92-93	497.67	56	34	9	0	0.19
	53X-5, 121-122	500.96	53	34	8	5	0.14
	53X-CC, 31-32	503.52	53	37	10	0	0.21
	54X-2, 88-89	505.73	55	34	11	0	0.19
	54X-5, 116-117	510.51	53	35	12	0	0.18
	54X-6, 76-77	511.61	50	38	12	0	0.17
	55X-2, 92-93	515.47	59	32	9	0	0.15
	55X-5, 131-132	520.36	60	30	9	0	0.20
	55X-6, 92-93	521.47	56	32	9	3	0.21
	56X-4, 45-46	527.30	26	17	4	52	0.20
	56X-4, 117-118	528.02	57	35	8	0	0.18
	57X-2, 20-21	533.75	57	29	9	5	0.31
	57X-3, 115-116	536.20	61	32	7	0	0.21
	57X-7, 3-4	541.08	58	35	7	0	0.17
	58X-4, 117-118	547.42	46	30	7	18	0.18
III	58X-6, 71-72	549.96	50	33	7	10	0.21
	58X-7, 19-20	550.94	43	26	5	26	0.35
	59X-2, 147-149	554.33	56	36	8	0	0.19
	59X-4, 117-118	557.02	47	34	7	11	0.17
	59X-7, 39-40	560.74	55	36	9	0	0.19
	60X-4, 119-121	566.75	59	33	8	0	0.18
	61X-4, 116-117	576.41	59	35	7	0	0.18
	61X-7, 5-6	579.80	54	33	7	5	0.11
	62X-2, 147-148	583.42	57	36	7	0	0.20
	62X-4, 147-148	586.42	59	33	8	0	0.18
	62X-6, 147-148	589.42	70	23	7	0	0.18
	63X-1, 83-84	590.78	73	20	7	0	0.14
	64X-2, 101-102	602.06	61	31	8	1	0.17
	64X-4, 86-87	604.91	67	25	8	0	0.16
	64X-5, 58-59	606.13	70	22	7	0	0.17
	65X-1, 4-5	609.29	16	9	2	72	0.13
	65X-2, 104-105	611.79	59	30	8	2	0.15
	65X-3, 108-109	613.33	64	29	7	0	0.18
	66X-1, 68-69	619.53	58	29	7	6	0.17
	67X-1, 91-92	629.36	32	22	5	41	0.14
	67X-3, 88-89	632.33	58	29	7	6	0.13
	67X-4, 114-115	634.09	46	24	5	24	0.18
	68X-1, 90.5-91.5	639.06	45	28	6	21	0.15
	68X-3, 71-72	641.86	59	33	8	0	0.13
	68X-6, 73-74	646.38	44	31	6	19	0.19
	69X-2, 148-149	650.73	56	36	8	0	0.15
	69X-4, 92-93	653.17	61	29	7	3	0.17
	70X-1, 118-119	658.63	49	29	8	15	
	70X-CC, 32-33	663.47	17	10	3	70	0.46
	71X-4, 118.5-119.5	672.84	28	17	4	51	0.11
	72X-1, 124-126	678.00	53	36	9	2	0.20
	73X-1, 117-119	687.53	58	37	4	0	0.16
	Mean Unit III:		54	32	8	6	0.19
IV	73X-2, 86-88	688.72	56	40	5	0	0.16

Note: This table is also available in **ASCII** format.

Table T6. Results of X-ray diffraction analysis of bulk-powder volcanic ash samples, Hole 1173A.

Core, section, interval (cm)	Depth	X-ray diffraction peak intensity (cps)												X-ray diffraction peak area (total counts)											
		Smectite	Illite	Chlorite	Clinoptilite	Hornblende	Cristobalite	Quartz	Plagioclase	Calcite	Pyroxene	Halite	Pyrite	Smectite	Illite	Chlorite	Clinoptilite	Hornblende	Cristobalite	Quartz	Plagioclase	Calcite	Pyroxene	Halite	Pyrite
190-1173A-																									
1H-3, 41-45	3.45	0	19	33	0	0	45	443	147	15	0	103	0	0	642	598	0	0	800	7,393	3,482	291	0	1,807	0
5H-1, 35-39	36.03	0	0	0	0	0	60	185	272	21	39	201	0	0	0	0	0	0	1,091	2,233	4,737	415	614	2,955	0
10H-6, 132-135	92.05	48	71	122	0	55	142	1,413	1,202	81	61	173	19	1,677	1,548	2,006	0	743	2,249	17,273	16,733	984	1,205	3,520	179
11H-5, 112-118	99.82	48	89	80	0	47	78	1,124	1,640	39	106	235	23	1,895	1,633	1,509	0	745	1,308	13,719	33,768	407	1,619	4,069	263
12H-2, 133-135	104.99	0	0	0	0	0	105	173	629	0	29	196	0	0	0	0	0	0	1,768	2,273	10,081	0	416	3,078	0
12H-6, 9-13	109.77	20	0	0	0	0	72	97	226	0	20	183	0	1,310	0	0	0	0	1,132	1,364	5,354	0	450	2,725	0
17H-5, 57-61	156.25	23	0	0	0	0	72	253	258	54	32	114	0	1,107	0	0	0	0	1,420	3,650	5,907	975	555	1,658	0
19H-1, 91-94	169.58	0	0	0	0	0	53	203	97	18	0	139	0	0	0	0	0	0	988	2,368	2,428	319	0	1,942	0
26X-1, 122-125	236.49	25	0	0	0	0	43	259	81	0	0	220	40	1,225	0	0	0	0	933	3,286	2,495	0	0	2,739	530
34X-7, 8-11	321.05	23	0	0	0	0	42	176	314	50	0	173	30	1,739	0	0	0	0	845	2,344	4,526	822	0	2,251	446
37X-3, 0-3	343.77	98	0	0	0	0	59	96	163	0	52	73	109	12,810	0	0	0	0	1,353	1,548	5,198	0	1,012	1,386	1,499
39X-1, 101-104	360.98	60	0	0	0	0	46	60	159	0	23	15	91	9,836	0	0	0	0	1,011	1,667	7,569	0	626	116	1,994
41X-6, 28-32	387.06	58	0	0	0	0	89	158	331	61	46	38	19	8,186	0	0	0	0	2,123	3,257	15,813	1,363	1,373	901	217
45X-1, 16-17	417.81	91	0	0	0	0	41	63	0	0	0	0	28	16,266	0	0	0	0	753	1,326	0	0	0	0	446
64X-4, 28-29	604.33	88	0	0	0	0	0	75	0	0	0	0	53	11,356	0	0	0	0	0	1,251	0	0	0	0	732
73X-2, 78-81	688.65	46	37	33	0	0	56	1,421	180	0	0	0	0	3,622	1,544	901	0	0	766	20,249	5,805	0	0	0	0

Table T7. Structural data, Hole 1173A. (**See table note.** Continued on next four pages.)

Core, section, interval (cm)	Depth (mbsf)	Cr az. (°)	Cr dip (°)	Cr line	Pm az.	Identifier	Notes
190-1173-							
1H	0	0	0			Bed	
2H	7.14	0	0			Bed	
3H	16.64	0	0			Bed	
4H	26.14	0	0			Bed	
5H	35.64	0	0			Bed	
6H	45.14	0	0			Bed	
7H	54.64	0	0			Bed	
8H-6, 50-50	72.14	203	90			Cleavage	Coring induced?
8H	64.14	0	0			Bed	
9H-1	73.64	0	0			Bed	
9H-2, 106-126	76.20	221	90			Cleavage	Coring induced?
9H-2, 126-128	76.40	180	90			Cleavage	Coring induced?
10H	83.14	0	0			Bed	
11H-3, 31-32	95.95	233	28			Bed	
11H-4, 9-13	97.23	180	31			Bed	
11H-5	98.64	0	0			Bed	
11H-6	100.14	0	0			Bed	
11H-7	101.64	0	0			Bed	
12H	102.14	0	0			Bed	
13H-1	111.64	0	0			Bed	
13H-2	113.14	0	0			Bed	
13H-3, 144-145	116.08	180	11			Bed	
13H-4	116.14	0	0			Bed	
13H-5	117.64	0	0			Bed	
13H-6	119.14	0	0			Bed	
14H	121.14	0	0			Bed	
15H	130.64	0	0			Bed	
16H	140.14	0	0			Bed	
17H	149.64	0	0			Bed	
18H	159.14	0	0			Bed	
19H-1	168.64	0	0			Bed	
19H-2	170.14	0	0			Bed	
19H-3, 100-105	172.64	0	22			Bed	
19H-4	173.14	0	0			Bed	
19H-5	174.64	0	0			Bed	
19H-6	176.14	0	0			Bed	
19H-7	177.64	0	0			Bed	
20H	178.14	0	0			Bed	
21H	187.64	0	0			Bed	
22H	197.14	0	0			Bed	
23H-1, 131-133	207.95	0	15			Bed	
23H-2, 85-87	208.99	331	18			Bed	
23H-3	209.64	0	0			Bed	
23H-4	211.14	0	0			Bed	
23H-5	212.64	0	0			Bed	
23H-6	214.14	0	0			Bed	
23H-7	215.64	0	0			Bed	
24H	216.14	0	0			Bed	
25X	225.64	0	0			Bed	
26X	235.24	0	0			Bed	
27X-1	244.94	0	5			Bed	
27X-2	246.44	0	0			Bed	
27X-3	247.94	0	78			Normal fault	1-cm displacement
27X-4	249.44	0	0			Bed	
27X-5	250.94	0	0			Bed	
27X-6	252.44	0	0			Bed	
27X-7	253.94	0	5			Bed	
28X	254.54	0	0			Bed	
28X-1, 141-144	255.95	284	80			Reverse fault	4-mm displacement
28X-7, 37-42	263.91	180	62			Normal fault	2-mm displacement
28X-6, 27-33	262.31	192	64			Normal fault	
29X-1, 0-9	264.04	176	80			Fault	Zone of anastomosing small faults
29X-1, 0-9	264.04	166	61			Fault	Zone of anastomosing small faults
29X-1, 57-65	264.61	149	90			Fault	3-mm displacement on small faults
29X-1, 76-80	264.80	180	60			Normal fault	1-cm displacement
29X-1, 76-80	264.80	180	90			Normal fault	1-cm displacement
29X-2, 69-75	266.23	243	79			Fault	
29X-3, 2-9	267.06	321	58			Normal fault	1-cm displacement

Table T7 (continued).

Core, section, interval (cm)	Depth (mbsf)	Cr az. (°)	Cr dip (°)	Cr line	Pm az.	Identifier	Notes
29X-1, 80-85	264.84	210	61			Normal fault	1.5-cm displacement
29X	264.04	0	0			Bed	
30X	273.64	0	0			Bed	
31X	283.24	0	0			Bed	
32X	292.94	0	0			Bed	
33X-1	302.64	0	0			Bed	
33X-2	304.14	0	0			Bed	
33X-3	305.64	0	0			Bed	
33X-4, 111-123	308.25	270	90			Normal fault	Zone of anastomosing small faults
33X-5, 0-5	308.64	270	90			Vertical fault	4-mm displacement
33X-5, 15-18	308.79	270	90			Fault	
33X-5, 62-64	309.26	270	90			Subvertical fault	3-mm displacement
33X-6, 14-20	310.28	206	53			Normal fault	5-mm displacement
34X	311.94	0	0			Bed	
35X	321.54	0	0			Bed	
36X-1	331.14	0	0			Bed	
36X-2	332.64	0	0			Bed	
36X-3, 150-151	335.64	0	4			Bed	
36X-4	335.64	0	0			Bed	
36X-5	337.14	0	0			Bed	
36X-6	338.64	0	0			Bed	
36X-CC, 0-18	339.95	213	64			Normal fault	
36X-CC, 0-18	339.95	219	69			Normal fault	
36X-CC, 30-36?	340.25	260	85			Fault	
37X-1 TO 6	340.74	0	0			Bed	
37X-7, 39-41	350.13	42	29			Fault	
38X	350.34	0	0			Bed	
39X	359.94	0	0			Bed	
39X-4, 46-60	364.90	150	74			Normal fault	1.5-cm displacement
40X-1	369.64	0	0			Bed	
40X-2	371.14	0	0			Bed	
40X-3, 100-150	373.64					Fractured zone	Steeply plunging slickenlines on discrete surfaces: coring induced?
40X-4, 0-10	374.14					Fractured zone	Steeply plunging slickenlines on discrete surfaces: coring induced?
40X-3, 0-100	372.64	0	0			Bed	
40X-3, 110-115	373.74			45		Slickenlines	Coring induced
40X-3, 119-123	373.83			90		Slickenlines	Coring induced
40X-3, 124-126	373.88			150		Slickenlines	Coring induced
40X-4, 12-47	374.26	162	16		202	Bed	
40X-4, 47-57	374.61	148	29			Bed	
40X-4, 96-109	375.10	0	25		135	Bed	
40X-4, 110-116	375.24	180	36		127	Bed	
40X-4, 116-136	375.30	195	19			Bed	
40X-5, 1-36	375.65	202	18			Bed	
40X-5, 37-48	376.01	0	10		141	Bed	
40X-5, 49-116	376.13	180	10		175	Bed	
40X-6, 1-33	377.15	218	25		178	Bed	
40X-6, 34-56	377.48	0	7			Bed	
40X-7, 1-35	378.65	229	22			Bed	
40X-CC, 1-35	379.11	0	0			Bed	
40X-7, 24-32	378.88	354	74			Color front	Unclear feature: fluid escape?
41X-1, 44-45	379.68	69	19			Bed	Isolated *Zoophycos*
41X-1, 90-95	380.14	186	52			Bed	
41X-1, 97-98	380.21	205	16			Bed	
41X-2, 29	381.03	207	7			Bed	
41X-2, 54	381.28	132	13			Bed	
41X-2, 74	381.48	220	18			Bed	
41X-2, 86-88	381.60	15	23		183	Bed	
41X-2, 100-102	381.74	118	25			Bed	
41X-3, 17	382.41	319	22			Bed	
41X-3, 104	383.28	177	2			Bed	
41X-3, 123	383.47	244	24			Bed	
41X-4, 29	384.03	45	8			Bed	
41X-4, 105	384.79	63	4			Bed	
41X-5, 27	385.51	208	12			Bed	
41X-5, 106	386.30	0	6			Bed	
41X-6, 34	387.08	338	13		48	Bed	Base of ash layer
41X-6, 113	387.87	252	6			Bed	
41X-7, 23	388.47	327	5			Bed	
41X-3, 22-70	382.46					Fractured zone	Steeply plunging slickenlines on discrete surfaces: coring induced?

Table T7 (continued).

Core, section, interval (cm)	Depth (mbsf)	Cr az. (°)	Cr dip (°)	Cr line	Pm az.	Identifier	Notes
41X-4, 46-50	384.20					Fractured zone	Steeply plunging slickenlines on discrete surfaces: coring induced?
42X-1, 61-63	389.45	163	10			Bed	
42X-1, 102-103	389.86	244	9			Bed	
42X-2, 26-32	390.60	327	18			Bed	
42X-3, 47	392.31	0	0			Bed	
42X-4, 23-27	393.57	180	16		181	Bed	
42X-4, 65-71	393.99	199	15			Bed	
42X-4, 72-80	394.06	0	20			Bed	
42X-5, 61-64	395.45	180	10			Bed	
42X-5, 66-70	395.50	0	5			Bed	
42X-5, 115-121	395.99	0	15		140	Bed	
42X-6, 138-139	397.72	146	7			Bed	
43X-1	398.44	0	0			Bed	
43X-2, 145-150	401.39	180	10			Bed	
43X-3, 24-30	401.68	0	14			Bed	
43X-3, 90-98	402.34	0	8			Bed	
43X-4, 11-19	403.05	180	14		212	Bed	
43X-5	404.44	0	0			Bed	
43X-6, 78-81	406.72	195	64			Normal fault	
44X-1, 71-72	408.75	0	9			Bed	
44X-1, 99-100	409.03	180	5			Bed	
44X-2, 125-127	410.79	225	14		224	Bed	
44X-3	411.04	0	0			Bed	
44X-4, 40-42	412.94	180	15			Bed	
44X-4, 76-78	413.30	16	18			Bed	
44X-5, 37-38	414.41	180	11			Bed	
44X-6, 146-147	417.00	116	9		191	Bed	
44X-2	409.50	0	0			Bed	
44X-3	410.00	0	0			Bed	
44X-4	408.04	0	0			Bed	
44X-5, 112-113	415.16	0	7			Bed	
44X-6	416.00	0	0			Bed	
44X-7	418.00	0	0			Bed	
44X-CC	419.00	0	0			Bed	
45X-5, 112-113	424.76	0	7			Bed	
45X-1	424.00	0	0			Bed	
45X-2	425.00	0	0			Bed	
45X-3	426.00	0	0			Bed	
45X-4	427.00	0	0			Bed	
46X-1, 79-82	428.03	158	58			Fault	Slickenlines 9× from core face >180
46X-3, 104-105	431.28	270	10			Bed	Apparent dip only
47X-2, 120-152	439.14					Foliated breccia	1.5-mm elongated fragments, slickensided
47X-3, 0-24	439.44					Foliated breccia	1.5-mm elongated fragments, slickensided
47X-5, 58-59	443.02	3	17			Bed	
47X-7, 7-9	445.51	24	24			Bed	
47X-7, 31-33	445.75	146	23		199	Bed	
48X-1, 50-52	446.34	169	25			Bed	
48X-1, 93-93	446.77	90	6		194	Bed	
48X-2, 33-33	447.67	315	10			Bed	
48X-2, 128-128	448.62	270	4			Bed	
48X-3, 30-31	449.14	302	13		156	Bed	
48X-4, 86-86	451.20	204	10			Bed	
48X-5, 14-14	451.98	340	12			Bed	
48X-6, 111-112	454.45	40	15		10	Bed	
48X-2, 98-99	448.32	119	32			Fault?	Slickensided, curviplanar surface
48X-2, 98-99	448.32			204		Slick	Slickenlines on above surface
48X-3, 104-106	449.88			209		Slick	Lineation
48X-3, 106-107	449.90	80	65			Fault?	Slickensided curviplanar surface
48X-3, 106-107	449.90			201		Slick	Slickenlines on above surface
48X-2, 80-80	448.14			198		Slick	
49X-1, 56-57	455.60	0	2			Bed	
49X-1, 103-104	456.07	304	19			Bed	
49X-2, 75-76	457.29	58	25			Bed	
49X-3, 14-14	458.18	351	12		243	Bed	
49X-4, 70-70	460.24	139	11		287	Bed	
49X-5, 82-82	461.86	122	19			Bed	
49X-6, 38-38	462.92	119	16		229	Bed	
49X-7, 10-13	464.14	0	11			Bed	
50X-4, 91-93	470.05	336	12			Bed	

Table T7 (continued).

Core, section, interval (cm)	Depth (mbsf)	Cr az. (°)	Cr dip (°)	Cr line	Pm az.	Identifier	Notes
50X-5, 12-14	470.76	341	15		236	Bed	
50X-6, 17-18	472.31	29	18			Bed	
50X-5, 72-76	471.36	327	18			Bed	
51X-1, 92-92	475.26	187	16		227	Bed	
51X-3, 114-116	478.48	26	13			Bed	
51X-5, 44-44	480.78	78	9		330	Bed	
51X-5, 106-107	481.40	24	14		340	Bed	
51X-7, 19-20	483.53	288	13		352	Bed	
52X-1, 0-150	484.04	0	0			Bed	
52X-2, 19-20	485.73	192	14		337	Bed	
52X-2, 118-121	486.72	194	20			Bed	
52X-3, 57-62	487.61	20	20		220	Bed	
52X-4, 4-22	488.58	0	18			Bed	
52X-5, 142-152	491.46					Microbreccia	Clay clasts in black matrix
52X-6, 114-121	492.68	317	25		315	Bed	
52X-6, 61-65	492.15	149	46			Fault	Slickensided
52X-6, 66-71	492.20	211	44			Fault	Healed, with adjacent microbreccia; same block as above
53X-1, 36-43	494.10	225	21			Bed	
53X-1, 94-98	494.68	313	20			Bed	
53X-1, 115-124	494.89	37	16			Bed	
53X-2, 52-59	495.76	344	27		254	Bed	
53X-4, 121-133	499.45	139	22		233	Bed	
54X-3, 122-129	507.56	38	11		147	Bed	
54X-4, 22-30	508.06	180	21		90	Bed	
54X-5, 54-65	509.88	238	29		329	Bed	
55X-1, 33-39	513.37	195	15		289	Bed	
55X-1, 127-136	514.31	48	32		328	Bed	
55X-5, 74-80	519.78	146	11		308	Bed	
56X-1, 133-140	523.67	121	12		247	Bed	
56X-4, 46-57	527.30	180	5		320	Bed	
57X-3, 67-70	535.71	338	13			Bed	
57X-5, 133-140	539.37	180	8			Bed	
58X-2, 109-109	544.33	131	9			Bed	
58X-3, 17-17	544.91	246	10			Bed	
58X-4, 111-111	547.35	116	27		10	Bed	
58X-7, 7-7	550.81	243	23		123	Bed	
59X-1, 26-26	551.60	198	9			Bed	
59X-3, 119-119	555.53	343	10		23	Bed	
59X-4, 13-14	555.98	127	16		27	Bed	
59X-5, 138-138	558.72	141	14		332	Bed	
60X-2, 19-19	562.73	90	8			Bed	Apparent dip only
60X-4, 94-94	566.48	270	6			Bed	Apparent dip only
61X-3, 30-30	574.04	239	6			Bed	
61X-6, 148-149	579.73	327	14			Bed	
61X-4, 61-78	576.02	90	39			Fold	Slump; apparent dip of fold axial plane in core face, but clearly a noncylindrical fold
62X	589.90						No bedding
63X	591.14						No bedding
64X	608.66						No bedding
65X-1, 84-86	610.10	120	8			Bed	
65X-3, 0-6	612.30	202	11			Bed	
65X-4, 120-125	614.99	132	29			*Zoophycos*	
65X-CC, 30-36	616.66	228	41			Bed	Contact between carbonate and claystone
65X-CC, 30-36	616.66	90	59			Dark vein	Apparent dip only
65X-CC, 30-36	616.66	228	41			White vein	
65X-CC, 30-36	616.66	319	90			White vein	
65X-CC, 30-36	616.66	335	90			White vein	
65X-CC, 30-36	616.66	344	90			White vein	
65X-CC, 30-36	616.66	330	90			White vein	
66X	620.48						No bedding; clasts slickensided
67X-1, 50-51	628.95	227	24			Aligned *Zoophycos*	
67X-5, 63-72	635.16	219	27			Aligned *Zoophycos*	
67X-5, 35-44	634.88	74	21			Aligned *Zoophycos*	
68X	646.41						No bedding
69X-4, 60-65	652.89	11	10			Bed	
69X-5, 78-92	654.66	344	72			Fault	
70X-1, 23-23	657.67	338	13			Bed	
70X-2, 73-73	659.67	41	14			Bed	
70X-2, 88-88	659.82	270	2			Bed	

Table T7 (continued).

Core, section, interval (cm)	Depth (mbsf)	Cr az. (°)	Cr dip (°)	Cr line	Pm az.	Identifier	Notes
71X-3, 66-67	670.81	346	8			Bed	
71X-3, 31-31	670.45	63	4			Bed	
72X-1, 62-62	677.36	229	9			Bed	
72X-1, 5-7	676.81	135	11			Bed	
73X-1, 63.5-65	686.99					White vein	Small (5 mm long) veins between more or less greenish claystones
74X	696.47						No bedding
75X-CC, 3-3	705.67	228	12			Bed	
76X	715.34						No bedding
77X	724.64						No bedding

Note: Cr az. = azimuth of plane in core reference frame, Cr dip = dip of plane in core and paleomagnetic reference frame, Cr line = plunge of line in core and paleomagnetic reference frame, Pm az. = azimuth of plane in paleomagnetic reference frame. This table is also available in ASCII format.

Table T8. Nannofossil events recognized, Site 1173.

Nannofossil zones	Datum events	Age (Ma)	Depth (mbsf)	Average sedimentation rate* (m/m.y.)
NN21b	FAD *Emiliania huxleyi* acme	0.085	55.26 ± 9.38	506.9
NN21a	FAD *Emiliania huxleyi*	0.26	118.39 ± 0.53	
NN20	LAD *Pseudoemiliania lacunosa*	0.46	128.56 ± 2.17	
	LAD *Reticulofenestra asanoi*	0.8	175.32 ± 2.83	
	FAD *Reticulofenestra asanoi*	1.06	203.44 ± 2.55	
	LAD *Helicosphaera sellii*	1.25	208.92 ± 2.93	82.9
	FAD *Gephyrocapsa oceanica*	1.8	237.99 ± 2.65	
NN19	LAD *Discoaster brouweri*	1.95	262.84 ± 1.65	
NN18	LAD *Discoaster pentaradiatus*	2.52	286.99 ± 1.50	
NN17	LAD *Discoaster surculus*	2.55	286.99 ± 1.50	
NN16	LAD *Reticulofenestra pseudoumbilicus* (>7 µm)	3.75	384.35 ± 0.22	
NN15	LAD *Amaurolithus* spp.	4.0	392.59 ± 1.50	
NN12	LAD *Discoaster quinqueramus*	5.54	406.43 ± 1.24	
NN11b	FAD *Amaurolithus primus*	7.2	447.21 ± 0.86	
NN11a	FAD *Discoaster quinqueramus*	8.6	478.31 ± 3.75	
NN10b	LAD *Reticulofenestra pseudoumbilicus* (>7 µm)	9.0	490.50 ± 8.44	
NN10a	LAD *Discoaster hamatus*	9.63	515.84 ± 7.06	33.6
NN9	FAD *Discoaster hamatus*	10.7	539.62 ± 2.33	
NN8	FAD *Catinaster coalitus*	10.9	549.34 ± 2.33	
NN7	FAD *Discoaster kugleri*	11.8	575.75 ± 14.55	
NN6	LAD *Sphenolithus heteromorphus*	13.6	646.35 ± 10.07	
	LAD *Helicosphaera waltrans*	14.0	720.62 ± 4.90	
	LAD *Discoaster musicus*	14.1	720.62 ± 4.90	

Notes: FAD = first appearance datum, LAD = last appearance datum. * = uncorrected for compaction.

Table T9. Interval and depth constraints of calcareous nannofossil events, Hole 1173A.

Event		Interval (cm)		Depth (mbsf)	
		Top	Bottom	Top	Bottom
		190-1173A-	190-1173A-		
B	*Emiliania huxleyi* acme	6H-1, 75-76	7H-4, 75-76	45.88	64.64
B	*Emiliania huxleyi*	13H-4, 75-76	13H-6, 75-76	116.89	119.89
T	*Pseudoemiliania lacunosa*	14H-4, 75-76	14H-CC	126.39	130.73
T	*Reticulofenestra asanoi*	19H-3, 75-76	19H-CC	172.39	178.25
B	*Reticulofenestra asanoi*	21H-CC	22H-3, 75-76	187.33	200.89
T	*Helicosphaera sellii*	22H-CC	23H-4, 70-71	205.99	211.84
B	*Gephyrocapsa oceanica*	25X-CC	26X-4, 96-97	235.33	240.70
T	*Discoaster brouweri*	28X-4, 71-72	28X-CC	259.75	264.48
T	*Discoaster pentaradiatus*	31X-2, 75-76	31X-4, 75-76	285.49	288.40
T	*Discoaster surculus*	31X-4, 75-76	31X-6, 75-76	288.49	291.49
T	*Reticulofenestra pseudoumbilicus* (>7 μm)	40X-CC	41X-4, 82-83	379.48	384.56
T	*Amaurolithus* spp.	42X-2, 75-76	42X-4, 75-76	391.09	394.09
T	*Discoaster quinqueramus*	43X-5, 75-76	43X-CC	405.19	407.67
B	*Amaurolithus primus*	47X-CC	48X-2, 73-74	446.35	448.07
B	*Discoaster quinqueramus*	50X-CC	51X-6, 21-22	474.56	482.05
T	*Reticulofenestra pseudoumbilicus* (>7 μm)	50X-CC	53X-4, 70-71	482.05	498.94
T	*Discoaster hamatus*	54X-4, 94-95	55X-CC	498.84	522.89
B	*Discoaster hamatus*	57X-4, 75-76	57X-CC	537.25	541.94
B	*Catinaster coalitus*	58X-4, 77-78	58X-CC	547.01	551.67
B	*Discoaster kugleri*	58X-CC	64X-CC	561.19	608.99
T	*Orthorhabdus serratus*	66X-CC	67X-CC	620.83	636.28
B	*Reticulofenestra pseudoumbilicus* (>7 μm)	67X-CC	69X-CC	636.28	656.42
T	*Sphenolithus heteromorphus*	67X-CC	69X-CC	636.28	656.42
T	*Helicosphaera waltrans*	74X-CC	75X-CC	686.80	705.93
T	*Discoaster musicus*	75X-CC	76X-CC	705.93	715.72

Note: B = bottom occurrence, T = top occurrence.

Table T10. Epoch boundaries, Site 1173.

Boundary	Depth (mbsf)	Event
Pleistocene/Pliocene	240.64	Olduvai (T)
late/early Pliocene	377.59	Gauss (O)
Pliocene/Miocene	406.43 ± 1.24	T *Discoaster quinqueramus*
late/middle Miocene	549.34 ± 2.33	B *Catinaster coalitus*

Notes: (T) = termination, (O) = onset. T = top occurrence, B = bottom occurrence.

Table T11. Calcareous nannofossil range chart, Zones NN21–NN19. (**See table notes.** Continued on next page.)

Epoch	Zones	Hole, core, section, interval (cm)	Depth (mbsf)	Preservation	Abundance	Amaurolithus primus	Braarudosphaera bigelowii	Calcidiscus tropicus	Calcidiscus leptoporus	Calcidiscus macintyrei	Ceratolithus cristatus	Ceratolithus cristatus var. telesmus	Coccolithus pelagicus	Coccolithus pelagicus (with bar)	Cyclolithus annulus	Discoaster spp.	Emiliania huxleyi	Florisphaera profunda	Gephyrocapsa ericsonii	Gephyrocapsa muellerae	Gephyrocapsa oceanica	Gephyrocapsa ornata	Gephyrocapsa spp. (<2 μm)	Hayaster perplexus	Helicosphaera carteri	Helicosphaera carteri var. wallichii	Helicosphaera inversa	Helicosphaera sellii	Holodiscolithus macroporus	Neosphaera coccolithomorpha	Oolithotus fragilis	Pontosphaera discopora	Pontosphaera japonica	Pontosphaera multipora	Pseudoemiliania lacunosa	Pseudoemiliania ovata	Reticulofenestra asanoi	Reticulofenestra minuta	Reticulofenestra minutula	Reticulofenestra pseudoumbilicus (>7 μm)	Reticulofenestra pseudoumbilicus (5–7 μm)	Reticulofenestra spp.	Rhabdosphaera clavigera	Scyphosphaera spp.	Sphenolithus grandis	Sphenolithus spp.	Syracosphaera pulchra	Syracosphaera spp.	Umbellosphaera tenuis	Umbilicosphaera hulburtiana	Umbilicosphaera jafari	Umbilicosphaera rotula	Umbilicosphaera sibogae var. foliosa	Umbilicosphaera sibogae var. sibogae
Pleistocene	NN21b	190-1173A- 2H-CC, 28-29	17.13	M	C												D	F			C		A		F							F										F					F		F				C
	NN21b	3H-CC, 34-35	26.16	M	C		F					F				R	D	F	F		C		A		F							F										F			R		F	F					C
	NN21b	4H-CC, 36-37	36.48	M	C			R	F	C	R	F					D	C	C	C	A				F	F						C										F					R	R	C				C
	NN21b	5H-CC, 17-18	45.72	M	C				C		F	F					D	C	C	C	A								R			F									C				F		R		F				
	NN21b	6H-1, 75-76	45.88	M	C			R	F						F		D	C	C	C	A				F							F									C		R			R		F	F		R	C
	NN21a	7H-4, 75-76	59.89	P	R												D																																					
	NN21a	8H-CC, 23-24	74.23	P	R				C								A			C	A											C		A											C		R	R	F	F			C
	NN21a	9H-CC, 14-15	83.61	G	C				C			F	F				C	D	C				F		R							R		C	C									R	R		F	R	F	F			F
	NN21a	10H-CC, 30-31	93.38	G	C																																																	
	NN21a	11H-CC, 0-1	102.27	G	C				F						R		A	C			C	D		F	F							F								R	R						F	R			C
	NN21a	12H-CC, 35-36	111.96	M	C				F								A	A			D	C																														C
	NN21a	13H-4, 75-76	116.89	M	C				F		R						A	A			D	C	A																										R			F	
	NN21a	13H-6, 75-76	119.89	M	C				C		R										C	D	F	A								R															R		R	R
	NN20	13H-CC, 10-11	120.94	P	R																																			A												
	NN20	14H-4, 75-76	126.39	M	F				F											C	D	C	A	R							R	R																R	F
	NN19	14H-CC		G	C				F						R		A	A	C	A			F	F					R	R		C	C	C																F
	NN19	15H-4, 74-75	135.88	M	F												A																A																		
	NN19	15H-CC, 36-37	140.36	P	R												A																A																		
	NN19	16H-4, 70-71	145.34	P	R				C								A		C	A	A	R	R	R			C	C												F		F	F
	NN19	16H-7, 45-46	149.59	P	R																												D																	
	NN19	17H-4, 75-76	154.89	P	R				C			F					C	A	A	A	F		C	C	C										F	F
	NN19	17H-6, 149-150	158.63		B																																															
	NN19	18H-7, 63-64	168.57	G	F				F		R						A	F	A	R	R	C	C	C	C	C								R
	NN19	19H-3, 75-76	172.39	G	F				C								A	C	C	A	A	C	C	
	NN19	19H-CC, 22-23	178.24	G	C				F								A	C	C	A	C	C	F	C	C	F	
	NN19	20H-CC		G	C																																																	
	NN19	21H-CC, 13-14	197.32	G	C																																																	
	NN19	22H-3, 75-76	200.89	G	C				C							C	D	A	C	C	
	NN19	22H-CC, 0-1	205.98	G	C				C				R			A	A	A	A	A	F	C	C	C
	NN19	23H-4, 70-71	211.84	G	C				C							A	A	A	A	R	C	C	
	NN19	23H-CC, 0-1	216.06	G	C				C		F		R		A	A	C	D	R	R	F	F	C	C
	NN19	24H-CC, 0-5	225.43	G	C				F		F	R	C		A	A	F	A	A	R	R	R	R	F	C	C	F	C	C	F	R	R	C	R
	NN19	25X-CC, 24-25	235.32	G	F				C						A	C	A	D	F	C	C	C	C	F	R	R	F
	NN19	26X-4, 96-97	240.7	M	F				C						C	D	A	
	NN19	26X-CC, 37-38	245.09	P	F				C	F				A	C	A	A	C	C	C	C	C
	NN19	27X-4, 45-46	249.89	P	F				C	R		F		A	C	A	F	C	C	C	C	R

Table T11 (continued).

Epoch	Zones	Hole, core, section, interval (cm)	Depth (mbsf)	Preservation	Abundance	Amaurolithus primus	Braarudosphaera bigelowii	Calcidiscus tropicus	Calcidiscus leptoporus	Calcidiscus macintyrei	Ceratolithus cristatus	Ceratolithus cristatus var. telesmus	Coccolithus pelagicus	Coccolithus pelagicus (with bar)	Cyclolithus annulus	Discoaster spp.	Emiliania huxleyi	Florisphaera profunda	Gephyrocapsa ericsonii	Gephyrocapsa muellerae	Gephyrocapsa oceanica	Gephyrocapsa ornata	Gephyrocapsa spp. (<2 μm)	Hayaster perplexus	Helicosphaera carteri	Helicosphaera carteri var. walichii	Helicosphaera inversa	Helicosphaera sellii	Holodiscolithus macroporus	Neosphaera coccolithomorpha	Oolithotus fragilis	Pontosphaera discopora	Pontosphaera japonica	Pontosphaera multipora	Pseudoemiliania lacunosa	Pseudoemiliania ovata	Reticulofenestra asanoi	Reticulofenestra minuta	Reticulofenestra minutula	Reticulofenestra pseudoumbilicus (>7 μm)	Reticulofenestra pseudoumbilicus (5–7 μm)	Reticulofenestra spp.	Rhabdosphaera clavigera	Scyphosphaera spp.	Sphenolithus grandis	Sphenolithus spp.	Syracosphaera pulchra	Syracosphaera spp.	Umbellosphaera tenuis	Umbilicosphaera hulburtiana	Umbilicosphaera jafari	Umbilicosphaera rotula	Umbilicosphaera sibogae var. foliosa	Umbilicosphaera sibogae var. sibogae
Pleistocene	NN19	27X-CC, 37-38	254.72	P	C	R			C	F			F		R	R		A		F	F		A		C											C	F		A	C	F													F
		28X-4, 71-72	259.75	P	F				C	C			F		F			A		F	F		A														F		A	C	F													
		28X-CC, 42-43	264.47	P	F				C	F			F	F	F			D		F	F		C			F											C	F		A	C	F													C

Notes: D = dominant, A = abundant, C = common, F = few, R = rare, P = poor, M = moderate, G = good. See "Biostratigraphy," p. 9, in the "Explanatory Notes" chapter. This table is also available in ASCII format.

Table T12. Calcareous nannofossil range chart, Zones NN18–NN9. (**See table notes**. Continued on next three pages.)

Epoch	Zones	Core, section, interval (cm)	Depth (mbsf)	Preservation	Abundance	Amaurolithus delicatus	Amaurolithus primus	Amaurolithus tricorniculatus	Calcidiscus leptoporus	Calcidiscus macintyrei	Calcidiscus tropicus	Catinaster calyculus	Catinaster coalitus	Ceratolithus cristatus	Ceratolithus cristatus var. telesmus	Coccolithus pelagicus	Discoaster asymmetricus	Discoaster bellus	Discoaster bergenii	Discoaster berggrenii	Discoaster bollii	Discoaster braarudii	Discoaster brouweri	Discoaster challengeri	Discoaster exilis	Discoaster hamatus	Discoaster loeblichii	Discoaster pentaradiatus	Discoaster prepentaradiatus	Discoaster quinqueramus	Discoaster spp.	Discoaster surculus	Discoaster tamalis	Discoaster triradiatus	Discoaster variabilis	Florisphaera profunda	Gephyrocapsa spp. (<2 µm)	Helicosphaera carteri	Helicosphaera carteri var. wallichii	Helicosphaera intermedia	Helicosphaera sellii	Helicosphaera stalis	Hughesius gizoensis	Oolithus fragilis	Pontosphaera japonica
		190-1173A-																																													
late Pliocene	NN18	29X-CC		P	F				C	C													C									C			F		A	F								
	NN18	30X-CC, 33-34	282.97	P	F				C							C	C						F								C				A									
	NN18	31X-2, 75-76	285.49	P	F					A						C							F												A									
	NN17	31X-4, 75-76	288.49	P	R												A												A					A	A				A					
	NN16	31X-6, 75-76	291.49	P	R																		A								A	C		A	C									
	NN16	32X-4, 78-79	298.22	P	R												A														A	A		A	A		R							
	NN16	32X-CC, 29-30	302.23	M	C				C	R	F			R	R	C							C					F			C			R	A		R		R				
	NN16	33X-CC, 42-43	311.12	P	F				F	F	F					F	C						C								C	F	R			C	A	A	A						F
	NN16	34X-4, 70-71	317.14	M	F									A									C										F				A	A		A					
	NN16	34X-CC, 36-37	321.74	P	F				C														C										F				F	A							
	NN16	35X-CC		P	R				C																																			
	NN16	36X-CC, 24-25	340.19	P	R				C														C								C			C	A									
	NN16	37X-CC, 32-33	350.52	M	C								C		F	R	R						R								R			R	A		C							
	NN16	38X-CC, 45-46	360.24	M	R						F		C	C		F							R								C													F
	NN16	39X-CC		G	C				F	C					R	F							R								R	C	R	R	R		F				F			
	NN16	40X-CC, 37-38	379.47	P	F																		C								C	F		F	F	F								
	NN16	41X-4, 82-82	384.56	P	F																																								
	NN16	41X-CC, 57-58	389.15		B																																								
early Pliocene	NN15-NN12	42X-2, 75-76	391.09	P	F	F			F							F							C								F		C			F	A								
	NN15-NN12	42X-4, 75-76	394.09	P	F										A								A								A		A												
	NN15-NN12	42X-CC			B																																								
	NN15-NN12	43X-5, 75-76	405.19	P	R																										A		A												
late Miocene	NN11b	43X-CC, 34-35	407.66	P	R																								F																
	NN11b	44X-4, 66-67	413.2	M	F	C			C							F															C	C	C		C										
	NN11b	44X-CC, 46-47	417.98	P	C		R		C							F															C	C	R		C										
	NN11b	45X-CC, 40-41	427.5	P	C		R	R	F	F						C															C	C			F										
	NN11b	46X-CC, 46-47	437.15	M	C	F			F	R	R					R															C	F			C										
	NN11b	47X-4, 73-74	441.67	P	C		F	F	C	F						F								C	C						C	C	C		C	F									
	NN11b	47X-CC		P	C		F	F		F						F								C	A						C	F	F	R	F	F									
	NN11b	48X-2, 73-74	448.07	M	C						C					C									C	A	F				C	C			C										
	NN11b	48X-CC			B																																								
	NN11a	49X-CC, 40-41	464.9	P	R											A															C	A				A	A	C							
	NN11a	50X-4, 75-76	469.89	P	F									A	C										C				C		A	A						C							
	NN11a	50X-CC, 47-48	474.55	M	C					F					C						R				F							F	F		F	C	C		F		R				

Table T12 (continued).

Epoch	Zones	Core	Depth (mbsf)	Preservation	Abundance	Pontosphaera multipora	Pseudoemiliania lacunosa	Pseudoemiliania ovata	Reticulofenestra haqii	Reticulofenestra minuta	Reticulofenestra minutula	Reticulofenestra pseudoumbilicus (>7 µm)	Reticulofenestra pseudoumbilicus (5–7 µm)	Reticulofenestra spp.	Rhabdosphaera clavigera	Scyphosphaera ventriosa	Sphenolithus abies	Sphenolithus grandis	Sphenolithus moriformis	Sphenolithus spp.	Syracosphaera pulchra	Umbilicosphaera jafari	Umbilicosphaera rotula
		190-1173A-																					
	NN18	29X-CC		P	F		C			C	A												
		30X-CC, 33-34	282.97	P	F		C				A		C										
		31X-2, 75-76	285.49	P	F						A		A										
	NN17	31X-4, 75-76	288.49	P	R																		
		31X-6, 75-76	291.49	P	R				A		A												
		32X-4, 78-79	298.22	P	R																		
late Pliocene		32X-CC, 29-30	302.23	M	C		C	C		A	A				F						F		C
		33X-CC, 42-43	311.12	P	F		C	C		A	A		A										C
		34X-4, 70-71	317.14	M	F				A		A		A										C
		34X-CC, 36-37	321.74	P	F				A		A	C											
	NN16	35X-CC		P	R		C	C			A	A											
		36X-CC, 24-25	340.19	P	R		C				A	A											
		37X-CC, 32-33	350.52	M	C		C	C			A	A											F
		38X-CC, 45-46	360.24	M	R			A	C		A	D											
		39X-CC		G	C	F	C	F			A	D			R	R						R	R
		40X-CC, 37-38	379.47	P	F		C	C			A	D											
		41X-4, 82-82	384.56	P	F							A					A						
early Pliocene		41X-CC, 57-58	389.15		B																		
	NN15-NN12	42X-2, 75-76	391.09	P	F						A						A						
		42X-4, 75-76	394.09	P	F																		
		42X-CC			B																		
		43X-5, 75-76	405.19	P	R																		
		43X-CC, 34-35	407.66	P	R						A	D											
		44X-4, 66-67	413.2	M	F						A	C	C	A			C		F	F			
	NN11b	44X-CC, 46-47	417.98	P	C			F			D	C	A	A		R	C	R	F	F			
		45X-CC, 40-41	427.5	P	C						C	D	C	F			C	C					
late Miocene		46X-CC, 46-47	437.15	M	C							D		A			F	C					F
		47X-4, 73-74	441.67	P	C						C	D	F	A									
		47X-CC		P	C			C			A	D	R	A									F
		48X-2, 73-74	448.07	M	C						C	D		C									
		48X-CC			B																		
	NN11a	49X-CC, 40-41	464.9	P	R						A												
		50X-4, 75-76	469.89	P	F					A		A	C			C	C						
		50X-CC, 47-48	474.55	M	C	F				D		A				C	C					C	F

Table T12 (continued).

Epoch	Zones	Core	Depth (mbsf)	Preservation	Abundance	*Amaurolithus delicatus*	*Amaurolithus primus*	*Amaurolithus tricorniculatus*	*Calcidiscus leptoporus*	*Calcidiscus macintyrei*	*Calcidiscus tropicus*	*Catinaster calyculus*	*Catinaster coalitus*	*Ceratolithus cristatus*	*Ceratolithus cristatus* var. *telesmus*	*Coccolithus pelagicus*	*Discoaster asymmetricus*	*Discoaster bellus*	*Discoaster bergenii*	*Discoaster berggrenii*	*Discoaster bollii*	*Discoaster braarudii*	*Discoaster brouweri*	*Discoaster challengeri*	*Discoaster exilis*	*Discoaster hamatus*	*Discoaster loeblichii*	*Discoaster pentaradiatus*	*Discoaster prepentaradiatus*	*Discoaster quinqueramus*	*Discoaster* spp.	*Discoaster surculus*	*Discoaster tamalis*	*Discoaster triradiatus*	*Discoaster variabilis*	*Florisphaera profunda*	*Gephyrocapsa* spp. (<2 µm)	*Helicosphaera carteri*	*Helicosphaera carteri* var. *wallichii*	*Helicosphaera intermedia*	*Helicosphaera sellii*	*Helicosphaera stalis*	*Hughesius gizoensis*	*Oolithus fragilis*	*Pontosphaera japonica*
		51X-CC, 41-42	484.24		B																																								
	NN10b	52X-CC, 44-45	493.96	P	R													A													A														
		53X-4, 70-71	498.94	P	R																																								
late Miocene		53X-CC, 48-49	503.68		B																																								
	NN10a	54X-4, 70-71	508.54	P	R							C	C											C	C					C	C														
	NN9	55X-CC, 44-45	522.88	P	F						F	F	F			F					C			C							C	F									F		R		
		56X-CC, 38-39	532.22	P	C			F				C	C			C		F			C	F		C		F					C	F					C		F			F	C			

Notes: D = dominant, A = abundant, C = common, F = few, R = rare, P = poor, M = moderate, G = good. See "Biostratigraphy," p. 9, in the "Explanatory Notes" chapter. This table is also available in ASCII format.

Table T12 (continued).

Epoch	Zones	Core	Depth (mbsf)	Preservation	Abundance	Pontosphaera multipora	Pseudoemiliania lacunosa	Pseudoemiliania ovata	Reticulofenestra haqii	Reticulofenestra minuta	Reticulofenestra minutula	Reticulofenestra pseudoumbilicus (>7 μm)	Reticulofenestra pseudoumbilicus (5–7 μm)	Reticulofenestra spp.	Rhabdosphaera clavigera	Scyphosphaera ventriosa	Sphenolithus abies	Sphenolithus grandis	Sphenolithus moriformis	Sphenolithus ssp.	Syracosphaera pulchra	Umbilicosphaera jafari	Umbilicosphaera rotula
late Miocene	NN10b	51X-CC, 41-42	484.24		B																		
		52X-CC, 44-45	493.96	P	R						A												
		53X-4, 70-71	498.94	P	R							D											
	NN10a	53X-CC, 48-49	503.68		B																		
		54X-4, 70-71	508.54	P	R					A	A	A	A				C						
	NN9	55X-CC, 44-45	522.88	P	F					C	D	C	C			F					C	C	
		56X-CC, 38-39	532.22	P	C					C	A	A	A										F

Table T13. Calcareous nannofossil range chart, Zones NN9–NN6.

Epoch	Zones	Core, section, interval (cm)	Depth (mbsf)	Preservation	Abundance	*Calcidiscus leptoporus*	*Calcidiscus macintyrei*	*Calcidiscus tropicus*	*Catinaster coalitus*	*Coccolithus miopelagicus*	*Coccolithus pelagicus*	*Coronocyclus nitescens*	*Cryptococcolithus mediaperforatus*	*Cyclicargolithus floridanus*	*Discoaster bellus*	*Discoaster bollii*	*Discoaster challengeri*	*Discoaster deflandrei*	*Discoaster exilis*	*Discoaster kugleri*	*Discoaster musicus*	*Discoaster pansus*	*Discoaster petaliformis*	*Discoaster* spp.	*Florisphaera profunda*	*Helicosphaera carteri*	*Helicosphaera vedderi*	*Helicosphaera waltrans*	*Orthorhabdus serratus*	*Pseudoemiliania lacunosa*	*Reticulofenestra haqii*	*Reticulofenestra minutula*	*Reticulofenestra pseudoumbilicus* (>7 µm)	*Reticulofenestra pseudoumbilicus* (5–7 µm)	*Reticulofenestra* spp.	*Sphenolithus abies*	*Sphenolithus heteromorphus*	*Sphenolithus moriformis*	*Triquetrorhabdulus milowii*	*Triquetrorhabdulus rugosus*	*Umbilicosphaera jafari*	*Umbilicosphaera rotula*
middle Miocene	NN9	190-1173A-																																								
		57X-CC, 48-49	541.93	P	R	C			F	C	C				C	C	C		C					C	C					C	C	C	A	A		C	C		F			C
		58X-4, 77-78	547.01	P	R					C																																	
	NN8	58X-CC, 45-46	551.66	P	R											A			A		C		A										A	A					F			
		59X-4, 76-77	556.6		B																																				
		59X-CC, 43-44	561.18	P	F		F			C	C			F		C	C															D	C	C		F	C					C
		60X-4, 74-75	566.28		B																																				
		61X-CC, 39-40	580.61		B																																				
		62X-4, 81-82	585.75		B																																				
		62X-CC, 39-40	590.29	P	R					F	F			F		C	F		C	F											A	A		A								
	NN7	63X-CC, 38-39	591.52		B																																				
		64X-4, 75-76	604.79	P	R					D				C																												
		64X-CC, 32-33	608.98	P	F	F					C			C	C	C	C				C		A							A		A	A				C				
		65X-CC, 39-40	616.69		B																																				
		66X-CC, 34-35	620.82	P	R					R	C	R		C		C	C				F		F			F					A	A	C	A				C			C	R
		67X-CC, 38-39	636.27	P	R				C		C	C		C		C	C				C		C					F			A	C	A	A				C			C	C
		68X-CC, 39-40	646.8	P	R																														D							
	NN6	69X-CC, 38-39	656.41	P	F									C																						D						
		70X-CC, 34-35	663.48		B																																				
		71X-CC, 49-50	675.13		B																																				
		72X-CC, 37-38	678.82	P	R																													D							
		73X-CC	689.41	P	R						A			A									A																			
		75X-CC, 28-29	705.92	P	R						C	C		A				A									F	C			C	D		A		F						
		76X-CC	715.72	P	C						C	F		C				A			F	F							F	R	C	D		C		C	C	R			C	F
		77X-CC	724.9	P	F																									D												

Notes: Abundance: D = dominant, A = abundant, C = common, F = few, R = rare. Preservation: P = poor, M = moderate, G = good. See **"Biostratigraphy,"** p. 9, in the "Explanatory Notes" chapter. This table is also available in **ASCII** format.

Table T14. Depths and ages of magnetic chrons and subchrons, Site 1173.

Depth (mbsf)		Polarity	Chron boundary	Subchron	Age (Ma)
Top	Bottom				
54.74	54.89	R		C1n-1?	
159.69	160.34	R	Brunhes/Matuyama	0.78	
160.34	160.59	N		Kamikatura?	
179.34	193.14	N		Jaramillo	0.99
193.14	197.74	R		C1r.2r	1.07
197.74	201.69	N		Cobb Mountain?	
240.64	242.29	N		Oldvai	1.77
256.49	260.59	R		C2r.1r	
260.59	261.19	N		Reunion?	
261.19	287.49	R		C2r.2r	1.95
291.69	333.39	N	Matuyama/Gauss	C2An.1n	2.581
333.39	338.44	R		Kaena	3.04
338.44	350.59	N		C2An.1r	3.11
350.59	361.59	R		Mammoth?	
374.39	374.74	R	Gauss/Gilbert	C2Ar	3.58
381.99	389.19	N		Cochiti?	
393.39	398.04	N		Nunivak?	
400.94	404.04	N		Sidufjall?	
406.94	412.74	N		Thvera?	
423.84	430.24	N	Gilbert/C3A	C3An.1n	5.894
433.54	439.44	N		C3An.2n	6.269
439.44	445.69	R		C3Ar	6.567
445.69	447.14	N	C3A/C3B	C3Bn?	
451.54	452.49	N	C3B/C4	C4n.1n	
452.89	455.19	N		C4n.2n	
478.94	491.49	R		C4r.1r	8.257
491.49	500.34	N	C4/C4A	C4An	8.699
500.34	501.39	R		C4Ar.1r	9.025
501.39	512.34	N	C4A/C5	C5n.1n	9.74
513.04	557.79	N		C5n.2n	
557.79	559.39	R		C5r.1r	10.949
578.49	580.99	N	C5/C5A	C5An.1n	11.935
581.49	586.74	N		C5An.2n	
589.90	590.25	R		C5Ar.1r	12.401
635.89	645.99	N	C5AB/C5AC	C5ACn	13.703
652.54	653.34	R		C5ACr	14.076
653.34	654.44	N	C5AC/C5AD	C5ADn	14.178
662.69	662.99	R		C5ADr	14.612

Notes: N = normal, R = reversed. ? = uncertain chron and subchron identification.

Table T15. Pore fluid compositions, Hole 1173A. (**See table note.** Continued on next page.)

Hole, core, section, interval (cm)	Depth (mbsf)	pH (ISE)	Alk (T) (mM)	Sal (R)	Cl (T) (mM)	SO$_4$ (I) (mM)	Na (CB) (mM)	Mg (T) (mM)	Ca (T) (mM)	K (I) (mM)	H$_4$SiO$_4$ (S) (µM)	NH$_4$ (S) (µM)	HPO$_4$ (S) (µM)
190-1173A-													
1H-1, 140-150	1.40	7.52	10.7	34.0	554.5	19.29	475	49.4	8.9	11.6	618	710	228.0
1H-2, 140-150	2.90	8.00	17.1	33.5	555.0	11.19	474	47.2	6.7	11.4	609	1370	
1H-3, 140-150	4.40	8.10	23.2	33.0	555.0	4.22	476	44.2	4.7	11.2	553	1530	268.0
1H-4, 140-150	5.90	8.06	29.4	33.0	556.0	0.00	475	45.1	3.7	11.1	556	1870	
1H-5, 80-90	6.80	8.02	30.0	33.0	556.0	0.00	476	44.5	3.9	10.8	609	1990	308.0
2H-1, 140-150	8.54	7.92	31.1	33.0	558.0	0.60	479	44.1	4.8	10.9	643	2900	
2H-2, 140-150	10.04	7.94	31.5	33.0	558.0	0.00	476	44.5	5.1	11.3	648	3380	138.0
2H-3, 140-150	11.54	7.97	31.9	33.5	558.0	0.00	476	44.3	5.0	11.2	706	3960	
2H-4, 140-150	13.04	8.07	32.0	33.0	559.5	0.00	480	43.2	4.9	11.0	665	4150	94.0
2H-5, 140-150	14.54			32.5	561.0	0.53	450	43.7	4.9	10.7	764	4650	
2H-6, 140-150	16.04	7.82	31.8	33.5	562.0	0.00	481	44.0	4.5	10.6	721	4740	165.0
2H-7, 61-71	16.75	7.82	30.9	33.5	562.5	0.00	483	42.5	4.7	11.2	778	4900	
3H-2, 140-150	19.54	7.59	32.6	33.0	563.5	0.24	487	42.6	4.3	10.7	697	5300	179.0
3H-4, 140-150	22.54	7.92	32.9	33.5	564.0	0.00	489	41.6	4.1	10.8	809	5610	
3H-5, 140-150	24.04	7.94	28.6	33.5		4.68				10.7	713	6180	152.0
4H-3, 140-150	29.28	8.02	36.9	33.7	563.5	0.00	491	42.4	4.2	10.6	623	5680	
4H-6, 140-150	33.78	8.02	36.8	34.5	564.5	0.00	490	43.3	4.4	10.3	634	5950	192.0
5H-3, 140-150	40.04	7.98	45.5	34.8	567.5	0.00	497	44.7	4.7	10.4	744	6260	
5H-5, 135-150	42.99	7.99	45.6	35.0	569.5	0.00	497	45.6	5.2	10.7	721	6120	147.0
6H-2, 135-150	47.99	7.52	45.1	35.0	569.5	3.81	499	47.1	6.7	10.2	677	5780	
7H-4, 135-150	60.49	7.65	53.5	35.5	570.5	0.00	502	45.5	7.3	10.2	744	5780	192.0
8H-4, 135-150	69.99	7.73	50.4	35.0	571.0	0.00	504	43.5	7.6	10.2	648	5210	
9H-4, 135-150	79.49	7.74	45.1	35.0	572.5	0.54	505	43.2	6.1	10.3	679	4970	89.0
10H-4, 135-150	88.99	7.86	38.5	34.0	573.0	0.71	506	41.2	4.9	10.3	775	4370	
11H-4, 135-150	98.49	7.64	35.5	34.0	574.0	0.00	509	35.8	7.1	10.5	755	4130	25.0
12H-4, 135-150	107.99	7.91	24.0	34.0	572.0	0.00	504	33.3	5.6	10.9	775	3750	
13H-4, 135-150	117.49	7.64	23.9	33.5	572.0	0.00	506	30.4	7.2	10.9	818	3380	16.0
14H-3, 135-150	125.49	7.73	20.4	33.0	572.0	0.00	507	29.7	5.8	11.1	789	3090	
15H-4, 135-150	136.49	7.69	19.8	33.0	573.0	0.00	510	27.3	7.6	10.4	883	3130	3.6
16H-4, 135-150	145.99	7.60	19.1	32.5	570.5	0.00	507	26.7	7.8	10.7	937	3050	
17H-4, 135-150	155.49	7.70	17.9	32.5	572.0	0.00	510	25.7	7.4	10.7	849	2680	0.6
18H-4, 135-150	164.99	7.80	19.5	33.0	573.0	0.00	515	24.3	8.0	10.7	876	2660	
19H-4, 135-150	174.49	7.45	19.0	32.5	574.0	0.00	514	24.5	8.8	10.1	863	2740	0.5
20H-4, 135-150	183.99	7.41	18.2	32.5	573.0	0.00	514	23.5	8.6	10.9	1089	2060	
21H-4, 135-150	193.49	7.56	19.4	32.5	573.0	0.00	516	22.9	8.8	10.1	952	2400	0.5
22H-3, 135-150	201.49	7.39	18.3	32.5	571.0	0.00	513	21.9	9.1	11.4	1120	2740	
23H-3, 135-150	210.99	7.38	16.5	32.5	571.0	0.00	513	21.1	9.7	10.1	1024	2670	0.5
24H-5, 135-150	223.49	7.55	18.0	32.5	572.0	0.00	518	19.7	10.3	10.3	1078	1900	
25X-4, 130-150	231.44			32.5	573.5	0.00	505	20.4	7.4	10.3	1235	2210	
26X-2, 130-150	238.04	7.66	17.7	32.5	570.0	0.84	519	18.9	10.5	9.7	1042	1990	0.5
27X-5, 125-150	252.19	7.73	13.1	32.2	569.0	0.45	516	16.7	11.1	9.5	1147	1690	
28X-5, 125-150	261.79	7.45	12.1	32.2	567.0	0.66	514	15.8	11.9	9.1	1185	1600	
29X-4, 125-150	269.79	7.61	9.8	32.0	567.0	1.05	517	13.6	12.2	9.2	1076	1550	
30X-3, 122-150	277.86	7.59	10.0	32.0	565.0	0.79	514	12.8	13.3	8.6	1188	1690	
31X-3, 125-150	287.49	7.57	8.7	32.0	564.0	0.65	512	11.8	14.3	9.0	1179	1130	
32X-3, 125-150	297.19	7.64	8.5	32.0	565.0	0.76	516	11.2	13.7	7.8	1230	1560	
33X-1, 125-150	303.89	7.80	7.5	32.0	566.0	0.82	514	9.1	16.9	7.9	1268	1210	0.9
34X-4, 125-150	317.69	7.73	4.8	32.0	563.0	1.32	510	7.4	19.3	5.8	1055	1550	
35X-5, 125-150	328.79	7.54	3.8	32.0	564.0	1.29	509	5.2	22.6	4.8	1136	1220	
36X-4, 125-150	336.89	7.73	4.2	32.0	563.0	0.92	507	4.9	23.4	4.1	1066	1190	0.9
37X-4, 125-150	346.49	7.87	4.2	31.0	552.0	1.53	494	5.5	25.8	3.0	229	0	
38X-2, 120-150	353.04	8.15	5.3	31.0	551.0	0.48	491	4.5	26.6	2.6	188	1060	0.2
39X-2, 120-150	362.64	7.79	6.1	31.0	545.0	1.99	486	4.6	28.2	2.2	188	1010	
40X-5, 120-150	376.84	7.54	6.6	30.0	528.0	2.07	469	4.4	29.1	1.8	209	720	
41X-5, 120-150	386.44	8.15	8.5	30.5	529.0	2.16	471	4.8	29.5	1.8	238	610	
42X-3, 120-150	393.04	8.16	8.0	31.5	546.0	3.87	488	7.3	28.1	2.4	215	840	
43X-5, 95-150	405.39			31.0	542.0	2.89	475	7.3	27.8	2.0	202	860	
44X-4, 125-150	413.79	7.89	10.2	31.0	540.0	2.73	485	6.5	27.4	2.1	299	700	
45X-5, 125-150	424.89	7.95	10.1	31.0	530.0	3.03	472	8.6	27.3	1.9	227	1000	0.2
46X-4, 100-150	432.74			31.0	538.0	4.47	471	9.2	27.4	2.0	279	800	
47X-4, 120-150	442.14			31.0	527.5	4.24	458	9.0	28.8	1.9	215	640	
48X-5, 120-150	453.04			30.5	518.5	3.78	449	8.3	29.1	1.9	163	710	0.2
49X-3, 120-150	459.24			31.5	519.0	5.81	448	10.5	29.2	1.9	229	930	
50X-5, 120-150	471.84			30.0	517.0	5.34	448	8.0	30.2	2.1	221	980	
51X-5, 120-150	481.54	7.92	12.4	30.0	511.0	4.81	454	7.8	30.5	1.9	242	980	0.2
53X-3, 120-150	497.94			30.0	497.0	5.11	426	7.9	31.3	1.7	37	690	
54X-5, 120-150	510.54			30.0	502.0	5.45	433	5.9	32.8	2.1	296	640	0.4
55X-2, 120-150	515.74	7.79	12.7	30.0	503.5	5.62	450	5.2	32.5	1.9	308	600	

Table T15 (continued).

Hole, core, section, interval (cm)	Depth (mbsf)	pH (ISE)	Alk (T) (mM)	Sal (R)	Cl (T) (mM)	SO_4 (I) (mM)	Na (CB) (mM)	Mg (T) (mM)	Ca (T) (mM)	K (I) (mM)	H_4SiO_4 (S) (µM)	NH_4 (S) (µM)	HPO_4 (S) (µM)
56X-4, 120-150	528.04			30.0	505.0	5.75	435	5.0	34.4	1.7	278	560	
57X-3, 120-150	536.24	7.79	12.3	30.0	503.0	5.77	446	4.8	34.5	1.8	292	510	
58X-4, 120-150	547.44			30.0	503.0	6.90	434	4.7	35.6	1.7	221	560	0.4
59X-4, 120-150	557.04			30.0	496.5	6.98	427	4.6	36.0	1.9	255	560	
60X-4, 120-150	566.74			30.0	496.0	7.67	424	4.5	38.1	1.8	190	520	
61X-4, 120-150	576.44	7.94	12.2	30.0	497.5	8.65	437	4.3	39.4	1.7	217	500	0.4
63X-1, 95-120	590.89			30.0	497.0	7.83	419	3.3	42.2	1.8	285	500	
64X-4, 135-150	605.39			30.0	496.0	9.69	417	4.0	44.3	1.7	305	380	
65X-3, 120-150	613.44			30.0	497.0	9.07	413	3.4	46.7	1.9	233	390	0.4
66X-1, 75-100	619.59			30.0	496.0	8.47	404	3.3	50.1	1.6		440	
67X-4, 115-150	634.09			30.5	509.5	10.07	415	2.2	53.9	1.8		390	
70X-1, 120-150	658.64			31.0	513.5	9.51	391	2.5	67.0	1.8	228	300	
71X-4, 120-150	672.84			31.5	516.0	8.98	358	4.8	82.2	1.6		230	
72X-1, 125-150	677.99			33.5	517.5	7.96	355	1.7	86.6	1.5		220	

Note: ISE = ion selective electrode, T = titration, R = refractometer, I = ion, CB = charge balance, S = spectrophotometry.

Table T16. Headspace gas and vacutainer analysis, Hole 1173A. (See table note. Continued on next page.)

Core, section, interval (cm)	Depth (mbsf)	Sample method	C_1/C_2	C_1 (ppm)	C_2 (ppm)	C_2= (ppm)	C_3 (ppm)	C_3= (ppm)
190-1173A-								
2H-1, 135-140	8.49	HS		16,744	0.0	0.0	0.0	0.0
2H-6, 64-65	15.28	VAC	339,437	848,593	2.5	0.0	0.0	0.0
2H-7, 44-45	16.58	VAC	323,101	872,374	2.7	0.0	0.0	0.0
3H-5, 0-5	22.64	HS		17,169	0.0	0.0	0.0	0.0
3H-5, 111-112	23.75	VAC	362,239	869,373	2.4	0.0	0.6	0.0
4H-2, 61-62	26.99	VAC	360,276	936,717	2.6	0.0	0.0	0.0
4H-7, 0-5	33.88	HS		12,429	0.0	0.0	0.0	0.0
4H-8, 11-12	35.49	VAC	370,255	925,637	2.5	0.0	1.0	0.0
5H-3, 95-96	39.59	VAC	336,924	876,001	2.6	0.0	0.6	0.0
5H-6, 0-5	43.14	HS		20,224	0.0	0.0	0.0	0.0
6H-3, 0-5	48.14	HS		8,715	0.0	0.0	0.0	0.0
7H-4, 92-93	60.06	VAC	321,823	901,104	2.8	0.0	1.2	0.0
7H-5, 0-5	60.64	HS		22,590	0.0	0.0	0.0	0.0
8H-4, 22-23	68.86	VAC	270,056	837,173	3.1	0.0	1.3	0.0
8H-5, 0-5	70.14	HS		27,511	0.0	0.0	0.0	0.0
9H-3, 31-32	76.95	VAC	270,647	920,199	3.4	0.0	1.4	0.0
9H-5, 0-5	79.64	HS		29,895	0.0	0.0	0.0	0.0
10H-3, 0-5	86.14	HS		10,226	0.0	0.0	0.0	0.0
10H-5, 135-136	90.49	VAC	192,220	442,106	2.3	0.0	0.0	0.0
12H-5, 0-5	108.14	HS		16,915	0.0	0.0	0.0	0.0
13H-5, 0-5	117.64	HS		9,674	0.0	0.0	0.0	0.0
14H-4, 0-5	125.64	HS		7,150	0.0	0.0	0.0	0.0
15H-5, 0-5	136.64	HS		10,104	0.0	0.0	0.0	0.0
16H-5, 0-5	146.14	HS		1,465	0.0	0.0	0.0	0.0
17H-5, 0-5	155.64	HS		4,814	0.0	0.0	0.0	0.0
18H-5, 0-5	165.14	HS		4,526	0.0	0.0	0.0	0.0
19H-5, 0-5	174.64	HS		3,234	0.0	0.0	0.0	0.0
20H-5, 0-5	184.14	HS		2,987	0.0	0.0	0.0	0.0
22H-4, 0-5	201.64	HS		2,109	0.0	0.0	0.0	0.0
23H-4, 0-5	211.14	HS		1,861	0.0	0.0	0.0	0.0
24H-5, 0-5	222.14	HS		1,300	0.0	0.0	0.0	0.0
25X-5, 0-5	231.64	HS		1,618	0.0	0.0	0.0	0.0
26X-4, 0-5	239.74	HS		1,122	0.0	0.0	0.0	0.0
27X-6, 0-5	252.44	HS	2,164	1,298	0.6	0.0	0.0	0.0
28X-6, 0-5	262.04	HS	1,551	1,086	0.7	0.0	0.0	0.0
29X-5, 0-5	270.04	HS	1,982	2,577	1.3	0.0	0.0	0.0
31X-4, 0-5	287.74	HS	955	1,051	1.1	0.0	0.0	0.0
32X-5, 0-5	298.94	HS		377	0.0	0.0	0.0	0.0
33X-3, 0-5	305.64	HS	74	238	3.2	6.6	0.0	0.0
34X-5, 0-5	317.94	HS		138	0.0	0.0	0.0	0.0
35X-4, 0-5	326.04	HS	635	762	1.2	0.0	3.0	0.0
36X-3, 0-5	334.14	HS	596	953	1.6	0.0	6.5	0.0
37X-5, 0-5	346.74	HS	377	566	1.5	0.0	4.7	0.0
38X-3, 0-5	353.34	HS	366	476	1.3	0.0	3.7	0.0
39X-3, 0-5	362.94	HS	146	132	0.9	0.0	0.7	0.0
40X-6, 0-5	377.14	HS	51	46	0.9	0.0	0.0	0.0
41X-6, 0-5	386.74	HS	46	46	1.0	0.0	0.0	0.0
42X-4, 0-5	393.34	HS	37	125	3.4	0.0	1.2	0.0
43X-6, 0-5	405.94	HS	38	68	1.8	0.0	0.0	0.0
44X-5, 0-5	414.04	HS	32	60	1.9	0.0	0.0	0.0
46X-5, 0-5	433.24	HS	35	87	2.5	0.0	0.7	0.0
47X-5, 0-5	442.44	HS	21	17	0.8	0.0	0.0	0.0
48X-6, 0-5	453.34	HS	37	55	1.5	0.0	0.0	0.0
49X-4, 0-5	459.54	HS		11	0.0	0.0	0.0	0.0
50X-5, 0-5	470.64	HS	27	32	1.2	0.0	0.0	0.0
51X-5, 0-5	480.34	HS	28	31	1.1	0.0	0.0	0.0
52X-2, 0-5	485.54	HS	29	61	2.1	0.0	0.0	0.0
53X-5, 0-5	499.74	HS	28	56	2.0	0.0	0.0	0.0
54X-5, 0-5	509.34	HS	21	30	1.4	0.0	0.0	0.0
55X-2, 0-5	514.54	HS	28	73	2.6	0.0	1.0	0.0
56X-5, 0-5	528.34	HS	30	75	2.5	0.0	1.0	0.0
57X-4, 0-5	536.54	HS	35	56	1.6	0.0	0.0	0.0
58X-5, 0-5	547.74	HS	19	127	6.7	0.0	3.0	0.0
59X-5, 0-5	557.34	HS	32	180	5.7	0.0	1.8	0.0
60X-5, 0-5	567.04	HS	29	43	1.5	0.0	0.0	0.0
61X-3, 0-5	573.74	HS	30	90	3.0	0.0	1.0	0.0
62X-5, 0-5	586.44	HS	9	26	2.8	0.0	2.5	0.0

Table T16 (continued).

Core, section, interval (cm)	Depth (mbsf)	Sample method	C_1/C_2	C_1 (ppm)	C_2 (ppm)	$C_2=$ (ppm)	C_3 (ppm)	$C_3=$ (ppm)
63X-1, 0-5	589.94	HS	19	111	5.8	0.0	3.9	0.0
64X-3, 0-5	602.54	HS	24	88	3.7	0.0	1.9	0.0
65X-4, 0-5	613.74	HS	35	380	10.8	0.0	4.7	0.0
66X-2, 0-5	619.84	HS	37	97	2.6	0.0	1.3	0.0
67X-5, 0-5	634.44	HS	43	1,076	25.0	0.0	10.7	0.0
68X-4, 0-5	642.64	HS	17	94	5.5	0.0	4.7	0.0
69X-5, 0-5	653.74	HS	45	171	3.8	0.0	1.8	0.0
70X-3, 0-5	660.44	HS	58	219	3.8	0.0	1.8	0.0
71X-5, 0-5	673.14	HS	68	388	5.7	0.0	2.9	0.0
72X-1, 0-5	676.74	HS	61	731	12.0	0.0	5.9	0.0
73X-2, 0-5	687.84	HS	92	285	3.1	0.0	1.1	0.0
74X-1, 0-5	695.94	HS	107	311	2.9	0.0	1.0	0.0
75X-CC, 0-5	705.64	HS	84	929	11.1	0.0	5.0	0.0
76X-CC, 0-5	715.34	HS	61	291	4.8	0.0	1.6	0.0
77X-CC, 0-5	724.64	HS	121	1,633	13.5	0.0	4.6	0.0

Note: HS = headspace, VAC = vacutainer.

Table T17. Carbon, nitrogen, sulfur, and hydrogen analyses, Hole 1173A. (**See table note.** Continued on next two pages.)

Core, section, interval (cm)	Depth (mbsf)	Inorganic C (wt%)	CaCO₃ (wt%)	TOC (wt%)	Organic C (wt%)	N (wt%)	S (wt%)	H (mg HC/g of sediment)
190-1173A-								
1H-1, 137-138	1.37	0.05	0.44	NA	NA	NA	NA	NA
1H-2, 127-128	2.77	0.03	0.31	0.61	0.58	0.12	0.07	0.64
1H-3, 112-113	4.12	0.35	2.93	NA	NA	NA	NA	NA
1H-4, 135-136	5.85	0.19	1.62	NA	NA	NA	NA	NA
1H-5, 77-78	6.77	0.15	1.30	NA	NA	NA	NA	NA
2H-1, 139-140	8.53	0.34	2.90	NA	NA	NA	NA	NA
2H-3, 139-140	11.53	0.54	4.57	NA	NA	NA	NA	NA
2H-5, 139-140	14.53	0.22	1.89	1.07	0.85	0.15	0.05	0.62
3H-2, 139-140	19.53	0.26	2.21	NA	NA	NA	NA	NA
3H-4, 135-136	22.49	0.21	1.82	0.75	0.53	0.10	0.11	0.46
3H-5, 139-140	24.03	0.21	1.76	NA	NA	NA	NA	NA
4H-3, 120-122	29.08	0.19	1.60	0.52	0.33	0.07	0.16	0.33
4H-6, 137-139	33.75	0.30	2.50	NA	NA	NA	NA	NA
5H-3, 132-133	39.96	0.27	2.31	0.93	0.65	0.14	0	0.52
5H-5, 130-131	42.94	0.31	2.58	NA	NA	NA	NA	NA
6H-1, 112-113	46.26	0.12	1.00	0.80	0.68	0.14	0.03	0.63
6H-2, 46-47	47.10	1.31	10.98	NA	NA	NA	NA	NA
7H-4, 131-132	60.45	0.32	2.67	NA	NA	NA	NA	NA
7H-7, 49-50	64.13	0.12	1.00	0.75	0.63	0.13	0.15	0.66
8H-1, 51-52	64.65	0.45	3.77	NA	NA	NA	NA	NA
8H-4, 130-131	69.94	0.27	2.25	0.82	0.55	0.11	0.13	0.54
9H-4, 129.5-130.5	79.43	0.05	0.46	0.54	0.48	0.09	0.15	0.56
10H-2, 103-104	85.67	0.08	0.71	0.60	0.52	0.11	0.05	0.58
10H-4, 131-132	88.95	0.14	1.17	NA	NA	NA	NA	NA
10H-6, 104-105	91.74	0.35	2.93	NA	NA	NA	NA	NA
11H-4, 114-115	98.28	0.32	2.67	0.77	0.45	0.10	0.17	0.57
12H-4, 44-45	107.08	0.04	0.37	0.31	0.27	0.08	0	0.58
12H-4, 134-135	107.98	0.11	0.92	NA	NA	NA	NA	NA
13H-4, 82-83	116.96	0.14	1.20	0.5	0.35	0.09	0	0.55
13H-4, 131-132	117.45	0.05	0.48	NA	NA	NA	NA	NA
14H-1, 103-104	122.17	1.75	14.62	NA	NA	NA	NA	NA
14H-3, 131-132	125.45	0.48	4.00	NA	NA	NA	NA	NA
14H-5, 102-103	128.16	0.45	3.82	0.85	0.39	0.11	0.05	0.58
15H-2, 95-96	133.09	1.18	9.83	NA	NA	NA	NA	NA
15H-4, 132-133	136.46	0.31	2.63	NA	NA	NA	NA	NA
15H-5, 59-60	137.23	0.07	0.62	0.34	0.27	0.07	0.47	0.56
16H-4, 94-96	145.58	0.52	4.40	NA	NA	NA	NA	NA
16H-6, 50-52	148.14	0.15	1.26	0.51	0.36	0.09	0.05	0.59
17H-4, 131-132	155.45	1.44	12.01	NA	NA	NA	NA	NA
18H-4, 131-133	164.95	0.36	3.04	NA	NA	NA	NA	NA
18H-6, 15-16	166.79	0.09	0.78	0.15	0.05	0.03	0.06	0.59
18H-6, 126-127	167.90	1.00	8.36	NA	NA	NA	NA	NA
19H-4, 132-133	174.46	0.41	3.45	0.84	0.43	0.12	0	0.65
20H-2, 133-134	180.97	0.23	1.98	0.67	0.43	0.10	0.17	0.67
20H-4, 131-132	183.95	1.36	11.33	NA	NA	NA	NA	NA
20H-5, 129-130	185.43	1.65	13.81	NA	NA	NA	NA	NA
21H-2, 66-67	189.80	0.18	1.50	0.56	0.38	0.11	0.04	0.68
21H-4, 110-111	193.24	0.60	5.07	NA	NA	NA	NA	NA
21H-6, 64-65	195.78	0.50	4.23	NA	NA	NA	NA	NA
22H-3, 131-132	201.45	0.42	3.56	0.85	0.43	0.11	0.08	0.69
22H-5, 95-96	204.09	1.15	9.59	NA	NA	NA	NA	NA
23H-3, 134-135	210.98	0.52	4.38	NA	NA	NA	NA	NA
23H-5, 136-137	214.00	0.08	0.70	NA	NA	NA	NA	NA
24H-1, 126-127	217.40	0.99	8.25	NA	NA	NA	NA	NA
24H-2, 130-131	218.94	0.14	1.20	0.38	0.23	0.08	0.62	0.62
24H-5, 129-130	223.43	0.09	0.77	NA	NA	NA	NA	NA
25X-1, 124-125	226.88	1.08	9.07	NA	NA	NA	NA	NA
25X-4, 128-129	231.42	0.42	3.56	0.61	0.18	0.08	0	0.72
25X-6, 124-125	234.38	1.00	8.36	NA	NA	NA	NA	NA
26X-2, 34-35	237.08	0.07	0.64	0.39	0.31	0.10	0.06	0.68
26X-6, 125-126	243.99	1.33	11.08	NA	NA	NA	NA	NA
27X-2, 105-106	247.49	1.05	8.80	NA	NA	NA	NA	NA
27X-5, 113-114	252.07	0.73	6.13	NA	NA	NA	NA	NA
28X-5, 116-117	261.70	0.66	5.56	NA	NA	NA	NA	NA
29X-3, 140-141	268.44	1.48	12.38	NA	NA	NA	NA	NA
29X-4, 118-119	269.72	0.36	3.04	0.65	0.28	0.09	0.29	0.70
30X-3, 119-120	277.83	0.32	2.71	0.72	0.39	0.11	0.27	0.66

Table T17 (continued).

Core, section, interval (cm)	Depth (mbsf)	Inorganic C (wt%)	CaCO₃ (wt%)	TOC (wt%)	Organic C (wt%)	N (wt%)	S (wt%)	H (mg HC/g of sediment)
31X-1, 131-132	284.55	0.71	5.94	NA	NA	NA	NA	NA
31X-3, 124-125	287.48	0.60	5.02	NA	NA	NA	NA	NA
32X-3, 97-98	296.91	0.08	0.69	0.37	0.29	0.06	0.22	0.67
32X-6, 134-135	301.78	0.53	4.41	NA	NA	NA	NA	NA
33X-1, 122-123	303.86	0.04	0.37	0.18	0.14	0.05	0.12	0.67
34X-4, 116-117	317.60	0.32	2.68	NA	NA	NA	NA	NA
34X-5, 56-57	318.50	0.87	7.31	NA	NA	NA	NA	NA
34X-CC, 18-19	321.56	0.23	1.94	0.47	0.23	0.09	0.27	0.70
35X-2, 145-146	324.49	0.33	2.79	NA	NA	NA	NA	NA
35X-3, 147-148	326.01	0.62	5.23	NA	NA	NA	NA	NA
35X-5, 107-108	328.61	0.22	1.88	0.72	0.49	0.12	1.84	0.77
36X-4, 92-93	336.56	0.62	5.24	NA	NA	NA	NA	NA
36X-6, 32-33	338.96	1.03	8.65	NA	NA	NA	NA	NA
36X-CC, 20-21	340.15	0.58	4.86	0.93	0.34	0.08	0.30	0.71
37X-4, 123-124	346.47	0.37	3.10	NA	NA	NA	NA	NA
37X-6, 41-42	348.65	0.27	2.26	0.56	0.29	0.01	0.36	0.64
38X-3, 3-4	353.37	0.24	2.02	NA	NA	NA	NA	NA
38X-5, 116-117	357.50	0.21	1.78	NA	NA	NA	NA	NA
38X-CC, 22-23	360.01	0.10	0.89	0.47	0.36	0.12	0.56	0.71
39X-2, 118-119	362.62	0.22	1.89	0.59	0.36	0.07	0.24	0.65
39X-5, 134.5-135.5	367.29	0.29	2.45	NA	NA	NA	NA	NA
40X-5, 115-116	376.79	0.39	3.27	0.70	0.31	0.09	0.24	0.68
41X-4, 109-110	384.83	0.49	4.08	NA	NA	NA	NA	NA
41X-7, 32-33	388.56	0.16	1.40	0.42	0.25	0.10	0.14	0.67
42X-2, 119-120	391.53	0.37	3.13	NA	NA	NA	NA	NA
42X-3, 119-120	393.03	0.55	4.60	NA	NA	NA	NA	NA
42X-7, 28-29	398.12	0.24	2.07	0.48	0.24	0.10	0.10	0.63
43X-3, 119-120	402.63	0.17	1.46	0.40	0.23	0.06	0.22	0.66
43X-5, 88-89	405.32	0.31	2.65	NA	NA	NA	NA	NA
44X-4, 115-116	413.69	0.26	2.22	NA	NA	NA	NA	NA
44X-CC, 29-30	417.81	0.13	1.15	0.35	0.21	0.06	0	0.69
45X-2, 60-61	419.74	0.37	3.11	NA	NA	NA	NA	NA
45X-5, 122-123	424.86	0.14	1.22	0.32	0.17	0.06	0	0.66
45X-7, 40-41	427.04	0.96	8.00	NA	NA	NA	NA	NA
46X-1, 127-128	428.51	0.13	1.12	NA	NA	NA	NA	NA
46X-4, 100-101	432.74	0.12	1.06	0.30	0.17	0.07	0.15	0.71
46X-5, 120-121	434.44	0.92	7.73	NA	NA	NA	NA	NA
47X-4, 114-115	442.08	0.14	1.24	0.31	0.16	0.07	0	0.68
47X-5, 129-130	443.73	0.33	2.78	NA	NA	NA	NA	NA
48X-5, 117.5-118.5	453.02	0.04	0.35	0.20	0.16	0.06	0	0.71
49X-3, 116-119	459.20	0.09	0.75	0.28	0.19	0.07	0	0.68
50X-5, 117-118	471.81	0.36	3.06	NA	NA	NA	NA	NA
51X-2, 40-41	476.24	0.22	1.87	0.55	0.32	0.01	0.15	0.67
51X-5, 116-117	481.50	0.05	0.49	NA	NA	NA	NA	NA
51X-6, 61-62	482.45	0.04	0.37	NA	NA	NA	NA	NA
52X-4, 44-45	488.98	0.24	2.05	0.56	0.32	0.10	0	0.62
52X-7, 40-41	493.44	0.02	0.23	NA	NA	NA	NA	NA
53X-3, 92-93	497.66	0.02	0.24	NA	NA	NA	NA	NA
53X-5, 125-126	500.99	0.73	6.15	NA	NA	NA	NA	NA
53X-CC, 31-32	503.51	0.05	0.49	NA	NA	NA	NA	NA
54X-2, 88-89	505.72	0.01	0.12	NA	NA	NA	NA	NA
54X-4, 94-96	508.78	3.98	33.18	NA	NA	NA	NA	NA
54X-5, 116-117	510.50	0.09	0.79	NA	NA	NA	NA	NA
54X-6, 76-77	511.60	0.11	0.96	0.36	0.25	0.09	0	0.68
55X-2, 92-93	515.46	0.07	0.62	NA	NA	NA	NA	NA
55X-5, 131-132	520.35	0.07	0.60	NA	NA	NA	NA	NA
55X-6, 92-93	521.46	0.15	1.27	NA	NA	NA	NA	NA
56X-4, 44-45	527.28	7.11	59.25	NA	NA	NA	NA	NA
56X-4, 118.5-119.5	528.03	0.17	1.43	NA	NA	NA	NA	NA
57X-2, 20-21	533.74	3.32	27.71	NA	NA	NA	NA	NA
57X-3, 115-116	536.19	0.06	0.52	0.27	0.21	0.07	0	0.78
57X-7, 4-5	541.08	0.05	0.46	NA	NA	NA	NA	NA
58X-4, 116-117	547.40	1.27	10.65	NA	NA	NA	NA	NA
58X-6, 70-71	549.94	0.81	6.75	NA	NA	NA	NA	NA
58X-7, 20-21	550.94	2.79	23.30	NA	NA	NA	NA	NA
59X-2, 147-149	554.31	0.12	1.05	NA	NA	NA	NA	NA
59X-4, 118-119	557.02	1.08	9.04	1.18	0.09	0.10	0	0.65
59X-7, 40-41	560.74	3.48	29.00	NA	NA	NA	NA	NA
60X-4, 119-121	566.73	0.05	0.48	NA	NA	NA	NA	NA

Table T17 (continued).

Core, section, interval (cm)	Depth (mbsf)	Inorganic C (wt%)	CaCO$_3$ (wt%)	TOC (wt%)	Organic C (wt%)	N (wt%)	S (wt%)	H (mg HC/g of sediment)
61X-4, 116-117	576.40	0.13	1.15	0.33	0.19	0.09	0.08	0.69
61X-7, 6-7	579.80	0.58	4.90	NA	NA	NA	NA	NA
62X-2, 146-147	583.40	0.09	0.77	NA	NA	NA	NA	NA
62X-4, 146-147	586.40	0.13	1.09	NA	NA	NA	NA	NA
62X-6, 146-147	589.40	0.22	1.85	0.50	0.27	0.10	0.10	0.68
63X-1, 83-84	590.77	0.11	0.94	NA	NA	NA	NA	NA
64X-2, 102-103	602.06	0.44	3.7	0.68	0.23	0.07	0.06	0.66
64X-4, 84-85	604.88	0.11	0.99	NA	NA	NA	NA	NA
64X-5, 58-59	606.12	0.1	0.87	NA	NA	NA	NA	NA
65X-1, 5-6	609.29	8.41	70.05	NA	NA	NA	NA	NA
65X-2, 103-104	611.77	0.43	3.6	0.64	0.20	0.07	0.03	0.64
65X-3, 107-108	613.31	0.26	2.18	NA	NA	NA	NA	NA
66X-1, 68-69	619.52	0.49	4.15	0.7	0.20	0.07	0.09	0.65
67X-1, 91-92	629.35	2.04	17.06	NA	NA	NA	NA	NA
67X-3, 87-88	632.31	0.69	5.81	NA	NA	NA	NA	NA
67X-4, 113-114	634.07	2.42	20.17	NA	NA	NA	NA	NA
68X-1, 90.5-91.5	639.04	1.52	12.67	NA	NA	NA	NA	NA
68X-3, 72-73	641.86	0.22	1.83	0.50	0.28	0.07	0.13	0.75
68X-6, 75-76	646.39	0.56	4.69	NA	NA	NA	NA	NA
69X-2, 147-148	650.71	0.14	1.17	0.34	0.20	0.07	0.14	0.71
69X-4, 91-92	653.15	0.25	2.13	NA	NA	NA	NA	NA
70X-1, 116-117	658.60	0.87	7.25	1.06	0.19	0.07	0	0.66
70X-CC, 31-32	663.45	6.66	55.54	NA	NA	NA	NA	NA
71X-4, 118-119	672.82	4.32	36.02	NA	NA	NA	NA	NA
72X-1, 124-126	677.98	0.19	1.59	0.41	0.22	0.06	0.04	0.71
73X-1, 117-119	687.51	0.01	0.15	NA	NA	NA	NA	NA
73X-2, 86-88	688.70	0.05	0.42	NA	NA	NA	NA	NA

Note: TOC = total organic carbon, HC = hydrocarbon.

Table T18. Total bacterial populations in sediments, Site 1173.

Depth (mbsf)	Bacterial cells (cells/cm³)
1.40	7.23×10^7
5.90	5.38×10^7
10.04	3.35×10^7
14.54	2.53×10^7
22.54	1.94×10^7
42.98	2.74×10^7
60.48	4.92×10^7
79.48	3.04×10^7
107.99	6.28×10^6
125.49	4.08×10^6
164.99	5.05×10^6
192.13	1.85×10^6
252.19	5.86×10^6
277.91	1.54×10^6
332.39	1.21×10^6
346.49	5.60×10^5
386.44	6.49×10^5
402.69	1.44×10^6
424.89	3.13×10^5
459.29	1.40×10^5
499.19	1.82×10^6
536.24	BD
566.74	BD
604.94	BD
641.89	BD
672.84	BD

Note: BD = below detection.

Table T19. Comparison of near-surface sediment bacterial populations at Site 1173A with data from nine other ODP sites with different overlying-water depths.

Location	ODP leg-site	Depth (mbsf)	Total bacteria (cells/cm^3)
Peru margin	112-681	150	1.05×10^9
Santa Barbara Basin	146-893	577	1.27×10^9
Japan Sea	128-798	900	7.82×10^8
Woodlark Basin	180-1115	1150	2.83×10^8
Cascadia margin	146-890	1326	6.95×10^8
Woodlark Basin	180-1109	2211	3.28×10^8
Juan de Fuca Ridge	139-857	2419	8.28×10^8
Cascadia margin	146-888	2516	5.32×10^8
Lau Basin	135-834	2703	6.12×10^8
Woodlark Basin	180-1108	3188	2.67×10^8
Amazon Fan	155-940	3195	5.62×10^8
Amazon Fan	155-934	3432	6.04×10^8
Eastern Equatorial Pacific	138-851	3760	2.08×10^8
Nankai Trough	190-1173	4791	7.23×10^7

Table T20. Drilling fluid intrusion estimated based on PFT tracer experiments, Hole 1173A.

Core, section	Sample weight (g)			Bulk density (g/cm³)	PFT peak area			Drill fluid (µL)/sediment (g)		
	Outside	Quarter	Center		Outside	Quarter	Center	Outside	Quarter	Center
190-1173A-										
4H-2	2.49	3.44	3.29	1.72	232.5	349.6	75.7	0.21	0.28	BD
4H-3	2.49	3.53	3.37	1.72	645.9	105.9	260.7	0.95	0.05	0.23
4H-4	3.63	3.23	3.96	1.60	361.3	36.7	253.0	0.32	BD	0.19
4H-5	3.75	3.88	3.56	1.66	97.5	38.2	82.3	0.04	BD	0.02
4H-6	3.57	3.96	3.65	1.78	31.0	37.0	29.3	BD	BD	BD
4H-7	2.82	4.19	3.51	1.78	1,478.1	58.8	198.0	2.01	BD	0.15
5H-1	2.65	3.21	3.05	1.65	457.0	101.7	727.9	0.60	0.05	0.86
5H-2	3.51	4.10	4.24	1.88	612.0	139.8	115.3	0.62	0.08	0.05
5H-3	3.56	4.49	3.95	1.72	2,691.2	255.1	110.2	2.88	0.16	0.05
5H-4	2.96	4.17	4.21	1.70	3,539.4	627.0	571.9	4.66	0.52	0.46
5H-5	3.57	3.36	3.35	1.70	23,612.7	1,358.3	82.4	25.68	1.51	0.03
5H-6	2.61	3.55	3.51	1.71	1,233.1	199.2	47.2	1.80	0.15	BD
28X-1	0.93	1.51	1.15	1.62	0.0	0.0	0.0	BD	BD	BD
28X-2	1.05	1.58	1.42	1.59	260.6	23.4	36.9	0.80	BD	BD
28X-3	1.27	1.63	1.18	1.64	159.2	52.5	30.0	0.33	BD	BD
28X-4	2.30	0.91	0.65	1.58	436.7	21.4	15.3	0.66	BD	BD
28X-5	0.89	0.75	0.75	1.60	129.6	46.1	34.8	0.33	BD	BD
28X-6	1.93	2.38	1.22	1.62	1,488.2	27.7	42.9	3.03	BD	BD
29X-1	1.08	1.01	0.72	1.76	402.7	51.3	37.0	1.34	BD	BD
29X-2	1.43	0.98	1.24	1.62	1,150.7	70.4	56.2	3.17	0.05	BD
29X-3	1.16	1.48	1.74	1.68	202.9	512.5	42.3	0.52	1.14	BD
29X-4	1.28	1.01	0.98	1.61	797.6	66.4	393.1	2.42	0.03	BD

Note: BD = below detection (0.01 µL drilling fluid).

Table T21. Fluorescent microsphere tracer experiments, Hole 1173A.

Core, section	Sample weight (g)			Microspheres/sediment (g)			Drill fluid (µL/g)		
	Outside	Quarter	Center	Outside	Quarter	Center	Outside	Quarter	Center
190-1173A-									
4H-2	2.49	3.44	3.29	BD	BD	BD	BD	BD	BD
4H-3	2.49	3.53	3.37	2,784,183	190	95	1.1×10^{-2}	1.0×10^{-6}	5.0×10^{-7}
4H-4	3.63	3.23	3.96	1,189,865	BD	BD	3.2×10^{-3}	BD	BD
4H-5	3.75	3.88	3.56	BD	BD	BD	BD	BD	BD
4H-6	3.57	3.96	3.65	BD	BD	BD	BD	BD	BD
4H-7	2.82	4.19	3.51	BD	BD	BD	BD	BD	BD
5H-1	2.65	3.21	3.05	21,800	BD	BD	7.9×10^{-5}	BD	BD
5H-2	3.51	4.10	4.24	35,246	3,223	BD	9.6×10^{-5}	8.0×10^{-6}	BD
5H-3	3.56	4.49	3.95	47,958	BD	BD	1.3×10^{-4}	BD	BD
5H-4	2.96	4.17	4.21	28,343	BD	BD	9.2×10^{-5}	BD	BD
5H-5	3.57	3.36	3.35	BD	BD	BD	BD	BD	BD
5H-6	2.61	3.55	3.51	BD	BD	BD	BD	BD	BD
28X-1	0.93	1.51	1.15	946	BD	BD	1.0×10^{-5}	BD	BD
28X-2	1.05	1.58	1.42	1,337	BD	BD	1.2×10^{-5}	BD	BD
28X-3	1.27	1.63	1.18	129	BD	BD	1.0×10^{-6}	BD	BD
28X-4	2.30	0.91	0.65	647	BD	7,487	3.0×10^{-6}	BD	1.1×10^{-4}
28X-5	0.89	0.75	0.75	1,261	190	267	1.4×10^{-5}	2.0×10^{-6}	3.0×10^{-6}
28X-6	1.93	2.38	1.22	5,763	6,619	4,732	2.9×10^{-5}	2.7×10^{-5}	3.7×10^{-5}
29X-1	1.08	1.01	0.72	24,943	1,422	535	2.2×10^{-4}	1.4×10^{-5}	7.0×10^{-6}
29X-2	1.43	0.98	1.24	1,395	379	2,809	9.0×10^{-6}	4.0×10^{-6}	2.2×10^{-5}
29X-3	1.16	1.48	1.74	8,833	6,246	BD	7.3×10^{-5}	4.1×10^{-5}	BD
29X-4	1.28	1.01	0.98	11,884	758	14,693	9.0×10^{-5}	7.0×10^{-6}	1.4×10^{-4}

Note: BD = below detection (~1000 spheres).

Table T22. Apparent formation factor from the needle-probe method, Hole 1173A. (**See table note.** Continued on next page.)

Core, section, interval (cm)	Depth (mbsf)	Probe axis	Lithologic type	Formation factor	Core, section, interval (cm)	Depth (mbsf)	Probe axis	Lithologic type	Formation factor
190-1173A-					10H-4, 123	88.87	y	Clayey silt	3.50
1H-4, 152	6.02	z	Clayey silt	2.57	10H-6, 38	91.08	z	Clayey silt	4.58
1H-4, 152	6.02	y	Clayey silt	2.43	10H-6, 38	91.08	y	Clayey silt	3.81
2H-6, 122	15.86	y	Clayey silt	4.06	10H-6, 107	91.77	z	Clayey silt	3.41
3H-3, 129	20.93	z	Clayey silt	3.01	10H-6, 107	91.77	y	Clayey silt	3.55
3H-3, 129	20.93	y	Clayey silt	2.99	11H-2, 44	94.58	z	Clayey silt	3.77
4H-8, 35	35.73	y	Clayey silt	4.01	11H-2, 44	94.58	y	Clayey silt	3.30
4H-8, 35	35.73	y	Clayey silt	3.99	11H-2, 95	95.09	z	Clayey silt	3.69
4H-8, 35	35.73	z	Clayey silt	4.15	11H-2, 95	95.09	y	Clayey silt	3.43
4H-8, 35	35.73	z	Clayey silt	4.16	11H-4, 39	97.53	z	Clayey silt	3.47
4H-8, 9	35.47	y	Sandy silt	3.96	11H-4, 39	97.53	y	Clayey silt	3.39
4H-8, 9	35.47	y	Sandy silt	3.95	11H-4, 103	98.17	z	Clayey silt	4.02
4H-8, 12	35.50	z	Sandy silt	4.06	11H-4, 103	98.17	y	Clayey silt	3.84
4H-2, 75	27.13	y	Sandy silt	4.02	11H-6, 41	100.55	z	Clayey silt	3.16
4H-2, 57	26.95	z	Sandy silt	4.19	11H-6, 41	100.55	y	Clayey silt	3.28
4H-2, 118	27.56	y	Clayey silt	2.93	11H-6, 91	101.05	z	Clayey silt	3.88
4H-2, 118	27.56	z	Clayey silt	3.09	11H-6, 91	101.05	y	Clayey silt	3.49
4H-4, 96	30.34	y	Clayey silt	3.25	12H-2, 56	104.20	z	Clayey silt	3.47
4H-4, 96	30.34	z	Clayey silt	3.23	12H-2, 56	104.20	y	Clayey silt	3.44
4H-6, 34	32.72	y	Clayey silt	3.89	12H-2, 96	104.60	z	Clayey silt	4.12
4H-6, 34	32.72	z	Clayey silt	3.97	12H-2, 96	104.60	y	Clayey silt	2.03
5H-2, 66	37.80	z	Clayey silt	3.07	12H-4, 36	107.00	z	Clayey silt	4.26
5H-2, 66	37.80	y	Clayey silt	3.13	12H-4, 36	107.00	y	Clayey silt	3.68
5H-3, 97	39.61	z	Clayey silt	3.55	12H-4, 94	107.58	z	Clayey silt	4.26
5H-5, 112	42.76	y	Sandy silt	4.36	12H-4, 94	107.58	y	Clayey silt	3.76
5H-5, 112	42.76	z	Sandy silt	4.81	12H-6, 43	110.07	z	Clayey silt	5.80
6H-2, 61	47.25	y	Clayey silt	3.44	12H-6, 43	110.07	y	Clayey silt	4.60
6H-2, 61	47.25	z	Clayey silt	3.55	12H-6, 92	110.56	z	Clayey silt	4.04
6H-2, 31	46.95	z	Clayey silt	3.53	12H-6, 92	110.56	y	Clayey silt	3.72
6H-2, 31	46.95	y	Clayey silt	3.72	13H-2, 41	113.55	z	Clayey silt	3.64
6H-3, 59	48.73	z	Clayey silt	3.84	13H-2, 41	113.55	y	Clayey silt	3.23
6H-3, 59	48.73	y	Clayey silt	3.66	13H-2, 88	114.02	z	Clayey silt	3.41
7H-2, 36	56.50	z	Clayey silt	3.06	13H-2, 88	114.02	y	Clayey silt	3.31
7H-2, 36	56.50	y	Clayey silt	2.98	13H-4, 68	116.82	z	Clayey silt	3.53
7H-2, 58	56.72	y	Sandy silt	4.57	13H-4, 68	116.82	y	Clayey silt	3.31
7H-4, 111	60.25	y	Clayey silt	3.51	13H-6, 43	119.57	z	Clayey silt	3.52
7H-4, 111	60.25	z	Clayey silt	3.72	13H-6, 43	119.57	y	Clayey silt	3.29
7H-6, 84	62.98	z	Clayey silt	3.90	13H-6, 94	120.08	z	Clayey silt	4.37
7H-6, 84	62.98	y	Clayey silt	3.44	13H-6, 94	120.08	y	Clayey silt	3.72
7H-6, 4	62.18	z	Sandy silt	4.09	14H-2, 60	123.24	y	Clayey silt	3.14
7H-6, 4	62.18	y	Sandy silt	4.17	14H-2, 60	123.24	z	Clayey silt	3.14
7H-6, 5	62.19	y	Sandy silt	3.92	14H-2, 106	123.70	y	Clayey silt	3.36
7H-6, 10	62.24	z	Clayey silt	3.98	14H-2, 106	123.70	z	Clayey silt	3.26
7H-6, 10	62.24	y	Clayey silt	3.45	14H-4, 58	126.22	z	Clayey silt	3.37
8H-2, 54	66.18	y	Clayey silt	3.42	14H-4, 58	126.22	y	Clayey silt	3.10
8H-2, 54	66.18	z	Clayey silt	3.38	14H-4, 107	126.71	y	Clayey silt	3.03
8H-2, 104	66.68	z	Sandy silt	3.73	14H-4, 107	126.71	z	Volcanic ash	3.97
8H-2, 104	66.68	y	Clayey silt	3.77	14H-4, 108	126.72	y	Volcanic ash	3.35
8H-4, 52	69.16	y	Clayey silt	3.57	14H-4, 108	126.72	z	Volcanic ash	3.83
8H-4, 52	69.16	z	Clayey silt	3.60	14H-6, 54	129.18	y	Clayey silt	3.31
8H-4, 121	69.85	z	Clayey silt	4.50	14H-6, 54	129.18	z	Clayey silt	3.49
8H-4, 121	69.85	y	Clayey silt	4.04	14H-6, 105	129.69	z	Clayey silt	3.21
8H-6, 106	72.70	y	Clayey silt	4.23	14H-6, 105	129.69	y	Clayey silt	3.09
8H-6, 106	72.70	z	Clayey silt	5.26	15H-2, 46	132.60	y	Clayey silt	3.52
8H-6, 80	72.44	y	Sandy silt	5.26	15H-2, 46	132.60	z	Clayey silt	3.80
8H-6, 80	72.44	z	Sandy silt	5.72	15H-2, 96	133.10	z	Clayey silt	3.21
8H-6, 61	72.25	z	Silt	3.75	15H-2, 96	133.10	y	Clayey silt	3.24
8H-6, 61	72.25	y	Silt	4.02	15H-2, 34	132.48	y	Volcanic ash	4.87
8H-6, 60	72.24	y	Silt	3.88	15H-2, 34	132.48	z	Volcanic ash	6.30
9H-4, 40	78.54	z	Clayey silt	3.38	15H-4, 55	135.69	z	Clayey silt	3.75
9H-4, 40	78.54	y	Clayey silt	3.27	15H-4, 55	135.69	y	Clayey silt	2.92
9H-4, 122	79.36	z	Clayey silt	3.69	15H-4, 96	136.10	y	Clayey silt	3.01
9H-4, 122	79.36	y	Clayey silt	3.82	15H-4, 96	136.10	z	Clayey silt	3.29
10H-2, 35	84.99	z	Clayey silt	3.32	15H-6, 56	138.70	z	Clayey silt	3.58
10H-2, 35	84.99	y	Clayey silt	3.23	15H-6, 56	138.70	y	Clayey silt	3.09
10H-2, 94	85.58	z	Clayey silt	4.11	15H-6, 107	139.21	y	Clayey silt	3.46
10H-2, 94	85.58	y	Clayey silt	6.93	15H-6, 107	139.21	z	Clayey silt	3.43
10H-4, 44	88.08	z	Clayey silt	3.36	16H-2, 55	142.19	z	Clayey silt	2.91
10H-4, 44	88.08	y	Clayey silt	3.09	16H-2, 55	142.19	y	Clayey silt	2.91
10H-4, 123	88.87	z	Clayey silt	3.62	16H-2, 105	142.69	z	Clayey silt	3.51

Table T22 (continued).

Core, section, interval (cm)	Depth (mbsf)	Probe axis	Lithologic type	Formation factor
16H-2, 105	142.69	y	Clayey silt	3.23
16H-4, 57	145.21	y	Clayey silt	3.03
16H-4, 57	145.21	z	Clayey silt	3.19
16H-4, 93	145.57	z	Clayey silt	5.17
16H-4, 93	145.57	y	Clayey silt	3.92
16H-6, 37	148.01	z	Clayey silt	3.37
16H-6, 37	148.01	y	Clayey silt	3.07
16H-6, 105	148.69	z	Clayey silt	3.09
16H-6, 105	148.69	y	Clayey silt	3.24
17H-2, 55	151.69	z	Clayey silt	3.79
17H-2, 55	151.69	y	Clayey silt	3.33
17H-2, 106	152.20	y	Clayey silt	3.00
17H-2, 106	152.20	z	Clayey silt	3.14
17H-4, 55	154.69	z	Clayey silt	3.37
17H-4, 55	154.69	y	Clayey silt	3.65
17H-4, 122	155.36	z	Clayey silt	3.29
17H-4, 122	155.36	y	Clayey silt	2.97
17H-6, 43	157.57	z	Clayey silt	3.11
17H-6, 43	157.57	y	Clayey silt	2.92
17H-6, 106	158.20	z	Clayey silt	6.02
17H-6, 106	158.20	y	Clayey silt	3.47
17H-6, 106	158.20	z	Clayey silt	5.00
18H-2, 59	161.23	z	Clayey silt	5.40
18H-2, 59	161.23	y	Clayey silt	4.66
18H-2, 105	161.69	z	Clayey silt	4.00
18H-2, 107	161.71	y	Clayey silt	3.79
18H-4, 54	164.18	z	Clayey silt	3.05
18H-4, 54	164.18	y	Clayey silt	2.93
18H-4, 105	164.69	z	Clayey silt	4.42
18H-4, 105	164.69	y	Clayey silt	2.91
18H-6, 67	167.31	z	Clayey silt	3.14
18H-6, 67	167.31	y	Clayey silt	3.11
18H-6, 117	167.81	z	Clayey silt	2.89
18H-6, 117	167.81	y	Clayey silt	2.71
19H-1, 88	169.52	z	Clayey silt	4.06
19H-1, 88	169.52	y	Clayey silt	4.05
19H-1, 135	169.99	z	Clayey silt	3.63
19H-1, 135	169.99	y	Clayey silt	3.69
19H-2, 66	170.80	z	Clayey silt	3.71
19H-2, 66	170.80	y	Clayey silt	3.27
19H-2, 142	171.56	z	Clayey silt	3.38
19H-2, 142	171.56	y	Clayey silt	3.31
19H-3, 72	172.36	z	Clayey silt	3.67
19H-3, 72	172.36	y	Clayey silt	3.29
19H-3, 135	172.99	z	Clayey silt	3.50
19H-3, 135	172.99	y	Clayey silt	2.90
19H-4, 89	174.03	z	Clayey silt	4.03
19H-4, 89	174.03	y	Clayey silt	3.97
19H-4, 147	174.61	z	Clayey silt	4.23
19H-4, 147	174.61	y	Clayey silt	3.55
19H-5, 78	175.42	z	Clayey silt	3.57
19H-5, 78	175.42	y	Clayey silt	3.39
19H-5, 141	176.05	z	Clayey silt	4.01
19H-5, 141	176.05	y	Clayey silt	4.00
19H-6, 69	176.83	z	Clayey silt	5.10
19H-6, 69	176.83	y	Clayey silt	3.25
19H-6, 128	177.42	z	Clayey silt	3.49
19H-6, 128	177.42	y	Clayey silt	3.43
20H-1, 78	178.92	z	Clayey silt	3.09
20H-1, 78	178.92	y	Clayey silt	2.99
20H-1, 139	179.53	z	Clayey silt	3.54
20H-1, 139	179.53	y	Clayey silt	3.61
20H-2, 64	180.28	z	Clayey silt	2.54
20H-2, 64	180.28	y	Clayey silt	2.34
20H-2, 120	180.84	z	Clayey silt	3.44
20H-2, 120	180.84	y	Clayey silt	3.47
20H-3, 69	181.83	z	Clayey silt	3.34
20H-3, 69	181.83	y	Clayey silt	3.12
20H-3, 131	182.45	z	Clayey silt	3.72
20H-3, 131	182.45	y	Clayey silt	3.43
20H-4, 66	183.30	z	Clayey silt	3.32

Core, section, interval (cm)	Depth (mbsf)	Probe axis	Lithologic type	Formation factor
20H-4, 66	183.30	y	Clayey silt	4.27
20H-4, 141	184.05	z	Clayey silt	4.47
20H-4, 141	184.05	y	Clayey silt	4.87
20H-5, 77	184.91	z	Clayey silt	3.52
20H-5, 77	184.91	y	Clayey silt	2.92
20H-5, 151	185.65	z	Clayey silt	3.85
20H-5, 151	185.65	y	Clayey silt	4.62
20H-6, 51	186.15	z	Clayey silt	3.97
20H-6, 51	186.15	y	Clayey silt	4.56
21H-2, 60	189.74	z	Clayey silt	3.30
21H-2, 60	189.74	y	Clayey silt	2.77
21H-3, 85	191.49	z	Clayey silt	2.84
21H-3, 85	191.49	y	Clayey silt	2.75
21H-4, 56	192.70	z	Clayey silt	3.49
21H-4, 56	192.70	y	Clayey silt	3.93
21H-5, 83	194.47	y	Clayey silt	3.19
21H-5, 83	194.47	z	Clayey silt	3.72
21H-6, 80	195.94	z	Clayey silt	3.16
21H-6, 80	195.94	y	Clayey silt	2.87
22H-5, 72	203.86	z	Clayey silt	3.13
22H-5, 72	203.86	y	Clayey silt	3.20
22H-3, 75	200.89	z	Clayey silt	3.02
22H-3, 75	200.89	y	Clayey silt	2.87
22H-1, 66	197.80	z	Clayey silt	2.99
22H-1, 66	197.80	y	Clayey silt	3.40
22H-6, 70	205.34	z	Clayey silt	4.69
22H-6, 70	205.34	y	Clayey silt	3.13
22H-6, 70	205.34	z	Clayey silt	5.48
22H-6, 70	205.34	y	Clayey silt	3.84
22H-4, 71	202.35	z	Clayey silt	3.44
22H-4, 71	202.35	y	Clayey silt	3.26
23H-1, 120	207.84	y	Clayey silt	3.78
23H-1, 123	207.87	y	Clayey silt	3.48
23H-1, 124	207.88	y	Clayey silt	2.87
23H-1, 129	207.93	y	Volcanic ash	3.47
23H-1, 129	207.93	z	Volcanic ash	3.59
24H-3, 84	219.98	z	Clayey silt	3.74
24H-3, 84	219.98	y	Clayey silt	2.75
24H-4, 71	221.35	y	Clayey silt	4.42
24H-6, 70	224.34	y	Clayey silt	2.96
24H-6, 70	224.34	z	Clayey silt	3.11
24H-1, 70	216.84	z	Clayey silt	3.31
24H-1, 70	216.84	y	Clayey silt	3.60
25H-1, 38	226.02	z	Clayey silt	2.91
25H-1, 38	226.02	y	Clayey silt	3.23
25H-1, 115	226.79	z	Clayey silt	3.87
25H-1, 115	226.79	y	Clayey silt	5.05
25H-2, 36	227.50	z	Clayey silt	4.47
25H-2, 36	227.50	y	Clayey silt	5.03
25H-2, 131	228.45	z	Clayey silt	3.00
25H-2, 131	228.45	y	Clayey silt	3.81
25H-3, 41	229.05	z	Clayey silt	4.40
25H-3, 41	229.05	y	Clayey silt	3.92
25H-3, 117	229.81	z	Clayey silt	5.32
25H-3, 117	229.81	y	Clayey silt	6.07
25H-4, 51	230.65	z	Clayey silt	3.06
25H-4, 51	230.65	y	Clayey silt	3.16
25H-4, 141	231.55	z	Clayey silt	3.33
25H-4, 141	231.55	y	Clayey silt	3.25
25H-5, 51	232.15	z	Clayey silt	3.11
25H-5, 51	232.15	y	Clayey silt	2.97
25H-5, 141	233.05	z	Clayey silt	2.86
25H-5, 141	233.05	y	Clayey silt	3.30
25H-6, 52	233.66	z	Clayey silt	3.11
25H-6, 52	233.66	y	Clayey silt	3.00
25H-6, 112	234.26	z	Clayey silt	3.73
25H-6, 112	234.26	y	Clayey silt	4.00
25H-7, 16	234.80	z	Clayey silt	3.33
25H-7, 16	234.80	y	Clayey silt	3.81

Note: This table is also available in **ASCII** format.

Table T23. Electrical conductivity and formation factor data for cubes, Hole 1173A. (**See table note.** Continued on next page.)

Core, section, interval (cm)	Depth (mbsf)	Electrical conductivity			Temp (°C)	Formation factor		
		x	y	z		x	y	z
190-1173A-								
26X-2, 30	237.04	1.67	1.65	1.54	25.2	3.19	3.22	3.45
26X-3, 113	239.37	1.65	1.67	1.59	25.2	3.22	3.19	3.35
26X-6, 117	243.91	1.69	1.62	1.44	25.2	3.16	3.29	3.69
26X-3, 74	238.98	1.40	1.60	1.59	25.2	3.79	3.33	3.35
27X-2, 104	247.48	1.67	1.60	1.48	24.9	3.17	3.32	3.57
27X-3, 104	248.98	1.56	1.62	1.48	24.9	3.39	3.27	3.58
27X-5, 32	251.26	1.64	1.55	1.52	24.9	3.22	3.41	3.48
27X-6, 52	252.96	1.65	1.66	1.55	24.9	3.21	3.19	3.42
28X-2, 71	256.75	1.63	1.61	1.37	24.1	3.19	3.24	3.81
28X-3, 85	258.39	1.64	1.65	1.57	24.1	3.18	3.16	3.32
28X-4, 82	259.86	1.56	1.71	1.59	24.1	3.34	3.05	3.27
28X-5, 67	261.21	1.53	1.51	1.44	24.1	3.41	3.44	3.62
28X-6, 69	262.73	1.49	1.38	1.26	24.1	3.49	3.78	4.14
29X-2, 67	266.21			1.26	24.1			4.12
29X-4, 74	269.28	1.55	1.48	1.39	24.1	3.37	3.51	3.74
30X-2, 62	275.76	1.38	1.44	1.34	24.1	3.77	3.62	3.89
30X-4, 60	278.74	1.43	1.37	1.29	24.1	3.65	3.81	4.03
30X-6, 53	281.67	1.62	1.44	1.14	24.1	3.21	3.61	4.56
31X-2, 32	285.06	1.26	1.35	1.28	24.0	4.12	3.86	4.07
31X-4, 29	288.03	1.39	1.15	1.36	24.0	3.75	4.50	3.81
31X-6, 83	291.57			1.26	24.0			4.13
32X-6, 4	300.48	1.40	1.42		24.0	3.70	3.66	
33X-2, 87	305.01	1.47	1.45	1.38	25.0	3.61	3.65	3.84
33X-3, 91	306.55	1.32	1.26	1.22	25.0	4.03	4.21	4.36
33X-4, 86	308.00	1.39	1.37	1.31	25.0	3.81	3.87	4.06
33X-6, 42	310.56	1.43	1.40	1.33	25.0	3.72	3.77	3.97
34X-2, 97	314.41	1.37	1.41	1.32	26.5	3.99	3.86	4.14
34X-3, 80	315.74	1.47	1.48	1.34	26.5	3.70	3.69	4.06
34X-5, 57	318.51	1.35	1.39	1.28	26.5	4.05	3.92	4.27
34X-6, 76	320.20	1.45	1.46	1.34	26.5	3.76	3.73	4.07
35X-2, 86	323.90	1.20	1.12	0.96	26.5	4.56	4.85	5.70
35X-4, 81	326.85	1.22	1.26	1.06	26.5	4.47	4.32	5.16
35X-6, 94	329.98	1.30	1.36	1.21	26.5	4.18	4.00	4.51
36X-2, 131	333.95	1.01	1.05	0.77	26.5	5.41	5.21	7.08
36X-4, 5	335.69	1.16	1.16	1.02	26.5	4.71	4.68	5.33
36X-6, 37	339.01	1.33	1.36	1.16	26.5	4.10	4.01	4.70
37X-2, 60	342.84	1.09	1.10	0.91	24.8	4.83	4.82	5.83
37X-4, 120	346.44	1.01	1.04	0.81	24.8	5.24	5.09	6.54
37X-7, 37	350.11	1.01	1.01	0.73	24.8	5.25	5.24	7.24
38X-2, 70	352.54	1.05	1.06	0.71	24.8	5.05	4.98	7.44
38X-4, 75	355.59	1.02	1.03	0.76	24.8	5.20	5.14	6.96
38X-6, 104	358.88	0.92	0.89	0.72	24.8	5.74	5.91	7.34
42X-2, 117	391.51	0.85	0.86	0.73	25.4	6.32	6.18	7.36
42X-4, 85	394.19	0.94	0.90	0.74	25.4	5.67	5.95	7.23
42X-6, 76	397.10	0.91	0.89	0.72	25.4	5.90	6.02	7.44
43X-2, 72	400.66	0.95	0.95	0.69	25.6	5.66	5.62	7.80
43X-4, 68	403.62	0.88	0.88	0.77	25.6	6.07	6.09	6.98
43X-6, 57	406.51	0.87	0.90	0.72	25.6	6.13	5.96	7.49
44X-2, 63	410.17	0.93	0.87	0.74	25.7	5.80	6.18	7.30
44X-4, 113	413.67	0.88	0.93	0.78	25.7	6.09	5.75	6.92
44X-6, 44	415.98	0.91	0.88	0.70	25.7	5.91	6.12	7.70
45X-2, 62	419.76	0.91	0.91	0.75	25.7	5.90	5.89	7.13
45X-3, 103	421.67	0.95	0.94	0.77	25.7	5.65	5.73	6.97
45X-5, 122	424.86	0.93	0.94	0.68	25.7	5.79	5.71	7.94
46X-3, 72	430.96	0.90	0.94	0.66	26.0	6.00	5.74	8.13
46X-6, 101	435.75	0.98	0.87	0.68	26.0	5.53	6.18	8.00
47X-3, 137	440.81	0.86	0.86	0.72	25.1	6.18	6.16	7.39
47X-6, 76	444.70	0.90	0.86	0.64	25.1	5.92	6.14	8.26
48X-2, 62	447.96	0.72	0.90	0.63	25.0	7.34	5.92	8.46
48X-4, 73	451.07	0.84	0.95	0.73	25.0	6.29	5.55	7.25
48X-6, 66	454.00	0.86	0.92	0.67	25.0	6.17	5.77	7.86
49X-2, 47	457.01	0.68	0.83	0.64	25.0	7.80	6.41	8.26
49X-4, 87	460.41	0.71	0.81	0.59	25.0	7.48	6.51	9.06
49X-6, 83	463.37	0.81	0.87	0.66	25.0	6.55	6.10	8.01
50X-2, 65	466.79	0.87	0.84	0.63	25.0	6.10	6.31	8.36
50X-4, 87	470.01	0.89	0.81	0.61	25.0	5.98	6.57	8.70

Table T23 (continued).

Core, section, interval (cm)	Depth (mbsf)	Electrical conductivity			Temp (°C)	Formation factor		
		x	y	z		x	y	z
50X-6, 100	473.14	0.86	0.87	0.62	25.0	6.15	6.07	8.53
51X-2, 67	476.51	0.80	0.81	0.61	25.0	6.59	6.53	8.68
51X-4, 62	479.46	0.78	0.81	0.65	25.0	6.83	6.55	8.11
51X-6, 62	482.46	0.74	0.82	0.61	25.0	7.17	6.48	8.68
52X-3, 60	487.64	0.86	0.83	0.60	25.5	6.21	6.44	8.89
52X-5, 86	490.90	0.76	0.77	0.56	25.5	7.06	6.94	9.48
52X-7, 40	493.44	0.77	0.73	0.56	25.5	6.99	7.29	9.61
53X-2, 40	495.64	0.79	0.80	0.59	25.5	6.76	6.66	9.12
53X-3, 89	497.63	0.75	0.74	0.61	25.5	7.14	7.24	8.83
53X-7, 20	502.94	0.73	0.76	0.54	25.5	7.28	7.04	9.97
54X-4, 72	508.56	0.76	0.74	0.54	24.8	6.95	7.10	9.84
54X-5, 114	510.48	0.70	0.73	0.54	24.8	7.51	7.21	9.76
54X-7, 17	512.51	0.72	0.70	0.52	24.8	7.38	7.53	10.07
55X-2, 55	515.09	0.77	0.72	0.53	25.1	6.87	7.39	9.97
55X-4, 69	518.23	0.75	0.73	0.50	25.1	7.12	7.32	10.72
55X-6, 89	521.43	0.76	0.76	0.49	25.1	6.99	7.02	10.75
56X-2, 79	524.63	0.73	0.75	0.52	26.7	7.48	7.32	10.53
56X-4, 115	527.99	0.77	0.72	0.49	26.7	7.15	7.58	11.21
56X-6, 72	530.56	0.78	0.73	0.54	26.7	7.05	7.54	10.10
57X-2, 42	533.96	0.71	0.71	0.47	25.0	7.51	7.50	11.33
57X-5, 62	538.66	0.71	0.73	0.44	25.0	7.46	7.25	12.05
57X-6, 95	540.49	0.70	0.72	0.46	25.0	7.59	7.31	11.58
58X-2, 101	544.25	0.64	0.70	0.49	25.0	8.26	7.53	10.86
58X-4, 14	546.38	0.70	0.67	0.52	25.0	7.53	7.89	10.19
58X-6, 3	549.27	0.70	0.70	0.62	25.0	7.62	7.57	8.55
59X-2, 70	553.54	0.64	0.72	0.46	25.0	8.33	7.33	11.56
59X-4, 108	556.92	0.73	0.72	0.48	25.0	7.30	7.32	10.96
59X-6, 34	559.18	0.65	0.69	0.49	25.0	8.14	7.67	10.91
60X-2, 30	562.84	0.71	0.71	0.49	25.0	7.45	7.47	10.91
60X-4, 57	566.11	0.65	0.73	0.48	25.0	8.15	7.26	10.97
60X-6, 46	569.00	0.68	0.69	0.54	25.0	7.83	7.69	9.82
61X-2, 71	572.95	0.65	0.77	0.54	25.3	8.23	6.90	9.81
61X-4, 92	576.16	0.72	0.64	0.44	25.3	7.43	8.31	12.19
61X-7, 32	580.06	0.61	0.62	0.45	25.3	8.72	8.54	11.89
62X-2, 60	582.54	0.68	0.70	0.44	25.3	7.80	7.60	12.07
62X-4, 51	585.45	0.64	0.67	0.44	25.3	8.30	7.99	12.19
62X-6, 65	588.59	0.65	0.67	0.43	25.3	8.15	7.95	12.50
63X-1, 83	590.77	0.74	0.67	0.42	24.8	7.16	7.94	12.63
64X-1, 87	600.41	0.67	0.68	0.40	24.8	7.90	7.74	13.11
64X-3, 111	603.65	0.71	0.68	0.43	24.8	7.43	7.74	12.23
64X-5, 51	606.05	0.66	0.65	0.42	24.8	7.95	8.10	12.72
65X-1, 71	609.95	0.68	0.68	0.42	24.7	7.74	7.75	12.54
65X-3, 114	613.38	0.67	0.72	0.46	24.7	7.89	7.28	11.48
65X-5, 3	615.27	0.62	0.64	0.42	24.7	8.50	8.18	12.50
66X-2, 45	620.29	0.62	0.55	0.48	24.5	8.48	9.56	10.89
67X-1, 89	629.33	0.49	0.52	0.38	24.5	10.70	10.03	13.72
67X-3, 85	632.29	0.60	0.59	0.36	24.5	8.72	8.93	14.54
67X-5, 87	635.31	0.49	0.49	0.39	24.5	10.81	10.65	13.44
68X-2, 36	640.00	0.63	0.62	0.39	24.2	8.34	8.49	13.37
68X-4, 91	643.55	0.61	0.59	0.38	24.2	8.62	8.82	13.88
68X-5, 85	644.99	0.57	0.62	0.38	24.2	9.17	8.47	13.74
69X-1, 43	648.17	0.58	0.66	0.44	24.0	8.97	7.88	11.73
69X-3, 94	651.68	0.56	0.61	0.38	24.0	9.27	8.50	13.59
69X-5, 35	654.09	0.55	0.55	0.34	24.0	9.45	9.48	15.13
70X-1, 44	657.88	0.56	0.62	0.36	24.0	9.31	8.43	14.45
70X-3, 25	660.69	0.55	0.52	0.37	24.0	9.37	9.92	14.12
71X-2, 132	669.96	0.52	0.60	0.30	24.0	9.94	8.71	17.45
71X-4, 84	672.48	0.60	0.55	0.36	24.0	8.60	9.48	14.46
72X-1, 98	677.72	0.61	0.52	0.29	24.0	8.58	10.00	17.75
73X-1, 96	687.30	0.57	0.55	0.31	24.0	9.16	9.38	16.94
74X-1, 24	696.18	0.52	0.51		24.0	10.07	10.23	

Note: x, y, z = probe axis.

Table T24. Summary of logging runs, Hole 1173A.

Log run	Tools	Logged interval
1	Hostile environment natural gamma ray sonde (natural gamma) Dual induction tool (resistivity) Accelerator porosity sonde (porosity) Hostile environment lithodensity sonde (lithodensity) Temperature/acceleration/pressure tool	97 to 338 mbsf
2	Hostile environment natural gamma ray sonde (gamma ray) Dual induction tool (resistivity) Accelerator porosity sonde (porosity) Hostile environment lithodensity sonde (lithodensity) Temperature/acceleration/pressure tool	358 to 40 mbsf
3	DSI (dipole sonic imager) Formation MicroScanner Natural gamma sonde (natural gamma)	65 to 373 mbsf

Table T25. Summary of downhole temperature measurements, Hole 1173A.

Depth (mbsf)	Tool	Measurement location	In situ temperature (°C)
35.1	Adara	Bottom of Core 4H	8.48
55.6	WSTP	After Core 6H	12.99
92.6	Adara	Bottom of Core 10H	18.27
111.6	Adara	Bottom of Core 12H	21.82
130.6	Adara	Bottom of Core 14H	24.56
198.1	DVTP	After Core 21H	38.48
284.2	DVTP	After Core 30X	54.16

Note: WSTP = water-sampling temperature probe, DVTP = Davis-Villinger temperature probe.